UNIVERSITY OF CALIFORNIA, SAN DIEGO

SEISMIC DESIGN, TESTING AND ANALYSIS OF REINFORCED CONCRETE WALL BUILDINGS

A dissertation submitted in partial satisfaction of the requirements for the degree

Doctor of Philosophy

in

Structural Engineering

by

Marios Panagiotou

Committee in charge:

Professor José I. Restrepo, Chair
Professor Yehuda Bock
Professor Joel P. Conte
Professor Enrique Luco
Professor Costas Pozrikidis

2008

The Dissertation of Marios Panagiotou is approved, and it is acceptable in quality and form for publication on microfilm:

_____

_____

_____

_____

_____

Chair

University of California, San Diego

2008

To my mother Rena

TABLE OF CONTENTS

LIST OF FIGURES

LIST OF TABLES

NOTATION

Chapter 2

a_g: Amplitude of sinusoidal input motion

C_μ: Nonlinear displacement coefficient

$C_{\mu,EP}$: Nonlinear displacement coefficient of Elastoplastic rule

F_e: Maximum force of elastic SDOF oscillator

F_y: Yield force of elastic SDOF oscillator

K_0: Stiffness of elastic SDOF oscillator or initial stiffness of nonlinear SDOF oscillator

K_u: Unloading stiffness of nonlinear SDOF oscillator with unloading stiffness degradation

M: Mass of SDOF oscillator

R: Force reduction factor

S_a: Spectral acceleration

S_d: Spectral displacement

T: Period of elastic SDOF or period corresponding to initial stiffness of nonlinear SDOF oscillator

T_p: Period of sinusoidal input motion

v: Relative velocity response of SDOF oscillator

v_e: Maximum relative velocity response of linear elastic SDOF oscillator

α: Unloading factor coefficient of nonlinear SDOF oscillator with unloading stiffness degradation

Δ: Relative displacement of SDOF oscillator

Δ_e: Maximum displacement of linear elastic SDOF oscillator

Δ_{in}: Maximum displacement of nonlinear SDOF oscillator

Δ_t: Total displacement

Δ_y: Yield displacement of nonlinear SDOF oscillator

Δ_0: Reference displacement to determine Flag hysteretic rule

ζ: Viscous damping ratio

λ: Scaling parameter of nonlinear response

μ: Displacement ductility

Chapter 3

F_{fi}: Total lateral force at at floor i due to mobilization of framing plastic mechanism at floor i

$F_{fi,c}$: Lateral force at wall with compression framing reactions at floor i due to mobilization of framing plastic mechanism at floor i

F_{fig}: Lateral force at gravity column at floor i due to mobilization of framing plastic mechanism at floor i

F_{fit}: Lateral force at wall with tensile framing reactions at floor i due to mobilization of framing plastic mechanism at floor i

F_{fiw}: Lateral force at wall at floor i due to mobilization of framing plastic mechanism at floor i

h_i: Distance of floor I from base of wall

L_f: Length of framing element

L_w: Length of wall

M_f: Yield moment at end of framing element

M_{fb}: System base moment at system centerline due to framing plastic mechanism in all floors

M_{fbi}: Base bending moment at the wall centerline due to framing reactions at floor i

M_{fbc}: Base bending moment at the wall centerline with compression framing reactions due to mobilization of framing plastic mechanism in all the floors

M_{fbt}: Base bending moment at the wall centerline with tensile framing reactions due to mobilization of framing plastic mechanism in all the floors

M_{fci}: Bending moment at the wall centerline at floor i due to framing reactions

M_{fi}: Yield moment at end of framing element at floor i

N_{fbg}: Axial force ta gravity column base due to mobilization of framing plastic mechanism in all the floors

V_f: Shear force at end of framing element with yield moment on both of its ends

V_{fi}: Shear force at end of framing element with yield moment on both of its ends at floor i

V_{fbc}: Shear force at base of wall with compressive framing reactions due to framing plastic mechanism along all the floors

V_{fbt}: Shear force at base of wall with tensile framing reactions due to framing plastic mechanism along all the floors

V_{fbg}: Shear force at gravity column base due to framing plastic mechanism along all the floors

V_{fbw}: Shear force at wall base due to framing plastic mechanism along all the floors

V_{fb}: System base shear force due to framing plastic mechanism along all the floors

Chapter 4

a_g: Ground acceleration

a_q: Modal acceleration of mode q

a_M: Base moment overstrength amplification factor for design of mid-height plastic hinge

A_w: Cross section area of core wall

a_1: First modal acceleration

a_2: Second modal acceleration

$C_{1,T}$: Mid-height bending moment amplification factor

EI: Section flexural rigidity

EI_e: Effective section flexural rigidity

EI_g: Gross section section flexural rigidity

EI_r: Reloading flexural rigidity of modified Takeda hysteretic rule

F_i: Force at floor i

$F_{q,i}$: Modal force of mode q at floor i

h: Floor height

h_i: Elevation height

h_{eq}: Modal height of mode q

h_{e1}: First modal height

h_{e2}: Second modal height

H: Wall height

i: Floor number

I: Cross section moment of inertia of core wall

L_{p1}: Equivalent plastic hinge length at base

L_{p2}: Equivalent plastic hinge length near mid-height

L_w: Length of wall

m: Lumped seismic mass per floor

M: Bending moment

M_i: Bending moment at floor i

M_0^o: Base bending moment at overstregth

$M_{1,0}$: First modal base bending moment

$M_{2,0}$: Second modal base bending moment

$M_{q,0}$: Modal base bending moment of mode q

$M_{q,i}$: Modal bending moment at floor i of mode q

$M_{q,H/2}$: Modal bending moment at mid-height of mode q

$M_{1,H/2}$: First modal bending moment at mid-height

$M_{2,H/2}$: Second modal bending moment at mid-height

M_t: Total mass

M_y: Reference yield moment

M_0: Base bending moment

M_1: First modal mass

M_2: Second modal mass

n: Number of floors and lumped masses

q: Mode number

P: Axial load acting on wall

r: Post-yield stiffness

R: Lateral force reduction factor

S_a: Spectral acceleration

S_d: Spectral displacement

t: Time

t_w: Thickness of wall

T: Period

T_q: Modal period

T_1: First modal period

T_2: Second modal period

V: Shear force

V_i: Shear force at floor i

$V_{q,0}$: Modal base shear force of mode q

$V_{1,0}$: First modal base shear force

$V_{2,0}$: Second modal base shear force

$V_{q,i}$: Modal shear force at floor i

V_0: Base shear force

W_t: Total seismic weight

w: Sesimic weight per floor

Γ_q: Participation factor of mode q

Δ_i: Lateral displacement at floor i

ε_y: Steel yield strain

Θ_i: Interstory drift ratio

μ: Displacement ductility factor

μ_φ: Curvature ductility factor

$\mu_{\varphi,i}$: Curvature ductility factor at floor i

ρ_l: Longitudinal reinforcing steel ratio

ρ_{lm}: Longitudinal reinforcing steel ratio of midheight plastic hinge of the DPH design concept.

φ^o: Probable flexural overstrength to design moment ratio

φ_y: Yield curvature

φ_u: Ultimate curvature

$\Phi_{q,i}$: Value of modal vector of mode q at floor i

Ω_h: Overstrength factor due to strain hardening

Chapter 5

C_μ: Inelastic displacement factor

C_1: First mode base shear coefficient

E_c: Concrete modulus of elasticity

I_e: Effective section moment of inertia

$F_{1,i}$: First mode lateral force at floor i

g: Acceleration of gravity

H: Wall height

i: Floor number

L_p: Equivalent plastic hinge length at base

m_i: Lumped seismic mass at floor i

M_i: Bending moment at floor i

M_t: Total seismic mass

M_n: Nominal bending moment

M_y: Reference yield moment

M_0: Base bending moment

M_1: First modal mass

n: Number of floors and lumped masses

r: Post-yield stiffness

S_d: Spectral displacement

t_w: Thickness of wall

T: Period

T_{cp}: Collapse prevention design period

T_e: Design effective period

T_{io}: Immediate occupancy design period

V: Shear force

$V_{1,0}$: First modal base shear force

W_t: Total seismic weight

w_i: Sesimic weight at floor i

x: Distance from base of wall to section of interest

Γ_1: First mode participation factor

Γ^*: First mode contribution factor at top floor n

$\Phi_{1,n}$: First mode vector value at top floor n

δ: Lateral displacement

$\delta_{p,n}$: Roof plastic lateral relative displacement

$\delta_{y,i}$: Yield lateral relative displacement at floor i

δ_n: Roof lateral relative displacement

$\delta_{y,n}$: Roof yield lateral relative displacement

$\delta_{u,n}$: Roof ultimate lateral relative displacement

ε_c: Concrete compressive strain

ε_y: Steel yield strain

θ: Interstory drift ratio or cantilever wall sectional rotation

$\theta_{y,n}$: Yield interstory drift ratio at top floor n

$\mu_{\delta u}$: Ultimate displacement ductility factor

μ_φ: Curvature ductility factor

λ: Geometrical coefficient

φ_y: Yield curvature

φ_u: Ultimate curvature

Chapter 6

a: Total floor acceleration (g)

a_g: Ground acceleration (g)

$a_{g,max}$: Peak ground acceleration (g)

$A_{w:}$ web wall cross section

C_S: Base shear coefficient

d_b: Steel rebar diameter (mm)

f_c': concrete compressive strength (ksi)

h: Total building height (m)

l_w: Length of web wall (m)

$M_{b,max}$: Maximum system base moment (kN-m)

M_{oE}: Theoretical web wall moment capacity for maximum measured curvature – Eastwards response (kN-m)

M_{oW}: Theoretical web wall moment capacity for maximum measured curvature – Westwards response (kN-m)

M_{fE}: Moment capacity of East end of slotted connection (kN-m)

M_{fW}: Moment capacity of West end of slotted connection (kN-m)

M_u: Design moment (kN-m)

P: Axial force in web wall (kN)

P_f: Axial force in web wall due to slotted slab connection (kN)

R: Response modification factor

S_a: Spectral acceleration (g)

S_d: Spectral displacement (m)

S_{DS}: Short period spectral response acceleration parameter

S_{D1}: Spectral response acceleration parameter at a T=1 sec

s_h: distance between confinement grids

T: Fundamental period of structure (sec)

T_2: Second mode period of structure (sec)

T_0: $0.2S_{D1}/S_{DS}$

T_S: S_{D1}/S_{DS}

t: Time (sec)

V: Shear force (kN)

V_b: Base shear force (kN)

$V_{b,max}$: Maximum system base shear force (kN)

V_{oE}: Base shear force corresponding to web wall moment capacity M_{oE} (kN)

$v_{g,max}$: Peak ground velocity (m/sec)

V_{oW}: Base shear force corresponding to web wall moment capacity M_{oW} (kN)

V_f: Shear force of slotted slab connection (kN)

V_p: Web wall probable shear strength (kN)

V_s: shear strength provided from shear reinforcement

V_u: Design shear force (kN)

W: Total seismic weight excluding foundation weight (kN)

Ω_{oM}: System moment overstrength

Ω_{os}: Section flexural overstrength

Ω_{oV}: System shear overstrength

γ: Normalized height of position of resultant lateral force

ε_s: Reinforcing steel strain

ε_y: Reinforcing steel yield strain

μ_φ: Curvature ductility

$\Theta_{r,max}$: Maximum roof drift ratio

ρ_l: Web wall longitudinal reinforcement ratio

ρ_{sh}: Web wall transverse reinforcement ratio

ρ_v: Confinement ratio in boundary elements

φ_y: Reference yield curvature (rad/m)

Chapter 7

a: Total floor acceleration (g)

a_g: Ground acceleration (g)

$a_{g,max}$: Peak ground acceleration (g)

$A_{w:}$ web wall area

C_S: Base shear coefficient

d_b: Steel rebar diameter (mm)

f_c': concrete compressive strength (ksi)

h: Total building height (m)

l_w: Length of web wall (m)

$M_{b,max}$: Maximum system base moment (kN-m)

M_{oE}: Theoretical web wall moment capacity for maximum measured base curvature – Eastwards response (kN-m)

M_{oW}: Theoretical web wall moment capacity for maximum measured base curvature – Westwards response (kN-m)

P: Axial force in web wall (kN)

S_a: Spectral acceleration (g)

S_d: Spectral displacement (m)

S_{DS}: Short period spectral response acceleration parameter

S_{D1}: Spectral response acceleration parameter at a T=1 sec

s_h: distance between confinement grids

T: Fundamental period of structure (sec)

T_2: Second mode period of structure (sec)

T_0: $0.2S_{D1}/S_{DS}$

T_S: S_{D1}/S_{DS}

t: Time (sec)

V_b: Base shear force (kN)

$V_{b,max}$: Maximum system base shear force (kN)

V_{oE}: Base shear force corresponding to web wall moment capacity M_{oE} (kN)

$v_{g,max}$: Peak ground velocity (m/sec)

V_{oW}: Base shear force corresponding to web wall moment capacity M_{oW} (kN)

V_p: Web wall probable shear strength (kN)

V_s: shear strength provided from shear reinforcement

W: Total seismic weight excluding foundation weight (kN)

γ: Normalized height of position of resultant lateral force

ε_s: Reinforcing steel strain

ε_y: Reinforcing steel yield strain

μ_φ: Curvature ductility

$\Theta_{r,max}$: Maximum roof drift ratio

ρ_l: Web wall longitudinal reinforcement ratio

ρ_{sh}: Web wall transverse reinforcement ratio

ρ_v: Confinement ratio in boundary elements

φ_y: Reference yield curvature (rad/m)

Chapter 9

$A_{c,d}$: Area of diagonal concrete strut truss elements

b_w: Width of wall

E_c: Concrete modulus of elasticity

E_s: Reinforcing steel modulus of elasticity

F_{y1+}: First characteristic positive yield force for determination of hysteretic rule

F_{y2+}: Second characteristic positive yield force for determination of hysteretic rule

F_{y1-}: First characteristic negative yield force for determination of hysteretic rule

F_{y2-}: Second characteristic negative yield force for determination of hysteretic rule

f_c': Concrete compressive strength

f_{cc}': Confined concrete strength

f_{ct}: Concrete tensile strength

f_y: Reinforcing steel yield strength

f_{ct}': Concrete tensile strength

h: Reference height of wall panel

K: Characteristic stiffness for determination of hysteretic behavior

K_{1+}: First reference stiffness for determination of hysteretic behavior

K_{2+}: Second reference stiffness for determination of hysteretic behavior

K_{1-}: First reference stiffness for determination of hysteretic behavior

K_{2-}: Second reference stiffness for determination of hysteretic behavior

l_w: Length of wall

l_d: Length of diagonal of wall panel

M_{cr}: Cracking moment

M_{fW}: Moment capacity of West end of slotted slab

M_{fE}: Moment capacity of East end of slotted slab

M_{cr}: Cracking moment

M_y: Yield moment for definition of hysteretic rule

n: Number of one direction diagonal concrete strut truss elements per panel

r: Post yield stiffness ratio

T_1: First mode period

T_2: Second mode period

ε_{cr}: Concrete cracking strain

ACKNOWLEDGEMENTS

The research work reported in this dissertation was carried out in the Department of Structural Engineering at the University of California San Diego under the guidance of Professor J. Restrepo.

The author sincerely thanks the Englekirk Board of Advisors, the Charles Pankow Foundation, the Portland Cement Association who provided financial support for this research work.

Special thanks are given to Professors E. Luco and J. Conte for the technical cooperation, their permanent interest, support and the fruitful discussions during these years.

In special I thank also Professor Robert Englekirk who gave me the opportunity to be the primary graduate student researcher in one of the greatest experimental efforts, like this of the UCSD 7-story building test.

I would like also to thank Professor F. Seible who brought me to UCSD after our personal contact in Athens in June 2003. This personal contact was after personal initiative of Professor I. Sigalas.

I express my deepest thanks to Professor I. Sigalas for his decisive contribution in the first steps of my graduate studies and his constant support all these years.

I owe my deepest thanks and gratitude to my supervisor Professor J. Restrepo for his invaluable technical advice, support and inspiration. Especially I thank him for giving me the opportunity to live five years close to a person of high ethics.

Finally I express my deepest gratitude to my father Agis, my mother Rena and my brother John for their continuous support and encouragement.

VITA, PUBLICATIONS AND FIELDS OF STUDY

VITA

June 2003	Diploma in Civil Eng., National Technical University of Athens
March 2005	M. Sc., Struct. Eng. University of California San Diego
June 2008	Ph. D., Structural Engineering, University of California San Diego

PUBLICATIONS

1. Hoehler, M.S., Panagiotou, M., Restrepo, J.I., Silva, J.F., Floriani, L., Bourgund, U., and Gassnerc, H., "Performance of Anchored Pipes in a 7 Story Building During Full-Scale Shake Table Tests". (Submitted for review January 2008 - Earthquake Spectra).

2. Panagiotou, M., and Restrepo, J.I., "Dual Plastic Hinge Concept for Arresting Higher Mode Effect on High-Rise Cantilever Wall Buildings". (Submitted for review - May 2008 - Earthquake Engineering and Structural Dynamics).

3. Panagiotou, M., Restrepo, J.I., and Conte J.P., "Shake Table Test of a 7-Story Full Scale Reinforced Concrete Wall Building Slice - Phase I - Rectangular Wall". (To be submitted in ASCE Journal of Structural Engineering).

4. Panagiotou, M., and Restrepo, J.I., "Shake Table Test of a 7-story Full Scale Reinforced Concrete Wall Building Slice - Phase II - T Wall". (To be submitted in ASCE Journal of Structural Engineering).

5. Panagiotou, M., and Restrepo, J.I., "Dynamic Nonlinear Strut and Tie Model

Calibration for the UCSD 7-Story Building Slice". (To be submitted to ACI Structural Journal).

6. Panagiotou, M., and Restrepo, J.I., "Non-Dimensional Response of Nonlinear SDOF Oscillators subjected to Sinusoidal Impulsive Excitation". (To be submitted in Earthquake Engineering and Structural Dynamics*)*.

7. Panagiotou, M., Geonwoo, K., and Restrepo, J.I., "Nonlinear Strut and Tie Modeling Shear-Critical Reinforced Concrete Walls". (under preparation).

8. Panagiotou, M., and Restrepo, J.I., "Modified lateral force procedure for seismic design of structural wall buildings". (under preparation).

9. Panagiotou, M., and Restrepo, J.I., "A two-performance level displacement based design approach for structural wall buildings". (under preparation).

FIELDS OF STUDY

Major Field: Structural Engineering

RESEARCH INTERESTS - AREAS OF SPECIALIZATION

- Performance-based Seismic Design of Structures.
- Dynamic Testing of Structures and Components.
- Dynamic Nonlinear Response of Structures and Nonstructural Components.
- Characterization of Earthquake Ground Motions for Analysis and Design
- Concrete Mechanics
- Dynamic Soil-Structure Interaction

ABSTRACT OF THE DISSERTATION

SEISMIC DESIGN, TESTING AND ANALYSIS OF REINFORCED CONCRETE WALL BUILDINGS

by

Marios Panagiotou

Doctor of Philosophy in Structural Engineering

University of California, San Diego, 2008

Professor José I. Restrepo, Chair

Large investments have recently been made for the construction of new medium- and high-rise buildings in California. In many cases performance-based designs have been the preferred method for these buildings. A main consideration in performance-based seismic design is the estimation of the likely development of structural and nonstructural damage limit-states given a hazard level. For this type of buildings efficient modeling techniques are required able to compute the response at different performance states. A research work was conducted at University of California San

Diego (UCSD) on the i) seismic design, ii) experimental response and iii) computational modeling of medium- and high-rise reinforced concrete wall buildings.

In the first part of this work a displacement-based seismic design method for use within performance-based is developed. Capacity design is used to control the mechanism of inelastic deformation. Based on principles of plastic analysis and structural dynamics the new formulation allows the computation of the effects of system overstrength and of the higher modes of response. Equal emphasis is given to displacement, force and acceleration demand parameters. The ground motion destructiveness potential is also determined. Application of the method to reinforced concrete wall buildings is discussed. The method is validated with the experimental response of a full-scale 7 story building. In addition a dual plastic hinge design concept for improving the performance and optimizing the construction of high-rise buildings is presented.

The second part presents the experimental research program, with extensive shake table tests, of a full-scale 7-story reinforced concrete wall building slice, that was conducted at UCSD. The base shear coefficient obtained by the proposed method, of the first part of the research work, described above was 50% of that required by the equivalent static method prescribed by the ASCE-7 code. In spite of the reduced amount of longitudinal reinforcing steel, all performance objectives were met. The response of the building was significantly influenced, as expected, by the interaction

of the main lateral force resisting wall with other structural elements (kinematic overstrength) and by the higher modes of response.

Finally the third part presents a dynamic nonlinear strut-and-tie modeling approach developed for the analysis and evaluation of damage limit-states in reinforced concrete walls. The modeling approach is verified with the response of the UCSD 7-story building test.

CHAPTER 1

1. INTRODUCTION

1.1 Background

Large investments have recently been made for the construction of new medium- and high-rise buildings in California. However, and quite paradoxically, buildings incorporating structural walls can be prohibitively expensive and difficult to build in the state. Structural engineers have often questioned that the current design lateral forces for structural wall buildings renders this attractive lateral force resisting system largely uneconomical and that significant savings could be made if lateral forces could be reduced, particularly in the foundation and in the lower levels of the walls where heavy congestion is observed.

At the same time, although current code seismic design procedures are still force-based dominated the concept of performance-based design is increasingly promoted not only in the scientific community but also in practice. As design provisions move toward meeting specific levels of performance, current codes are largely prescriptive and empirical. Future codes will include performance objectives in an attempt to limit both structural and non-structural damage. Development of seismic design procedures that lead to buildings that meet the functional construction and ultimately cost objectives but also attain seismic performance objectives is required. Moreover efficient computational approaches, which can be used both by

practitioners and researchers, able to compute the damage states of this type of buildings are required to support the performance-based design framework.

1.2 Performance-based design (PBD)

Over the last decade performance-based design has been promoted not only in the scientific community but also in practice. Performance objectives are expressed as an acceptable level of damage such as immediate occupancy, life safe or collapse prevention, given intensity of ground motion and importance classification of the structure.

The ATC-33 project, sponsored by the Federal Emergency Management Agency (FEMA), for the seismic retrofit of buildings, was the first standardization of performance-based design. In ATC-33 performance levels are predicted through the use of specific design parameters (element force and displacement demands). This approach was adopted by SEAOC's (Structural Engineers Association of California) Vision 2000 project (SEAOC 1995) and extended to include the design of new buildings. The FEMA-273 NEHRP (National Earthquake Hazard Reduction Program) Guidelines for Seismic Rehabilitation of Buildings (FEMA 1997), resulting from the ATC-33 project, and the Vision 2000 report define the current state of practice in performance-based engineering. Both in the FEMA-273 and the Vision 2000 report the design is component- rather than system-based.

1.3 Displacement-based Design (DBD)

Within the framework of performance-based design a number of interesting displacement-based design approaches have been developed over the last few decades. Sullivan et al. (2003) reviewed a number of methods available in the literature and a state-of-the-art report was issued on this topic (Fib 2003). One of the claims is that few of these methods are suitable for design because they have only been developed partially and can only be used if the geometry of the sections is known a priori. In addition almost all do not account for the dynamic effects of the higher modes, while none of these methods explicitly address the effect of kinematic overstrength discussed in Chapter 3.

1.4 Experimental Work on the Seismic Response of Reinforced Concrete Wall Buildings

A variety of quasi-static cyclic tests of RC walls have been conducted. Fiorato et al. (1983) tested three 1/ 3 RC wall of I-shape cross section. Mestyanek (1986) reports three 1 / 3 to 1 / 2 scale model walls failing in shear. Taylor et al. (1998) and Thomsen and Wallace (2004) tested six 1 / 4 scale wall specimens with rectangular, T-wall and barbell-shaped cross sections including wall specimens with openings at their base. Salonikios et al. (1999) tested eleven wall specimens with aspect ratio less than 1.5. Massone (2004) tested 10 shear critical 1 / 3 scale wall specimens. Ile et al. (2005) tested three full scale U–shape wall specimens.

The number of the dynamic (shake-table) experimental studies of RC walls which has been conducted is smaller. Bertero et al. (1984) tested a 1 / 5 scale five-story frame - wall dual system. Pinho (2000) tested different large scale wall specimens. Coehlo et al. (2006) tested dynamically on a shake table a 1 / 3 scale of a five-story building including the floor slabs consisted of an H-section wall with openings in the web part of the wall at every floor. Lestuzzi and Bachmann (2007) tested six 1 / 3 scale walls.

1.5 Modeling of Reinforced Concrete Wall Buildings

The modeling approaches for RC walls can be divided in to three main categories: i) Microscopic finite element (FE) methods, ii) Fiber element models, iii) Macroscopic strut-and-tie methods.

Finite-element methods using the smeared and discreet crack approaches and advanced nonlinear-material models have been developed by Cervenka and Gerstle (1971), Stevens et al. (1991), Maekawa et al. (2003). Finite-element methods using plasticity models have been developed by Hibbit et al. (2002), Feenstra and de Borst (1993), Park and Klingner (1997).

Fiber element models have been used by Petrangeli (1999). Orakcal et al. (2004) developed a model of multiple vertical elements, similar to the fiber element models, to model RC walls.

Lattice and strut-and-tie models have been also been used to evaluate the nonlinear behavior of RC structures and members. To et al. (2001, 2003) and Park et al. (2007), used strut-and-tie models for the nonlinear analysis of RC beams, columns, and their subassemblies subjected to monotonic or cyclic loading. Further, Miki (2004) used a nonlinear lattice model to estimate the monotonic, cyclic and the dynamic response of columns and piers.

1.6 Dissertation Summary

This dissertation is divided in to three main parts discussing the i) seismic design, ii) experimental response, and iii) computational modeling of reinforced concrete wall buildings. It is consisted of ten chapters. Chapters 2 to 5 cover the theoretical aspects of this work on the seismic design of RC wall buildings. Chapters 6 to 8 present the experimental aspects on RC wall buildings and Chapter 9 discusses the computational modeling of RC wall buildings. Chapter 10 includes the conclusions and the recommendations based on this work.

The first part (Chapters 2 to 5) presents the development of a new displacement-based seismic design method for use within performance-based. Capacity design is used to control the mechanism of inelastic deformation. Based on principles of plastic analysis and structural dynamics this new formulation allows the computation of the effects of system overstrength and of the higher modes of response. Equal emphasis is given to displacement, force and acceleration demand parameters. Determination of the ground motion destructiveness potential is also

included in the method. Application of the method to high-performance multistory reinforced concrete core-wall buildings is discussed. The method is compared with the experimental response of a full-scale 7 story building. The development of a dual plastic hinge design concept for improving the performance of high-rise buildings is also presented.

The second part (Chapters 6 to 8) presents the experimental research program, with extensive shake table tests, of a full-scale 7-story reinforced concrete wall building slice, that was conducted at UCSD. The base shear coefficient obtained by the proposed method described above was 50% of that required by the equivalent static method prescribed by the ASCE-7 code. In spite of the reduced amount of longitudinal reinforcing steel, all performance objectives were met. The response of the building was significantly influenced, as expected, by the interaction of the main lateral force resisting wall with other structural elements (kinematic overstrength) and by the higher modes of response.

Finally the third part (Chapter 9) presents a dynamic nonlinear strut-and-tie modeling approach developed for the analysis and evaluation of damage limit-states in reinforced concrete walls. The modeling approach is verified with the response of the UCSD 7-story building test as well with the experimental response of walls failing in shear.

1.6.1 Chapter 2 - Response of Nonlinear SDOF Oscillators to Pulse-type Excitations

This chapter investigates the response of nonlinear single degree of freedom (SDOF) oscillators, of different hysteretic behavior, subjected to three kinds of sinusoidal pulse-type excitation. These type of motions can represent many of the characteristics of strong near fault earthquakes. The nonlinear response is presented in a specific normalized form using the equal ductility response spectra, where the key parameter is the ratio of the initial period of the SDOF to the period of the input motion T / T_P. Six types of nonlinear piecewise linear hysteretic rules, representing different types of structural systems, are considered. A clear trend between the shape of the hysteretic rule and the maximum displacement demand is revealed. Force reduction factors and the relation between the maximum linear and nonlinear displacement demand are presented. Design implications based on the hysteretic characteristics of the nonlinear SDOF and the input motion are addressed.

1.6.2 Chapter 3 - Kinematic Overstrength in RC Wall Buildings

This chapter discusses the effect of framing in buildings with walls as the main lateral force resisting elements. Framing in this type of buildings occurs through framing beams or floor slabs. Based on fundamental concepts of structural mechanics and plastic analysis, the effect of framing is estimated for the cases of framing between walls or framing between wall and gravity columns. Simplified expressions for the developed lateral forces in the different elements and the corresponding bending moment and shear forces due to framing are presented.

1.6.3 Chapter 4 - Effect of Higher Modes and a Dual Plastic Hinge Concept for Arresting Higher Modes Effects on High-Rise Cantilever RC Wall Buildings

The first part of this chapter discusses the effect of higher modes in cantilever wall buildings. Lumped mass Euler-Bernoulli cantilevers are used to obtain instantaneous modal characteristics, applicable to linear and nonlinear response. Study of the modal characteristics helps to better understand the effect of higher modes on the nonlinear dynamic response of tall buildings.

The second part of this chapter presents a dual plastic hinge design concept to better control the seismic response of tall reinforced concrete cantilever wall buildings to strong shaking. This concept is prompted by the need to arrest the effect of the higher modes of response, which can significantly increase the flexural demands in these buildings and to optimize construction. Buildings with 10, 20 and 40 stories are designed under three different approaches: ACI-318, Eurocode 8, which has similar provisions to the New Zealand 3101 concrete design standard, and the proposed dual plastic hinge concept. The buildings are designed for and subjected to three specific historical strong near-fault ground motions. The investigation clearly shows the dual hinge design concept is effective at arresting the effects of the second mode of response. An advantage of the concept is the relaxation of the reinforcement details in large portions of the walls.

1.6.4 Chapter 5 - Seismic Design of RC Wall Buildings

This chapter presents a displacement-based seismic design approach for reinforced concrete wall buildings. The method focuses on buildings where all the nonlinear response is developed at a single plastic hinge at the base of the walls. Two distinct performance levels are considered: immediate occupancy and collapse prevention. Initially only the first mode of response is employed to estimate the required base strength. In a second stage the effects of kinematic overstrength and the dynamic effect of the higher modes, discussed in Chapters 3 and 4, respectively, are considered to estimate the maximum shear force demand along the height of the walls.

1.6.5 Chapter 6 - UCSD Shake Table Test of a 7-Story RC Wall Building – Phase I – Rectangular Wall

This chapter presents Phase I of the experimental aspects of this research study. Key results gained from a 7-story reinforced concrete building slice built at full-scale and tested on the NEES-UCSD Large Outdoor High-Performance Shake Table are presented. The building was tested in two phases. In Phase I the building had a rectangular load bearing wall acting as the main lateral force resisting element. The seismic design of the building followed a displacement-based design approach for specific performance objectives at two hazard levels. The design resulted in a reduced amount of longitudinal reinforcement in the wall compared to that required by current code force-based methods. The building was subjected to four historical input ground motions recorded in California, including the strong intensity near-fault Sylmar record of the 1994 Northridge earthquake that induced significant nonlinear response. The

building responded very satisfactory to the motions and met all performance objectives. Important results regarding the effect of coupling between walls and the slab on the system overstrength and the effect of higher modes are discussed.

1.6.6 Chapter 7 - UCSD Shake Table Test of a 7-Story RC Wall Building – Phase II – T-Wall

This chapter presents Phase II of the experimental aspects of this research study. In Phase II the main load bearing wall was reconfigured as a T-wall with moderate amount of longitudinal reinforcement, acting as the main lateral force resisting element. The main objective of this Phase was to test the effect of the flange, which was not connected to the web wall during Phase I of the test program, in a load bearing T-wall. The building was subjected to four historical input ground motions recorded in California, including the strong intensity near-fault Sylmar record. The building responded satisfactorily to the motions. Important results regarding the effect of flange in tension, the interaction between the wall and the slab, and the higher modes effect are presented.

1.6.7 Chapter 8 - UCSD Shake Table Test of a 7-Story RC Wall Building – Phase II – Non Structural Components Response

This chapter presents the experimental response of the non-structural components during Phase II of the 7-story RC wall building test discussed in Chapter 7. The non-structural components consisted of pipe systems anchored on the

building. These tests also provide data on floor accelerations and acceleration amplification for nonstructural components in buildings during seismic events.

1.6.8 Chapter 9 - Computational Modeling of RC Wall Buildings

This chapter presents the research work on the computational modeling of RC wall buildings. A nonlinear strut and tie modeling approach for reinforced concrete walls is developed. The proposed model physically implements shear-flexure interaction due to yielding of horizontal reinforcement and crushing-softening of diagonal concrete struts. Longitudinal, transverse and variable angle diagonal truss elements are used to represent the concrete and the reinforcing steel of reinforced concrete wall panel. Nonlinear stress-strain relationships are used to model the hysteretic material behavior. The modeling approach is verified through the reproduction of the experimental response of Phase-I of the UCSD 7-Story building test, discussed in Chapter 6.

CHAPTER 2

2. NON-DIMENSIONAL RESPONSE OF NONLINEAR SDOF OSCILLATORS SUBJECTED TO SINUSOIDAL IMPULSIVE EXCITATION

2.1 Summary

This study investigates the response of nonlinear single degree of freedom (SDOF) oscillators, of different hysteretic behavior, subjected to three kinds of sinusoidal pulse-type excitation. These types of motion can represent many of the characteristics of strong near fault earthquakes. The nonlinear response is presented in a specific normalized form using the equal ductility response spectra, where the key parameter is the ratio of the initial period of the SDOF to the period of the input motion T / T_P. Six types of nonlinear piecewise linear hysteretic rules, representing different types of structural systems, are considered. A clear trend between the shape of the hysteretic rule and the maximum displacement demand is revealed. Force reduction factors and the relation between the maximum linear and nonlinear displacement demand are presented. Design implications based on the hysteretic characteristics of the nonlinear SDOF and the input motion are addressed.

2.2 Introduction

The estimation of the displacement demand of a structure is of primary concern in seismic design. The elastic response spectrum has historically been the main tool for establishing displacement demands, even for structures which are deliberately designed to respond well into the nonlinear domain. In order to make a consistent use of the elastic response spectrum, a relation between the maximum inelastic and elastic displacement is required. Code provisions (ASCE 2006, FEMA 2000) use period dependent coefficients to estimate the nonlinear displacement demand from the elastic design spectrum. Recently developed displacement-based methodologies (Restrepo and Preti 2006, Priestley et al. 2007) also require the relation between the linear and nonlinear displacement demands.

Some near fault earthquake ground motions are characterized by distinct acceleration, velocity and displacement pulses. These pulses are the result of fault rupture directivity effects, first described by Housner and Trifunac (1967). The effect of near fault records on flexible structures was first extensively discussed by Bertero et al. (1978). Near fault records have been correlated in studies with physical characteristics such as the magnitude of the earthquake, the distance from the fault and the type of rupture (Abrahamson 2000, Alavi 2000, Mavroeidis 2004, Somerville 2000 and 2003). These pulses can be represented by simple waveforms which capture many of the characteristics of the strong near fault earthquake records.

The normalized response of an elasto-plastic SDOF oscillator to strong ground motion and sinusoidal pulses was first presented in the pioneering work of Veletsos and Newmark (1960) and Veletsos et al. (1965). In these studies the response of the elastic-plastic system was normalized to the response of an elastic system having the same stiffness as the initial stiffness of the inelastic system. The normalization of the inelastic response to the response of the linear SDOF oscillator and the derivation of equal ductility spectra (Veletsos 1965, Chopra 2001) is widely used in response analysis. Lateral force reduction factors R or behavior factors are central quantities in force-based seismic design codes.

Makris (2004) made a significant contribution. He used the concept of self similarity to present the response of an inelastic SDOF to sinusoidal input motions, in a non-dimensional form. In this study the nonlinear response was normalized to the characteristics of the sinusoidal input ground motion.

Mavroeidis (2004) used waveforms to study the nonlinear response of SDOF oscillator to near fault ground motions. Mavroeidis (2003) and Ruiz-Garcia (2003) presented the nonlinear response of elastoplatic systems to near field ground motions. These studies presented mean value results of equal ductility spectra of elastoplastic SDOF oscillator, subjected to real or simulated pulse type excitations. In the studies of (Mavroeidis 2003, Ruiz-Garcia 2003) the period of the pulse, T_p, or the main period component of the input motion were key parameters. These periods were used to present the nonlinear response in a normalized form.

The main advantage of normalization is that the response of a nonlinear SDOF oscillator subjected to a single frequency sinusoidal pulse, is only dependent on two ratios: the force reduction factor R defined as the ratio of the maximum elastic force to the yielding force of the nonlinear oscillator and T / T_p the ratio of the initial period of the structure to the period of the sinusoidal pulse. Based on this key observation, the relation between the response of the linear and nonlinear SDOF oscillator subjected to pulse-type sinusoidal excitation depends only on the ratio T / T_p for any target ductility μ.

2.3 Definitions

Fig. 2.1(a) shows a schematic representation of the linear and nonlinear force-displacement response of a SDOF oscillator. The ratio of the maximum force of the linear oscillator F_e to the to the yielding force of the nonlinear oscillator F_y, defines the strength reduction or behavior factor R (Eq. 2.1). The ratio of the maximum displacement of the nonlinear oscillator Δ_{in} to the to the maximum displacement of the linear oscillator Δ_e, defines the the inelastic displacement factor C_μ (Eq. 2.2). C_μ is related to the force reduction factor R through the displacement ductility μ, defined as the ratio of the maximum Δ_{in} to the yield displacement Δ_y of the nonlinear SDOF oscillator (Eq. 2.3), based on Eq. 2.4. In Eq. 2.4 K_0 is the stiffness of the linear SDOF and equal to the initial stiffness of the nonlinear SDOF oscillator.

$$R = \frac{F_e}{F_y} \tag{2.1}$$

$$C_\mu = \frac{\Delta_{in}}{\Delta_e} \tag{2.2}$$

$$\mu = \frac{\Delta_{in}}{\Delta_y} \tag{2.3}$$

$$C_\mu = \frac{\mu\Delta_y}{RF_y / K_0} = \frac{\mu\Delta_y}{R\Delta_y} = \frac{\mu}{R} \tag{2.4}$$

The main control parameters of a nonlinear SDOF oscillator are: the yielding force F_y, the yielding displacement Δ_y, the initial stiffness $K_0 = F_y / \Delta_y$ and the post yield stiffness ratio r which defines the ratio of the post-yield to the initial stiffness K_0. If M is the mass of the linear or nonlinear SDOF oscillator, its corresponding period or initial period is $T = 2\pi(M/K_0)^{1/2}$. Further parameters are required to define the response characteristics of nonlinear oscillators exhibiting hysteretic response that is more complex than those observed for an elasto-plastic oscillator.

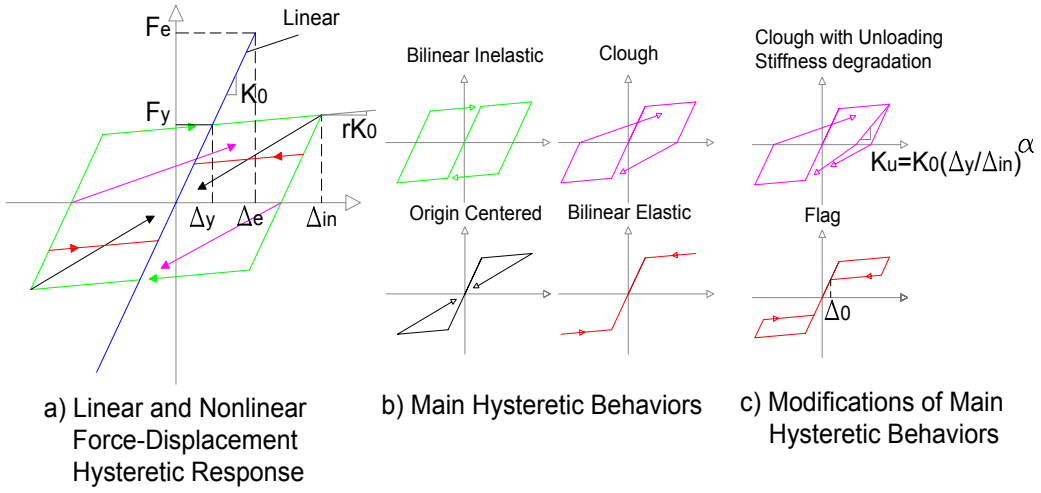

Figure 2.1. (a) Linear and Nonlinear Force-Displacement Hysteretic Response of SDOF oscillator (b) Characteristic nonlinear hysteretic behaviors c) Modifications of Main Hysteretic Behaviors.

Fig. 2.1(b) plots the hysteretic response characteristics of the SDOF oscillators considered in this study. Four piecewise linear hysteretic rules are considered: The

Bilinear Inelastic response representing the behavior of a steel structure, the Clough hysteretic response representing a reinforced concrete structure, the Origin Centered response and the Nonlinear Elastic corresponding to a precast concrete structure incorporating unbonded tendons and discrete gap openings. The Flag response is modification of the nonlinear elastic response with supplemental hysteretic damping. For the fully determination of this rule the additional parameter Δ_0 is required to describe the supplemental hysteretic damping after yielding. The Clough response with stiffness degradation is a modification of the Clough hysteretic rule with stiffness degradation during the unloading part. The stiffness in the unloading part K_u is controlled from the unloading parameter α which relates the initial and the unloading stiffness.

2.4 Non-Dimensional Response of Nonlinear SDOF Oscillators

Fig. 2.2 shows the two key aspects of the non-dimensional character of the response of a nonlinear SDOF oscillator subjected to a sinusoidal input motion of period T_P. For clarity Fig. 2.2 shows the monotonic envelope of the nonlinear response. The normalized response is independent of the amplitude of the motion a_g. If μ is the displacement ductility of a non-linear SDOF oscillator of strength F_y and initial stiffness K0 to a sinusoidal input motion of period T_P and amplitude ag, then also μ is the displacement ductility of a non-linear SDOF oscillator of strength λF_y and initial stiffness K_0 to a sinusoidal inputs motion of period T_P and amplitude λa_g. The normalized response is independent also from the period of the motion. If μ is the displacement ductility of a non-linear SDOF oscillator of strength F_y and initial

stiffness K_0 to a sinusoidal input of period T_P and amplitude a_g, then also μ will be the displacement ductility of a non-linear SDOF oscillator of strength F_y and initial stiffness $(1 / \lambda)K_0$ to a sinusoidal input of period λT_P and amplitude a_g.

The normalized response of a nonlinear SDOF oscillator to a sinusoidal input motion depends on: (a) the normalized strength of the oscillator to the amplitude of the motion F_y / a_g (b) the normalized initial period of the oscillator to the period of the pulse T / T_P and not on the single value of the amplitude and the period of the motion. The normalized response of a linear SDOF oscillator (F_e, Δ_e) subjected to single frequency sinusoidal excitation depends also only on T / T_P. Thus the normalized nonlinear to the linear response of a SDOF oscillator subjected to a single frequency sinusoidal input motion, for any target ductility μ, depends only on the ratio T / T_P.

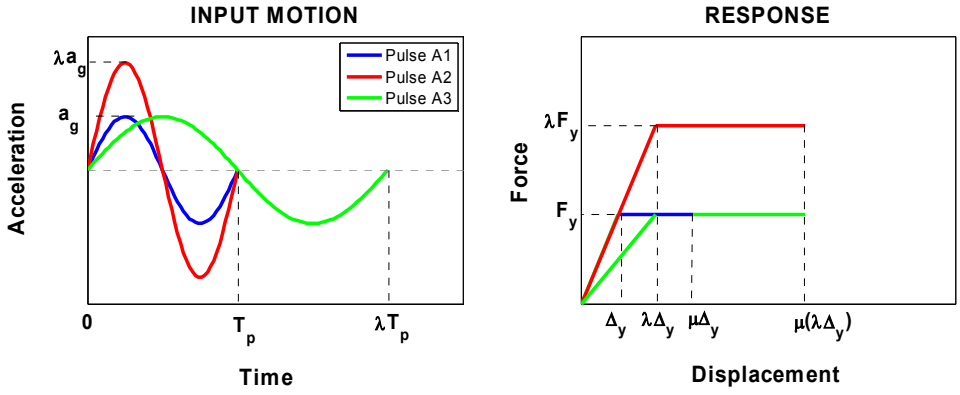

Figure 2.2. Non-dimensional character of nonlinear response to (a) amplitude, (b) period of motion.

2.5 Selection of Sinusoidal Pulse -Type Excitations

Three sinusoidal pulses, representing some of the main kinematics of strong ground motions, are considered (Makris 2004). Fig. 2.3 plots the acceleration, velocity

and displacement time histories of the three pulses considered for the same peak ground acceleration and same frequency content (period of pulse T_P). Pulse A corresponds to a forward ground displacement, Pulse B to a forward and backward (half cycle) ground displacement and Pulse C to a complete cycle of ground displacement. These type of pulses have been observed in many near fault records and in many cases can be directly correlated to the type of dislocation. Pulse A and B have the same duration but pulse C is longer.

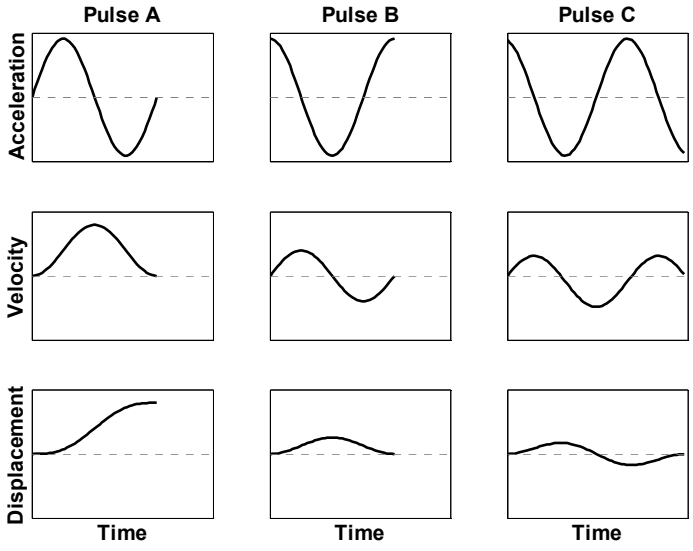

Figure 2.3. Sinusoidal pulses of same maximum acceleration. Acceleration, velocity and displacement time histories.

2.6 Equal Ductility Response Spectra for Sinusoidal Pulses

This section presents equal ductility inelastic response spectra for the three sinusoidal pulses considered. Zero viscous damping is used to investigate only the effect of the hysteretic response. The analysis was performed using the computer program Inspect of the computer suit Ruaumoko (Carr 1998). The sample period is

0.006 sec and the convergence error of the target ductility is equal to 1%. The analysis includes the free vibration part of the response during which the maximum nonlinear displacement response occurs in some cases.

Fig. 2.4 plots the inelastic displacement factors C_μ versus the period ratio, of the initial (elastic) period of the SDOF to the pulse period T / T_p, for four different target ductilities μ, for the four main hysteretic behaviors considered. Fig. 2.5 plots the force reduction factor R versus the period ratio T / T_P for the same ductilities and hysteretic rules. Figs 2.4 and 2.5 are two ways of presenting the normalized equal ductility inelastic response spectra for different hysteretic rules.

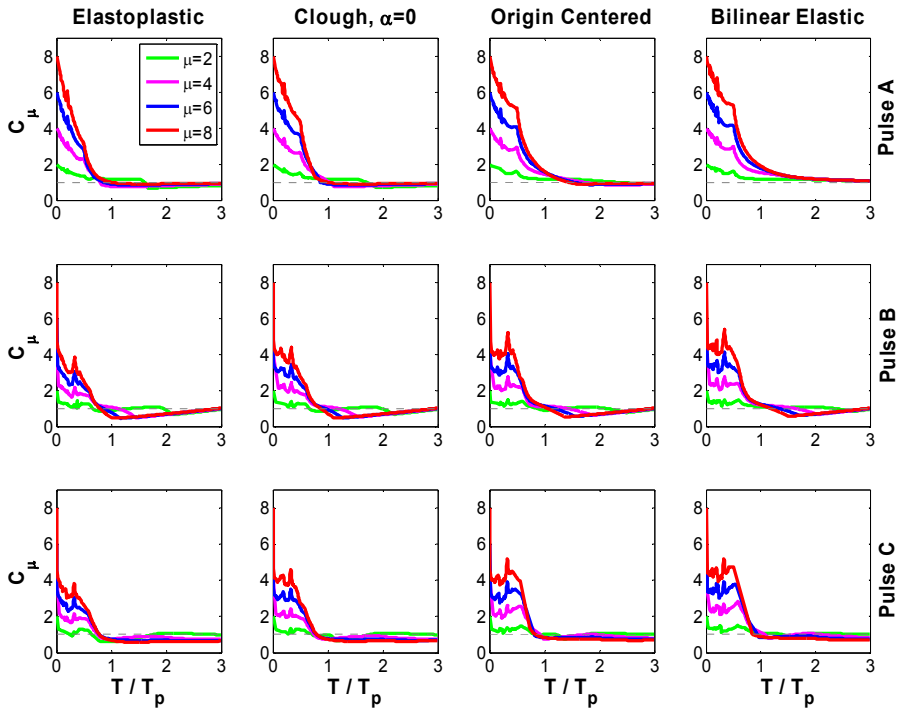

Figure 2.4. Equal ductility inelastic response spectra in terms of C_μ, r=0.

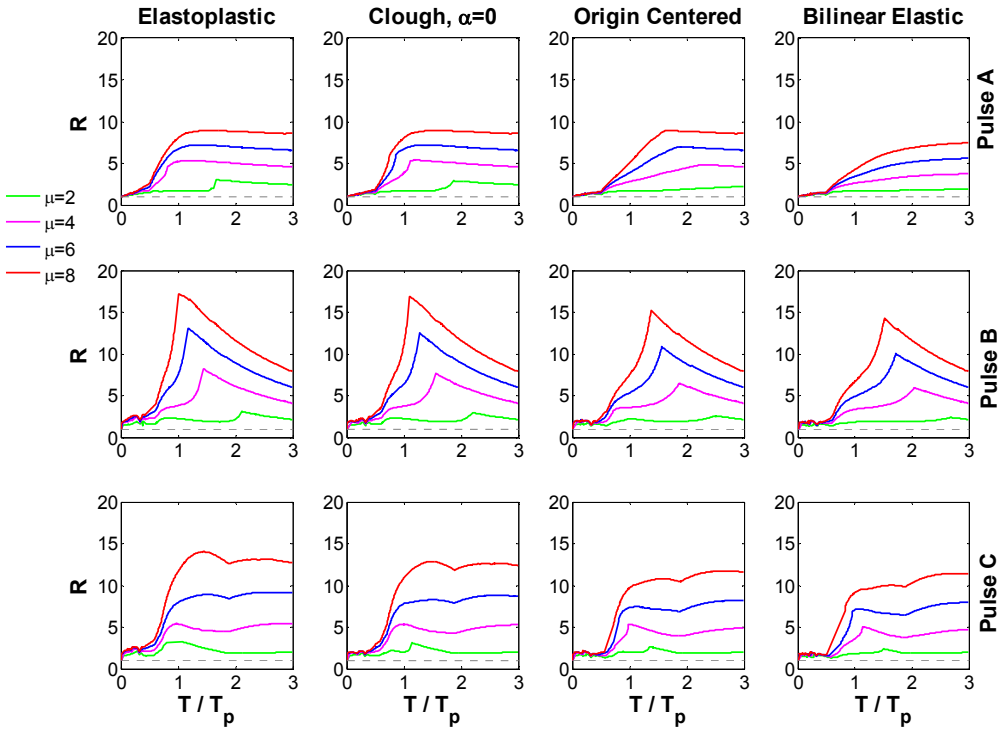

Figure 2.5. Equal ductility inelastic response spectra in terms of R, r=0.

Two main regions of the normalized response depicted in Fig. 2.4 are identified for all type of pulses and all type of hysteretic rules. The first extends from $T / T_p = 0$ to T / T_p about 1, depending on the type of pulse, the hysteretic rule and the target ductility. In this region, coefficient C_μ overall increases as T / T_p decreases. This first region can be subdivided in two sub-regions with the boundary value of T / T_P about 0.5 for all pulses and hysteretic rules. From T / T_p between 0.5 and 1, C_μ decreases more rapidly with increase of T / T_p. The second region starts from the end of the first region (T / T_p about 1) and extends to large values of T / T_p. In this range coefficient C_μ is rather invariant to T / T_p and ranges close to unity.

As the ratio of T / T_p tends to zero or equivalently the period of the pulse increases in relation with the initial period of the non-linear SDOF oscillator, coefficient Cμ overall increases and tends to μ. That is, coefficient R tends to 1. For a target ductility μ the higher the period of the excitation pulse (T_p) in comparison with the initial period of the SDOF oscillator (T) the higher the value of coefficient Cμ and smaller the value of coefficient R required for this target ductility. As the ratio of T / T_P decreases the response of the nonlinear SDOF oscillator becomes more vulnerable to yielding and additional decrease of the normalized strength (increase of R) causes increase of the ductility demand. As the ratio of T / T_P increases the excitation is felt as higher frequency from the SDOF and coefficient C_μ tends to one for large values of the ratio T / T_P. When the period of the pulse is significantly shorter than the initial period of the SDOF oscillator, the displacement of the linear and non-linear SDOF oscillator becomes similar.

Fig. 2.5 shows that as T / T_p decreases, R decreases, indicating that for a target ductility the normalized strength should increase, and at the limit when ratio T / T_p = 0 the strength should shall be equal to the strength of the linear oscillator, since coefficient R = 1. Especially for T / T_p between 0 and 0.5 the strength reduction factor is almost constant and close to unity implying that increased strength, close to the strength of the linear oscillator, is required for any target ductility. As the ratio T / T_p increases from 0 to 1, coefficient R increases rapidly, implying that the required strength in relation with the elastic can be relaxed for any target ductility.

For all type of pulses and hysteretic rules the overall normalized response in terms of coefficients C_μ and R displays a similar trend. The above presented normalized results of C_μ can explain some of the available results (Ruiz-Garcia 2003, Chopra 2001) of mean values of C_μ factors corresponding to Elastoplastic SDOF oscillators subjected to strong near fault ground motions. These studies present Cμ or R factors, gradually decreasing with increase of structural period T, and tending to 1 for period of the order of 1 sec. This is because most of the available records used in these studies do not include strong acceleration pulses with periods greater than T_p=1 sec.

2.7 Effect of Hysteretic Rules on Equal Ductility Spectra

This section investigates the effect of the hysteretic rule on the equal ductility response spectra. Fig. 2.6 plots the inelastic displacement coefficients Cμ of the Clough, Origin Centered and Bilinear Elastic hysteretic rules, respectively, normalized to the inelastic displacement coefficient $C_{\mu,EP}$ of the elastoplastic rule. The inelastic displacement coefficients are given versus the ratio T / T_P for the three pulses investigated and for ductility values of μ=4 and μ=8.

The hysteretic rule has an important effect on coefficient Cμ for specific ranges of ratio T / T_p. A common feature is that in the ranges of T / T_p where a difference exists, the Elastoplastic rule results in smaller coefficient C_μ than the Clough rule. In turn, the Clough rule results in smaller values of coefficient C_μ than

the Origin-Centered rule. The Bilinear Elastic rule results in the larger values of coefficient C_μ.

Depending on the type of pulse and the target ductility the different hysteretic rules can result in significantly larger values of coefficient C_μ in comparison with the Elastoplastic rule. For pulse type B and ductility μ=8 the Bilinear Elastic rule results in a coefficient C_μ 2.6 times larger in comparison with the Elastoplastic rule for $T / T_p = 1.1$. For pulse type A and ductility μ=4 the Clough rule results in a coefficient C_μ 1.6 times larger in comparison with the Elastoplastic rule for a value of ratio $T / T_p = 0.8$.

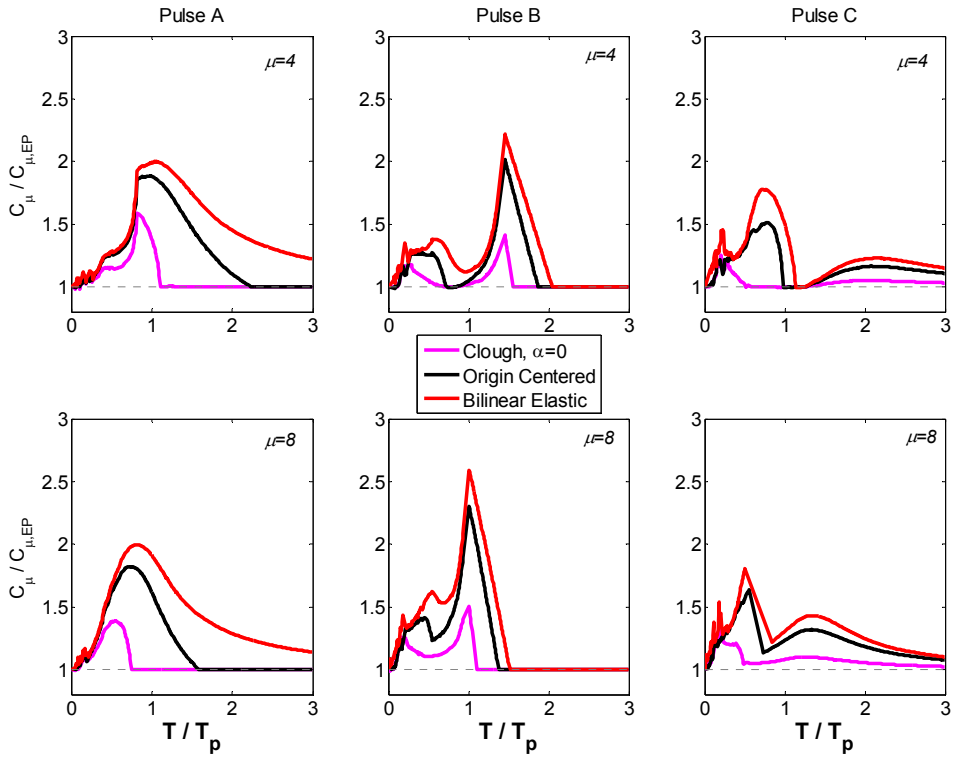

Figure 2.6. Equal ductility inelastic response spectra in terms of C_μ vs ratio T / T_P – Effect of hysteretic rule, r=0.

The trend regarding the effect of the hysteretic rules is clear indicating that, in these ranges of T / T_p where a difference between the different rules exists, the more the hysteretic dissipation per cycle of the rule the smaller the inelastic displacement ratio for a specific target ductility. For a specific target ductility μ, the larger value of coefficient C_μ is equivalent to smaller lateral strength reduction R. This implies that the specific rule requires larger lateral strength for the specific target ductility.

Depending on the type of pulse and target ductility there are ranges of the value of ratio of T / T_p where all the hysteretic rules result in the same value of the coefficient C_μ. A common feature for all type of pulses and target ductilities is that the Clough and the Elastoplastic rule have the same value of the coefficient C_μ for smaller value of the ratio T / T_P than the Origin Centered rule. The Origin Centered and the Elastoplastic rule have the same value of the coefficient C_μ for smaller value of the ratio T / T_P than the than the Bilinear Elastic rule.

For these ranges of the ratio T / T_P where a difference exists in the value of coefficient C_μ of two different hysteretic rules considered, the maximum nonlinear displacement of at least one of the hysteretic rules occurs after a first yielding and unloading in the force-displacement hysteretic relation. For the hysteretic rules considered, same initial stiffness and lateral strength results in identical maximum response, if this occurs before any yielding and unloading. The hysteretic rules considered differ in the part after a first yield and unloading in the force-displacement relation. There is a clear trend regarding the effect of the unloading path and the shape

of the hysteretic rule on the maximum inelastic displacement. The next section presents an example to indicate the effect of the unloading path in the displacement response.

2.8 Effect of Hysterisis Unloading Path – Example in Time Domain

In this section the time response of the nonlinear SDOF oscillators of three different hysteretic rules is considered for the case of a force reduction factor R=3. The nonlinear SDOF oscillators are subjected to a pulse type A with a period ratio $T / T_P = 0.65$. The Elastoplastic, Clough and Bilinear Elastic hysteretic rules are considered with a post yield stiffness ratio r=0. Fig. 2.7 shows the hysteretic response in terms of force normalized to the yield force of the nonlinear SDOF oscillator F_y versus relative displacement normalized to the maximum relative displacement of the linear elastic SDOF Δ_e. Fig. 2.7 shows also the time histories of the relative displacement Δ normalized to the maximum relative displacement of the linear elastic SDOF Δ_e, the relative velocity v normalized to the maximum relative velocity of the linear elastic SDOF v_e. In addition Fig. 2.7 shows the time histories of the total displacement Δ_t normalized to the maximum relative displacement of the linear elastic SDOF Δ_e and the total acceleration a normalized to the yield acceleration a_y of the nonlinear SDOF oscillator.

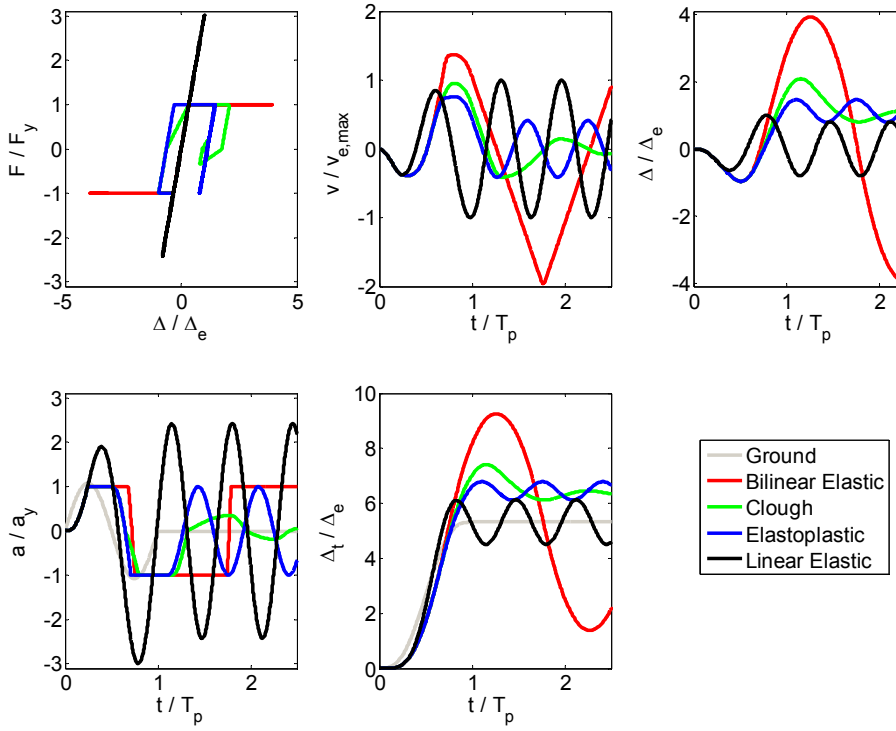

Figure 2.7. Comparison of response of three different hysteretic rules for T / Tp = 0.65 and R = 3, r = 0. Cases where the maximum response occurs after the first yield and unload.

The hysteretic response of the Bilinear elastic rule results in significantly higher relative displacement in comparison with the Clough rule which results in higher relative displacement than the Elastoplastic rule. Due to the same hysteretic characteristics during the first part of the response, before the first yielding, the three rules attain their maximum negative relative displacement at $t / T_p = 0.515$ and this max relative displacement is $\Delta / \Delta_e = -0.967$. At this instant of time the ground acceleration has changed sign which is same to sign of the mass total acceleration. The Elastoplastic and the Clough rules, due to their unloading characteristics start to reduce and change sign of the mass total acceleration which reaches and exceeds the

ground acceleration earlier than the Bilinear Elastic rule. The Bilinear Elastic rule, during the unloading continues to have its maximum positive total acceleration and builds larger relative displacement in comparison to the ground. The maximum relative displacement for all these nonlinear systems occurs after the end of the excitation ($t / T_p = 1$) during the free vibration.

The above example indicates the effect that the unloading path of the hysteretic rule can have on the maximum displacement demand. For these cases where the maximum displacement occurs after a first yield and unloading, the longer the unloading path the more pronounced the effect of the unloading hysteretic characteristics on the maximum displacement demand. The hysteretic rules studied under the specific pulses indicate that the response could be linked to the energy dissipation characteristics per cycle of the hysteretic rule.

2.9 Effect of Pulse Type on Equal Ductility Spectra

This section investigates the effect of the type of pulse on C_μ for the three different pulses considered. Fig. 2.8 compares the coefficients C_μ of the three different pulses for the four main hysteretic rules. Pulses B and C results in similar coefficients C_μ for almost all the period ratios, for any target ductility and hysteretic rule. Pulse A results in much higher coefficients C_μ in comparison to pulses B and C for values of the ratio T / T_p between 0 and 0.7 for all the hysteretic rules. For the Origin Centered and the Bilinear Elastic rules, Pulse A gives significantly higher values of C_μ for T / T_p between 0.7 and 1.3. For pulses B and C is that C_μ, from C_μ tending to μ for T / T_p

tending to 0, C_μ decreases to a significantly smaller value (around μ / 2) for a very small increase of the ratio T / T_p. This is a characteristic of pulses B and C which have a sudden increase in acceleration for zero time.

The coefficient C_μ indicates the ratio of the maximum displacement of the nonlinear SDOF oscillator to the maximum displacement of the linear elastic SDOF oscillator. Thus the comparison of the coefficient C_μ of the different pulses indicates only the inelastic potential character of the motion and not the maximum displacement demand developed of the nonlinear SDOF oscillator. To estimate the maximum displacement demand the elastic demand should be also be considered.

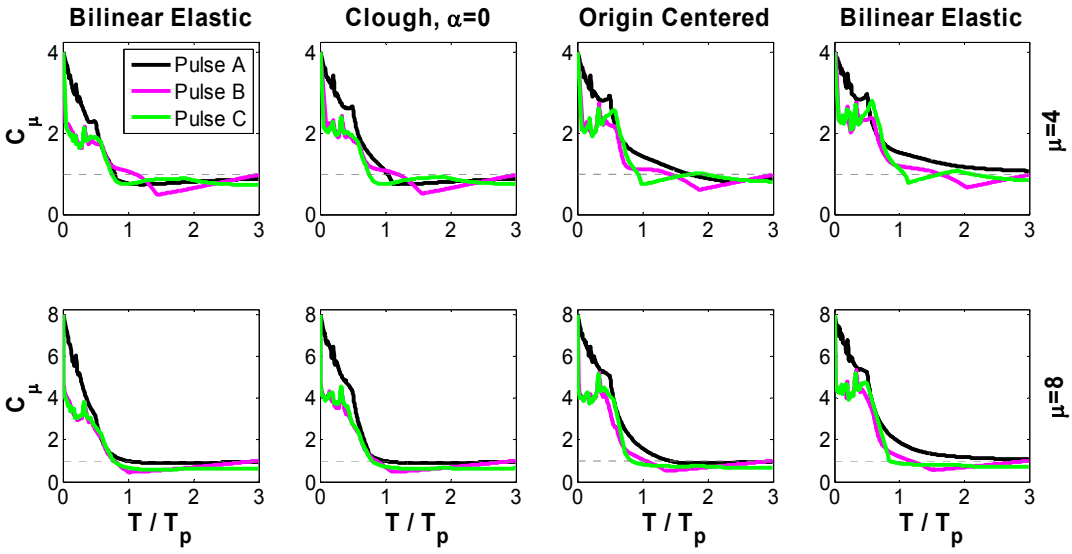

Figure 2.8. Comparison of C_μ factors for the different type of pulses.

Fig. 2.9 plots the normalized elastic acceleration and displacement response spectra versus the period ratio T / T_p for the three different pulses. Pulses B and C

result in higher demand for values of T / T_P smaller than 1 when pulse A shows higher demand for values of the ratio T / T_p larger than 1.3. Combination of Figs. 2.8 and 2.9 gives an estimation of the maximum nonlinear displacement demand.

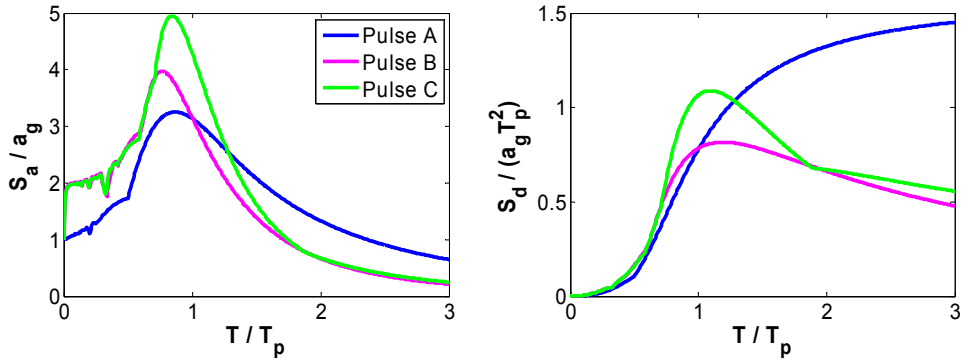

Figure 2.9. Normalized elastic acceleration and displacement response spectra.

2.10 Evolution of Nonlinear Response in the Different Regions of Equal Ductility Spectra

For an insight in the evolution of the nonlinear response Fig. 2.10 plots the force-displacement hysteretic response, for the Elastoplastic rule for five values of the ratio T / $T_{p,}$ for pulses A and B. For each value of the ratio T / T_p the force displacement response is plotted for five values of the force reduction factor R including unity which corresponds to the linear elastic response. The force F is given normalized to the maximum force F_e of the elastic SDOF oscillator, while the relative displacement Δ is given normalized to the maximum displacement Δ_e of the elastic SDOF oscillator.

For both pulses the effect of increase of R (reduction of the strength) is more pronounced regarding the developed ductility demand for smaller values of the ratio T / T_p. For large values of the ratio T / T_p corresponding to high frequency excitation in respect to the structural initial period (or equivalently very flexible structure in respect to the excitation) the maximum inelastic deformation is almost equal to the elastic for all the R factors (equal displacement concept). For T / T_p larger or equal than one we see that specific reduction in the lateral strength can lead to maximum inelastic displacements smaller to the maximum elastic displacement of the SDOF oscillator.

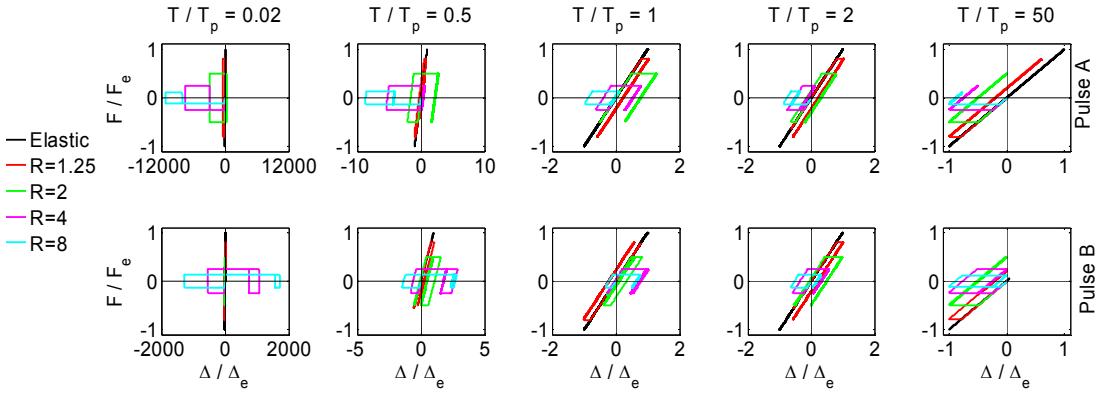

Figure 2.10. Evolution of nonlinear response for Elastoplastic behavior, five values of T / T_p and five R factors.

Depending on the ratio T / T_p, the force reduction factor R and the type of pulse the response can have a more cyclic character with high ductility demand on both sides of the response. This can be important for types of structures where the relation between the maximum developed ductility on each side of the response is important for the performance. This can be the case of a concrete structure where the

maximum compression on the one side of the response will affect the performance on the reverse side where maximum tension will be developed.

2.11 Influence of Post-Yield Stiffness

This section describes the effect of the effect of the post yield stiffness on the inelastic response of a SDOF oscillator. Three different values of post yield stiffness ratio are considered r = 0%, 1% and 10%. Fig. 2.11 plots the coefficient C_μ for the three types of pulses for the Bilinear Inelastic rule.

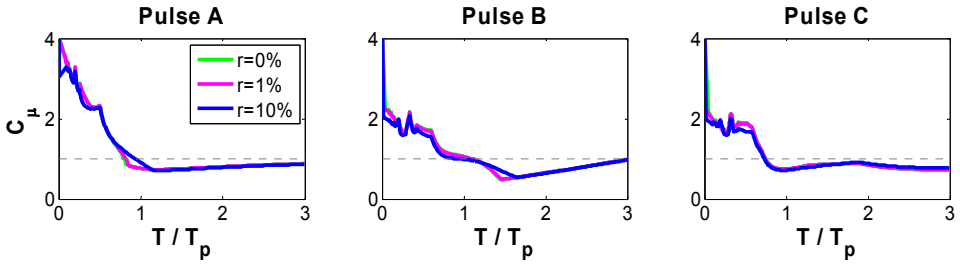

Figure 2.11. Effect of post yield stiffness ratio r on C_μ – Bi-linear Inelastic rule, μ=4.

The effect of the post yield stiffness ratio r is somehow important, in reducing the coefficient C_μ, only for large target ductility and for values of T / T_p between 0 and 0.2. There are ranges of T / T_p where an increase in the post yield stiffness ratio r results in an increase of the coefficient C_μ but this happens in regions where small values of C_μ are observed ($T / T_p > 0.9$). This is again the case where the maximum response occurs after a first yielding and unloading in the force-displacement response. In this case due to increase of the post yield stiffness the response in the first excursion decreases resulting in increased response in the reverse excursion.

The effect of the post yield stiffness ratio for the other types of hysteretic behavior and different target ductility is similar. Overall we see that the post yield factor can be only important for very small values of T / T_p and very large values of ductility. In these cases the system responds with its post yield stiffness for a long path. For all the other ranges the effect of the post yield stiffness ratio is negligible and the inelastic displacement demand is dominated by the effect of yielding and the type of hysteretic behavior.

2.12 Influence of Unloading Branch Stiffness of Clough Rule

This section investigates the effect of the unloading stiffness degradation of the Clough type rule. The unloading stiffness is expressed based on the unloading factor α (see Fig. 2.1(b)). Fig. 2.12 plots the C_μ factor for all the type of pulses for ductility 4, for three values of α, where $\alpha=0$ corresponds to Clough rule without unloading stiffness degradation. Increase of the stiffness degradation results in small increase of C_μ for specific ranges of T / T_p depending on the type of pulse and target ductility.

For pulse A the effect is maximum for T / T_P between 0.8 and 1.2, with the maximum effect to be on the order of 40%. For pulse B the effect is less pronounced and occurs for T / T_p between 1.2 and 1.5. For pulse C an effect exists for T / T_p between 0.5 and 0.8 resulting in a maximum increase of C_μ of about 30%. In these ranges of the ratio T / T_p where the unloading stiffness degradation affects C_μ, the maximum displacement of one or more of the rules considered occurs after a first yielding and unloading. In these ranges of T / T_p increase of unloading stiffness

degradation results in increased maximum displacement on the reverse excursion after a first yield. The same results hold true for other ductility with slightly larger effect with increase of ductility μ. However the effect is not significant and overall the response is dominated by the main characteristics of the Clough type behavior.

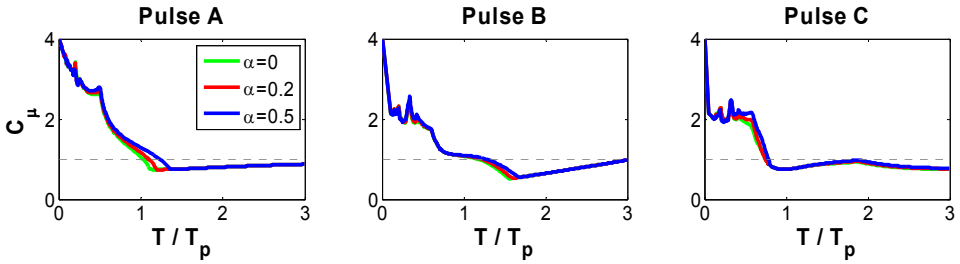

Figure 2.12. Effect of stiffness degradation on Clough rule, μ=4.

2.13 Influence of Supplemental Hysteretic Dissipation

This section investigates the effect of supplemental hysteretic dissipation on precast systems incorporating unbonded post tension. The nonlinear elastic behavior is considered for zero supplemental hysteretic dissipation and the flag type hysteretic rule for cases of supplemental hysteretic dissipation. The description of this hysteretic behavior requires the additional definition of the ratio of the displacements $r_d = \Delta_0 / \Delta_y$ (Fig. 2.1(b)) which defines the amount of hysteretic dissipation. Smaller ratios correspond to larger supplemental damping and more hysteretic energy dissipation per cycle.

Fig. 2.13 plots the variation of the C_μ factor with the normalized period for the three pulses for ductility μ=4. Four values of the ratio Δ_0 / Δ_y are considered: 1, 0.75, 0.5, 0.25. The effect of additional hysteretic dissipation depends on the type of pulse.

For pulse A the effect is somehow important only for values of the ratio T / T_p larger than 0.9, where C_μ takes small values. For pulse B there is an effect for T / T_p between 0.2 and 2. For pulse type C there is an effect for T / T_P between 0.2 and 1.2. For both cases the maximum effect of the additional hysteretic dissipation is to reduce the C_μ by 25%.

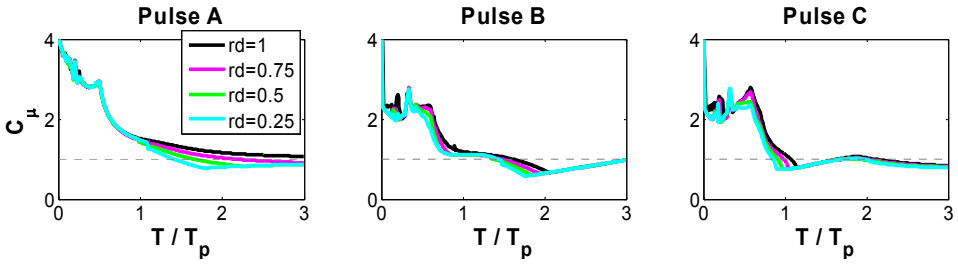

Figure 2.13. Effect of hysteretic damping of Flag-shape hysteretic rule on C_μ, μ=4.

The case where the additional hysteretic dissipation results in variation of C_μ correspond to cases where the maximum response of one or more of the hysteretic rules compared happens after a first yielding and unloading. The effect of the supplemental damping results in a different unloading path after the first yielding, resulting in smaller ductility demand. This enhances the previous implication regarding the effect of the shape of the hysteretic rule (different unloading path) on coefficient C_μ for specific ranges of the ratio T / T_p. Overall the effect of additional hysteretic damping is not significantly important for the period ranges T / T_p indicated above. The inelastic displacement demand of the Flag type rule is dominated by the main characteristics of the Nonlinear Elastic behavior.

2.14 Effect of Viscous Damping

The dimensionless character of the response is preserved if the oscillators are not undamped (Makris 2004). This section investigates the effect of viscous damping on the linear and non-linear response of SDOF oscillators to the three pulses considered. Fig. 2.14 plots the C_μ factor for Elastoplastic rule and ductility μ=4 for the viscous damping ratios ζ=0, 5, 10 and 20%. The important result is that C_μ is practically independent of the amount of viscous damping. In some ranges of the ratio T / T_p increase of the viscous damping causes even increase of C_μ. Similar results hold true for any target ductility and hysteretic behavior.

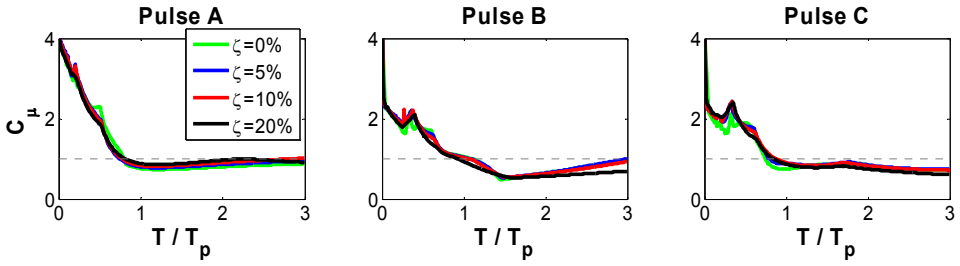

Figure 2.14. Equal ductility inelastic response spectra in terms of C_μ vs normalized period T / T_P – Effect of viscous damping – Elastoplastic rule-μ=4.

While the ratio of the maximum nonlinear to the maximum linear displacement is practically unaffected, the maximum linear displacement is significantly affected by viscous damping. Figure 2.15 plots the normalized acceleration and displacement response spectra for five different values of viscous damping ratio. For T / T_P between 0 and 0.5 where the maximum coefficient C_μ are observed for any ductility, the elastic demand is not affected significantly even for large values of viscous damping. The

viscous damping is more effective in the normalized period range T / T_P between 0.8 and 1 and the effect decreases for T / T_P larger than 2.

The combined effect of viscous damping on the elastic and inelastic response indicates that for small values of T / T_P where the structure is vulnerable to any reduction of the lateral strength, an increase of the viscous damping doesn't contribute significantly to the reduction of the ductility demand. Added damping will not benefit a low strength structure for small values of ratio T / T_p. Added strength is the only help in this period range. For T / T_P between 0.5 and 1.5 the demand is reduced with increase of the viscous damping.

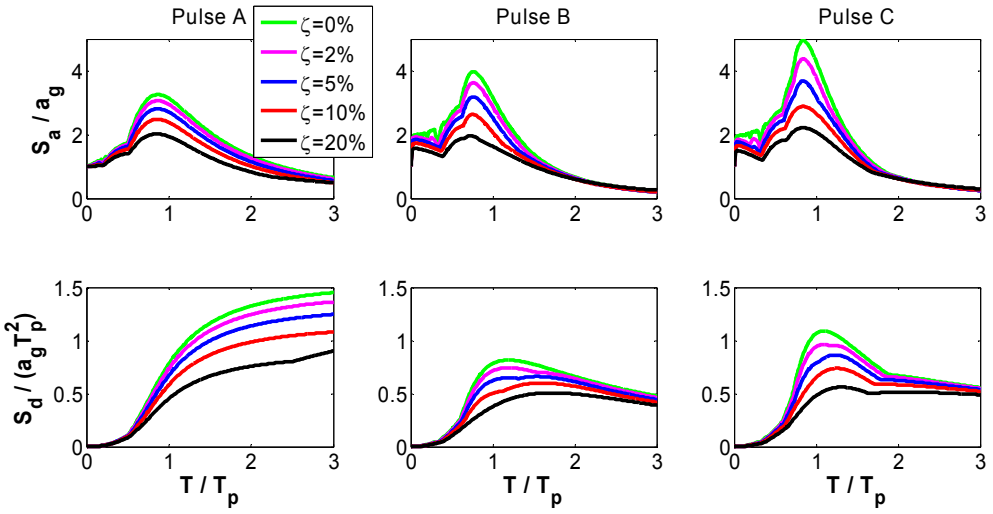

Figure 2.15. Normalized acceleration and displacement response spectra – Effect of viscous damping.

2.15 Summary and Conclusions

This chapter investigated the response of nonlinear SDOF oscillators, with different hysteretic characteristics, subjected to three types of impulsive sinusoidal excitation. These types of excitation represent many of the characteristics of the strong near-fault ground motions. Pulse A corresponds to a forward ground displacement, Pulse B to a forward and backward (half cycle) ground displacement and Pulse C to a complete cycle of ground displacement. Six piecewise linear hysteretic rules were considered: The Bilinear Inelastic, Clough, Clough with unloading stiffness degradation, Origin Centered, Nonlinear Elastic and the Flag hysteretic rule. The main conclusions are:

1. The normalized response of the nonlinear to the linear SDOF oscillator, in terms of force reduction factor R or displacement coefficient C_μ, for any target ductility μ and hysteretic behavior, depends only on the ratio T / T_P of the initial period of the SDOF oscillator to the period of the sinusoidal pulse.
2. For all the pulses and hysteretic behaviors, two characteristic regions of variation of C_μ (or R equivalently) with T / T_P can be identified. The first region extends from T/T_P between 0 and about 1. In this range, C_μ has a large value, tending to μ for $T / T_P=0$. In this region strength close to the elastic strength is required for any target ductility μ. The second region is for T / T_P larger than 1. In this region C_μ ranges around 1 for any target ductility μ.
3. The effect of hysteretic behavior is important for all type of pulses at specific ranges of T / T_P. In these ranges of T / T_P a clear trend exists between the shape of the hysteretic behavior of the nonlinear SDOF oscillator and the maximum

displacement demand. Overall the larger the energy dissipation per cycle of the hysteretic rule the smaller the maximum nonlinear displacement demand. Thus the Bilinear Inelastic rule shows a significantly smaller coefficient C_μ in comparison with the Bilinear elastic rule.

4. Details of the hysteretic behavior like the post yield stiffness, the unloading stiffness degradation as well as supplemental hysteretic damping are not significant. The nonlinear response is dominated by the main characteristics of the hysteretic behavior like the initial stiffness the lateral strength and the main shape of the hysteretic rule.
5. Pulse A results in significantly larger values of coefficient C_μ, in comparison to pulses B and C, for values of T / T_P less than 0.5 for all the hysteretic rules and target ductilities μ.
6. The effect of viscous damping while it is insignificant on the coefficient C_μ significantly reduces the linear elastic and nonlinear demand for ranges of T / T_P between 0.5 and 1.5.

CHAPTER 3

3. KINEMATIC OVERSTRENGTH IN REINFORCED CONCRETE WALL BUILDINGS

3.1 Summary

This chapter discusses the effect of framing in buildings with walls as the main lateral force resisting elements. Framing in these types of buildings occurs through framing beams or floor slabs. Based on fundamental concepts of structural mechanics and plastic analysis, the effect of framing is estimated for the cases of framing between walls or for the case of framing between wall and gravity columns. Simplified expressions for the developed lateral forces in the different elements and the corresponding bending moment and shear forces due to framing are presented.

3.2 Introduction

A usual case in reinforced concrete (RC) buildings with walls as the main lateral force resisting elements is the framing between walls or between walls and gravity columns through beams or floor slabs. In such systems, framing increases the system moment capacity as well as the shear and inertia forces that the walls and the floor diagrams need to sustain, respectively.

Current code provisions do not directly address the effect of framing in these types of buildings. Codes like ASCE-7 (ASCE 2006) use empirical factors, like the system overstrength factor Ω_o, to account for the maximum shear force that the walls

have to resist due to system overstrength. Bertero et al. (1984) indicated the important effect that framing elements can have in building systems including RC walls.

This chapter discusses the effect of framing in buildings with walls as the main lateral force resisting elements. Based on fundamental concepts of structural mechanics and plastic analysis, the effect of framing is estimated for the cases of framing between walls or for an interior wall among gravity columns. Simplified expressions of the developed lateral forces in the different elements and the corresponding bending moment and shear forces due to framing are presented.

3.3 Structural Mechanics Concepts

Fig. 3.1 shows a schematic representation of two two-dimensional cases of framing in RC buildings with walls as the main lateral force resisting element. Fig. 3.1(a) shows the case of framing between two structural walls. Fig. 3.1(b) shows the case of framing between a wall and two gravity columns. The framing can be through framing beams or through floor slabs. Fig. 3.1 assumes highly nonlinear response state of the walls, with development of a plastic hinge at their base.

During this state of the response, the walls' ends deform significantly due to tensile chord elongation or compression chord shortening, see Fig. 3.1. Due to deformation compatibility the framing elements have to follow the deformations of the end of the walls and yield at their ends. The end reactions of the framing elements act

as concentrated bending moments and axial forces in the ends of the walls and at the gravity columns.

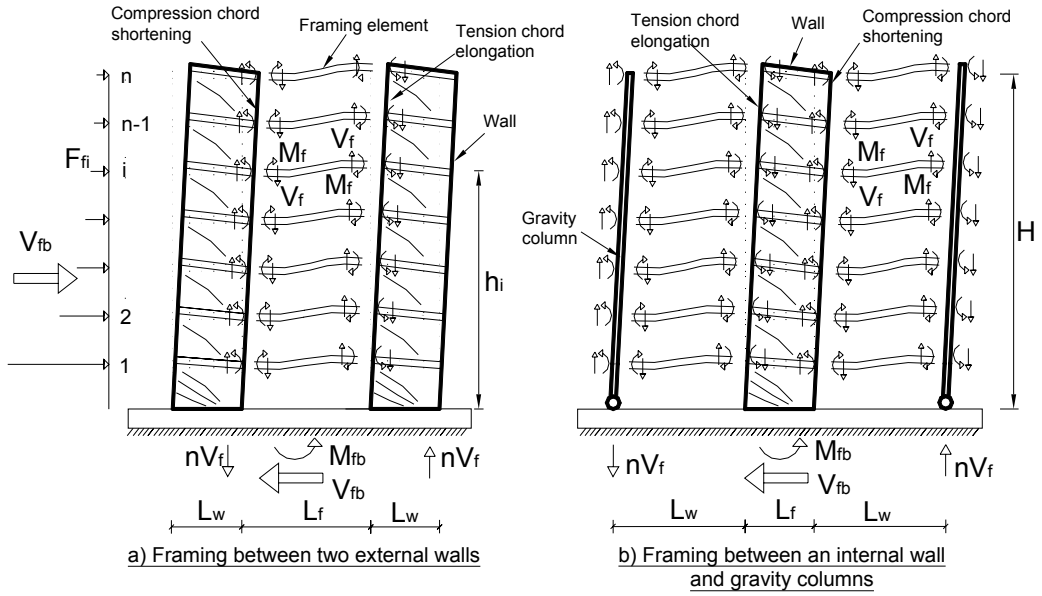

Figure 3.1. Deformed state of RC wall building with a plastic hinge developed at the wall's base. Plastic framing actions, reactions, variation of internal forces and system lateral forces.

For the case of framing with beams the framing end actions are the plastic moment at the ends and the corresponding shear forces. For the case of framing through the floor slabs the framing end actions are the accumulated actions due to yield of the slab along a specific length, see Fig. 3.2. Fig 3.2 shows a floor plan view of a building with parallel RC walls, on both sides, as the lateral force resisting elements. Due to deformations of the ends of the walls the yield lines indicated are developed. Knowing the plastic moment capacity per unit length m_f of the slab, the

corresponding framing reactions M_f and V_f at the ends of the walls can be estimated based on fundamentals of plastic analysis.

The developed framing end reactions, as it will be shown below, can cause significant variation of the lateral forces and the corresponding bending moments and shear forces along the height of the walls and the gravity columns. To estimate the effect of framing in this chapter, it is assumed that the framing elements have enough shear capacity to develop the plastic mechanism without shear failure.

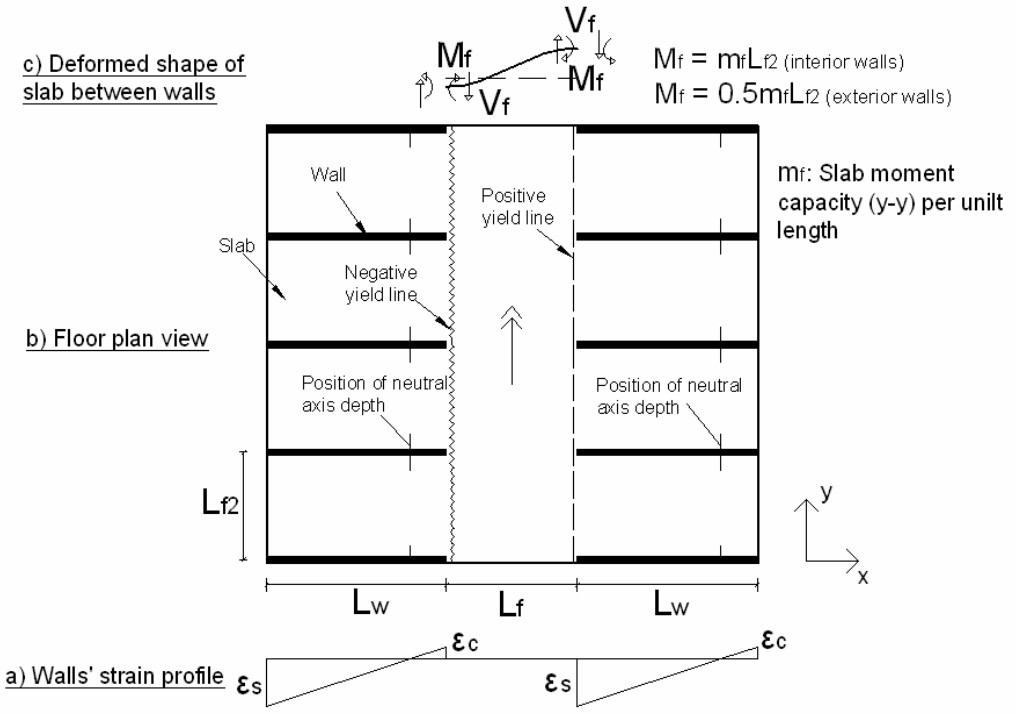

Figure 3.2. Floor plan view of a RC wall building in a highly nonlinear response state. Strain profile in the walls, slab yield lines and deformed shape of the slab between the walls.

3.3.1 Framing between Walls

Fig. 3.3 considers the case of framing between two walls of equal length L_w through a framing element of length L_f at a height h_i from the base of the walls, similar to the case of Fig. 3.1(a), and shows the free body diagram of the forces due to the plastic framing actions only. It is assumed that the wall has developed its base moment capacity while the plastic moment has been reached on both ends of the framing element due to deformation compatibility as explained above. The plastic moment capacity at the end of the framing element at floor i is M_{fi}. The shear force at the ends of the framing element, due to the end plastic moments, is:

$$V_{fi} = \frac{2M_{fi}}{L_f} \tag{3.1}$$

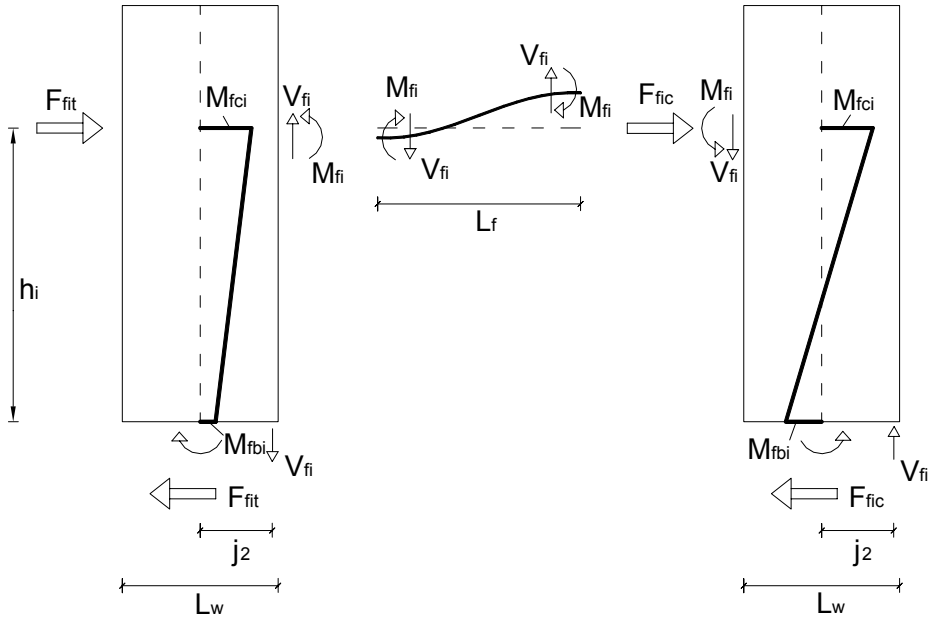

Figure 3.3. Free body diagram of forces developed due to mobilization of framing plastic mechanism at floor i for the case of framing between two external walls.

The shear force framing reactions V_{fi} at the two ends of the framing element, apply tension in the left wall and compression in the right wall. A concentrated bending moment M_{fi} is also applied at the ends of both walls because of the bending moment framing end reactions. The combination of applied axial force and bending moment at the ends of the walls result in an applied moment at the centerline of the walls:

$$M_{fci}=V_{fi}\frac{L_w}{2}+M_{fi} \tag{3.2}$$

Substituting Eq. 3.1 in Eq. 3.2 the applied moment at the centerline of the walls is expressed based on the plastic moment capacity at the ends of the framing elements and the geometrical characteristics as:

$$M_{fci}=M_{fi}\left(\frac{L_w}{L_f}+1\right) \tag{3.3}$$

Considering now that both the walls are responding in the nonlinear range the resultant internal tensile force T at the base of the walls is controlled by the base section strain profile and is slightly affected from the applied axial force V_{fi} due to the framing reactions. The additional axial force V_{fi} modifies the resultant internal compressive force resisted from concrete. This resultant compressive force is located at a distance j_2 from the centerline of the wall. Due to equilibrium the variation of the internal compressive force will be equal to V_{fi} and thus, assuming $j_2 \approx 0.5L_w$, the variation of the wall base moment capacity is:

$$M_{fbi}=V_{fi}\frac{L_w}{2}=M_{fi}\frac{L_w}{L_f} \tag{3.4}$$

In the wall at which the framing shear force reactions V_{fi} apply compression, M_{fbi} results in increase of the wall base moment capacity while in the wall at which the framing shear force reactions V_{fi} apply tension, M_{fbi} decreases the wall base moment capacity. Knowing the applied moment at the centerline of the walls M_{ci}, and the variation of the base moment M_{fbi} due to the framing reactions, the lateral forces F_{fit} and F_{fic} can be estimated as:

$$F_{fit}=\frac{M_{fci}\text{-}M_{fbi}}{h_i}=\frac{M_{fi}}{h_i} \tag{3.5}$$

$$F_{fic}=\frac{\left(M_{fci}+M_{fbi}\right)}{h_i}=M_{fi}\frac{\left(1+2\frac{L_w}{L_f}\right)}{h_i} \tag{3.6}$$

The total additional lateral force required to mobilize the framing plastic mechanism at floor i is:

$$F_{fi}=F_{fit}+F_{fic}=\frac{2M_{fi}\left(1+\frac{L_w}{L_f}\right)}{h_i} \tag{3.7}$$

The lateral force F_{fi} is inversely proportional to the height h_i. Thus mobilization of the plastic framing mechanism in the lower floors generates larger lateral forces. If we consider the case of mobilization of the full plastic mechanism of the framing elements along the height we have the resultant lateral force profile of Fig.

3.1. This profile varies significantly from a first mode lateral force profile and affects greatly the final lateral force profile in this type of buildings. Eqs. 3.5 and 3.6 show that F_{fic} is larger than $F_{fit.}$ Thus the wall which undergoes compression, due to the framing reactions, is the wall which has to resist the larger part of the additional shear force F_{fi}.

Now if we consider yield of all the framing elements along the height, with plastic moment capacity of the ends of the framing elements $M_{fi}=M_f$ in all the floors, the developed forces at the base of the walls due to framing are estimated from the cumulated results from floors i = 1 to n based on Eqs. 3.4 to 3.7 as:

$$M_{fbt} = M_{fbc} = \frac{L_w}{L_f}\sum_{i=1}^{n} M_{fi} = n\frac{L_w}{L_f}M_f \tag{3.8}$$

$$V_{fbt} = \sum_{i=1}^{n} F_{fit} = \frac{M_f}{h}\sum_{i=1}^{n}\frac{1}{i} \tag{3.9}$$

$$V_{fbc} = \sum_{i=1}^{n} F_{fic} = \frac{M_f}{h}\left(1+2\frac{L_w}{L_f}\right)\sum_{i=1}^{n}\frac{1}{i} \tag{3.10}$$

$$V_{fb} = \sum_{i=1}^{n} F_{fi} = \frac{2M_f\left(1+\frac{L_w}{L_f}\right)}{h}\sum_{i=1}^{n}\frac{1}{n} \tag{3.11}$$

While the base moment capacity of one of the walls reduces and the other's increases due to the frame reactions the system base moment capacity always increases by:

$$M_{fb} = 2nM_f \frac{L_w}{L_f} \tag{3.12}$$

As an example the effect of framing of a 7-story building with $L_w = L_f$ and moment capacity of the framing elements $M_f = 0.02M_w$, where M_w is the moment capacity of the walls is considered. Assuming an effective height of first mode of response $h_{e,1} = 0.7H = 4.9h$, where h is the floor height, the first mode base shear corresponding to yield at the base of the wall, without considering the framing, is $V_{1,b} = M_w / (4.9h)$. From Eq. 3.10 the additional lateral force due to framing, at the wall which feels compression due to framing reactions, is $V_{fbc} = M_w / (6.43h) = 0.76\ V_{1,b}$. Thus for this case mobilization of the full framing plastic capacity results in an increase of the base shear corresponding to the flexural strength of the wall only of 76%. Regarding the increase in the system base moment strength from Eq. 3.13 we have $M_{fb} = 0.28\ M_w$ and thus the increase of the base moment capacity is $0.28M_w / (2M_w) = 14\%$.

3.3.2 Framing between Wall and Gravity System

Fig. 3.3 considers the case of framing of an interior wall among gravity columns. For this case, no variation of the wall axial load occurs due to the shear force framing reactions V_{fi}. Thus the wall base bending moment capacity does not change

due to framing. The shear force and bending moment framing reactions result in a bending moment at the centerline of the wall:

$$M_{fci}=2V_{fi}\frac{L_w}{2}+2M_{fi}=2M_{fi}\left(\frac{L_w}{L_f}+1\right) \tag{3.13}$$

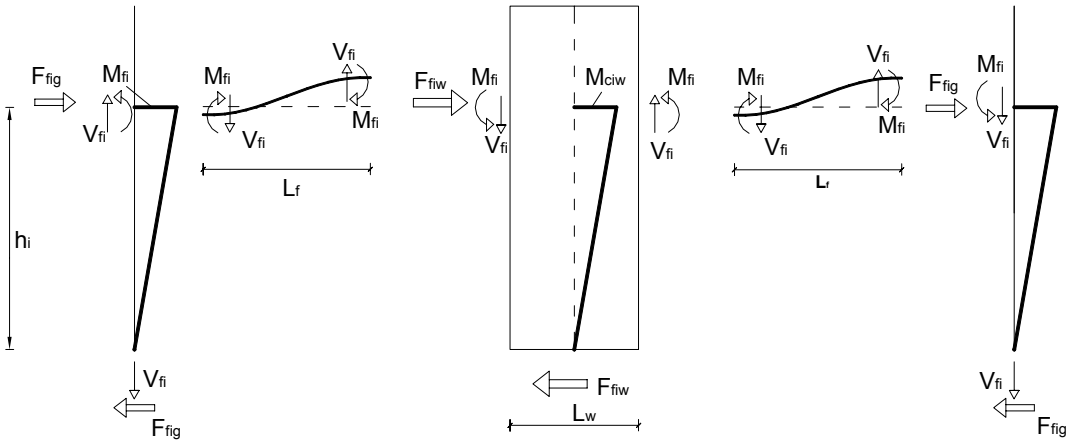

Figure 3.4. Free body diagram of forces developed due to mobilization of framing plastic mechanism at floor i for the case of framing between an internal wall among gravity columns.

and the lateral force in the wall due to this moment is:

$$F_{fiw}=\frac{M_{fci}}{h_i}=\frac{2M_{fi}}{h_i}\left(\frac{L_w}{L_f}+1\right) \tag{3.14}$$

In the gravity columns the bending moment framing reaction results in a lateral force:

$$F_{fig}=\frac{M_{fi}}{h_i} \tag{3.15}$$

The lateral force developed in the wall is at least two times larger than the shear forces attracted from the gravity columns. For mobilization of the complete framing plastic mechanism along the floors the shear forces, at the base of the wall and the gravity columns are:

$$V_{fbw}=\sum_{i=1}^{n}F_{fiw}=\frac{2M_f}{h}\left(\frac{L_w}{L_c}+1\right)\sum_{i=1}^{n}\frac{1}{i} \tag{3.16}$$

$$V_{fbg}=\sum_{i=1}^{n}F_{fig}=\frac{M_f}{h}\sum_{i=1}^{n}\frac{1}{i} \tag{3.17}$$

The total shear force attracted by the system is:

$$V_{fb}=V_{fbw}+2V_{fbg}=\frac{2M_f}{h}\left(\frac{L_w}{L_f}+2\right)\sum_{i=1}^{n}\frac{1}{i} \tag{3.18}$$

Accumulation of the shear force framing reactions results in a tensile and a compressive force on the left and right gravity column, respectively. The axial forces at the base of the gravity columns due to framing are:

$$N_{fbg}=nV_f=n\frac{2M_f}{L_f} \tag{3.19}$$

The pair of these axial forces at the base increase the system base moment capacity at the centerline of the wall by:

$$M_{fb}=2N_{fbg}\left(L_f+\frac{L_w}{2}\right)=4nM_f\left(1+\frac{L_w}{2L_f}\right) \quad (3.20)$$

3.4 Design Implications

The previous sections indicated that framing in RC buildings with walls as the main lateral force resisting element can cause i) increase of the shear forces that have to be resisted from the walls and the gravity columns ii) increase of the system moment capacity along the height, iii) variation of the axial forces in the gravity columns.

The additional system lateral forces due to mobilization of the framing plastic mechanism have to be resisted primarily by the walls and secondarily by the gravity columns if they exist. Depending on the relative moment capacity of the framing elements and the wall base moment capacity, the resultant additional shear force due to framing can be of similar order or even exceed the shear forces corresponding to the flexural strength of the walls alone. This is important for the capacity design of the walls in such buildings and is further discussed in Chapter 5.

Except from increase of the system shear forces, mobilization of the framing plastic mechanism can cause significant variation of the axial forces in the gravity columns. These axial forces can cause decompression of the gravity column or excessive compression. This is also critical for the design of the gravity columns.

Framing also causes an increase in the building system moment capacity. Usually in design of such buildings, the effect of framing is ignored in the estimation of the required bending moment capacity of the walls. The increase in the moment capacity can be taken advantage of to reduce the required flexural strength and thus the longitudinal reinforcement of the walls. The increase of the system's base bending moment capacity should be also considered for the capacity design of the foundation. Lastly increase of the system moment capacity results in increase of the floor accelerations and consequently in the inertia forces that the diaphragms and the non-structural components may have to resist. This is also further discussed in Chapter 5.

To estimate the effect of framing in this chapter, two-dimensional interaction between the walls, the framing slab (or beam) and the gravity columns was considered. For buildings with non-uniform geometry the effect of framing may require three-dimensional nonlinear analysis of the slab. Even in these cases the concepts of kinematic compatibility between the walls, the framing elements and the gravity system in combination with plastic analysis can be applied to estimate the effect of framing.

CHAPTER 4

4. EFFECT OF HIGHER MODES AND A DUAL PLASTIC HINGE CONCEPT FOR ARRESTING HIGHER MODE EFFECTS ON HIGH-RISE CANTILEVER WALL BUILDINGS

4.1 Summary

This chapter proposes a dual plastic hinge design concept to better control the seismic response of tall reinforced concrete cantilever wall buildings to strong shaking. This concept is prompted by the need to arrest the effect of the higher modes of response, which can significantly increase the flexural demands in these buildings and to optimize construction. Lumped mass Euler-Bernoulli cantilevers are used to model the buildings and obtain instantaneous modal characteristics, applicable to linear and nonlinear response. These models also help to discuss the effect of higher modes on the nonlinear dynamic response of tall buildings. Buildings with 10, 20 and 40 stories are designed under three different approaches: ACI-318, Eurocode 8, which has similar provisions to the New Zealand 3101 Concrete Design Standard and National Building Code of Canada, and the proposed dual plastic hinge concept. The buildings are designed for and subjected to three specific historical strong near-fault ground motions. The investigation clearly shows the dual hinge design concept is effective at arresting the effects of the second mode of response. An advantage of the concept is the relaxation of the reinforcement details in large portions of the walls.

4.2 Introduction

Derecho et al. (1981), while examining the results of a comprehensive study on the nonlinear dynamic response of reinforced concrete cantilever walls of high-rise buildings, pointed out: The difference between UBC-76 and 0.9 fractile normalized (bending) moments is particularly significant near mid-height. At about two-thirds of the height of the walls, the 0.9 fractile (bending) moments exceed the corresponding UBC moments by as much as 100 percent for the longer period. Despite this observation, codes in United States have not recognized the significant effect higher modes have on the bending moment demands in cantilever walls of high-rise buildings. In contrast, codes like Eurocode 8 (CEN 2004), which has similar design provisions for cantilever wall buildings to the New Zealand 3101 Concrete Design Standard (NZS 3101 2006) and the National Building Code of Canada (NRCC 2005), do recognize the higher mode effects. These codes incorporate specific provisions that stemmed from the pioneering work of Blakeley et al. (1975).

Design codes recognize the difficulties in ensuring elastic response of the lateral force resisting system in buildings. These codes recommend the use of reduced lateral forces in design. As a result, these codes recognize the possibility of developing nonlinear deformations in some parts of the structural system during a rare and strong intensity earthquake. Nonlinear deformations in cantilever walls occur preferably in flexure in regions defined as plastic hinges. Traditionally a single plastic hinge has been advocated in the seismic design of each wall in these buildings (CEN 2004, NZS 3101 2006, NRCC 2005, Paulay and Priestly 1992, Panagiotou and

Restrepo). Plastic hinges are generally selected to develop at the base of the walls in vertically regular buildings, or at the top of a podium in buildings with podiums or at the ground floor in buildings with floors below grade. Detailing of the reinforcement in the plastic hinge regions is critical to ensure deformation demands have a low probability of exceeding the capacity in these rare events. So, codes include prescriptive requirements to ensure a certain degree of ductility in potential plastic hinge regions.

Seismic design codes such as Eurocode 8 (EC8), the New Zealand 3101 Concrete Design Standard (NZS-3101) and the National Building Code of Canada (NBCC) use Capacity Design (CD) to ensure elastic response in regions other than the plastic hinges. In these codes the flexural design envelope varies linearly from the expected flexural overstrength at the wall base to zero at the top. The intention of such linear variation is to consider the effect of the higher modes. More recently Panneton et al. (2006) and Priestley et al. (2007) have found that the linear variation of bending moment with height does not always preclude the spread of plasticity into the upper regions. Priestley et al. proposed a bilinear bending moment envelope to overcome this shortcoming. This envelope starts at the base with the expected flexural overstrength, ends at zero moment at the top, and passes through a mid-height moment $M^{o}_{H/2}$ given by:

$$M^{o}_{H/2}=C_{1,T}\ \varphi^{o}\ M_{u},\ \text{where}\ C_{1,T}=0.4+0.075\,T_{1}\left(\frac{\mu}{\varphi^{o}}-1\right)\geq 0.4 \tag{4.1}$$

In which φ^o is the wall base expected flexural overstrength factor given by M_0^o/M_u , where M_0^o is the expected flexural overstrength accounting for all sources of strength increase above the design bending moment and is evaluated with a strength reduction of unity, M_u is the design bending moment, T_1 is the fundamental period and μ the displacement ductility factor.

Codes such as ACI-318 (2005) are based on the premise that plasticity is concentrated at the base of the walls only (Wallace et al. 2002). However, these codes do not use CD, and thus do not recognize the effect of base overstrength and of higher modes. So, plasticity is likely to spread anywhere in the upper levels of the walls as is been pointed out by Moehle et al. (2007). The main problem with the design by this code is that undesirable premature modes of response other than flexure could develop in the upper regions. This is because these regions are not specially detailed for ductility.

One initial problem in the design of cantilever walls in tall buildings is the evaluation of the bending moment and shear force demands. It is common practice to obtain these demands from a modal response spectrum analysis (MRSA) using an accepted modal combination method. Elastic forces obtained from the modal combinations are reduced by a force reduction factor to obtain design forces. Rodriguez et al. (2002) suggested that inelastic response at the base of cantilever walls ameliorates the first mode only. Consequently, the relative contribution of the higher modes to response quantities like bending moments and shear forces, increases with an

increase in ground motion intensity augmenting the curvature ductility demand at the base. For this reason, these researchers challenged the modal superposition methods developed for calculating design quantities in linear systems and recommended in codes for use in nonlinear systems. They claimed that such methods produce nonconservative demands. Panneton et al. (2006), Priestley et al. (2007) and Panagiotou and Restrepo (2007) and have arrived at similar conclusions.

To shed light into the nonlinear dynamic response of cantilever wall buildings, this chapter looks into the effect of higher modes, and especially of the second mode. The modal characteristics of such buildings are identified with simple models. In particular, this chapter examines the modal properties of Euler-Bernoulli cantilevers of uniform mass having regions of reduced flexural rigidity. The regions of reduced rigidity in these nonprismatic members mimic the instantaneous flexural rigidity of well-developed plastic hinges subjected to increased rotation. This study also serves as a platform to propose a dual plastic hinge concept useful for the design of high-rise reinforced concrete wall buildings. Note that from the static's viewpoint the notion of dual hinges is nearly unthinkable. However, under dynamic excitation this notion is not only thinkable but is favorable to the system's response and attractive from the design and constructability viewpoints. This is because, the second hinge at an intermediate height in the cantilever wall is specifically intended to arrest the large bending moment demands imposed by the second mode.

4.3 Dual Plastic Hinge Design Concept

Fig. 4.1 shows three possible approaches of where plasticity can develop in cantilever wall buildings. Fig. 4.1(a) shows the first approach. Plasticity develops anywhere along the height of the walls, and is termed here Extended Plasticity (EP) in this chapter. The second approach, shown in Fig 4.1(b), is that of a Single Plastic Hinge (SPH). This hinge develops only at the wall base. The third approach, proposed by the authors and shown in Fig. 1 (c), allows two plastic hinges in a wall, one at the base and the second one at mid-height and is termed the Dual Plastic Hinge (DPH) design concept.

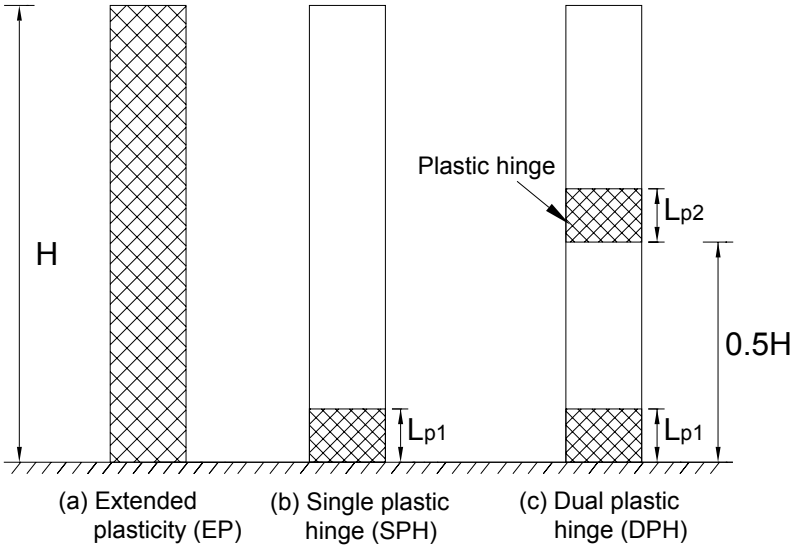

Figure 4.1. Three different cases of plasticity location in an Euler-Bernoulli cantilever.

The EP and the SPH approaches have clear disadvantages. In the EP approach yielding up the height in walls would typically require special reinforcement detailing practically everywhere up the walls height. Extended yielding, as inferred in the EP approach, is theoretical in nature. In practice the longitudinal reinforcement is

detailed to show stepped bending moment capacity diagrams that envelope the code's demand. These steps in the capacity diagrams form critical flexural strength discontinuities where inelastic response concentrates. In the SPH approach the rigorous use of CD to preclude yielding above the plastic hinge region can result in longitudinal reinforcement ratios that exceed those calculated at the base of the walls. The need for these large ratios will be discussed later with the design examples chosen.

The mid-height plastic hinge DPH design concept, see Fig. 4.1(c), overcomes the disadvantages of EP and SPH approaches. Like the bottom plastic hinge, the mid-height plastic hinge can be designed to meet specific objectives such as curvature ductility or strain demands for which design alternatives to the current force-based approaches may be more suitable. The base and mid-height regions of the wall where plastic hinges will develop are designed following a strength hierarchy. This hierarchy is needed to ensure the first mode of response alone does not develop the mid-height plastic hinge. CD is subsequently employed to keep the remaining portion of the walls elastic and ease the detailing of the reinforcement there. So, on one hand the performance of the building is controlled as is in the SPH design approach. On the other hand the ease of detailing and/or reduction in the longitudinal reinforcement along a significant portion of the walls' height in the DPH design concept brings significant optimization to construction compared with the SPH design approach.

4.4 Modal Characteristics of Lumped Mass Euler-Bernoulli Cantilevers

The linear and nonlinear dynamic response of cantilever wall buildings is better understood if the modal characteristics of such systems are identified. Fig. 4.2 shows the mass and flexural rigidity distributions of a 20-story lumped-mass Euler-Bernoulli cantilever. The cantilever shown in Fig. 4.2 is able to respond nonlinear only in the base plastic hinge. The nonlinear moment curvature relation of the plastic hinge region is represented by a Clough hysteretic rule shown in Fig. 4.2(c). The part of the cantilever outside the plastic hinge is linear elastic and has a flexural rigidity EI_e.

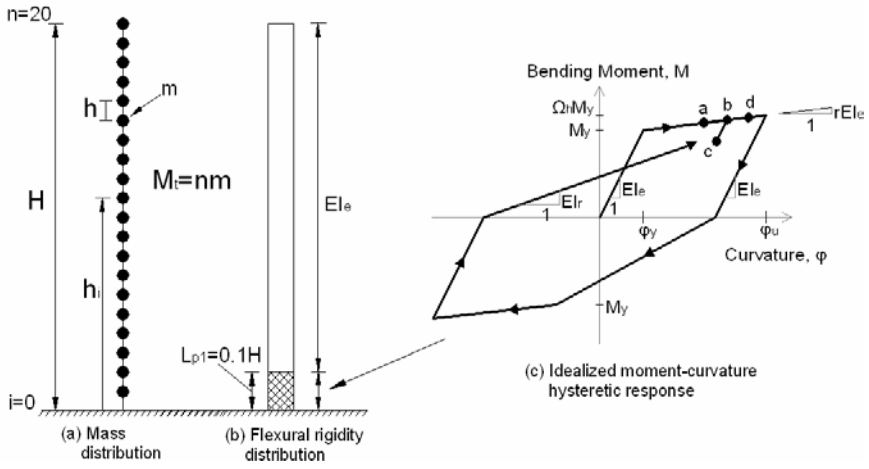

Figure 4.2. Mass and flexural rigidity distributions of a 20-story lumped-mass Euler-Bernoulli SPH cantilever.

At any instant of time the tangent flexural rigidity in the plastic hinge region is known and, thus, the instantaneous modal characteristics are computed based on the mass and flexural rigidity distributions. The notion of instantaneous modal characteristics has been used in the past from different researchers (Miller et al. 1978, Elgamal et al. 1985, Skinner et al. 1993). Being able to compute the variation of the

modal characteristics with time, the lateral forces can be written as the sum of the modal forces $F_{q,i}$, where q is the mode number and i the level considered, as follows:

$$F_i(t)=\sum_{q=1}^{n} F_{q,i}(t)=\sum_{q=1}^{n}\left[\Gamma\ \Phi\right]_{q,i}(t)\,m\,a_q(t) \tag{4.2}$$

In Eq. 4.2 $\left[\Gamma\ \Phi\right]_{q,i}(t)$ is the vector of the instantaneous contribution modal factors and is equal to the product of the participation factor Γ_q with the mode shape vector $[\Phi]_{q,i}$, (Chopra 1991) m is the mass at floor i and a_q is the time dependent modal acceleration response of mode q. To estimate the effect of flexural rigidity distribution in the cantilever walls of Fig. 4.1, the cantilever models depicted in Fig. 4.3 are examined. The models are 20 lumped-mass cantilevers of height H, constant mass per floor, and total mass M_t.

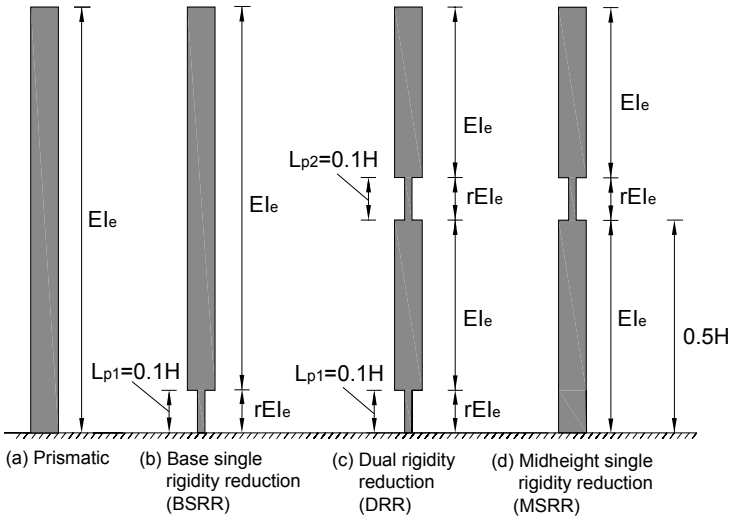

Figure 4.3. Euler-Bernoulli cantilevers with different flexural rigidity distributions.

Four possible distributions of the flexural rigidity in height in the cantilever are also depicted in Figs 4.3(a) to 4.3(d). The model of Fig. 4.3(a) is that of a +prismatic

cantilever of constant flexural rigidity EI_e. This model is used as a simple representation of a cantilever wall during its elastic response or during an immediate reversal after yielding. Fig. 4.3(b) shows the case of reduced flexural rigidity at the wall base, termed here base single rigidity reduction (BSRR). This model gives the instantaneous modal characteristics of a SPH cantilever when a plastic hinge forms at the base and the flexural rigidity there decreases to rEI_e, where r is the ratio between the post-yield and initial flexural rigidities. The reduced flexural rigidity rEI_e matches the post-yield flexural rigidity in the moment-curvature hysteretic response in Fig. 4.2(c).

The case depicted in Fig. 4.3(c) is termed here the dual rigidity reduction (DRR). This case gives the instantaneous modal characteristics when two plastic hinges form in the DPH cantilever and the flexural rigidity there decreases to rEI_e. The mid-height plastic hinge forms between 0.5 and 0.6 of the cantilever's height. The selection of the mid-height plastic hinge location is discussed latter. Lengths L_{p1} and L_{p2} are deliberately constrained by proper detailing of the longitudinal reinforcement in design. In this Chapter these lengths are assumed $L_{p1} = L_{p2} = 0.1H$. The case depicted in Fig. 4.3(d) is termed here the mid-height single rigidity reduction (MSRR) and corresponds to the case where for the DPH concept at an instant of time only the mid-height plastic hinge responds with its reduced stiffness.

Fig. 4.4 shows the main modal characteristics of the lumped-mass models depicted in Fig. 4.2 when the post-yield flexural rigidity ratio is r = 2%. The modal

characteristics are not sensitive to the number of masses but some of them are sensitive to the post-yield flexural rigidity ratio r, and to the plastic hinge length ratios L_{p1} / H and L_{p2} / H. Fig. 4.4(a) plots the normalized modal force vector $F_{q,i} / (ma_q) = \Gamma_q \Phi_{q,i}$, for the first two modes of these cantilevers. Fig. 4.4(b) plots the normalized modal bending moment vector $M_{q,i} / (M_t\, a_q\, H)$, where M_t is the total seismic mass and a_q is the modal acceleration. Fig. 4.4(c) plots the modal shear force vector $V_{q,i} / (M_t\, a_q)$. Table 4.1 summarizes the main modal characteristics calculated, including the first and second mode periods T_1 and T_2, the modal base moments $M_{q,0}$, the modal mid-height moments $M_{q,H/2}$, the modal base shear forces $V_{q,0}$ and the modal heights h_{eq} as defined in Chopra (2001), for the different flexural rigidity distributions shown in Fig. 4.3. Table 4.1 and Fig. 4.4 indicate that the most important effect of flexural rigidity reduction on the modal characteristics is the significant decrease of the second modal base moment for the BSRR case. Table 4.1 indicates the effect of reduction of flexural rigidity on the second modal period is much more important on the DRR case.

For the BSRR case the normalized first mode base bending moment is 51 times greater than the normalized second mode base bending moment. Thus, in cases where the second modal acceleration a_2 is, for example, 7 times the first modal acceleration a_1 the contribution of the second mode to base moment is 4.2 times smaller than that of the first mode.

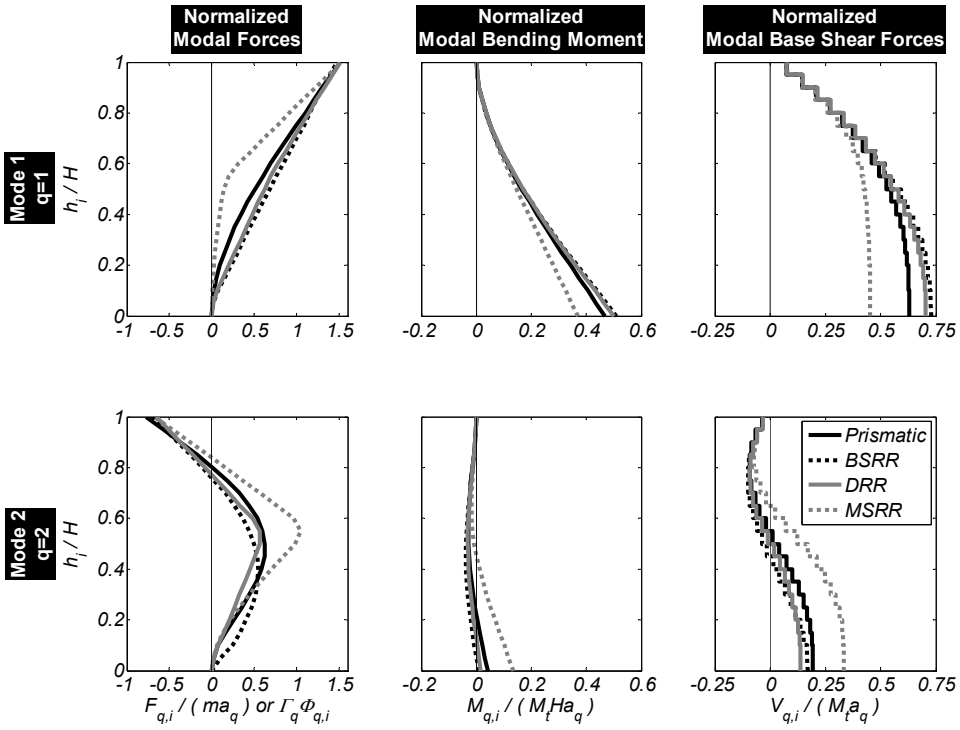

Figure 4.4. Normalized modal forces, modal bending moment and modal shear forces of a 20-story lumped-mass cantilever flexural beam with different flexural rigidity distribution, r=2%.

Table 4.1. Modal characteristics of 20-story lumped mass Euler-Bernoulli cantilevers.

Mode		Prismatic	MSRR	BSRR	DRR
1	Modal eriod T_q	T_1	1.74 T_1	5.21 T_1	5.21 T_1
2		$T_2=T_1 / 6.3$	2.13 T_2	1.47 T_2	4.27 T_2
1	Normalized modal base moment $M_{q,b} / (M_t H a_q)$	0.468	0.370	0.511	0.501
2		0.041	0.135	0.010	0.017
1	Normalized modal midheight moment $M_{q,0.5H} / (M_t H a_q)$	0.165	0.147	0.170	0.170
2		-0.029	-0.008	-0.037	-0.031
1	Normalized modal base shear force or norm. modal mass $V_{q,b} / (M_t a_q) = M_q / M_t$	0.629	0.451	0.729	0.704
2		0.193	0.335	0.171	0.137
1	Normalized modal height h_{eq}	0.744	0.819	0.701	0.712
2		0.215	0.401	0.058	0.123

To show the relative importance of the second modal acceleration a_2 on the bending moment demand in the SPH wall design, Fig. 4.5 depicts the normalized bending moment and shear force diagrams and their envelopes. These diagrams considered only the first two modes of the BSSR and prismatic cases and were calculated using Eq. 4.2. Diagrams for three different values of the ratio of a_2 / a_1 are shown when modal accelerations a_1 and a_2 have equal signs, that is, when $sgn(a_2 \times a_1) = 1$ and also when they have opposite signs, that is, when $sgn(a_2 \times a_1) = -1$. The lowest ratio of $|a_2 / a_1|$ corresponds to elastic or limited ductility response, or to the response to a ground motion with small frequency content around the second period.

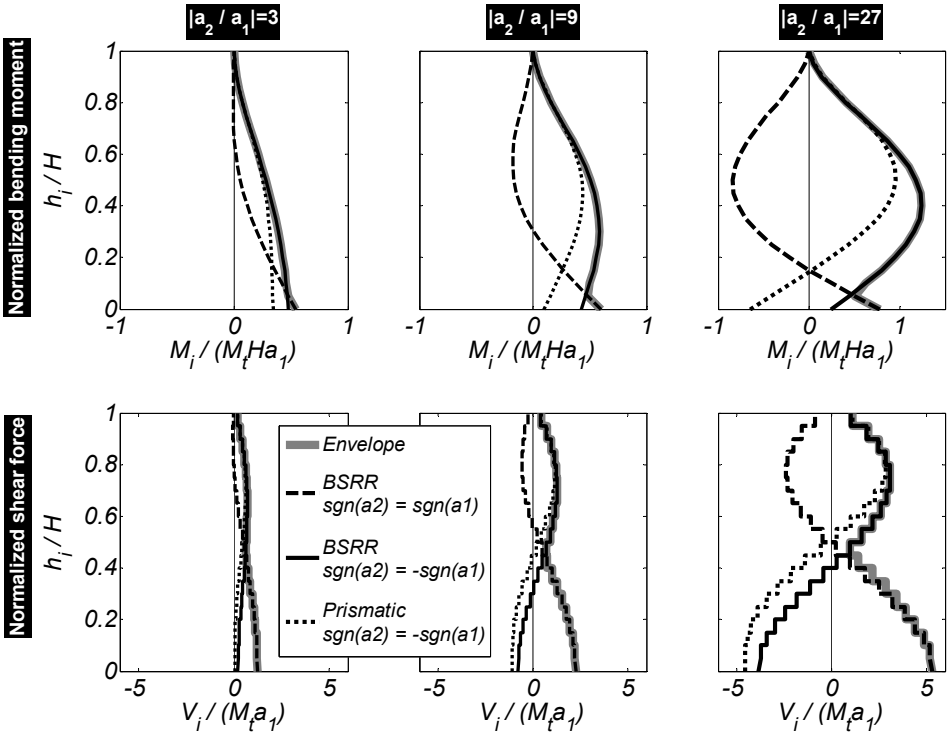

Figure 4.5. Normalized bending moment and shear force envelopes for a 20-lumped mass Euler-Bernoulli cantilever wall obtained from Eq. 4.2.

Conversely, the highest ratio of $|a_2 / a_1|$ corresponds to significant plastic base rotation response or response to a ground motion with significant high frequency content around the second period. The BSRR normalized modal force vectors are used when $sgn(a_2 \times a_1) = 1$ since they are compatible with the flexural rigidity during differential increase in base moment and curvature, see path a-b in Fig. 4.2(c). Both the vectors corresponding to the prismatic and the BSRR case are used when $sgn(a_2 \times a_1) = -1$. This is because for $sgn(a_2 \times a_1) = -1$ second modal moment decreases the base moment and may cause a reversal and a regain of the elastic properties in the plastic hinge region, see path b-c in Fig. 4.2(c). It is noted that in Fig. 4.5 the same ratio a_2 / a_1 is used for both the BSRR and prismatic cases. This is despite the fact that for the prismatic case the normalized first modal base moment is 10 times larger than the normalized second base modal moment, while it is 50 times larger for the BSRR case. This implies that during unloading the ratio of a_2 / a_1 it is probable to be significantly affected from the modified relation of the normalized modal base moments.

The case when $sgn(a_2 \times a_1) = 1$ results in the maximum base bending moment and base shear force demands. Conversely, the maximum mid-height bending moment happens when $sgn(a_2 \times a_1) = -1$. We observe that for large values of $|a_2 / a_1|$ the moment at mid-height can exceed the moment at the base. We also note that even for large values of $|a_2 / a_1|$ for the BSRR case, the base moment is not significantly affected from the second mode. In these cases second mode of response is not significantly affected from the flexural rigidity reduction caused by a plastic hinge at the base, and a_2 is not significantly reduced. This implies, as pointed out by Rodriguez

et al. (2002), that second mode spectral accelerations should not be reduced with the large R factors used for first mode response for the case of BSRR corresponding to design according to EC8 and NZS-3101.

An advantage of the DPH concept is the ability to bound modal accelerations a_1 and a_2 and thus arrest the effect of the second mode in the response. Consider the instant of time when the bottom and mid-height plastic hinges develop and are undergoing the same curvature sign. Assume the upper bound scenario when both hinges reach the probable flexural overstrengths M_0^o and $M_{H/2}^o$ at the base and mid-height, respectively. Further, assume that all the contribution to the bending moment demand is solely because of modes 1 and 2. This results in the following two-by-two system of equations:

$$M_{1,0} + M_{2,0} = M_0^o \tag{4.3}$$

and

$$M_{1,H/2} + M_{2,H/2} = M_{H/2}^o \tag{4.4}$$

$M_{1,0}$ and $M_{2,0}$ are the DRR moment contributions of the first and second modes towards the base bending moment, respectively. $M_{1,H/2}$ and $M_{2,H/2}$ are the DRR moment contributions of the first and second modes towards the mid-height bending moment, respectively. According to Table 4.1 these moments are given by:

$$M_{1,0} = 0.501\, M_t H\, a_1 \text{ and } M_{2,0} = 0.017\, M_t H\, a_2 \tag{4.5}$$

and

$$M_{1,H/2} = 0.170\, M_t H\, a_1 \text{ and } M_{2,H/2} = -\,0.031 M_t H\, a_2 \quad (4.6)$$

The solution of the system of equations gives approximate upper bound values of the maximum modal accelerations of a_1 and a_2. Depending on the relative values of M_0^o and $M_{H/2}^o$, solutions with same or different sign of a_1 and a_2 exist. Solutions with different signs of a_2 and a_1 for same signs of M_0^o and $M_{H/2}^o$ give a larger absolute value of a_2.

4.5 Numerical Validation of the Different Design Approaches

This section examines the design and nonlinear dynamic response of 10, 20 and 40-story representing core-wall buildings. The buildings were designed for the 5% response spectra of specific ground motions that had distinct near-fault characteristics. The design was forced-based. The base moment demand was estimated from a MRSA, as prescribed by ASCE 7 (2006). The elastic design quantities were divided by a force reduction factor R=5. The buildings were designed with three different approaches: ACI-318 building code (2005), SPH according to EC8, NZS-3101 or NBCC and the proposed DPH design concept. Each building was designed for each of the three motions with each of the design approaches. Thus, in total there were twenty seven case studies. A nonlinear time-history analysis was carried out for each building using as input the design ground motion. The following sections give details about the designs, modeling, ground motions and summarize the main results obtained.

4.5.1 Building Description and Designs

The lateral force resistance in buildings studied was solely provided by a reinforced concrete core-wall. Fig. 4.6 shows the floor plan view of the core wall buildings. Table 1 lists the main characteristics of the buildings including the floor height h, the seismic weight w per floor and axial load P per floor acting on the wall, as well as the main building and core-wall geometrical properties and longitudinal reinforcement ratios. The axial stresses at the wall bases are also listed in this table based on a specified concrete compressive strength of $f_c^{'}$ = 41.3 MPa. The yield curvature was defined as $\varphi_y = 2\varepsilon_y / L_w$, where $\varepsilon_y = 0.002$ is the yield strain of the reinforcing steel and L_w the core wall length (Priestley et al. 2007). The longitudinal reinforcement steel ratios, ρ_l, at the wall base for the design for the different earthquake records are listed in Table 4.2. These ratios were calculated from first principles of concrete mechanics using the actual reinforcement provided, specified material properties and a strength reduction factor for bending and axial force equal to 0.9. The wall thickness was chosen in each case to ensure a base longitudinal reinforcement ratio $0.4\% \leq \rho_l \leq 1.5\%$.

For the MRSA the effective flexural rigidity of EI_e=0.5EIg recommended by FEMA 356 (2000) formed the basis for estimating the design lateral forces. Table 4.2 lists the design base moments and base shear forces. The first two modal periods determined from the FEMA 356 recommendation. It is noted that because of the large variation of the spectral accelerations at period T= 1 sec the minimum base shear requirement of ASCE-7 was not considered in the design of the 40-story buildings.

Table 4.2. Main characteristics of buildings considered.

	10-story			20-story			40-story		
	SYLOV 360	TAK 090	RIN 228	SYLOV 360	TAK 090	RIN 228	SYLOV 360	TAK 090	RIN 228
Floor height h (m)		3.4			3.4			3.4	
Building height H (m)		33.5			67.1			134.1	
Floor plan view dimension L_o (m)		12.2			24.4			45.7	
Axial load / floor N (kN)	516	633	817		1653			6614	
Base axial stress N / ($f_c'A_g$)	0.03	0.03	0.03		0.08			0.14	
Seismic weight / floor w (kN)	1183	1301	1484		4322			15996	
Core-wall length L_w (m)		4.6			8.2			15.2	
Core-wall thickness t_w (m)	0.21	0.30	0.46		0.30			0.76	
Core-wall area A_g (m^2)	3.7	5.2	7.5		9.7			44.1	
Core-wall gross moment of inertia I (m^4)	11.8	15.9	21.5		101.3			1545.9	
Core-wall yield curvature φ_y (rad / m)		0.00091			0.00050			0.00027	
Provided long. reinf. steel ratio at wall base ρ_l (%)	1.1	1.4	1.5	1.5	1.5	0.9		0.4	
Provided long. reinf. steel ratio at midheight for DPH design ρ_{lm} (%)	0.5	0.7	0.8	0.7	0.7	0.4		0.4	

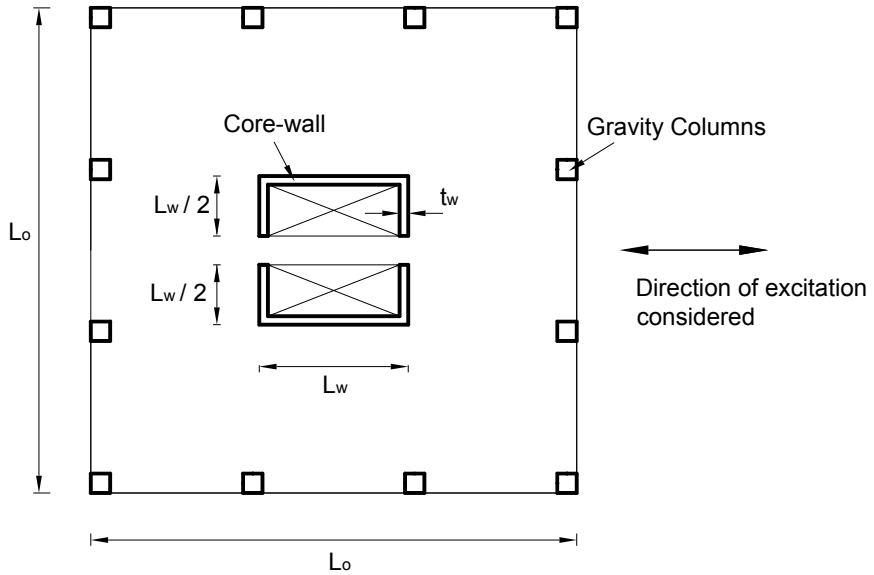

Figure 4.6. Floor plan view of the buildings.

For the MRSA the effective flexural rigidity of $EI_e=0.5EI_g$ recommended by FEMA 356 (2000) form the basis to estimate the design lateral forces. Table 4.3 lists the design base moments and base shear forces. To make the different design cases comparable, the base moment capacity of each building were set identical for the same design motion, but the moment capacity up the height of the walls varied because of the specific requirements of each approach. It is noted that because of the large variation of the spectral accelerations at period T= 1 sec the minimum base shear requirement of Eq. 12.8-6 of ASCE-7 was not considered in the design of the 40-story buildings.

Table 4.3. Normalized design base bending moment and base shear force from MRSA.

	SYLOV	TAK	RIN
	360	090	228
Normalized Base Bending Moment M_u / (WH)			
10-story	0.089	0.138	0.193
20-story	0.047	0.048	0.035
40-story	0.014	0.013	0.019
Normalized Base Shear Force V_u / W			
10-story	0.127	0.193	0.258
20-story	0.117	0.093	0.088
40-story	0.055	0.054	0.082

4.5.2 Designs based on ACI-318 2005 building code

The bending moment envelopes for the ACI-318 design were obtained from a MRSA. In the 10- and 20-story buildings the expected flexural strengths at the core-wall base were calculated 20% greater than the design moments. Expected flexural strengths were calculated from first principles of concrete mechanics using the actual

reinforcement detailed. Furthermore, calculations assumed that the actual concrete compressive and reinforcing steel yield strengths were 8% greater than those specified and the strength reduction factor was one. The longitudinal reinforcement in these buildings was curtailed at four locations ensuring the nominal flexural strength envelope was greater than the design envelope following current recommended practice NEHRP (2006). For the 10-story walls the longitudinal reinforcement layout changed at floors 2, 4 and 6. For the 20-story the longitudinal reinforcement layout changed at floors 4, 8 and 12. Expected flexural strengths at these elevations were 20% greater than the design bending moments there. The reduction of axial force along the height decreased the flexural strength by $0.45L_wP$ at each level, where Lw is the length of the core-wall. The longitudinal reinforcement of the 40-story walls required at the base was just above the minimum. Boundary elements met ACI-318 requirements and extended a distance equal to 19, 15 and 8% of the building height from the base of the walls for the 10-, 20-, and 40-story buildings, respectively.

4.5.3 Single Plastic Hinge (SPH) Design Approach

The design bending moment at the base of the core-walls was the same as the ACI-318 design. The remaining portion of the core-walls was assumed elastic. This assumption was made to prove the adequacy of the current CD design recommendations in EC8 and NZS-3101 concerning the effect of higher modes, and of the recent proposal made by Priestley et al. (2007) and given by Eq. 4.1.

4.5.4 Dual Plastic Hinge (DPH) Design Concept

For comparative purposes the expected flexural strength at the base of the core-wall in this design was made equal to that of the previous two approaches. We note that this was done despite a MRSA should not be used as the basis for the design of cantilever beams with the dual-hinge concept because this design directly considers the effects of the first and second modes independently. To ensure the development of the base plastic hinge, the flexural design at the location of the mid-height plastic hinge followed a design hierarchy, described below, whereas those portions of the walls away from the plastic hinges were assumed elastic. Thus, design bending moments for the mid-height plastic hinge were calculated from the following two steps:

(i) Calculate the expected flexural overstrength at the base of the wall M_0^o. In this study the expected flexural overstrength $M_0^o = M_y \Omega_h$ at the wall base was calculated as the product of the expected flexural strength $M_y = 1.2M_u$, where M_u the design bending moment at the wall base, and the hardening overstrength factor $\Omega_h = 1 + r(\mu_\varphi - 1)$, see Fig. 4.2(c). With r = 2% and assuming $\mu_\varphi = 16$ the hardening overstrength factor is $\Omega_h = 1.3$.

(ii) Determine the design mid-height bending moment derived from the first mode lateral forces:

$$M_{H/2} = \Psi M_0^o \tag{4.7}$$

where factor Ψ is the ratio of the mid-height bending moment to the base bending moment estimated from a first mode lateral force distribution. An analysis of

Euler-Bernoulli cantilever beams with different number of equal lumped masses indicates factor Ψ varies little as shown above. A value of factor Ψ = 0.33 was chosen in this study. The bending moment calculated from Eq. 4.2 was used for the design for flexure and combined axial force at the stem of the mid-height plastic hinge. Based on Eq. 4.2 and considering that the expected flexural strength of the mid-height plastic hinge $M_{y,H/2} = 1.2M_{H/2}$ the expected flexural strength there is $M_{y,H/2} = 0.52\ M_y$ where M_y is the expected base flexural strength. For the 40-story buildings minimum reinforcement requirements governed. This resulted in $M_{y,H/2} = 0.59\ M_y$.

4.5.5 Analytical Model

Because of the explanatory nature of the concept, simple nonlinear analytical tools and simple models were used in this investigation. All floors had identical lumped masses. One-component Giberson beam elements (Giberson 1969) modeled the core-walls. One such beam element represented a core-wall segment between two consecutive floors. The plastic hinge length at each end was assumed to be half the element length. Flexural strengths in the models were computed using expected material properties. With the expected flexural strength M_y and the yield curvature φ_y, the flexural rigidity was defined by $EI_e = M_y / \varphi_y$. In this study the elastic portion of the walls in the SPH and DPH designs used flexural rigidities determined from the expected flexural strengths at a height of 0.3H. The Clough hysteretic rule characterized the moment-curvature relationships in the plastic hinges, see Fig. 4.2(c). The secant flexural rigidity to the expected flexural strength in this model ignored completely the tension stiffening effect because this effect was deemed negligible for

the strong design ground motions. A post-yield flexural rigidity ratio r = 0.02 was assumed in the model. The stiffness of the gravity load system was not considered. Finally, all walls were fixed at the base.

The computer program Ruaumoko (Carr 1998) computed the modal properties as well as the nonlinear dynamic time history analyses (NDTHA). Table 4.4 lists the first two modal periods for all the case studies. The periods obtained from each design approach vary within a small range. Such variation is due to the different amounts of longitudinal reinforcement provided in the elastic portions of the walls. Large displacement theory was selected for the analyses and the P-Delta effect caused by the displaced floor weights was conservatively assumed to be resisted by the core wall. To maintain consistency with the spectra used, Caughey constant 5% viscous damping ratio was used in all the modes (Chopra 2001, Carr 1998). Modes of inelastic deformation other than flexure were not considered.

Table 4.4. Modal periods obtained ignoring concrete tension stiffening.

		Design for MRSA based on $0.5I_g$		ACI-318		Eurocode 8		DPH Concept	
		T_1 (sec)	T_2 (sec)	T_1 (sec)	T_2 (sec)	T_1 (sec)	T_2 (sec)	T_1 (sec)	T_2 (sec)
10-story	SYLOV360	1.04	0.16	2.26	0.43	2.01	0.31	2.11	0.35
	TAK090	0.94	0.15	1.81	0.36	1.64	0.26	1.73	0.28
	RIN228	0.87	0.14	1.52	0.31	1.39	0.22	1.44	0.24
20-story	SYLOV360	2.63	0.41	4.66	0.83	4.17	0.64	4.50	0.71
	TAK090	2.63	0.41	4.60	0.87	4.18	0.64	4.27	0.69
	RIN228	2.63	0.41	5.62	0.98	3.92	0.57	4.87	0.78
40-story	SYLOV360	5.00	0.79	8.88	1.60	7.71	1.20	8.66	1.43
	TAK090	5.00	0.79	8.88	1.60	7.91	1.24	8.69	1.43
	RIN228	5.00	0.79	8.88	1.60	7.96	1.25	8.70	1.43

4.5.6 Ground Motions

Each building was analyzed for the near-fault ground motion it was designed for. The ground acceleration time histories and the 5% damped acceleration and displacement response spectra are depicted in Fig. 4.8. Two of them, the SYLOV360 and the RIN228 were recorded in the Mw 6.6 1994 Northridge earthquake. The third record is the TAK090 from the Mw 7.2 1995 Great Hanshin earthquake. All the three records have large spectral accelerations between T = 0 and 1.6 sec, which is the period range of the second mode in all cases. The SYLOV360 record is characterized by a strong pulse of two cycles resulting in maximum spectral accelerations at T = 0.35 sec. The RIN228 motion has a strong one-cycle pulse with main period of about T_p = 0.8 sec. The TAK090 motion has multiple cycles of T_p = 0.35 and 1.2 sec resulting in large spectral accelerations at these periods.

The motions used in this study, with distinct strong pulses with period content T_p in the period range of the second mode for the buildings considered, caused large excitation of the second mode of response. The destructiveness of these motions in terms of second, and higher, mode excitation is due to the fact that result not only in large second mode spectral but also in significant first mode spectral accelerations that are highly correlated in the time domain with the second modal accelerations.

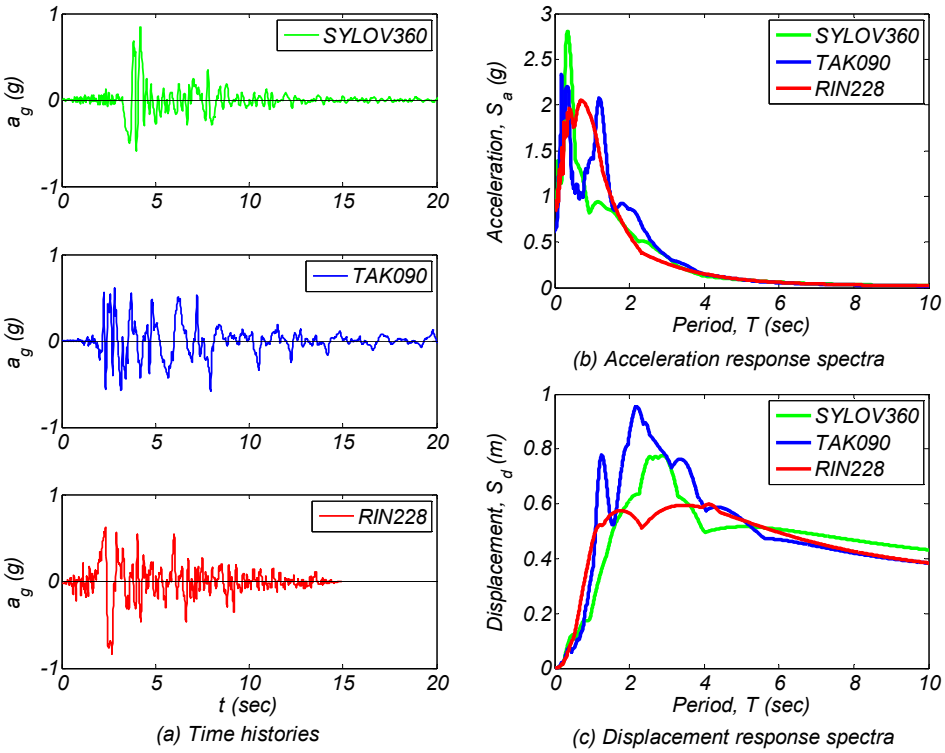

Figure 4.7. Earthquake ground motions time histories, acceleration and displacement response elastic spectra for 5% damping.

4.5.7 Results of the Analyses

Figs. 4.8 and 4.9 plot the bending moment envelopes for the ACI-318 and SPH design approaches, respectively. Fig. 4.10 compares the bending moment envelopes obtained from the NDTHA for the ACI-318, SPH and DPH designs. An analysis of the different responses for each design approach will follow.

Each plot in Fig. 4.8 shows three bending moment envelopes: (i) MRSA; (ii) expected flexural strength established from the final design, labeled ACI-Exp.; and (iii) demand obtained from the NDTHA, labeled ACI-NDTHA. The bending moment

envelopes have been normalized by the product of the total seismic weight and height of the structure, W_tH.

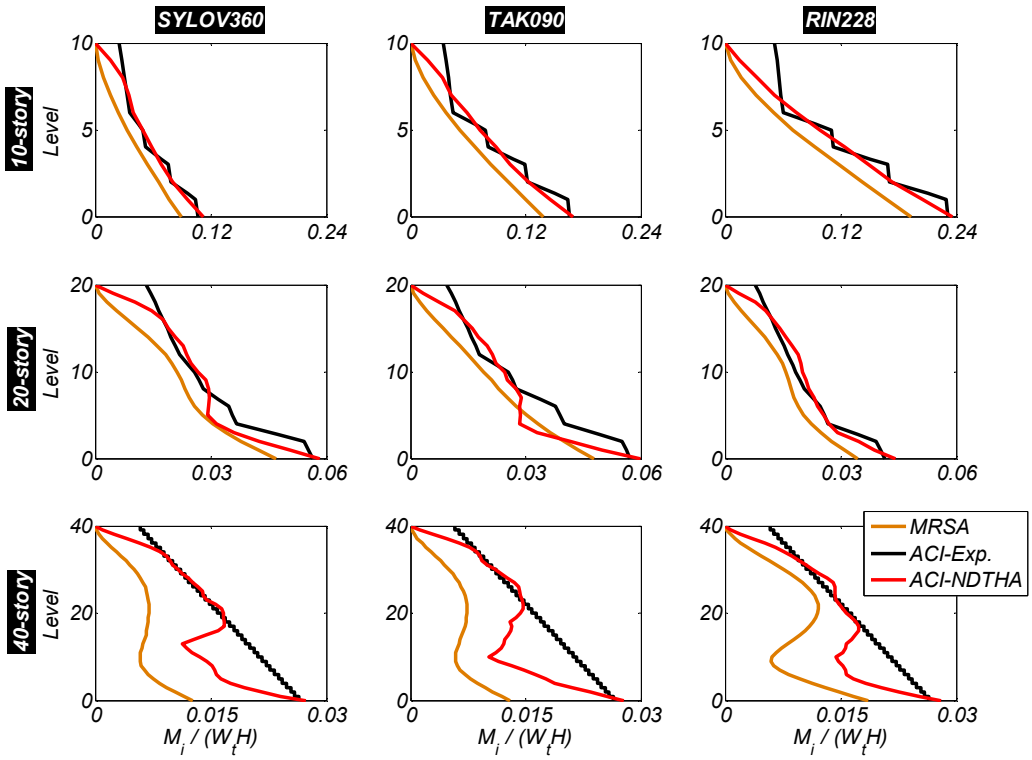

Figure 4.8. Normalized bending moment envelopes for ACI design case.

We observe that the bending moment envelopes obtained from the NDTHA reach or exceed the expected flexural strength not only at the base but also in at least another region in the walls. In the 10- and 20-story buildings the demand exceeds the expected capacity in those regions of the walls that have flexural discontinuities due to termination of longitudinal reinforcement. In the 40-story buildings plasticity is also observed up in the walls. It will be shown later on that the curvature ductility demands in those plastic regions in the upper portions of the walls are not negligible. This

observation is significant because in practice plasticity up the height in the walls is not expected by practicing engineers when using the ACI-318 design approach.

Fig. 4.9 plots the bending moment envelopes for with the SPH design approach. Each plot includes four envelopes: (i) MRSA; (ii) design envelope prescribed by EC8 or NZS-310, labeled EC8; (iii) design envelope proposed by Priestley et al. (2007) and given by Eq. 4.1; (iv) demand obtained from NDTHA, labeled SPH-NDTHA. The bending moment envelopes have been normalized by the product of the total seismic weight and total height of the structure, WtH.

The design envelope given by Eq.4.1 and plotted in Fig. 4.9 was computed with an overstrength factor φo = 1.56, a displacement ductility μ = 5 and the fundamental periods listed in Table 3 for each building. Factor φo was calculated as $\varphi^{o} = \Omega_h \, M_y / M_u$, where $\Omega_h = 1.3$ and $M_y / M_u = 1.2.$ The displacement ductility μ was found to be equal to the R factor, thus confirming the assumption of equal elastic and inelastic displacement demands also for long-period single-degree-of-freedom oscillators Chopra (2001). For the 40-story buildings, where minimum reinforcement is required at the base, φo was larger than 1.56 because the expected flexural strength at the base M_y was more than 1.2 times larger than the design moment M_u.

Fig. 4.9 shows clearly that there are very large differences between the shapes of the bending moment envelopes obtained from the MRSA and the NDTHA, and the differences become more pronounced in the 20- and 40-story buildings. As pointed out by others (Blakeley 1975, Panneton 2006, Priestley 2007, Rodriguez 2007, Panagiotou 2007), the second and other higher modes are not greatly affected by the base plasticity as inferred by the MRSA and this is the main reason for the differences in shapes. This figure also shows that the bending moment envelopes obtained from the NDTHA exceed the EC8 linear design envelopes in all cases studied except one. So, the present study confirms the observations made by Panneton et al. (2006) and Priestley et al. (2007) that the current linear design envelope recommended by EC8 and other similar codes does not provide sufficient protection against yielding in the upper portions of the walls as intended in CD. Fig. 4.10 shows also that the bending moment envelopes obtained from the NDTHA are all within the design envelope proposed by Priestley et al. except for two of the three 40-story buildings.

A main finding of the analysis for the SPH design approach is the practical difficulty that arises from ensuring elastic response in the walls except at the base. For example, if the 20-story walls are designed in accordance with the envelope proposed by Priestley et al., the required longitudinal reinforcement ratios at mid-height are ρ_{lm} = 3.5, 3.5 and 2.3% for the SYLOV360, TAK090 and RIN228 design motions, respectively. Similarly, for the 40-story buildings the reinforcement ratios required at mid-height are ρ_{lm} = 4.2, 4.3 and 4.3% for the same design motions. These reinforcement ratios are large to excessive. The reason for the large ratios is the larger

bending moment demands combined with smaller axial forces acting on the walls at mid-height. In summary, the SPH design approach requires large amounts of longitudinal reinforcement in the intermediate portion of the walls and this is associated with significant structural congestion and higher cost.

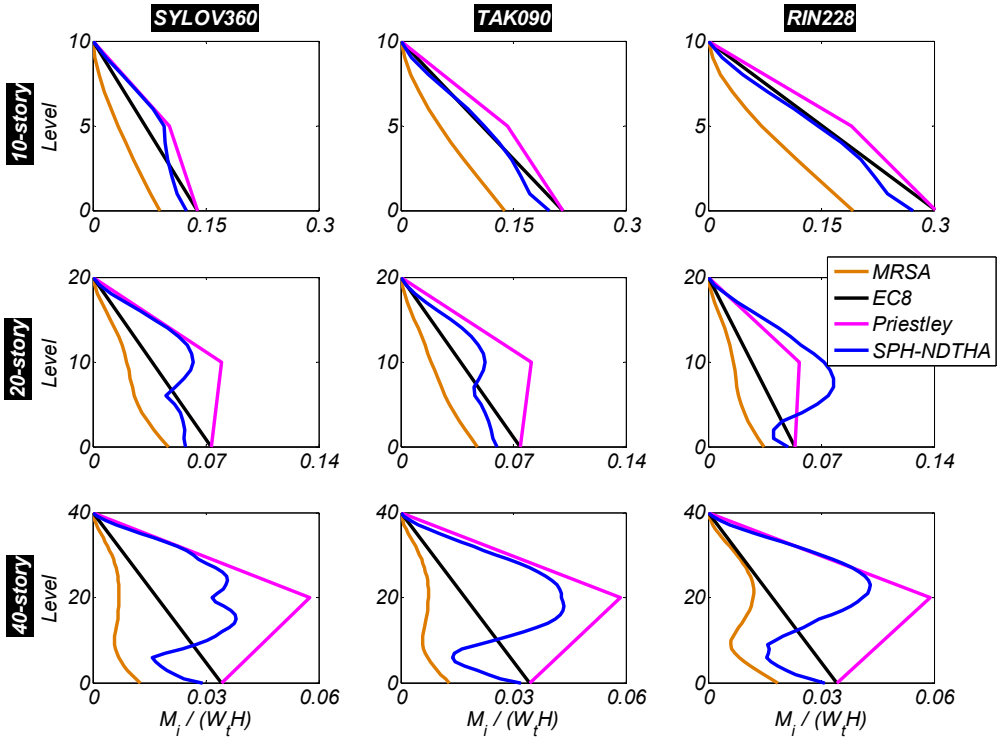

Figure 4.9. Normalized bending moment envelopes for SPH design case. Comparison of design bending moment envelopes based on MRSA, EC8 [2], Priestley et al. [9] and obtained from NDTHA.

The reduction in bending moment demands in the DPH design concept is observed in Fig. 4.10 where the bending moment envelopes obtained from the NDTHA for the ACI-318, SPH and DPH design approaches for the nine buildings are compared.

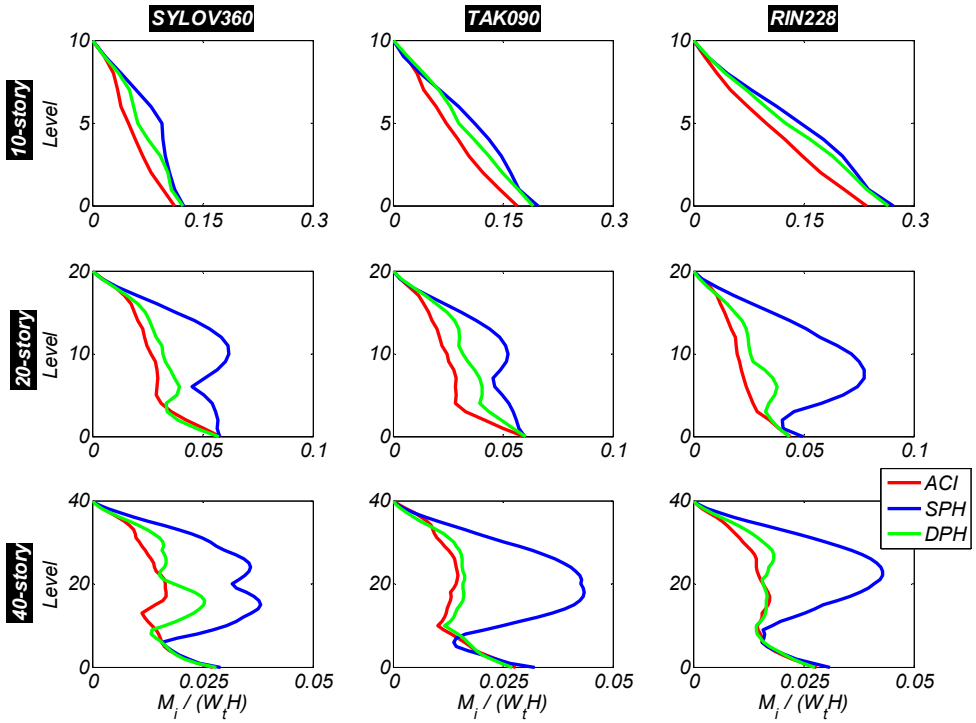

Figure 4.10. Bending moment envelopes obtained from the NDTHA for the three design approaches.

The bending moment envelopes have been normalized by the product of the total seismic weight and total height of the structure, W_tH. As expected, the SPH design approach consistently shows the greatest bending moment demands in the intermediate portion of the walls while the DPH design concept effectively limits these demands. Limiting the intermediate height bending moments in the DPH design approach makes it possible to obtain longitudinal reinforcement ratios that are comparable, if not less, than those at the wall bases, see Table 4.4.

The best metric to judge the extent and magnitude of plasticity in the walls is by analyzing the curvature ductility demands. The authors discussed before the

approximation in the curvatures given by the Giberson beam elements. Fig. 4.11 shows the curvature ductility demands for the cases studied. Curvature ductilities were computed as the maximum absolute curvature obtained from the NDTHA divided by the yield curvature. Fig. 8 clearly illustrates the concentration of the plasticity in regions along the wall height in the ACI-318 designs, labeled ACI in this figure. The curvature ductility demand in the upper part of the 10-story buildings exceeds 13 in one case and reaches 17 in another, which if upon model refinement is found to be correct, requires special detailing to sustain such a demand. For two of the 20-story buildings and for one of the 40-story buildings the curvature ductility demand observed at 60% of the height reaches the relatively large value of 9. The remaining 20- and all the 40-story buildings also yield above a height 0.6H, although the ductility demand there is rather moderate and may be attained if some detailing of the reinforcement designed for these regions. We note that in all analyses yielding takes place in the upper portions of the walls well above the boundary elements mandated by ACI-318. From the observations made, the authors recommend a revision of the ACI-318 requirements for determining the extent of well-detailed boundary elements or a revision of the entire design approach.

The SPH design has, in seven out of the nine cases, the largest base curvature ductility demands, see Fig. 4.11. This is due to constraining plasticity to a single plastic hinge. The DPH design concept concentrates the plasticity at two specific regions along the height not exceeding 0.2 of the total building height, see Fig. 4.11. For the 10-story buildings the DPH design significantly reduces the extent and

magnitude of curvature ductility demand in the upper part of the building in comparison with ACI-318, and in all cases the curvature ductility demands are small or modest. For the 20-story buildings the DPH design significantly reduces the extent and one case the magnitude also of curvature ductility demand in the upper part of the building in comparison with ACI-318, and in all cases the curvature ductility demands are small or modest. For the 40-story buildings the mid-height plastic hinge does not completely spread throughout the allocated length $Lp_2 = 0.1H$. This is because of the significant effect of axial load on the flexural strength of the lightly reinforced 40-story walls. At the base of the walls the DPH design results in curvature ductility demands in between or even smaller than the demands obtained from the other two approaches. The curvature ductility demands in the 40-story buildings are greater for the DPH design concept than for the ACI-318 design and reaches a maximum of 12 for the RIN228 motion. In all these cases curvature ductility demands can be achieved with proper detailing.

We note that in the 20-story buildings responding to SYLOV360 and TAK090 the plastic hinge at the base did not develop. This is because the designs followed the FEMA 356 recommendations of using an effective section flexural rigidity equal to 0.5EIg. This value is significantly larger than the flexural rigidities between 0.10 and 0.3EIg, calculated from the final designs. This is a characteristic of force-based design provisions, which can result in overestimation of the required base strength in some cases.

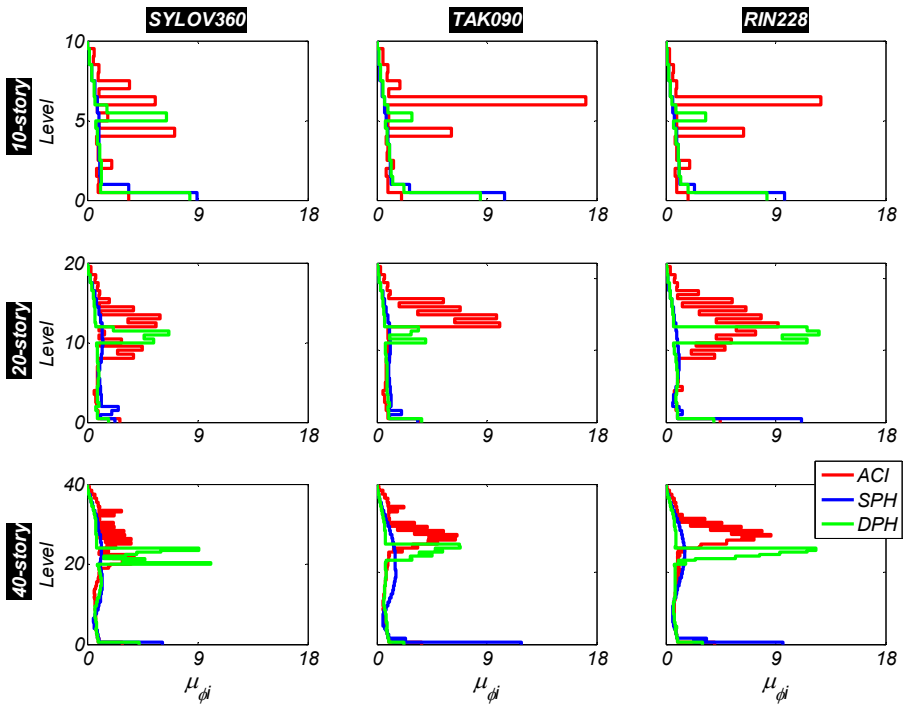

Figure 4.11. Curvature ductility envelopes obtained from NDTHA for the three design approaches.

Panagiotou and Restrepo (2008) observed experimentally high shear force amplifications during the shake table testing of a structural wall. Such amplifications have been observed by other researchers through analytical work (Derecho 1979, Blakeley 1975, Priestley 2007, Panagiotou 2007, Park 1975, Eberhard 1993, Rutenberg 2006, Filiatrault 1994) and were observed also in this study. Fig. 4.12 presents the shear force envelopes obtained from the NDTHA. These forces have been normalized by the total seismic weight W_t. A close comparison of the shear force envelopes obtained for the buildings in each design approach does not reveal clear trends. It can be observed that the DPH design concept does not always reduces the shear forces in cantilever wall buildings. Furthermore, for all cases the base shear

forces range between 2 and 5 times the design base shear forces calculated from the MRSA. This is because of the reduction of the higher mode spectral accelerations with the large value of R = 5 used in the MRSA. The authors concur with Panneton et al. (2006) in that shear forces obtained from MRSA are no indication of the forces developed by inelastic walls.

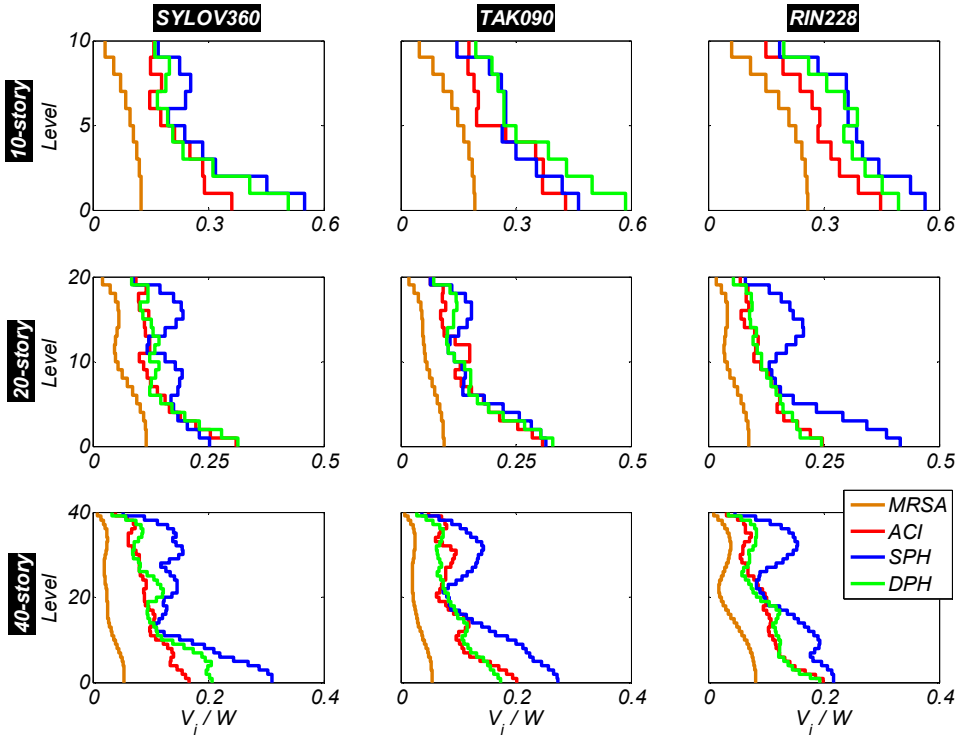

Figure 4.12. Normalized shear force envelopes obtained from NDTHA.

Fig. 4.13 plots the normalized lateral displacement envelopes for each of the cases analyzed. Lateral displacements have also been normalized by the total height. The maximum roof drift ratio, defined as the maximum roof lateral displacement at the top of the wall over the wall height, is practically independent of the design approach, save the case of the 10-story building designed for and subjected to SYLOV360 motion and the 20-story building designed and subjected to the RIN228

motion. This is due to the similar first modal periods for the different design approaches and to the almost constant spectral displacements for the periods of interest. Differences in the lateral displacement envelopes are observed primarily for the 10-story buildings. The SPH design results in quasi-linear displacement envelopes. This is because of the concentration plastic rotation of the wall around its single plastic hinge at the base. In contrast, the ACI-318 design approach results in the more curved displacement envelope due to the propagation of yielding along the wall height.

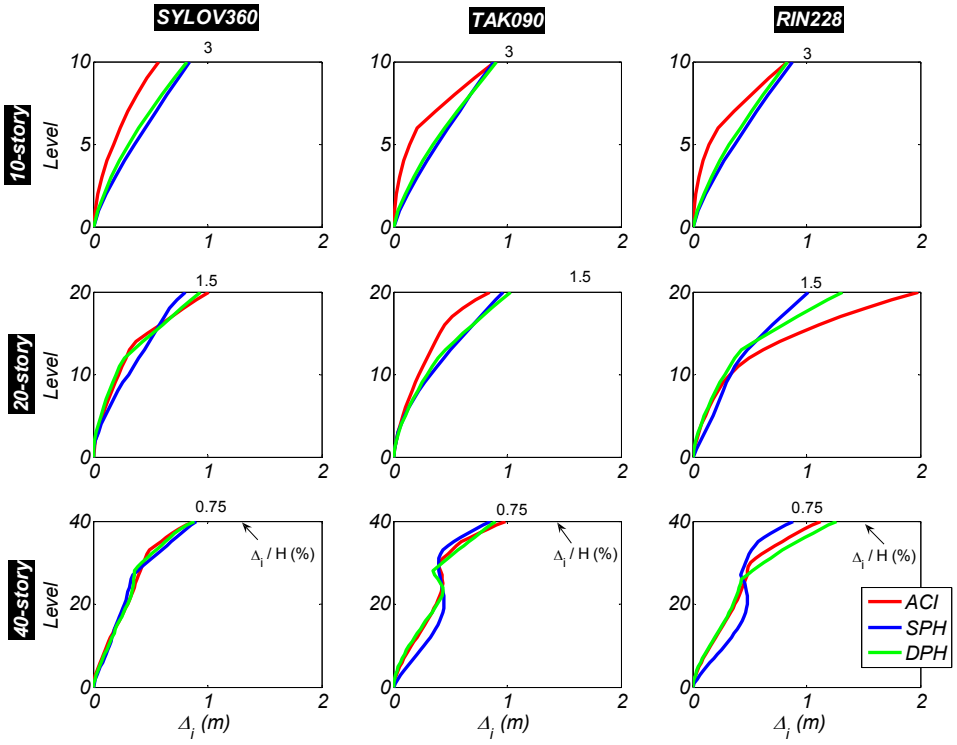

Figure 4.13. Lateral displacement response envelopes obtained from NDTHA.

Fig. 4.14 compares the interstory drift ratio envelopes. The ACI-318 design results in the highest values of interstory drift in the upper part of the walls. There are

cases where the ACI-318 design approaches or even exceeds 5% interstory drift ratios. This is due to localized yielding that occurs at about 0.6H. The maximum interstory drift values in the DPH design are consistently smaller than those computed for the ACI-318 design approach. The SPH design approach gives in 7 out of 9 cases the smallest values of interstory drift at the upper part of the building, and larger, but moderate, values at the base. This is due to concentration of rotation in the plastic hinge at the base of the wall.

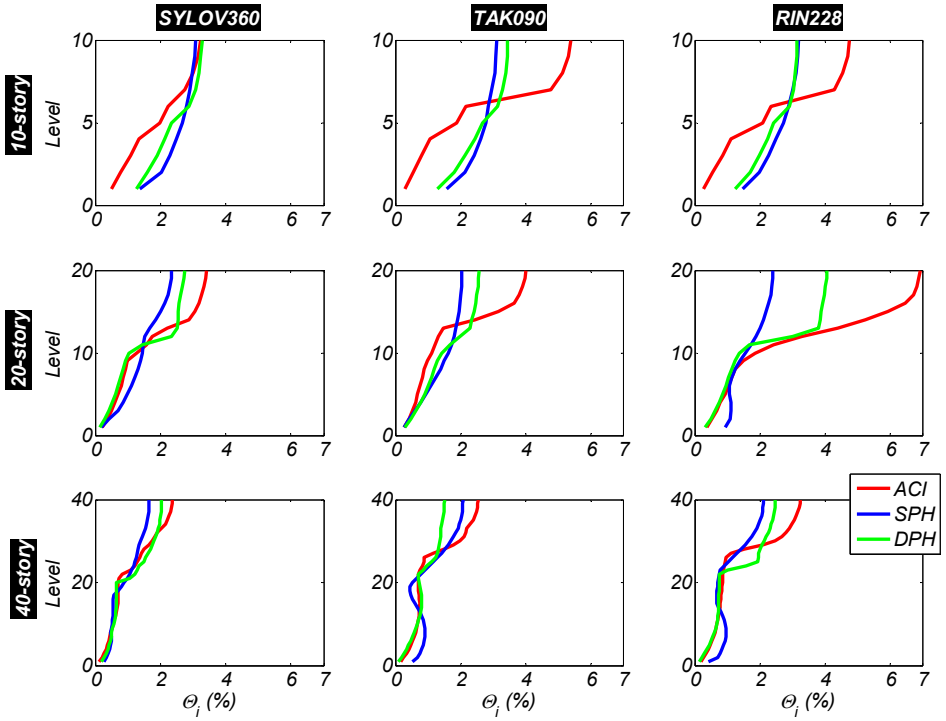

Figure 4.14. Interstory drift ratio envelopes obtained from NDTHA.

Residual lateral displacements should be an important design objective in tall building design. Fig. 4.15 plots the residual lateral displacement profiles observed for the case studies. With the exception of one case, the ACI-318 designs result in the

highest values of residual roof displacement for the 20-and 40-story buildings. In the ACI-318 designs residual displacements increase very significantly above a height 0.6H, where the maximum curvature ductility demand was computed. The DPH design approach shows the largest residual roof displacements in one of the 40-story buildings.

From the observations in this study and pending further studies, the authors suggest decreasing the ductility demand in the mid-height plastic hinges in the taller buildings. This will also cause reduction of the residual displacements and can be achieved by increasing the flexural strength of the mid-height plastic hinges.

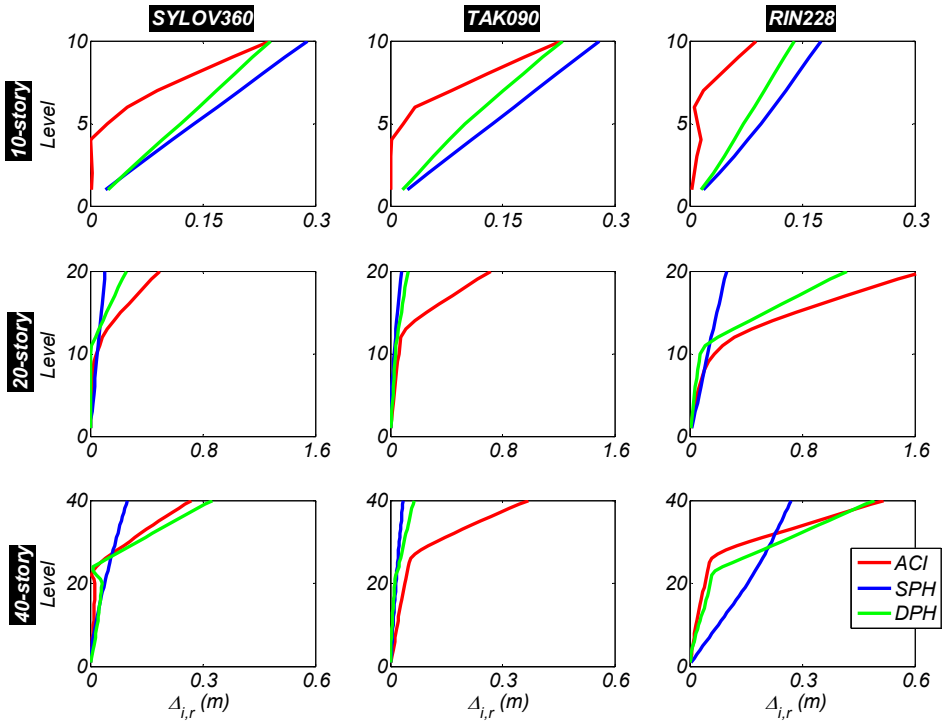

Figure 4.15. Lateral residual displacement response envelopes obtained from NDTHA.

4.6 Summary and Conclusions

This Chapter discussed the effect of higher modes, and especially of the second mode, on the nonlinear dynamic response of cantilever reinforced concrete wall buildings. It proposed a dual plastic hinge concept to better control the seismic response of these buildings to strong shaking. This chapter investigated the seismic response of cantilever wall buildings designed using three different approaches: (i) ACI-318, (ii) a single plastic hinge concentrated at the base of the walls according to EC8, NZS-3101 or the NBCC, and (iii) the proposed dual hinge concept where one plastic hinge concentrated at the wall base and another develops near mid-height. Nonlinear dynamic analyses of these buildings were carried out for three strong near-fault ground motions. The investigation led to the following conclusions:

1. Near fault ground motions including strong pulses, characterized by large elastic spectral accelerations in the range of the second translational mode in high-rise cantilever buildings are likely to have a significant influence on the bending moment and shear force demands in the walls. Currently design codes do not address such large demands explicitly.

2. The second mode response is not significantly affected by the development of plasticity at the base of the walls as is often assumed when performing a code based modal response spectrum analysis. In light of this observation it is concluded that modal superposition approaches, that are appropriate for obtaining design parameters in linear systems, be revised for appropriate use in nonlinear systems.

3. Designs of cantilever wall buildings following the current ACI-318 building code are likely to result in unintended concentration of nonlinear deformations higher

up in the walls where elastic response is generally expected. Current detailing requirements may not ensure controlled flexural response in such regions. This study also observed large interstory drift ratios as well as a large concentration of residual rotations at about 60% of the walls' height in the ACI designs.

4. Codes like EC8, NZS-3101 and NBCC allow the development of plastic hinges at the wall bases only. The results presented in this chapter indicate that, under the near fault ground motions considered in this chapter, bending moment demands at intermediate height in walls developing base plastic hinges compare closely or even exceed the base bending moments. Such intermediate height moment demands are not recognized in the code prescriptive requirements for Capacity Design. Hence, elastic response up the height in walls may not actually occur as intended. It is recommended that current design provisions be examined and appropriately revised.

5. The proposed dual plastic hinge design concept, in which plastic hinges are allowed to form at the wall base and near mid-height while ensuring elastic response elsewhere, was found to have significant advantages: reduction in the amount of longitudinal reinforcement when compared to the EC8, NZS-3101 and NBCC designs, and ease of detailing along most of the height. This concept can be easily implemented in design, bringing a reduction in the amount of longitudinal reinforcement and of transverse reinforcement in a significant portion of the walls. The method when used as highlighted in this chapter may result in large residual rotations at the mid-height plastic hinges in taller buildings.

6. The need of increase of the flexural strength of the mid-height plastic hinge of the proposed dual plastic hinge approach should be further studied for the case of taller buildings.

7. This study concurs with studies reported in the literature on the effect of higher modes of response on the shear force demands in cantilever wall buildings. Shear force demands in buildings are much greater than those determined from modal response spectrum analyses.

CHAPTER 5

5. A TWO–PERFORMANCE LEVEL DISPLACEMENT BASED SEISMIC DESIGN PROCEDURE FOR RC WALL BUILDINGS

5.1 Summary

This chapter presents a displacement-based seismic design approach for RC wall buildings. The method focuses on buildings where all the nonlinear response is developed at a single plastic hinge at the base of the walls. Two performance levels are explicitly considered: i) immediate occupancy and ii) collapse prevention. Initially only the first mode of response is employed to estimate the required base strength of the walls. In a second stage the effects of system overstrength, due to section and kinematic overstrength as well as the dynamic effect of the higher modes are considered to estimate the maximum shear force demand along the height of the walls required to capacity design them.

5.2 Introduction

Within the philosophical framework of performance-based seismic design, methods which design for specific performance objectives under different level of excitation intensity are required. Strains are used to evaluate the performance of structural components while interstory drift and floor accelerations are used to evaluate the performance of non-structural components.

In the past decades a number of interesting displacement-based design approaches have been developed. Sullivan et al. (2003) has reviewed a number of methods available in the literature and a State-of-the-art report has been issued on this topic (Fib 2003). One of the claims is that few of these methods are suitable for design because they have only been developed partially and can only be used if the geometry of the sections is known a priori. In addition only a few of them account for the dynamic effects of the higher modes, and this in an empirical manner, while none of these methods address the effect of system overstrength. The later refers to the effect of interaction between structural walls and elements framing to them in RC wall buildings.

This chapter presents a displacement-based design methodology that explicitly considers two performance levels: immediate occupancy and near collapse. The design approach focuses on the design of buildings incorporating cantilever structural walls as the primary lateral-force resisting system. The effects of kinematic system overstrength, due to coupling between the walls and elements framing to them, as well as this of the dynamic effect of the higher modes are directly considered in order to capacity design the structure.

5.3 Performance Objectives

Two performance levels, corresponding to different levels of ground motion intensity, are explicitly considered. Immediate occupancy is the first performance-level. In this level, the building is expected to behave elastically or with limited

yielding, and non-structural elements are expected to display insignificant damage. The second performance level characterizes the response of the building under increased intensity earthquake ground motion. Extensive yielding and nonlinear inelastic response is anticipated in this performance level until near collapse. Under this performance level, critical regions in the building, in this case at the base of some structural walls are expected to display significant damage, requiring extensive structural and non-structural repairs. The performance objectives are determined through specific strain limits for the concrete and the reinforcing steel as well with interstory drift limits as described below.

5.3.1 Immediate Occupancy

This performance level corresponds to small or moderate earthquake excitation. Limited damage is anticipated on the building with minimum yielding of the reinforcing steel. To achieve this, the curvature at the critical wall section, at the base of the wall, should not to exceed the yield curvature φ_y. The yield curvature is defined as the curvature when the section attains the reinforcement tensile yield strain ε_y or the concrete extreme fibre attains strain $\varepsilon_c = 0.2\%$ (Priestley 2007). For such levelS of strain, concrete spalling is avoided and residual cracking is controlled. To limit non-structural damage, the interstory drift ratio is limited to $\theta \leq 1\%$.

5.3.2 Near-collapse Prevention

This performance level considers a severe earthquake excitation. Significant structural and nonstructural damages are expected at this performance level. To

control structural damage the maximum tensile strain of the reinforcing steel is limited to $\varepsilon_s \leq 5\%$. To preclude crushing of the confined concrete and buckling of the longitudinal reinforcement, the maximum allowable concrete compressive strain is limited to $\varepsilon_c \leq 2\%$.

5.4 First Mode Design – Determination of Wall Base Strength

In this part of the design approach termed as first mode design the required base strength of the wall is determined. Two main assumptions take place in this part of the approach: i) only the first mode of the response is considered ii) the effect of kinematic system overstrength is ignored. Fig. 5.1(a) shows a cantilever structural wall with seismic mass m_i at floor i. Figs. 5.1(b) to (e) give a graphical representation of the main steps of the approach as follows:

1. Define the target displacements $\delta_{y,n}$ and $\delta_{u,n}$ corresponding to the two performance levels of the cantilever wall, see Fig. 5.1(b).
2. Transform the target displacements of step 1 to target displacements of equivalent linear singe degree of freedom (SDOF) oscillators ($\delta_{y,n} / \Gamma^*$, $\delta_{u,n} / (C_\mu \Gamma^*)$), see Fig. 5.1(c).
3. From the displacement design spectra for the two performance levels, based on the target displacements of the linear SDOF oscillators of step 2 estimate the target periods (T_{io}, T_{cp}), see Fig. 5.1(d). The design target period T_e is the minimum of these two periods $T_e = \min [T_{io}, T_{cp}]$.

4. Based on the target period T_{max} and the first modal mass $M_{e,1}$ estimate the first mode base shear force as $V_{1,b} = \frac{\delta_{y,n}}{\Gamma^*}\left(\frac{2\pi}{T_e}\right)^2 M_1$, see Fig. 5.1(e).

5. Distribute the first mode base shear along the height to estimate the design first mode lateral forces, see Fig. 5.1(e).

The next sections describe in detail the five steps of the design approach.

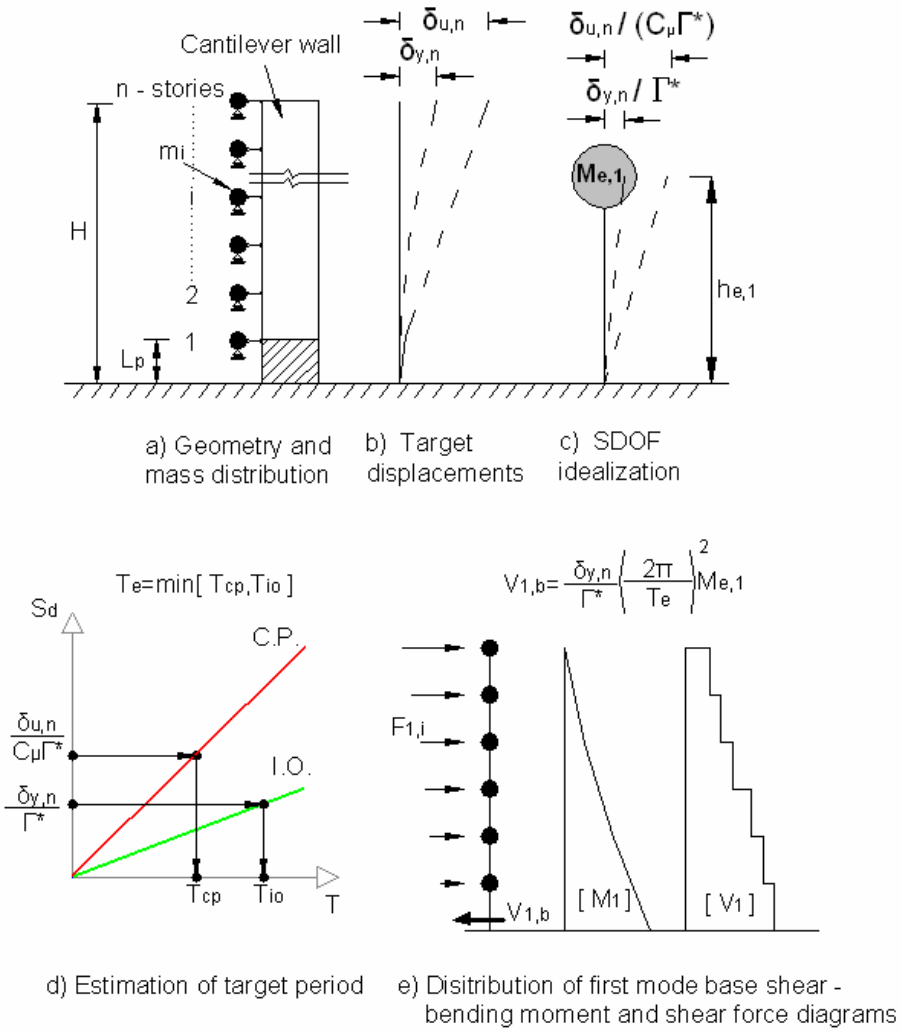

Figure 5.1. Schematic representation of first mode design.

5.4.1 Structural Mechanics Concepts

5.4.1.1 Immediate Occupancy

We consider the simple case of a single prismatic cantilever load bearing wall of height H, see Fig. 5.2. Assuming an inverted triangle distributed lateral force and flexural deformations only, the deflected shape δ(x) and slope θ(x) can be determined from Eqs. 5.1 and 5.2, respectively, as follows:

$$\theta(x)=\left(x+\frac{x^4}{8H^3}-\frac{3}{4}\frac{x^2}{H^2}\right)\frac{2}{3}\frac{V_b}{E_cI_e}H=\left(x+\frac{x^4}{8H^3}-\frac{3}{4}\frac{x^2}{H^2}\right)\frac{M_b}{E_cI_e} \tag{5.1}$$

$$\delta(x)=\left(x^2+\frac{x^5}{20H^3}-\frac{x^3}{2H}\right)\frac{M_b}{2E_cI_e} \tag{5.2}$$

where M_b and V_b are the moment and shear force at the base of the wall, respectively, x is the distance from the base of the wall to the section of interest, E_c is the elastic modulus of concrete and I_e is the effective moment of inertia that considers the effects of concrete loss of tension stiffening.

The curvature at the elastic limit, φ_y, is given from Eq. 5.3, where λ is a geometrical coefficient (Priestley et al. 2007), ε_y is the yield strain of the reinforcement and L_w is the wall length. Priestley et al. (2007) reports values for λ ranging between 1.7 and 2.25 for different sections. At the elastic limit, the moment at the base, M_b, of the wall equals the nominal bending moment, M_n. The yield curvature can also be expressed in terms of the moment acting at the section and the

material and geometrical properties of the section from Eq. 5.4. For a prismatic cantilever structural wall with a triangular lateral force distribution the maximum slope $\theta_{y,n}$ occurs at the top of the building, when x = H based on Eq. 5.1. Substituting Eqs. 5.3 and 4 in Eq. 1 for x = H this maximum slope $\theta_{y,n}$ is related with the geometrical characteristics of the building from Eq. 5.5. Knowing the building's height and the tensile strain of reinforcing steel we observe that the maximum slope or interstory drift depends only on the wall length. In the same sense, substituting Eqs. 5.3 and 5.4 in Eq. 5.2 for x = H the maximum relative displacement, occurring on the roof, is related to the geometrical characteristics based on Eq. 5.6.

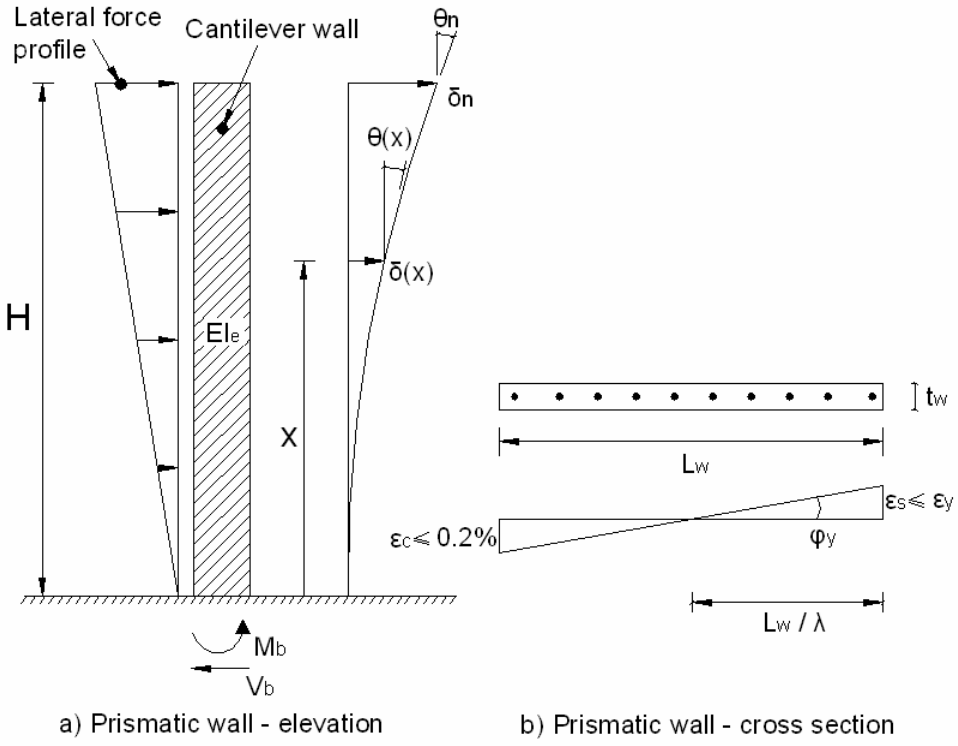

Figure 5.2. Structural mechanics concept used for the immediate occupancy performance level.

$$\varphi_y = \lambda \frac{\varepsilon_y}{L_w} \tag{5.3}$$

$$\varphi_y = \frac{M_n}{E_c I_e} \tag{5.4}$$

$$\theta_{y,n} = \frac{3}{8} \lambda \frac{H}{L_w} \varepsilon_y \tag{5.5}$$

$$\delta_{y,n} = \frac{11}{40} \lambda \frac{H^2}{L_w} \varepsilon_y \tag{5.6}$$

5.4.1.2 Near-collapse Prevention

We consider the case where the nonlinear inelastic response is concentrated at the base of the structure with the formation of a flexural plastic hinge of length L_p, see Fig. 5.3(b). The curvature at each of the two-strain limits can be identified from a moment-curvature analysis of the section, see Fig. 5.3(a), for different reinforcement ratios and axial load. The minimum curvature is considered as the limiting curvature (ε_s=5% or ε_c=2%) for this performance-level. The limiting curvature defines the ultimate curvature ductility of the section $\mu_{\varphi u} = \varphi_u / \varphi_y$ which is equal to the ratio of the limiting curvature φ_u to the yield curvature φ_y. The plastic curvature distribution in the plastic hinge region is assumed to have a rectangular shape as shown in Fig. 5.2(c). The base plastic curvature φ_p is defined as the difference of between the base ultimate and the base yield curvature and is related to the curvature ductility through Eq. 5.7.

$$\varphi_p = (\mu_{\varphi u} - 1)\varphi_y \tag{5.7}$$

Based on the curvature profile of Fig. 5.3(c) the displacement profile corresponding to these curvatures is estimated as the sum of the elastic and plastic displacement, see Fig. 5.3(d):

$$\delta_{u,n}=\delta_{y,n}+\delta_{p,n}=\frac{11}{40}\lambda\frac{H^2}{L_w}\varepsilon_y+\varphi_p L_p\left(H-\frac{L_p}{2}\right) \tag{5.8}$$

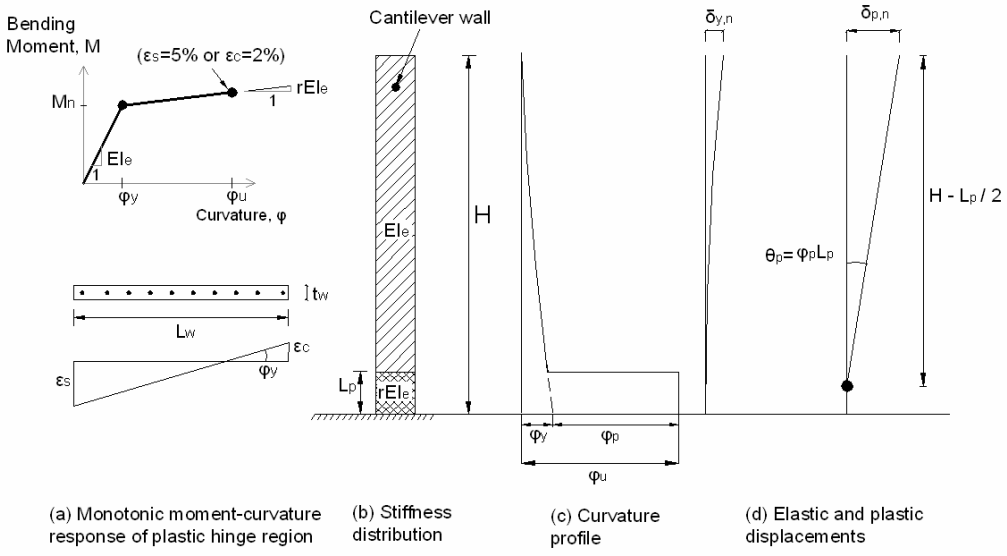

Figure 5.3. Structural mechanics concept used for the near collapse performance level.

Substituting Eq. 5.7 in Eq. 5.8 the maximum roof displacement can be related to the maximum curvature ductility as follows:

$$\delta_{u,n}=\delta_{y,n}+\delta_{p,n}=\frac{11}{40}\lambda\frac{\varepsilon_y}{L_w}H^2+(\mu_{\varphi u}-1)L_p\left(H-\frac{L_p}{2}\right) \tag{5.9}$$

Based on the expressions of the ultimate (Eq. 5.8) and the yielding displacement (Eq. 5.6) the displacement ductility can be related to the curvature ductility as follows:

$$\mu_{\delta u}=\frac{\delta_{u,n}}{\delta_{y,n}}=1+3.6\frac{(\mu_{\varphi u}-1)\left(H-\frac{L_p}{2}\right)L_w L_p}{\lambda H^2\varepsilon_y} \tag{5.10}$$

5.4.2 Equivalent Linear SDOF Structural Idealization

The response of the MDOF cantilever wall of Fig. 5.1(b) is transformed to the response of equivalent linear SDOF oscillators of mass $M_{e,1}$ as shown in Fig. 5.1(c). For the idealization of the MDOF structure to equivalent linear SDOF oscillators the first mode contribution factor $\Gamma^* = \Gamma_1\Phi_{1,n}$ which is the product of the first mode participation factor Γ_1 and the value of the first mode shape vector on top of the wall $\Phi_{1,n}$ are required. For cantilever walls of uniform mass and stiffness Γ^* ranges between 1.35 and 1.5, while the $M_{e,1}$ ranges between 0.65 and 0.75 depending on the number of masses. The modal characteristics Γ^* and $M_{e,1}$ can be estimated from modal analysis. The stiffness distribution of the wall is not known until the end of the design since the length of the wall is not known. Alternatively they can be estimated with the Rayleigh method based on Eqs. 5.12 and 5.13, respectively. In Eqs. 5.12 and 5.13 w_i is the seismic weight at floor i and $\delta_{y,i}$ the yield lateral relative displacement at floor i and g the acceleration of gravity.

$$\Gamma^* = \Gamma_1\Phi_{1,n} = \frac{\sum_{i=1}^{n} w_i \left(\delta_{y,i}/\delta_{y,n}\right)}{\sum_{i=1}^{n} w_i \left(\delta_{y,i}/\delta_{y,n}\right)^2} \tag{5.11}$$

$$M_{e,1} = \frac{1}{g}\frac{\left(\sum_{i=1}^{n} w_i \delta_{y,i}\right)^2}{\sum_{i=1}^{n} w_i \delta_{y,i}^{\ 2}} \tag{5.12}$$

Regarding the equivalent target displacements of the linear SDOF oscillators, for the immediate occupancy performance level the corresponding target displacement is $\delta_{y,n} / \Gamma^*$. For the collapse prevention performance level, the target displacement target nonlinear displacement $\delta_{u,n}$ of the MDOF is transformed to the target displacement of the nonlinear SDOF oscillator $\delta_{u,n} / (\Gamma^*)$. Finally the target displacement of the nonlinear SDOF oscillator is transformed to the target displacement of the linear SDOF oscillator $\delta_{u,n} / (C_\mu \Gamma^*)$, where C_μ is the inelastic displacement factor as defined in chapter 2.

5.4.3 Estimation of Design Quantities

5.4.3.1 Minimum Required Wall Length

For the immediate occupancy performance level a limit of the maximum interstory drift is established to minimize damage in the non-structural components Limitation of the maximum interstory drift which occurs on top of the wall and is given from Eq. 5.5 results in a minimum required wall length. For example for $\theta_{y,max}$ =1%, $\lambda = 2$ and $\varepsilon_y = 0.2\%$, Eq. 5 results in minimum wall length:

$$L_w = \frac{H}{6.67} \tag{5.13}$$

Note that the geometrical relationship given by Eq. 5.13 is independent of the seismicity level. The seismicity level could be accounted for if the tension stiffening effect is taken into account in the derivation of the equations. Having determined the

minimum wall length L_w from Eq. 5.13 the roof yield displacement $\delta_{y,n}$ is estimated from Eq. 5.6.

5.4.3.2 First Mode Base Shear and Design Actions

Having determined the SDOF target displacements $\delta_{y,n} / \Gamma^*$ the target period T_{io} is estimated from the immediate occupancy displacement spectrum. In the same way, from the target SDOF displacement $\delta_{u,n} / (C_\mu \Gamma^*)$ the target period T_{cp} is estimated from the collapse prevention displacement spectrum. Since C_μ depends on the period T, iteration is required to estimate C_μ. The final target design period T_e is the smallest of the two target periods defined above, $T_e = \min (T_{io}, T_{cp})$. Knowing the effective period T_e the design first mode base shear coefficient and the design first mode base shear force are estimated from Eqs. 5.14 and 5.15, respectively:

$$C_1 = \frac{1}{g} \frac{\delta_{y,n}}{\Gamma^*} \left(\frac{2\pi}{T_e} \right)^2 \tag{5.14}$$

$$V_{1,b} = C_1 M_{e,1} g = \underbrace{\left(\frac{2\pi}{T_e} \right)^2 M_{e,1}}_{K_e} \frac{\delta_{y,n}}{\Gamma^*} \tag{5.15}$$

The design first mode base shear is distributed along the height based on the first mode contribution vector $\Gamma_1[\Phi_1]$:

$$F_{1,i} = \frac{\Gamma_1 \Phi_{1,i}}{\sum_{i=1}^{n} \Gamma_1 \Phi_{1,i}} V_{1,b} = \frac{\Phi_{1,i}}{\sum_{i=1}^{n} \Phi_{1,i}} V_{1,b} \quad (5.16)$$

If the Rayleigh method is used to estimate the first mode shape, then Eq. 5.17 is used to distribute the design first mode base shear force as follows:

$$F_{1,i} = \frac{w_i \delta_{y,i}}{\sum_{i=1}^{n} w_i \delta_{y,i}} V_{1,b} \quad (5.17)$$

Based on the design lateral forces, the first mode design shear forces and bending moments along the height are estimated.

5.5 Discussion - Limitations of the First Mode Design Approach

The previous sections presented the main steps of the approach used to estimate the design base strength of a cantilever wall. This part of the design approach was based on two main assumptions: i) only the first mode of the response was considered and ii) the effect of the coupling elements between the walls on the system overstrength were ignored. The effects of tension stiffening and foundation flexibility were not considered. The first can be important for the immediate occupancy performance level. The design procedure can be appropriately modified to account for the effect of tension stiffening and foundation flexibility.

Because of the first assumption the second and higher modes of response were ignored. For the immediate occupancy performance level where the response at the base is nearly elastic, the second mode of response may be important for the maximum interstory drift demand, especially for tall buildings. While for the required base strength the second and higher modes are ignored, they should be considered for the estimation of the moment demand on the upper part of the wall as well for the estimation of the shear force demand along the height of the wall.

The second assumption ignored the effect of kinematic system overstrength. In Chapter 3 we saw that the contribution of system overstrength in the base moment capacity can be important. From a design point of view, ignoring the effect of kinematic overstrength for determining the required base strength is conservative since increase of the base moment capacity results in reduction of the displacement demand. While ignoring the effect of system overstrength is conservative for estimation of the design base moment capacity, it should not be ignored for estimation of the shear force capacity along the height of the wall as shown in chapter 3. The next section presents a design procedure accounting for the effect of higher modes and kinematic system overstrength on the shear force demand along the height of the structure.

5.6 Modified Lateral Force Procedure (MLFP)

This section presents a modified design approach for the capacity design of structural wall buildings accounting for the effects of static system overstrength and the dynamic higher mode effects. The method is restricted in the case of structural

wall buildings with a plastic hinge only at the base of the walls. The method has the following four distinct steps:

Step 1 - First Mode Design Lateral Forces. The first step is the determination of the first mode design lateral forces. These are the forces related with the required base flexural strength of the wall. Any force-based or displacement-based method, like this described above, can be used for the determination of these forces.

Step 2 - Static System Overstrength. Once the design of the critical regions in the walls where the plastic hinges is developed, the designer will establish the increased lateral forces necessary to achieve the target lateral displacement. In this step explicit consideration is made to the flexural overstrength of the critical section of the wall and to the kinematic overstrength caused by the elements framing into the walls at each floor. These are the lateral forces corresponding to the system overstrength. These forces can be determined by hand or by making use of an adaptive pushover analysis.

Step 3 - Dynamic effects. The dynamic effects, in this case the forces of second mode of response are quantified and are combined with the lateral forces established in Step 2. The combination of these two set of forces recognizes that peak values, may not occur simultaneously.

Step 4 - Design of Elastic Regions. Following Capacity Design principles and having explicitly determined the sources of overstrength and the dynamic effects, design envelopes are obtained and other regions in these walls can be designed.

The lateral forces for the design in shear of all the regions in the walls is given by Eq.5.18. F_{oi} are the forces corresponding to the static overstrength of the system. These forces are the sum of the forces corresponding to the flexural strength of the wall including overstrength F_{woi} and the forces corresponding to the kinematic overstrength due to framing F_{fi} as discussed in Chapter 3. $\Gamma_2\Phi_{2i}$ is the contribution vector of mode 2. Eq. 5.19 gives an approximate expression for $\Gamma_2\Phi_{2i}$ based on the study presented in Chapter 4. Factor $\rho_{12} \leq 1$ accounts for the correlation of the maxima of modes 1 and 2. For value of ρ_{12} equal to 1 the maximum contribution of the second mode is considered. Further study is under progress for the statistical determination of ρ_{12}. Forces due to the second mode of response are multiplied with the correlation factor ρ_{12} and then combined with the static system overstrength lateral forces.

$$F_i = F_{oi} + \rho_{12} F_{2i} = F_{woi} + F_{fi} \pm \rho_{12} \Gamma_2 \Phi_{2i} m S \alpha_2 \qquad (5.18)$$

$$\Gamma_2 \Phi_{2i} = \min\left[4.28\frac{h_i}{H},\ 0.6,\ -2.5\frac{h_i}{H} + 1.85 \right], \text{ where } 0 < h_i/H < 1 \qquad (5.19)$$

Having determined the lateral forces, the shear force envelopes are calculated. For the design envelopes the absolute value of the contribution of the second mode is

added to this of the static forces to capture the effect of both signs of second mode response. The positive sign increases the demand at the base while the negative sign increases the demand in the upper part of the building as explained in chapter 4.

The floor accelerations are estimated from Eq. 5.20. The acceleration of each individual contribution is simply the ratio of the corresponding force to the seismic mass of the specific floor. Eq. 5.20 includes the factor $a_{hi}a_{gmax}$ accounting for the contribution of the third mode and higher (termed here the higher high modes) along the height of the structure. Values of a_{hi}, and ρ_{12} are being investigated.

$$a_i = a_{oi} + \rho_{12}\left|a_{2i}\right| + a_{hi}a_{gmax} = \frac{F_{oi}}{m} + \rho_{12}\left|\Gamma_2 \Phi_{2i} Sa_2\right| + a_{hi}a_{gmax} \qquad (5.20)$$

To visualize the shape and relevant magnitude of the individual contributions on the lateral force, acceleration, shear force and bending moment envelopes Fig. 5.4 plots the individual and cumulative contribution due to first mode lateral forces overstrength of the wall section, kinematic overstrength and dynamic second mode response. The schematic representation considers a seven-story structure with an internal wall among gravity columns as presented in chapter 3. The design spectral acceleration of the second mode is four times larger than the spectral acceleration corresponding to the design first mode forces and the modal correlation factor ρ_{12} is equal to 0.5. The flexural capacity of the framing system M_f is equal to 2% of the base moment due to flexural strength of the wall and the length of the wall L_w is equal to the length of the framing elements L_f.

Even for this small moment capacity of the framing system, the contribution of framing to the base shear is equal to the base shear corresponding to the flexural strength of the wall. Lateral forces and thus floor accelerations are strongly affected by the framing action. The second mode greatly affects the shear forces and floor accelerations The contribution of the second mode to the base shear is 70% of the shear force determined from the first mode lateral forces. The combined effects of system overstrength and the second mode result in a base shear force 3.2 times the base shear force calculated from the first mode lateral forces.

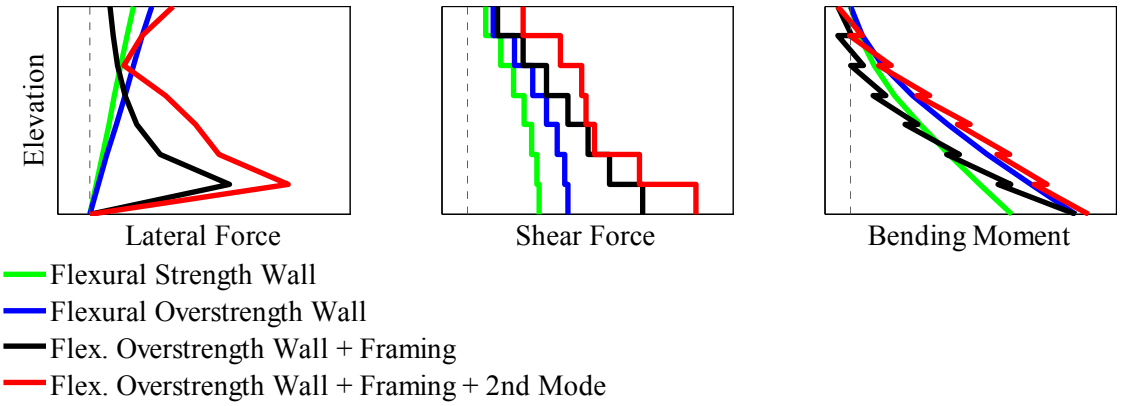

Figure 5.4. Schematic representation of lateral force, shear force and bending moment envelopes of a 7-story building accounting for kinematic overstrength and 2nd mode of response.

CHAPTER 6

6. SHAKE TABLE TEST OF A 7-STORY FULL SCALE BUILDING SLICE PHASE I: RECTANGULAR WALL

6.1 Summary

This chapter presents key results gained from a 7-story reinforced concrete building slice built at full-scale and tested on the George E. Brown Jr. Network for Earthquake Engineering Simulation Large Outdoor High-Performance Shake Table of the University of California at San Diego. The building was tested in two phases. In Phase I the building had a rectangular load bearing wall acting as the main lateral force resisting element. The seismic design of the building followed a displacement-based design approach for specific performance objectives for two hazard levels. The design resulted in a reduced amount of longitudinal reinforcement in the wall if compared to that required by current code force-based methods. The building was subjected to four historical input ground motions recorded in California, including the strong intensity near-fault Sylmar record that induced significant nonlinear response. The building responded very satisfactory to the motions and met all performance objectives. Important results regarding the effect of coupling between walls and the slab on the system overstrength and the effect of higher modes are discussed.

6.2 Introduction

Reinforced concrete walls are excellent at resisting lateral forces in low to medium rise buildings in high-seismic regions. However, and quite paradoxically, buildings incorporating structural walls can be prohibitively expensive and difficult to build when designed conforming to current codes. Practicing engineers in United States have often questioned current codes which make this attractive lateral force resisting system congested and difficult to build, especially in the foundation and in the lower levels of the walls. Hence, significant savings could be made if the congestion of the reinforcement could be eased. A way to reduce congestion is to reduce the design lateral forces. Displacement-based design methods provide an answer in this direction (Restrepo and Preti 2005, Englekirk 2003, Fib 2003). Often such methods suggest that walls can be designed for specific performance objectives while requiring less amounts of longitudinal reinforcement.

This chapter presents key results of Phase I of a shake table test on a full-scale slice of a 7-story reinforced concrete residential building. The seismic design followed a displacement-based method that resulted in significantly less flexural reinforcement than that required by the ASCE-7 code (ASCE 2006). The test program took place in the new Large High-Performance Outdoor Shake Table (LHPOST) funded by the National Science Foundation through the George E. Brown Jr. Network for Earthquake Engineering Simulation (NEES) program and located at the Robert and Natalie Englekirk Structural Engineering Center of the University of California at San Diego. The full-scale building slice was subjected to historical input ground motions

recorded in Southern California that represent a range of seismic demands up to the design earthquake during the period October 2005 and January 2006.

The test addressed four issues relevant to construction optimization: (i) longitudinal reinforcement reduction, (ii) use of a single curtain of reinforcement to transfer shear, (iii) use of Capacity Design to control the nonlinear response of the structure, and (iv) the use of resistance-welded reinforcement in the boundary elements of first level of the walls.

6.3 Description of the Test Structure

The test structure represented a slice of a 7-story multistory residential load bearing wall building located in Los Angeles, California. The building was tested in two phases and results from Phase I are presented below. The response in Phase II is discussed in chapter 7.

In Phase I the lateral force resistance was provided by a 3.66 m long load bearing reinforced concrete rectangular wall, termed here the web wall. The web wall was 0.20 m thick at the first and seventh levels and 0.15 m elsewhere. The web wall provided lateral force resistance in the East-West direction of loading and supported seven 0.20 m thick slabs spaced at 2.74 m. Two transverse walls built East and West of the web wall provided lateral and torsional stability. The West wall was a precast segmental that was jointed using mortar bed joints and then prestressed. This wall had a footing that enabled it to rock in the East-West direction. The East wall, termed here

the flange wall, was 4.87 m long, 0.20 m thick at the first floor and 0.15 m thick elsewhere. The web and the flange walls were cast into footings that were tied down to the shake table moving platen. Fig. 6.1 shows an overall view of the test building and its main components and Fig. 6.2 gives the main dimensions. The building height, measured from the top of the foundation, was 19.2 m. The total weight excluding the foundation was 2045 kN. Table 6.1 lists the tributary seismic weights in the building.

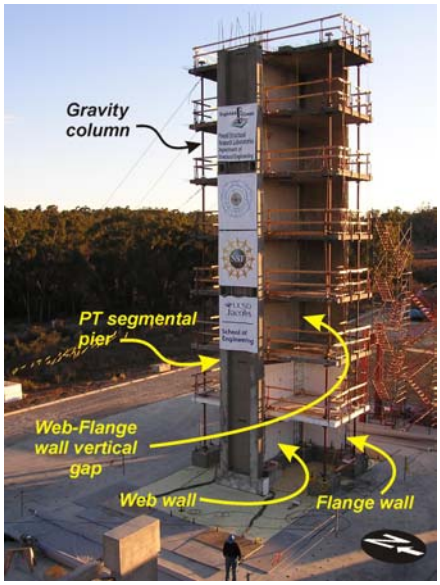

Figure 6.1. South-West View of Building.

The slab between the web and the flange walls was 0.61 m wide and had two 140 mm deep by 51 mm wide slots on both ends. Under this arrangement the slab acted like a near pin-ended link enabling the transfer of in-plane shear, bending moment, and axial force transverse but a reduced capacity to transfer out-of-of plane shear and bending moment. A 0.61 m wide vertical gap between the web and the flange was left in this phase to avoid any shear flow transfer between the web and

Table 6.1. Seismic Weights* (kN)

Reference&	Web Wall	Slab	Flange Wall	Segmental Wall	All other	Total
SW0	22.2	0.0	30.8	19.5	0.0	***72.6***
SW1	38.9	168.6	54.9	39.0	8.4	***309.8***
SW2	33.4	156.0	48.0	39.0	8.4	***284.9***
SW3	33.4	156.0	48.0	39.0	7.9	***284.4***
SW4	33.4	156.0	48.0	39.0	7.6	***284.1***
SW5	33.4	156.0	48.0	39.0	7.6	***284.1***
SW6	38.9	156.0	48.9	39.8	7.6	***291.2***
SW7	22.2	156.0	30.2	20.2	6.0	***234.7***
Total	***255.8***	***1104.8***	***357.0***	***274.7***	***53.5***	***2045.8***

* Does not include the foundation

& Refer to Fig. 2 for location of the lumped seismic weights

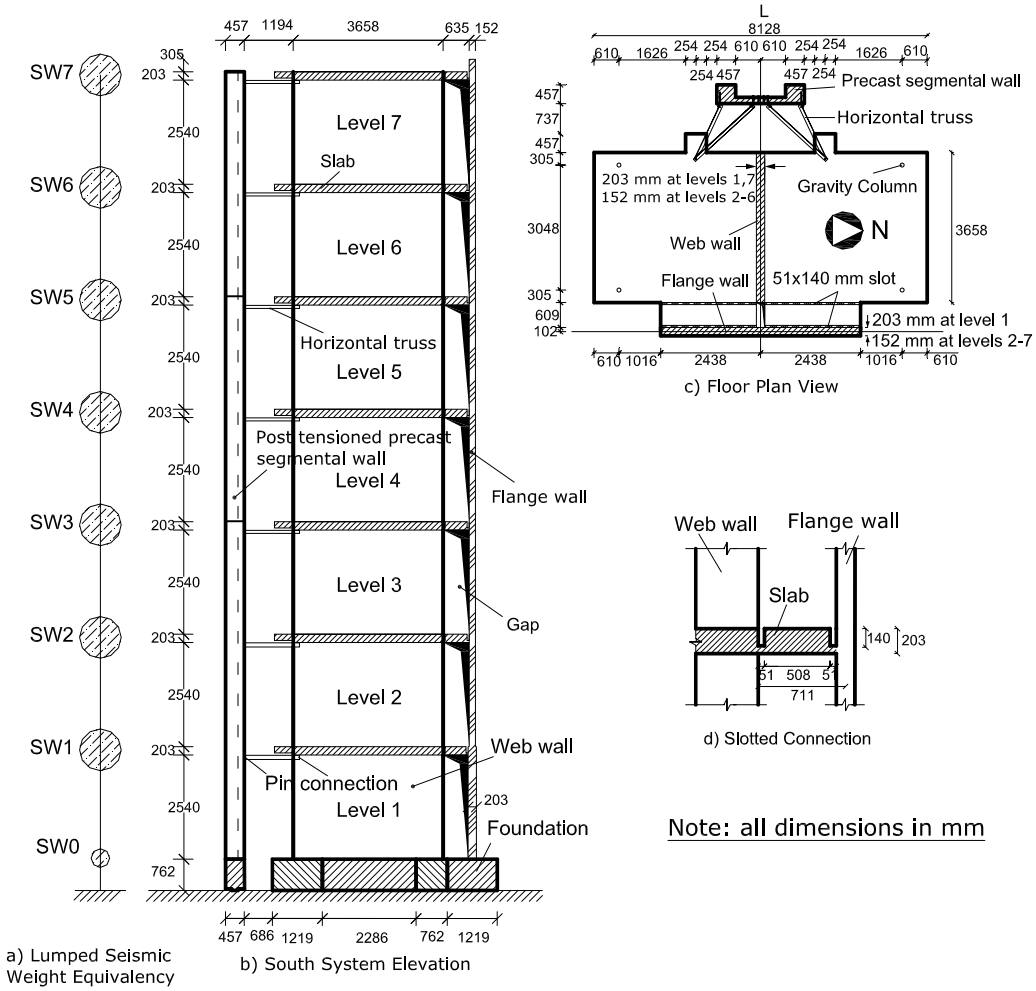

Figure 6.2. Test Structure Geometry and Lumped Seismic Weights

flange walls. Horizontal hoops protruded from each of the walls and overlapped at 102 mm in this gap to ensure monolithic T-wall behavior in Phase II. The slab North and South ends were supported on four gravity columns (102 mm diameter grout filled extra strong steel pipe). Gravity columns had pinned ends and were able to carry axial tension and compression.

Figs. 6.3 and 6.4 show relevant wall and slab reinforcing details. The web wall had boundary elements in levels 1 and 7 only, refer to Fig. 6.2 for the levels in the building. The detailing of the reinforcement at level 7 was identical to that at level 1. This is because at some point in the test program it was envisaged that the wall could be coupled at the top by a stiff beam that would force a plastic hinge there. The transverse reinforcement in the boundary elements consisted of #3 weld-resistance grids at s_h=102 mm. The distance s_h was selected to provide adequate lateral stability to the longitudinal reinforcement. The ratio of the distance between the grids s_h to the diameter of the longitudinal #5 bars (d_b = 15.7 mm) was s_h/d_b=6.42. The length of the boundary elements was approximately the expected wall neutral axis depth. The West end boundary elements were longer than those in the East because in Phase II the flange in tension would result in a deeper neutral axis. The volumetric confinement ratio at the boundary elements was ρ_v=1.36%. In levels 2 to 6 the lap-splice had #3 hairpin transverse bars at 203 mm. The longitudinal reinforcement enclosed by the grids in the boundary elements consisted of 8 #5 longitudinal bars. The middle portion of the wall was detailed with a single longitudinal reinforcement curtain of #4 bars at 254 mm.

At levels 2 to 6 the web wall longitudinal and transverse reinforcement were detailed in a single curtain. The longitudinal reinforcement consisted of 4 #7 bars at each end and 11 #4 bars spaced at 254 mm in between. In levels 2 to 6 the transverse reinforcement consisted of a single curtain of #4 bars at 203 mm. The longitudinal reinforcement ratio in the web wall was ρ_l=0.66% at levels 1 and 7 and ρ_l=0.81% elsewhere. The transverse reinforcement ratio was ρ_{sh}=0.31% at levels 1 and 7 and ρ_{sh}=0.4% elsewhere.

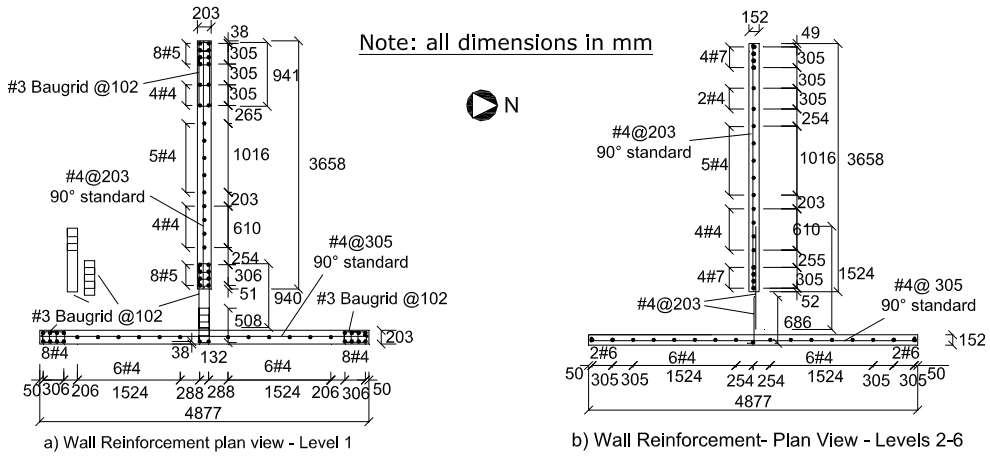

Figure 6.3. Test Structure – Plan View of Reinforcement

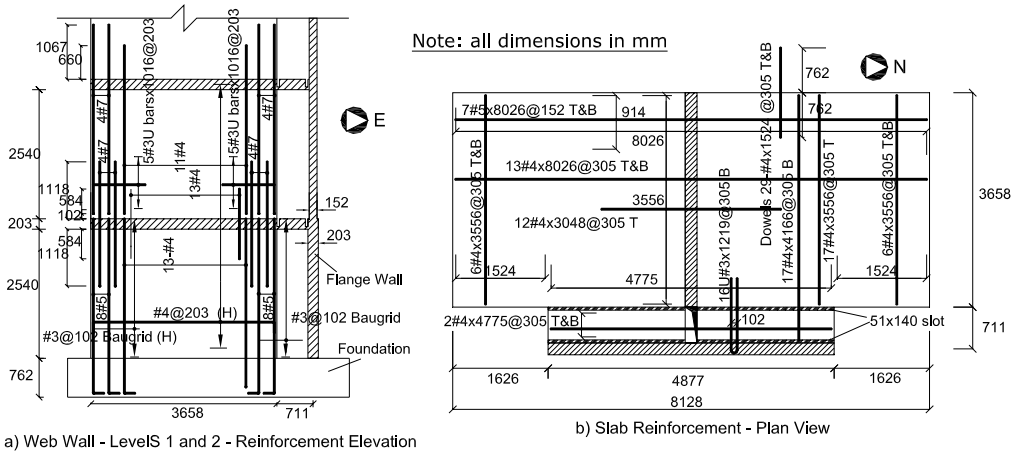

Figure 6.4. Web Wall Levels 1&2 and Slab Reinforcement

The walls and slabs were built using tunnel form construction. So, horizontal construction joints in the wall were at the top of the slab and again at 102 mm from the top of the slab. Concrete with specified compressive strength of 27.6 MPa and ASTM A615 Grade 60 steel reinforcement were used. The average yield strength measured of the reinforcing steel was 455 MPa, the average strain at 0.2% offset for the resistance weld confining reinforcement was 518 MPa and the average concrete compressive strength at the day of the final test was 37.9 MPa. Specific material properties are listed in chapter 7.

6.4 Seismic Design

The seismic design of the building followed a displacement-based design method and targeted the following performance objectives: (i) At immediate occupancy, corresponding to a demand from commonly occurring earthquakes with 50% probability of exceedance in 50 years of exposure: (a) maximum tensile strain in the reinforcement of 1%, (b) maximum compressive strain in the concrete of 0.4% and (c) maximum interstory drift of 1%. (ii) At life safety, corresponding to a demand from a rare earthquake with 10% probability of exceedance in 50 years of exposure: (a) maximum tensile strain in the reinforcement of 5%, (b) maximum compressive strain in the concrete of 1%, and (c) maximum roof drift ratio of 3%. The design resulted in base shear force coefficient of C_s=14.7%.

If the building was designed using the design provisions prescribed by ASCE-7 (ASCE 2006), the fundamental period given by Eq.. 12.8-7 would be T=0.45 sec.

The upper limit of the fundamental period based on paragraph 12.8.2 of ASCE-7 would be T=0.63 sec. For these periods the design base shear coefficients obtained from the spectrum of the design earthquake for the design earthquake and for a response modification factor R =5 are C_s = 0.37 and 0.28, respectively. These two values are significantly greater than a coefficient C_s=0.147 required by the displacement-based design approach. This significant difference in the estimation of the design base shear coefficient is largely due to the way of determining the fundamental period T. Force-based code provisions use relations that have been obtained from low-amplitude building vibrations to determine the fundamental period. Such relations do not account for the mass, and effective stiffness of the actual system. The displacement-based design approach resulted in an effective fundamental period for the design earthquake of T=1.06 sec. This period was obtained by ignoring the tension stiffening of the concrete. This value is significantly larger than the period calculated from the code equations.

It can be argued that the maximum inelastic displacement demand for structures expected to respond highly nonlinear during the design earthquake is better related to the effective fundamental period. For moderate earthquakes, where limited nonlinear response of the structure is expected, a period related to partial loss of the concrete tension stiffening may be more appropriate. This implies the use of two different periods in displacement based design for different performance levels.

The design followed Capacity design principles (Paulay and Priestley 1992), which requires a clear identification of a single mechanism of inelastic deformation. In the prototype building flexural plastic hinges were selected to develop only at the base of the walls. Capacity design considered the section overstrength at the wall base. As a result and because of the decrease in width and in axial force at level 2, the amount of longitudinal reinforcement there increased. In this wall the detailing of the longitudinal reinforcement deliberately constrained the spread of plasticity to within level 1. Further, in the capacity design of the wall for shear it was necessary to evaluate the effect of kinematic overstrength due to coupling between the walls through the slab and the effect of higher modes. Panagiotou et al. (2007) gives a detailed discussion of the design of the web wall.

6.5 Experimental Program

6.5.1 NEES-UCSD Shake Table

Testing was performed on the unidirectional 20-MN vertical payload LHPOST. This shake table was built with partial funding from the National Science Foundation and is administered under NEES. The shake table currently operates in a single-degree-of-freedom configuration reproducing motions in the East-West direction. Details of LHPOST are described elsewhere (Van den Einde et al. 2004, Ozcelik et al. 2007).

6.5.2 Input Ground Motions

The building was subjected to four historical earthquakes recorded in Southern California, each of increased intensity. Prior and between earthquake tests the building was subjected to long-duration ambient vibration tests and to long-duration low-amplitude 0.5-25Hz band clipped white noise (WN) tests with root-mean-square (RMS) amplitudes of 2%, 3% and 5% g. The 3% g RMS WN tests, excited the web wall beyond cracking but within the elastic limit of the reinforcement. These tests were used for system identification and evaluation of damage progression in the building (He et al. 2006).

The acceleration time-histories as well as the acceleration and displacement response spectra of the earthquake input motions, as reproduced by LHPOST, are plotted in Fig. 6.5. The low intensity input motion EQ1 was the longitudinal component from the VNUY station recorded during the 1971 M_w 6.6 San Fernando earthquake. The two medium intensity input motions EQ2 and EQ3 were the transverse component record from the VNUY station obtained during the 1971 M_w 6.6 San Fernando earthquake and the longitudinal component from the WHOX station recorded during the 1994 M_w 6.7 Northridge earthquake, respectively.

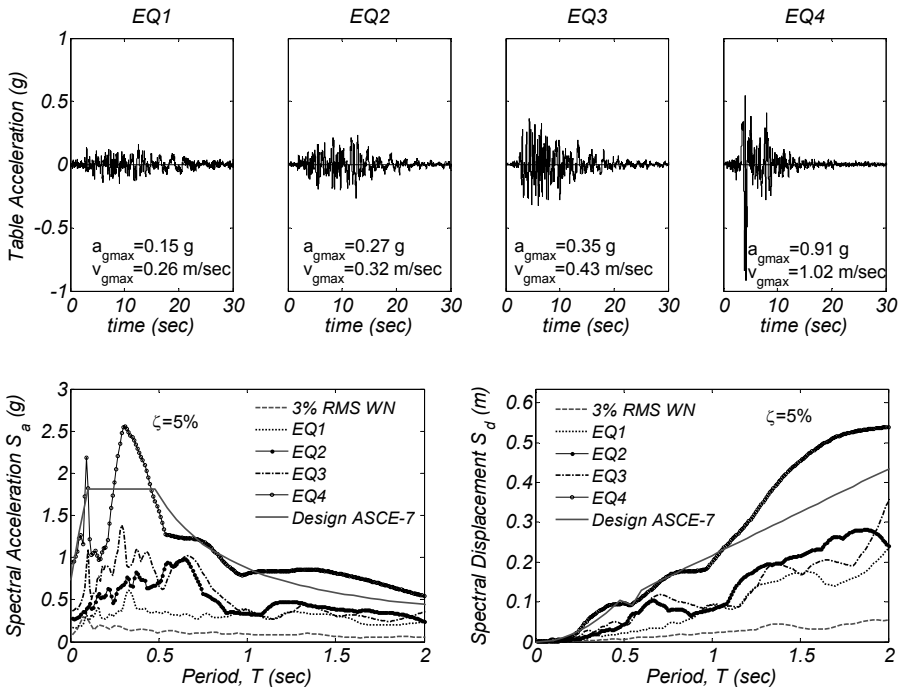

Figure 6.5. Phase I Time Histories and Response Spectra of Recorded Table Ground Motions.

The large intensity input motion EQ4 was the Sylmar Olive View Med 360^o recorded during the 1994 M_w 6.7 Northridge earthquake. Fig. 6.5 shows also the spectrum for the design earthquake obtained from ASCE-7 (ASCE 2006) for site class C for the site, for $S_{DS} = 1.81$ g, $S_{D1} = 0.87$ g, $T_0 = 0.10$ sec. and $T_S = 0.48$ sec. This figure also plots the response spectra for a 3 minute long 3% RMS WN whose intensity was low relative to the earthquake motions.

The fundamental period of the building calculated assuming gross section properties for all elements was T=0.50 sec. As mentioned above, the fundamental period of the building calculated ignoring the contribution of concrete tension

stiffening in the web wall was T=1.06 sec. These two periods provided suitable upper and lower bounds for the fundamental period and were used to select the input ground motions. Note in Fig. 6.5 that motions EQ1, EQ2 and EQ3 have similar ordinates in the bandwidth between 0.9 and 1.1 sec. Note, however, the frequency content of motion EQ1 is much smaller than that of motions EQ2 and EQ3 in the bandwidth between 0 and 0.9 sec. In contrast, input motion EQ3 is richer in high frequency content than the other two motions. Note also that input motions EQ2 and EQ3 have similar spectral ordinates in the bandwidth between 0.5-1 sec.

The response spectrum of input motion EQ4 matched closely the spectrum for the design earthquake calculated for the site according to ASCE-7 in the bandwidth between 0.5-1 sec. The acceleration response spectrum of this motion, as obtained from the motion recorded on the LHPOST has two pronounced peaks. One peak is at 0.31 sec and the other at 0.1 sec. The former peak is because of the acceleration pulse recorded by the station while the latter peak is because of the oil column resonant period of the combined LHPOST-Test structure.

Table 6.2 shows the probability of exceedance for an exposure of 50 years for the motions selected and for T= 0.5 and T = 1.0 sec. These periods match closely the upper and lower bound fundamental periods estimated for the building. Motion EQ1 adequately tested the immediate occupancy objectives of the building, which were anchored to a 50% probability of exceedance in 50 years of exposure. Further, motion EQ4 was above that needed to test the life safety performance objectives, which were

anchored to a 10% probability of exceedance in 50 years of exposure. Motions EQ3 and EQ4 were moderately intense and provided data for damage progression and model calibration. These two motions did not test any specific design performance objective.

Table 6.2. Probability of Exceedance in 50 Years of Exposure of Test Motions (%)

	T=0.5 sec	T=1.0 sec
EQ1	63.7	26.5
EQ2	24.5	32.7
EQ3	27.8	26.5
EQ4	5.8	6.1

6.6 Instrumentation

An extensive ensemble of sensors was deployed throughout the building to measure its response. The ensemble comprised 139 DC-coupled accelerometers, 88 displacement transducers, and 314 strain gages. These sensors were sampled at 240 Hz and subjected to an antialiasing filter at 50 Hz. Also, an array of seven 50 Hz, 3mm resolution differential GPS displacement sensors were deployed to measure total lateral displacements (Bock et al. 2006). Finally, 17 cameras recorded and broadcast online the response of different parts of the building.

Fig. 6(a) shows the horizontal and vertical accelerometers deployed on the roof. Fig. 6.6(b) shows the external and internal concrete instrumentation on the first two levels of the web wall. The displacement transducers attached externally to the concrete close to the edges of the web wall recorded fixed-end rotations, and smeared

surface strains and curvatures. Horizontal displacement transducers near the base of each level recorded sliding shear displacements. Diagonal string potentiometers recorded wall panel shear deformations. Fig. 6.6(b) shows also the strain gages placed on the reinforcing bars on levels 1 and 2 of the web wall.

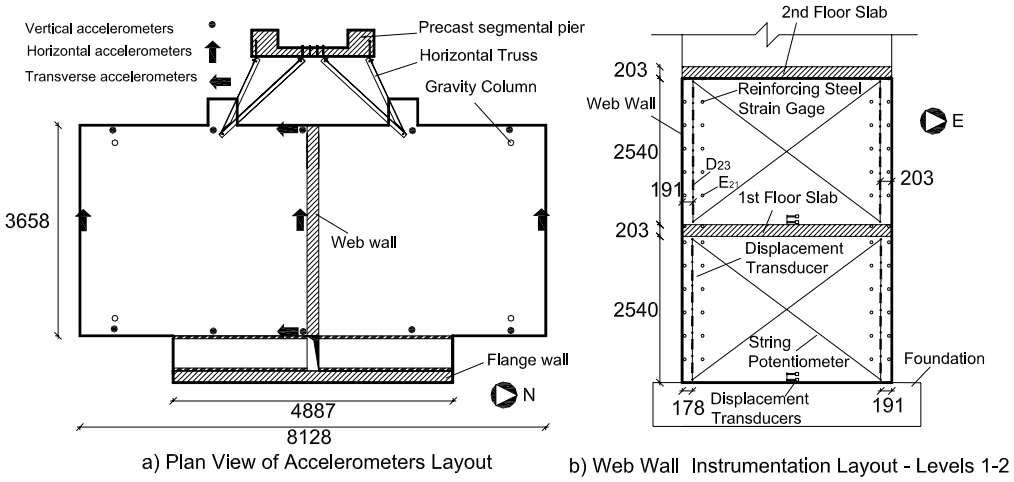

Figure 6.6. (a) Plan view of position of accelerometers, (b) Elevation of displacement transducers and strain gages on levels 1 and 2 of web wall.

6.7 Test Results

6.7.1 General Observations

The use of four earthquake input motions with distinct features and intensities allowed the monitoring of the development of different damage states in the test structure. Overall, the response was slightly nonlinear for motion EQ1, limited nonlinear for the "medium" intensity motions EQ2 and EQ3 and extensively nonlinear for motion EQ4. Table 6.3 lists the maximum values of relevant response variables measured in tests EQ1 to EQ4.

Fig. 6.7 plots the variation of the building's first two longitudinal mode periods with testing. A fundamental period of T=0.51 sec was obtained from the 3% g RMS WN tests at the beginning of the experimental program. This is very similar to the theoretical fundamental period obtained from a 3-D model of the building using uncracked section properties. The experimental program clearly showed the dependency of the fundamental period on the intensity of the WN tests (He 2006). Periods cited below were extracted from 3% g RMS WN tests. Before test EQ1 the fundamental period had shifted to T=0.59 sec. This shift was because of the partial loss of tension stiffening in the concrete caused by twenty five 2% and 3% g RMS WN tests applied before. After test EQ1 the fundamental period had shifted to T=0.65 sec. After tests EQ2 and EQ3 the fundamental period had changed to 0.82 and 0.88 sec., respectively. The changes in period were the result of the gradual loss of tension stiffening across the cracked concrete. Finally, after test EQ4 the fundamental period augmented to T=1.16 sec. In contrast with the first mode, the second mode period is slightly affected from the induced damage and remains almost constant and equal to T_2=0.1 sec.

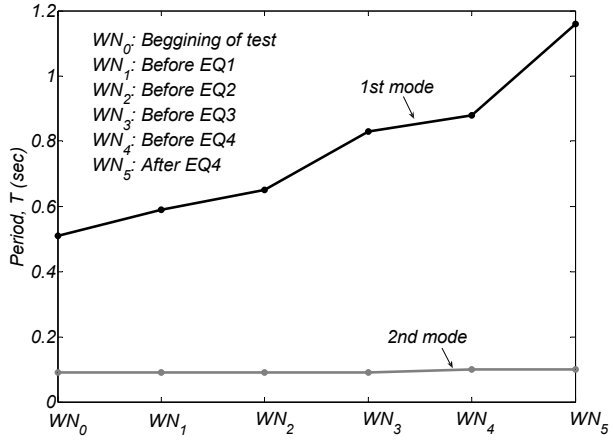

Figure 6.7. Variation of period of first two longitudinal modes.

The reference yield curvature calculated from a moment-curvature analysis of the critical section was $\varphi_y=0.0034/l_w$ where l_w is the length of the web wall. The curvature ductility, defined as the ratio of the maximum curvature to the reference yield curvature, was 3.1, 3.3 and 8.2 in tests EQ2 to EQ4, respectively. In test EQ1 the maximum curvature was less than the reference yield curvature. Curvature ductilities observed confirm that under tests EQ2 and EQ3 the web wall exhibited limited nonlinear response, while significant nonlinear response occurred in test EQ4.

Table 6.3. Maximum Recorded Values of Relevant Parameters

	EQ1	EQ2	EQ3	EQ4
Roof Relative Lateral Displacement (m)	0.05	0.14	0.16	0.40
Roof Drift Ratio (%)	0.28	0.75	0.83	2.06
Interstory Drift Ratio (%)	0.35	0.89	1.03	2.36
System Base Moment (kN-m)	5368	8351	8353	11495
System Base Shear Force (kN)	420	632	704	1225
Roof Acceleration (g)	0.43	0.61	0.75	1.10
Peak Ground Acceleration (g)	0.15	0.27	0.35	0.91
Roof / Peak Ground Acceleration	2.81	2.27	2.11	1.21
Longitudinal Bar Tensile Strain (%)	0.61	1.73	1.78	2.85
Concrete Compressive Strain (%)	-0.07	-0.17	-0.18	-0.39
Web Wall Base Curvature x Wall Length	0.0020	0.0107	0.0114	0.0282
Tensile Chord Growth (mm)	7.2	24.6	27.5	64.8
Compressive Chord Shortening (mm) (190mm from web wall end)	-7.2	-9.9	-6.5	-10.4
Joint Shear (Sliding) deformations (mm)	0.1	0.4	0.5	2.5
Strain Rates (m/m/secx100)	3.7	39.7	6.3	19.7

Test EQ1 displaced the building to a roof drift ratio Θr = 0.28%. The maximum recorded interstory drift ratio was 0.35% or 1.25 Θ_r. The tensile strain recorded in the web wall longitudinal reinforcement in level 1 during test EQ1 reached 0.61% or 2.7 times the yield strain. On the opposite end, the compressive strain in the concrete cover at the base of the wall reached -0.07% in this test. Maximum shear

deformations along the construction joints were 0.1 mm only. Cracking of the wall was widespread and was visible up to level 4. Residual cracks were extremely thin and were barely noticeable. In summary, test EQ1 gave conclusive validation of the performance objectives selected for immediate occupancy.

The response of the building to tests EQ2 and EQ3 was similar, although there were some subtle differences, especially in those response variables sensitive to high frequency content. The roof drift ratios measured in these tests were Θ_r = 0.75 and 0.83%, respectively. Recorded interstory drift ratios in these tests were 1.19 and 1.24 of their respective roof drift ratios. Moderate yielding occurred in the web walls longitudinal reinforcement, which reached a tensile strain of 1.73% and 1.78% in these tests. The concrete compressive strain measured in tests EQ2 and EQ3 was -0.17% and -0.18%, respectively. Maximum shear deformations along the construction joints were 0.4 and 0.5 mm for tests EQ2 and EQ3, respectively. As listed in Table 6.3 the highest strain rate in the longitudinal reinforcement was measured during test EQ2. This was caused by the spread of the Lüders bands into the gaged portion of the bars during this test. Strain rates resulted in 7% increase of the steel yield strength during test EQ2 according to coupon tested to the same strain rate and strain history.

In test EQ4 the maximum roof drift and interstory drift ratios were 2.06% and 2.36%, respectively. That is, the interstory drift ratio in this test was $1.15\Theta_r$. A comparison of the ratios between the interstory roof drift and the roof drift ratios in all tests shows a consistent reduction with the progression of testing. This is also a signal

of development of localized plasticity at the base of the wall, which increased as the displacement demands in the tests increased. In this test the tensile strain in the longitudinal reinforcement in the plastic hinge at the base of the wall reached 2.85% and the concrete compressive strain there reached -0.39%. This strain level in the concrete corresponds very well with the limited spalling of the concrete cover observed at the wall base. The weld resistance confinement grids provided excellent lateral stability to the reinforcing bars once the concrete cover spalled off. Maximum shear deformations along the construction joints were small at 2.5 mm. Assuming that all the measured shear force, V, was resisted from the web wall with area A_w, the ratio V/A_w was equal to $0.27\sqrt{f_c'}$, where f_c'=32.4 MPa. This value of shear stress was significantly smaller than value $0.66\sqrt{f_c'}$ of eq. 11.5.7.9 of ACI-318 (ACI 2005) corresponding to the upper bound of the probable shear strength provided from the shear reinforcement (V_s).

Test EQ4 ended with a surprise lap-splice failure in the West end of the web wall at the base of level 2. This lap-splice survived the peak imposed demand unscathed but degraded afterwards. The lap-splice failure was manifested by a large split crack. Besides splitting of the concrete in this region, residual crack widths were about 1.3 mm. The roof residual lateral displacement recorded after this test was only 12.7 mm.

Overall for the tests the single curtain of reinforcement had excellent behavior. In spite of the thin aspect ratio of the web wall, no out of plane stability deformations

were measured. In summary, for the level of damage noted the building survived the design earthquake with limited damage. The building structure did not present obvious life-safety hazards. The building was perhaps not immediately operational but would have needed minimum repairs only. Furthermore, strains and roof drift ratios in test EQ4 were smaller than those limits set to meet the life safety performance objectives in the displacement-based design approach.

Fig. 6.8 presents the state of cracking in levels 1 and 2 of the web wall after test EQ4. Fig. 6.8(a) shows the diagonal flexural pattern recorded on level 1 after test EQ4. The limited spalling of the concrete cover at the base of the web wall is shown in Fig. 6.8(b). Fig. 6.8(c) shows the split vertical crack that developed as a result of the lap-splice failure at the West end on level 2.

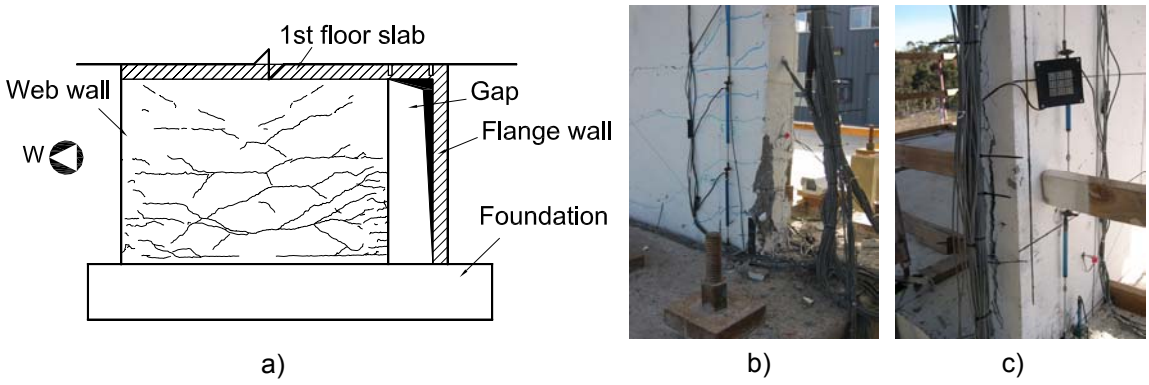

Figure 6.8. Observed damage of the web wall after test EQ4. a) North side view of web wall – level 1, b) West bottom end of web wall – level 1, c) West bottom end of web wall – level 2.

6.7.2 Hysteretic Response

Fig. 6.9 shows the system base moment versus roof lateral relative displacement response for tests EQ1 to EQ4. Positive displacement is towards West. The system base moment was estimated as the tributary seismic mass times the total floor acceleration and times the distance of the mass to the base of the wall. The system base moment also accounted for the small P-Delta effects as well as for the small mass rotatory moment. Total floor accelerations were calculated as the average of the three horizontal accelerometers at each floor (see Fig. 6.6 (a)). Lateral displacements were calculated from the acceleration measured in the three horizontal accelerometers at every floor using an appropriate algorithm. The calculated displacements were in excellent agreement with those measured with GPS displacement sensors (Bock et al. 2006). Fig. 6.9 also shows the web wall design moment, M_u, and the theoretical flexural strengths M_{oE}, M_{oW} calculated for the wall for the maximum East and Westwards measured curvature, respectively. Flexural strengths M_{oE} and M_{oW} were calculated from a moment-curvature analysis for the "as-built" section, using measured material properties for an axial force of P=809 kN. The maximum measured wall curvature for East and Westwards response was 7.72×10^{-3} and 7.09×10^{-3} rad/m, respectively.

The base shear force versus roof lateral displacement hysteretic response is plotted in Fig. 6.10. This figure also shows the design base shear force, $V_{u,}$ and the East and Westwards base shear forces, V_{oE}, $V_{oW,}$ calculated using an adaptive

pushover analysis (Satyarno et al. 1998) of the web wall only when it reached the flexural strengths M_{oE} and $M_{oW,}$ respectively.

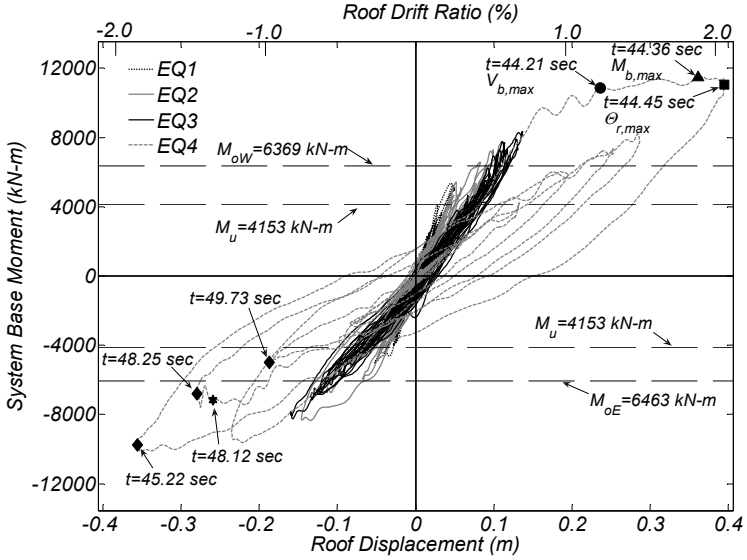

Figure 6.9. Roof Relative Lateral Displacement vs System Base Bending Moment.

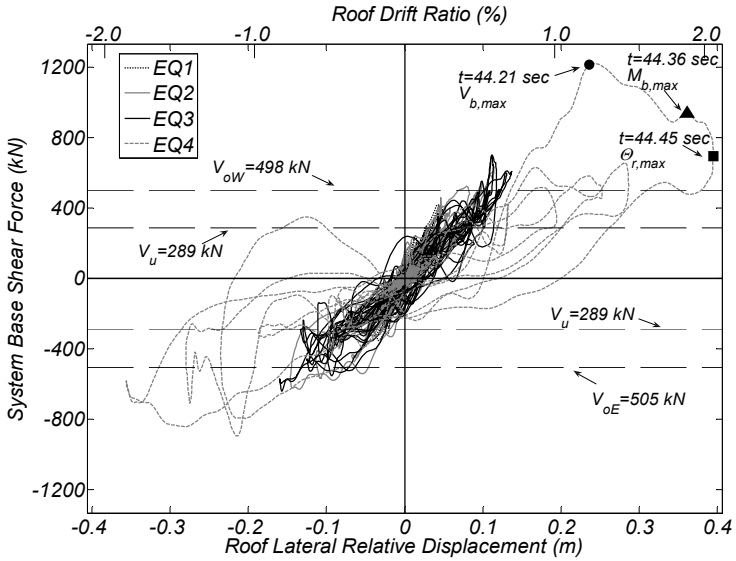

Figure 6.10. Roof Relative Lateral Displacement vs System Base Shear Force.

Examination of the system base moment and base shear force hysteretic responses shows: (i) significant system overstrength and (ii) erratic loop traces in the base shear force hysteretic response when compared to the loops observed from the base moment hysteretic response. The overstrength factor calculate as the ratio of maximum measured and design system base moment was Ω_{oM}=2.76. The observed system base moment overstrength was largely because of: (i) section flexural overstrength, and (ii) kinematic overstrength. These two sources of overstrength will be examined in detail in the following sections.

The overstrength factor calculated as the maximum measured and the design base shear force was Ω_{oV} = 4.29. The difference in magnitude between Ω_{oM} and Ω_{oV} is largely caused by the higher modes in the response of the test structure. The influence of the higher modes will also be discussed below.

6.7.3 Section Flexural Overstrength

The maximum curvature attained in the plastic hinge that developed in the web wall during test EQ4 was 7.72×10^{-3} rad/m which equals a curvature ductility μ_{φ}=8.17. The theoretical flexural strength matching to this curvature was 6368 kN-m. So, the theoretical section flexural overstrength, defined as the ratio of the flexural strength and the design moment was Ω_{os}=1.53. This overstrength factor was chiefly the result of the use of the strength reduction factor in design, a larger than specified yield strength in the reinforcement, and excess of longitudinal reinforcement. The magnitude obtained for Ω_{os} is well within the expected range of values.

Testing of reinforcing bar coupons subjected indicate that the maximum moment for Eastwards response was slightly affected by strain aging. Strain aging can result in increase of reinforcing steel strength (Restrepo et al. 1994). For test EQ4 relevant experimental program (Panagiotou et el. 2007) showed that the post yield strength of the reinforcing steel on the West end of the web wall increased by 7%. This resulted in approximately 5% increase of the web wall moment capacity for Eastwards response.

6.7.4 Kinematic Overstrength

Kinematic overstrength is defined here as the increase in resistance caused by the interaction between the cantilever web wall and those elements framing into it (Bertero et al. 1985). This interaction can cause significant increase of the shear force demand in walls. In this test kinematic overstrength was the result of deformation compatibility between the web wall, the flange wall, the slab and the restrain provided by the gravity columns.

A source of kinematic overstrength was warping and bending of the slab caused by the deformed web wall (that is, wall tensile chord growth and smaller wall compressive chord shortening). The slab warped and bent because of the constraint provided by the gravity columns, see Fig. 6.11. Table 6.3 lists the elongation and shortening of the tensile and compressive chord of the web wall during the tests. During test EQ4 the tensile chord lengthened 64.8 mm. This growth caused significant tension and compression axial forces in the gravity columns. Fig. 6.12 plots the base

moment resisted by the two pairs of gravity columns versus the roof relative lateral displacement during tests EQ1 to EQ4. This moment was calculated by taking moments about the centerline of the web wall of the axial forces measured in the gravity columns. The axial force in the gravity columns was calculated from the measured strain in a column calibrated in a universal testing machine. In test EQ4 the maximum moment resisted by the first level gravity columns was 12% of the maximum measured system base moment and 33% of the design moment M_u.

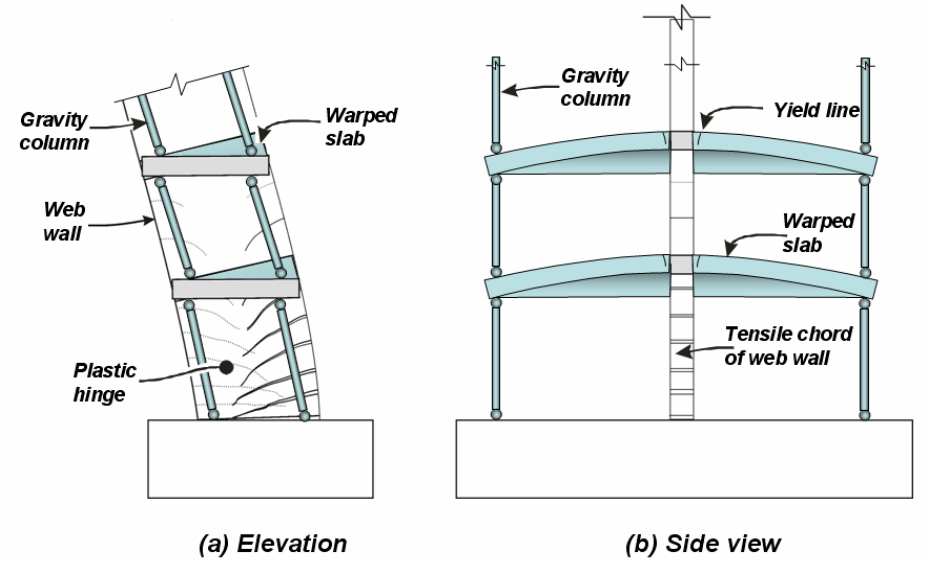

Figure 6.11. Exaggerated deformed shape explaining the kinematic overstrength caused by the coupling of wall, slab and gravity columns.

Another source of kinematic overstrength was the slotted slab between the web and the flange walls. Elongation and shortening of the East chord of the web wall occurred for Westwards and Eastwards displacement response, respectively. Such change in length was negligible in the flange wall. Thus, the slotted slab was forced to rotate and to develop positive and negative yield lines along the slots (Fig. 6.13). The

negative and positive moment capacity along yield lines next to the flange wall was M_{fE}=6.22 kN-m/m and the moment capacity on the yield line next to the web wall was M_{fW}=10.2 kN-m/m. Calculations point out that axial force caused by the flange wall inertial mass had minor influence on the moment capacities cited above.

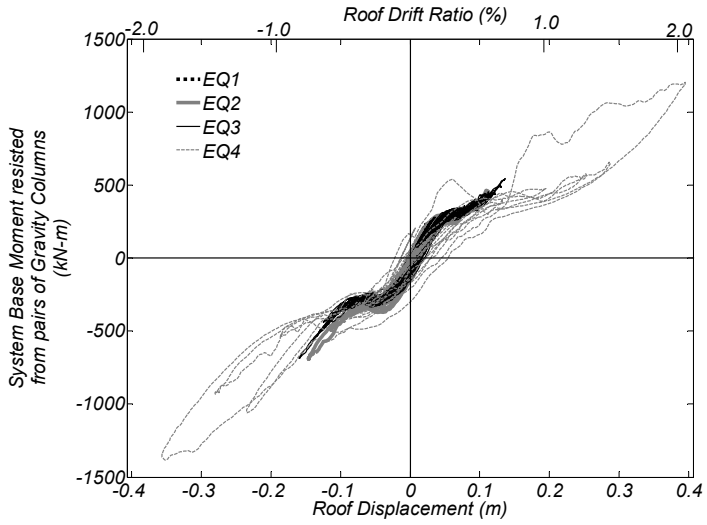

Figure 6.12. Roof Relative Lateral Displacement vs Overturning Moment resisted by the two pairs of gravity columns.

These moments capacities are small and so are the shear forces per unit length. However, the total shear force developed along the yield lines is not negligible. This is because of the length of the slots. Accumulation of the shear forces in the seven floors caused an axial force at the East edge of the web wall and at the West edge of the flange wall equal to P_f = 921 kN. For Westwards response this force increased the axial compressive load in the web wall while decreased it for Eastwards response. The variation of the axial force N_f in the flange and the web wall caused an increase of the system moment resistance of approximately 3658 kN-m and 946 kN-m for West and Eastward response, respectively. Such moments are 32% and 9% of the maximum

measured wall moment for West and Eastward displacement response. In comparison with the design moment M_u, these moments are 90% and 22% respectively.

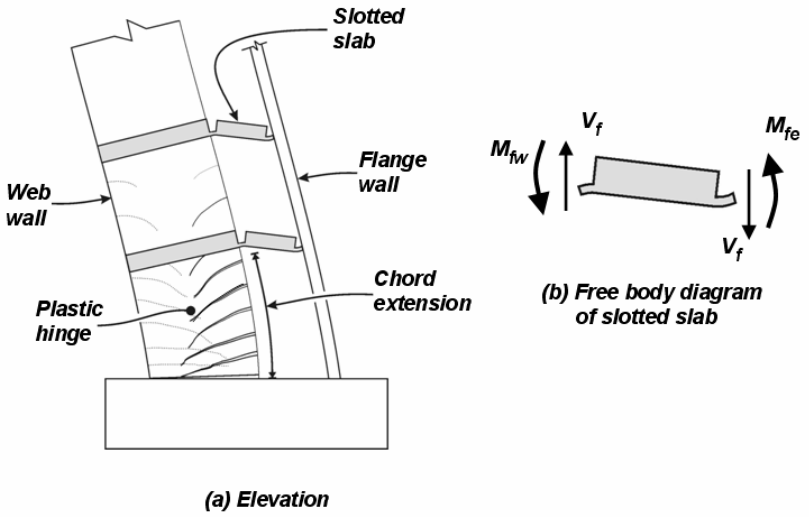

Figure 6.13. Exaggerated deformed shape explaining the kinematic overstrength caused by the slotted slabs.

It is noted that the above discussion was based on unidirectional moment of the slotted connection and zero axial force. However, a more accurate assessment of this effect should consider all the three components of the response (bending moment about the longitudinal and transverse x-y axes respectively as well as warping) as well as the variation of the axial force in the slotted connection. Detailed results of 3-D and 2-D finite element analysis have been performed (Panagiotou et al. 2007).

The decomposition of the system base moment resistance for Westwards response shows: (i) 55% of the maximum moment recorded in test EQ4 was due to the moment capacity of the web wall, (ii) 32% was due to the coupling of the web and the

flange walls through the slotted slab, (iii) 10% was carried by the pairs of gravity columns, and (iv) 3% was carried by the two transverse walls.

The increase of the system base moment due to kinematic overstrength increased the shear force demand on the web wall. Besides, such force increase was greater than the base moment increase because the kinematic interaction lowered the height of the resultant lateral force resultant (Panagiotou and Restrepo 2007).

The authors note that any direct extrapolation of the kinematic interaction observed to building systems is premature. The presence of the gravity columns in such close location to walls is not a common case in many buildings. However, there are cases where such columns are in the near proximity of walls. In such cases a first order analysis, as commonly used in office practice, is unable to indicate the large compression and tension axial forces these columns will carry. Another point is that the coupling effect of the slab can be notoriously much greater in a real building because in this test the slab was deliberately slotted.

6.7.5 Higher Mode Effects

Previous sections dealt with sources of overstrength that a static analysis of a well-conceived analytical model can reproduce. However, some response quantities are affected by the building's dynamic response. In the literature this is commonly referred to as the higher modes (Park and Paulay, 1975).

Fig. 6.14 plots the table acceleration, the roof relative displacement, the system base shear force and the system base moment time-histories for test EQ4 between t=43.2 and 50.2 sec. Maximum test response quantities occurred during this time bracket. For example, the maximum base shear force, $V_{b,max}$, happened at t= 44.21 sec., the maximum system base moment, $M_{b,max}$, occurred at t = 44.36 sec. and the maximum roof drift ratio $\Theta_{r,max}$, was recorded at t =44.45 sec. Also, the lap-splice failed at t= 48.12 sec. and the maximum strain on the second level after the lap-splice failed was recorded at t =48.25 sec. All these events are also plotted in the system base moment and shear force hysteretic responses depicted in Figs. 6.9 and 6.10, respectively.

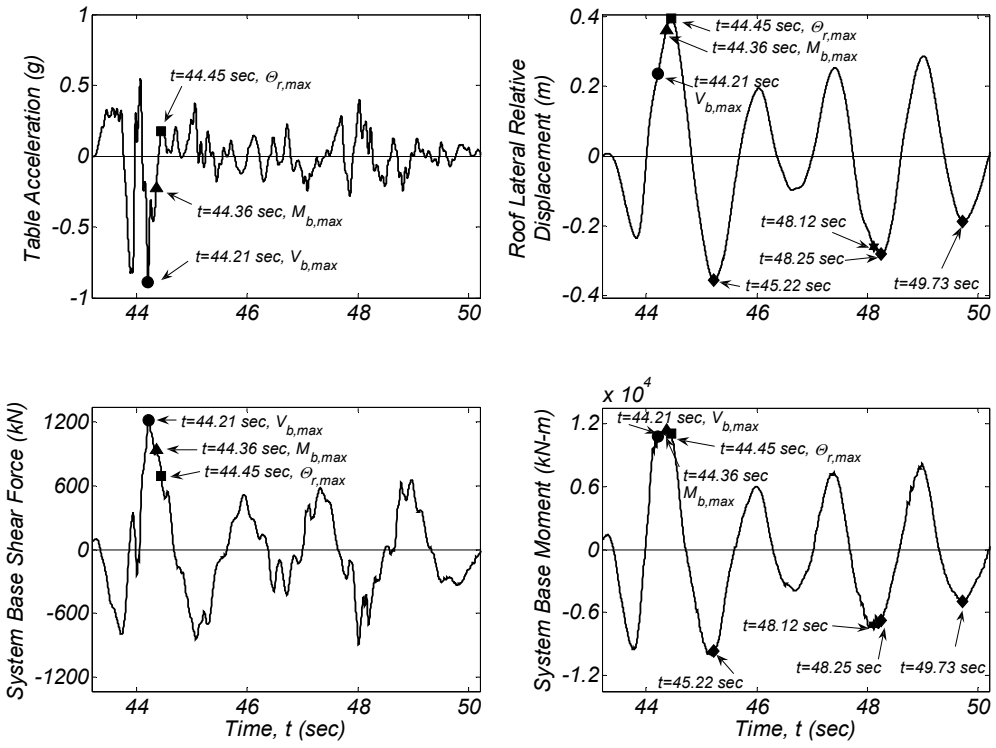

Figure 6.14. EQ4 – time histories between time t=43.2 sec and 50.2 sec of a) table acceleration, b)roof relative lateral displacement, c) system base shear force, d)system base moment.

In test EQ4 the peak ground acceleration, $a_{g,max}$,and the system base shear force, $V_{b,max,}$ occurred at t=44.21 sec. The peak ground acceleration in this motion is the result of a local pulse override with amplitude of about 0.5g and 0.1 sec. duration. The frequency content and amplitude of this local acceleration pulse affects the excitation and contributes to the higher modes, especially to the second mode that had a period of about 0.1 sec. The total acceleration profile in the building at t=44.21 sec. is plotted in Fig. 6.15. The acceleration profile at this instant of time is significantly affected by the peak ground acceleration. Note that the resultant lateral seismic force at this time is located at 46% of the height of the building. Fig. 6.15 also shows the measured horizontal acceleration profiles at the $M_{b,max}$ and $\Theta_{r,max}$. These two profiles have a more linear shape. It is characteristic that the three acceleration profiles have a common point between levels 4 and 5. This location is the nodal point of the second mode-shape. The acceleration profiles below this point show more or less a linear change between the acceleration of this point and the ground acceleration.

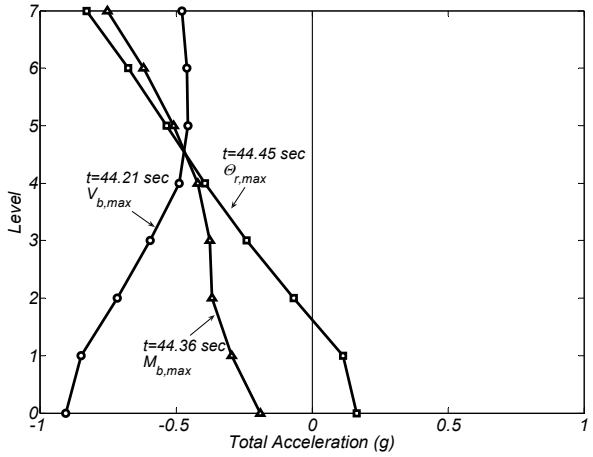

Figure 6.15. Total acceleration profile at characteristic instants during test EQ4.

Fig. 6.16 plots the position of the resultant lateral force in tests EQ1 to EQ4 and in two WN tests versus the base shear coefficient. The position was determined as the ratio of the measured system base moment and the base shear force. WN1 and WN4 were 3%g RMS WN tests before EQ1 and before EQ4, respectively. The points plotted in Fig. 6.16 are for those cases where the system base moment exceeded 90% of the maximum overturning moment measured in each test. This figure also shows the location of the lateral force obtained from the static component of the displacement-based design procedure. The design seismic coefficient, as well as that obtained from the adaptive pushover analysis when the web wall reached its flexural strength M_{oW}, are also plotted as vertical lines in this figure. Note that in tests WN1, WN4 and EQ1, when the building had limited nonlinear response, the resultant lateral force varied little with an average location at about 72% of the building height. The same trend holds true for test EQ2.

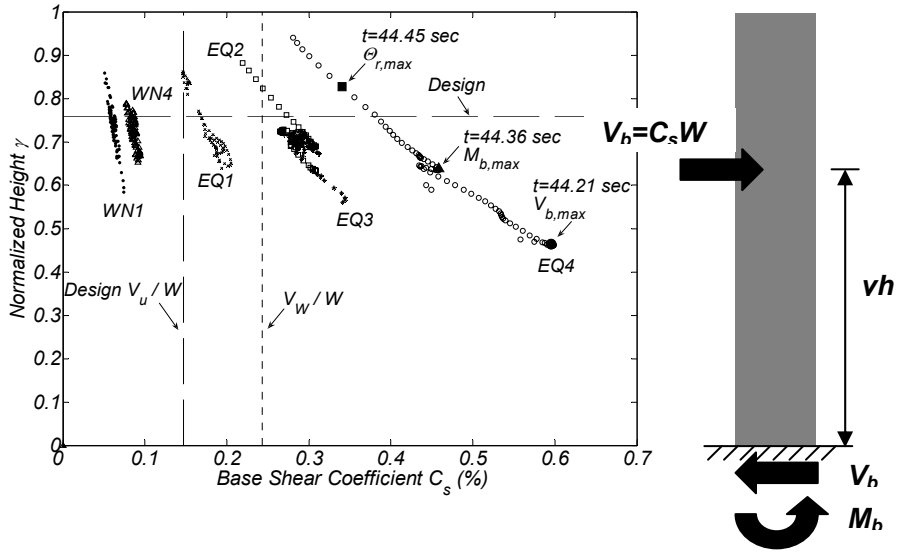

Figure 6.16. Normalized effective height of resultant system seismic force versus base shear coefficient.

Test EQ3 showed a decrease of the height of the resultant lateral force. This is because motion EQ3 was richer in high frequency content than motion EQ2, see Fig. 6.5. In test EQ4, that showed large nonlinear response, the location of the resultant lateral force varied significantly. At t = 44.21 sec. this force was only at 46% of the building height. So, this explains the increase of the base shear force while the system base moment remained almost constant. This observation clearly highlights the difference in magnitude between the moment and shear force overstrength factors Ω_{oM} and Ω_{oV}. The reduction in the location of the lateral force resultant occurred because of (i) the second mode of response, (ii) the ground acceleration during maximum base moment response, and (iii) the coupling of the web and flange walls through the slab (Panagiotou and Restrepo 2007).

6.7.6 Response Envelopes

Fig. 6.17 plots the envelopes of the main response quantities for tests EQ1 to EQ4. Fig. 6.17(a) shows the lateral relative displacement envelope. For increased inelastic response the development of a plastic hinge at the base resulted in concentration of rotation in this region and in almost a linear displacement profile from levels 3 to 7. Fig. 6.17(e) illustrates the interstory drift ratio envelopes recorded during the tests EQ1 to EQ4. In all tests, interstory drift ratios increased in each level up to level 3 and then remained nearly constant.

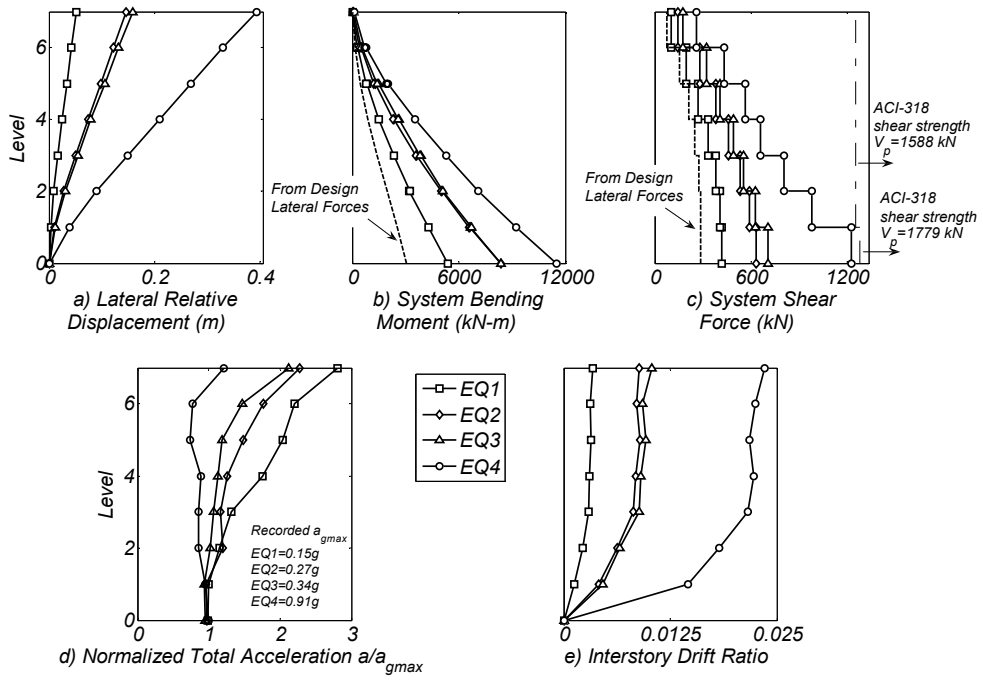

Figure 6.17. Phase I - Response Envelopes.

Figs. 6.17(b) and (c) depict the system bending moment and shear force envelopes, respectively. These plots also show the shear force and design bending moment calculated from the design lateral forces of the displacement-based procedure. Figure 6.17(c) also plots the probable shear strength of the web wall calculated from ACI-318 (2005) for a concrete compressive strength of 37.9 MPa and reinforcement yield strength of 455 MPa.

The shape of the shear force envelope in test EQ4 differs from the envelopes observed for tests EQ1 to EQ3. The shear force envelope in test EQ4 has a nearly constant step per floor, while the shear force envelope in the other tests is closer to that expected from a first mode distribution of lateral forces. Panagiotou and Restrepo

(2007) showed the second mode and coupling of the web and the flange walls through the slab were responsible for the shape of the shear force envelope observed in test EQ4.

Figure 6.17(d) plots the total floor acceleration envelopes. Total floor accelerations were normalized by the peak ground acceleration. For as long as the building remained elastic or nominally elastic, that is, incipient curvature ductility demand and floor accelerations were greater than the peak ground acceleration. This is consistent with the dynamic amplification expected from an elastic system. The roof magnification reached 2.81, 2.27, 2.11 and 1.21 in tests EQ1 to EQ4, respectively. In test EQ4, when significant nonlinear response occurred, total floor accelerations were closer in magnitude to the peak ground acceleration, indicating saturation of the response. This observation is consistent with the theoretical work presented by Rodriguez et al. (2002).

6.7.7 Strain Envelopes and Lap-splice Response

Fig. 6.18 shows the concrete and reinforcing steel tensile strain envelopes of levels 1 and 2 on the West and East end of the web wall. Tensile strains in the concrete surface and in the reinforcing bars were similar during tests EQ1 to EQ3. In test EQ4 the two strains were remarkably different at the base of level 2 on both ends see Fig. 6.16(a) and (c). This is because of the bond slip caused by deterioration of the lap splice that was more pronounced in the Westmost web wall longitudinal bars. During EQ4 a large split crack occurred at the West lap-splice at the base of level 2.

Note that the lap-splice region of the West end occurred two cycles past the peak Eastwards displacement. Fig. 6.19 plots the concrete and steel strain time histories in the lap-splice from time t=43.0 sec to t=51.0 sec. The instant of times where $V_{b,max}$, $M_{b,max}$ and $\Theta_{r,max}$ occurs are marked. The three instants of time where the peak Eastwards displacement response happened (t=45.22, 48.25, 49.73 sec.) as well as the onset of the lap splice failure (t=48.12 sec) are also marked. The exact position of the externally attached to the concrete displacement transducer and the strain gage attached to the reinforcing steel rebar are indicated in Fig. 6.6(b). The stains measured in the steel and the concrete are similar even at the instant of time of maximum Eastwards displacement response at t=45.22 sec. After t=48.12 sec. the concrete tensile strain increased rapidly and greatly exceeded the steel tensile strain, demonstrating significant bond slip and eventually failure of the lap-splice.

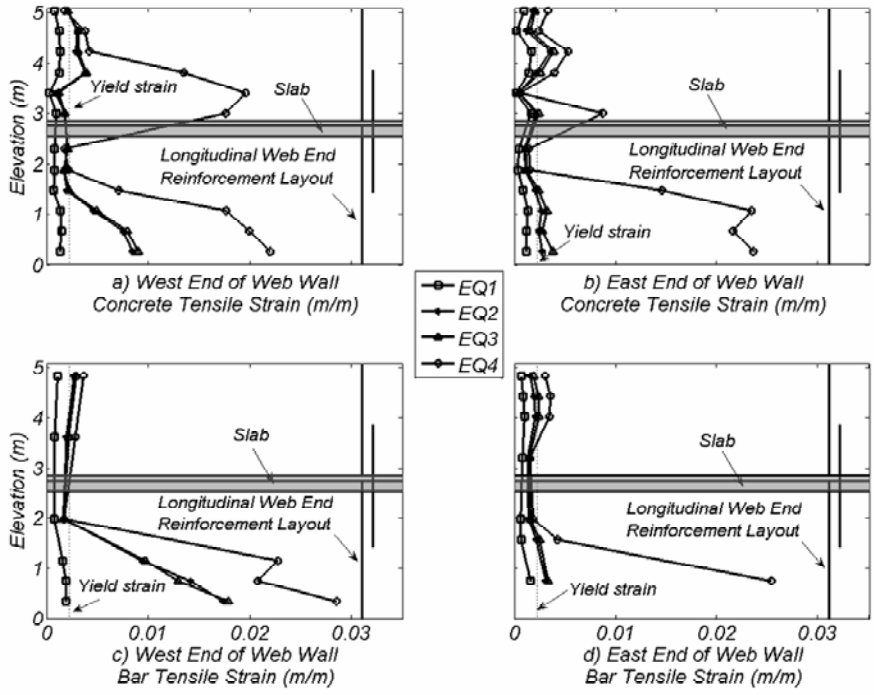

Figure 6.18. Concrete and Reinforcing Steel Tensile Strain Envelopes.

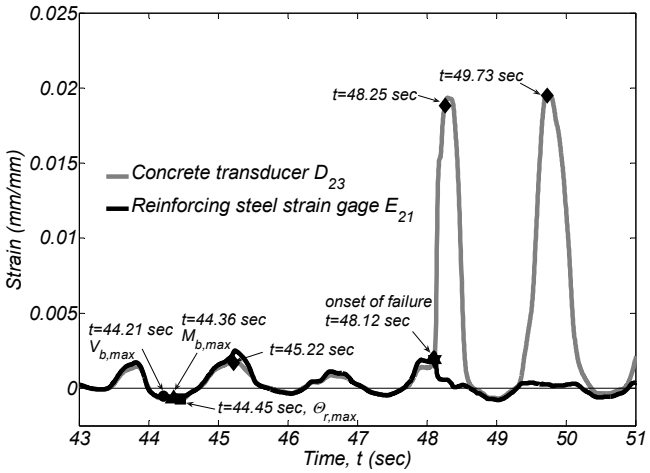

Figure 6.19. Comparison of concrete surface and bar strains in level 2 of West end of web wall during test EQ4.

6.8 Conclusions

This Chapter described the shake table response of a 7-story load bearing wall building slice built at full-scale. The building was designed for a site in Los Angeles following a displacement-based design method combined with Capacity Design. The design resulted in a significant reduction in the reinforcement when compared to that required by current code force-based design methods. The building was tested under four historical earthquake records of Southern California, including the strong intensity near-field motion recorded at the Sylmar station during the 1994 Northridge Earthquake. The response spectrum from the Sylmar motion matched closely that of the design earthquake calculated for the site.

The response of the building to the input motions was excellent overall. From the response observed we can draw the following conclusions:

1. Displacement-based design methods can provide a rational means for seismic design. Since these methods are directly aimed at specific performance objectives, they can be important tools in performance-based design. Such designs can be combined with Capacity Design procedures to effectively control the inelastic system response. In the test of the building slice all the performance objectives selected for immediate occupancy and for life-safety were met.
2. Three dimensional interaction effects between the wall and the slabs referred here to as kinematic overstrength caused significant increase of the shear force demand in the walls. Given the undesirable outcomes of shear failures in reinforced concrete buildings, such larger force demands should be accounted for in design.
3. Dynamic effects observed in the response of the building system can augment the shear force demand in individual walls and significantly increase the total accelerations along the height of the structure.
4. Lap-splices should be avoided at least twice the depth of a wall from the critical region at which a plastic hinge will develop. Other means of providing bar splicing should be considered instead.
5. Resistance welded grids acting as transverse reinforcement in the boundary elements of walls provided excellent longitudinal bar stability after spalling of the concrete cover.
6. The elongation of the tension chord in reinforced concrete walls can induce large tensile and compressive forces in gravity columns near to such walls. These forces cannot be quantified from routine first order analysis carried out by practicing engineers. Simple sketches displaying the deformed shape of the lateral force

resisting elements can highlight the need to specially detail some of these gravity load resisting elements.

7. A single curtain of transverse reinforcement was successfully used in the test building. The use of such detail can result in accelerated construction and should be allowed in design.

CHAPTER 7

7. SHAKE TABLE TEST OF A 7-STORY FULL SCALE BUILDING SLICE PHASE II: T-WALL

7.1 Summary

This chapter presents key results gained from Phase II of testing of a 7-story reinforced concrete building slice built at full-scale and tested on the George E. Brown Jr. Network for Earthquake Engineering Simulation Large Outdoor High-Performance Shake Table of the University of California at San Diego. In Phase II the main load bearing wall was reconfigured as a T-wall with moderate amount of longitudinal reinforcement, acting as the main lateral force resisting element. Main objective of Phase II was to test the effect of the flange, which was not connected to the web wall during Phase I of the test program, in a load bearing T-wall. The building was subjected to four historical input ground motions recorded in California, including the strong intensity near-fault Sylmar record. The building responded satisfactorily to the motions. Important results regarding the effect of flange in tension, the interaction between the wall and the slab, and the higher modes effect are presented.

7.2 Introduction

A load bearing T-wall provided lateral force resistance of the full-scale slice in Phase II of the test. During Phase I of the test, discussed in chapter 6, the flange and the web part of the T-wall were practically decoupled enabling the testing of a rectangular web wall. The building in Phase I was designed, for two

performance levels, using a displacement and capacity-based methodology which resulted in significantly less flexural reinforcement than that required by the ASCE-7 code (ASCE 2006). During Phase I, the test building was subjected to four historical input ground motions recorded in Southern California that represent a range of seismic demands up to the design earthquake. At the end of testing the web wall suffered moderate structural damage, which was manifested by the loss of concrete cover at the wall base where a flexural plastic hinge developed and by splitting of the concrete at the lap-splice of the longitudinal bars at the base of the second level.

After completion of Phase I, the specimen was partially repaired and the connection between the web and the flange of the T-wall was established for Phase II. The main purpose of Phase II was to test the effect of the flange wall in a load bearing T-wall. During Phase II, the full-scale building slice was subjected to the same four input ground motions used in Phase I. The test program took place at the new Large High-Performance Outdoor Shake Table (LHPOST) funded by the National Science Foundation through the George E. Brown Jr. Network for Earthquake Engineering Simulation (NEES) program.

The overall test program addressed four issues relevant to construction optimization: (i) longitudinal reinforcement reduction, (ii) use of single curtain of reinforcement to transfer shear, (iii) use of Capacity Design to control the nonlinear response of the structure, and (iv) the use of resistance-welded reinforcement in the boundary elements of first level of the walls.

In Phase II the combined effects of the flange wall in tension, the effect of coupling between the T-wall and the slabs and the effect of higher modes on the maximum shear force demand was a primary concern. Combination of these effects was expected to significantly augment the maximum shear demand and the required shear strength of the web part in a load bearing T-wall. In anticipation of these demands the wall shear design was Capacity Designed.

7.3 Description of the Test Structure

In Phase II a load bearing T-wall provided lateral force resistance in the East-West direction of loading. Fig. 7.1 shows an overall view of the test building and its main components. The web of the T-wall, termed here web wall, was 4.26 m long, 0.20 m thick at the first and seventh levels and 0.15 m elsewhere.

Figure 7.1 South West View of Building.

The flange of the T-wall, termed here the flange wall, was 4.87 m long, 0.20 m thick at the first floor and 0.15 m thick elsewhere. The T-wall supported seven 0.20 m thick slabs spaced at 2.74 m. The flange of the T-wall and a wall built on the West end of the web wall provided lateral and torsional stability. This wall was precast segmental and was jointed using mortar bed joint and post tensioning. This wall had a footing that enabled the wall to rock in the East-West direction. The T-wall was cast into a footing that was tied down to the shake table moving platen. Phase II also incorporated suspended pipes overhanging from the South portions of level 1, 4, 7 slabs. Fig. 7.2 gives the main dimensions. Figs. 7.3 and 7.4 show the main reinforcing details of the T-wall. The total weight excluding the foundation was 2127 kN. Table 7.1 lists the tributary seismic weights in the building.

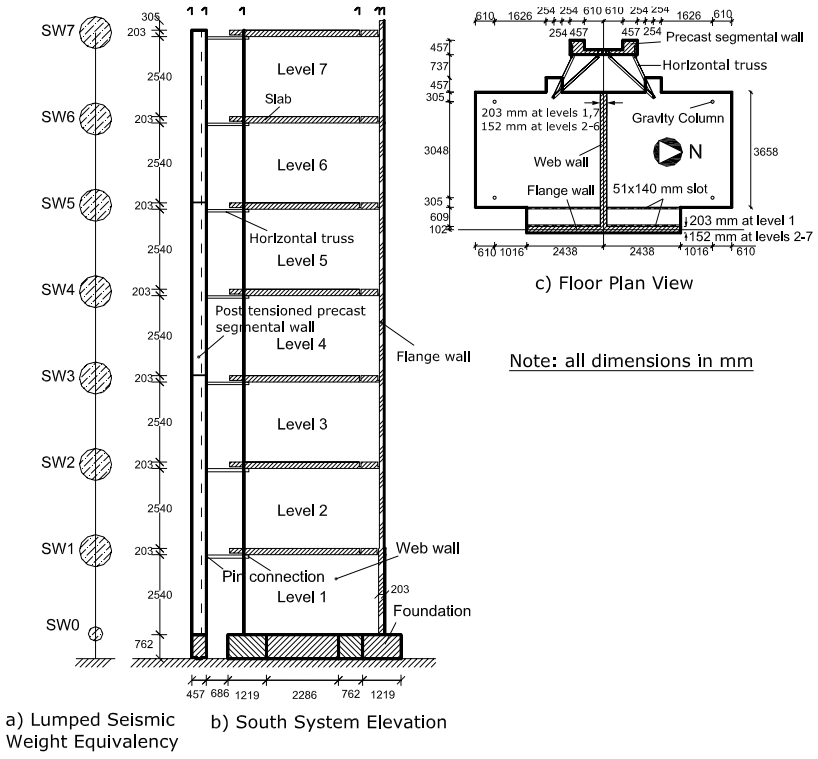

Figure 7.2. Test Structure Geometry and Lumped Seismic Weights.

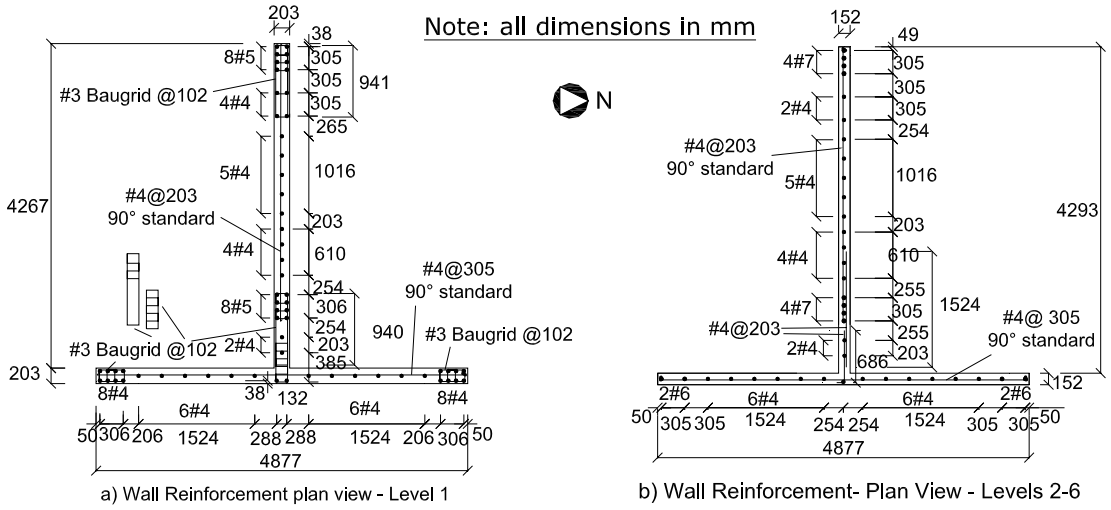

Figure 7.3. Test Structure – Plan View of Reinforcement.

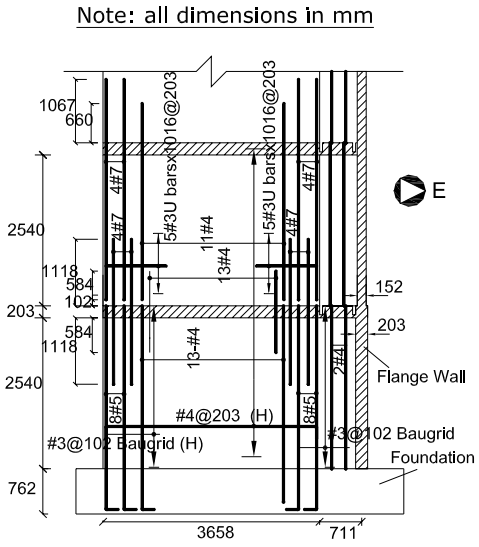

Figure 7.4. Web Wall Levels 1&2 and Slab Reinforcement.

Table 7.1. Seismic Weights* (kN)

Reference&	Web Wall	Slab	Flange Wall	PT Column	All other	Pipes	Total (with pipes)
SW0	25.9	0.0	30.8	19.5	0.0	0.0	***76.3***
SW1	45.4	168.6	54.9	39.0	8.4	12.9	***329.2***
SW2	38.9	156.0	48.0	39.0	8.4	0.0	***290.4***
SW3	38.9	156.0	48.0	39.0	7.9	0.0	***289.9***
SW4	38.9	156.0	48.0	39.0	7.6	12.9	***302.5***
SW5	38.9	156.0	48.0	39.0	7.6	0.0	***289.6***
SW6	45.4	156.0	48.9	39.8	7.6	0.0	***297.7***
SW7	25.9	156.0	30.2	20.2	6.0	12.9	***251.3***
Total	***298.4***	***1104.8***	***357.0***	***274.7***	***53.5***	***38.7***	***2127.1***

- Without foundation & Refer to Fig. 2 for location of the lumped seismic weights

7.4 Experimental Program

7.4.1 NEES-UCSD Shake Table

Testing was performed on the unidirectional 20-MN vertical payload LHPOSTT. This shake table was built with partial funding from the National Science Foundation and is administered under NEES. This shake table currently operates in a single-degree-of-freedom configuration reproducing motions in the East-West direction. Details of LHPOST are described elsewhere (Van den Einde et al. 2004, Ozcelik et al. 2007).

7.4.2 Input Ground Motions

The building was subjected to the same four historical earthquakes used in Phase I of testing. As in Phase I, prior and between earthquake tests the building was subjected to long-duration ambient vibration tests and to long-duration low-amplitude

0.5-25Hz band clipped white noise (WN) tests with root-mean-square (RMS) amplitudes of 2%, 3% and 5% g. The 3%g RMS WN tests excited the web wall beyond cracking but within the elastic limit of the reinforcement. These tests were used for system identification and evaluation of damage progression in the building.

The acceleration time-histories as well the acceleration and displacement response spectra of the earthquake input motions reproduced by LHPOST are plotted in Fig. 7.5. The low intensity input motion EQ1 was the longitudinal component from the VNUY station recorded during the 1971 M_w 6.6 San Fernando earthquake. The two medium intensity input motions EQ2 and EQ3 were the transverse component record from the VNUY station obtained during the 1971 M_w 6.6 San Fernando earthquake and the longitudinal component from the WHOX station recorded during the 1994 M_w 6.7 Northridge earthquake, respectively. The large intensity input motion EQ4 was the Sylmar Olive View Med 360^o recorded during the 1994 M_w 6.7 Northridge earthquake. Fig. 7.5 shows also the spectrum for the design earthquake obtained from ASCE-7 (ASCE 2006) for site class C for the site, for $S_{DS} = 1.81$ g, $S_{D1} = 0.87$ g, $T_0 = 0.10$ sec. and $T_S = 0.48$ sec. This figure also plots the response spectra for a 3 minute long 3% RMS WN whose intensity was low relative to the earthquake motions.

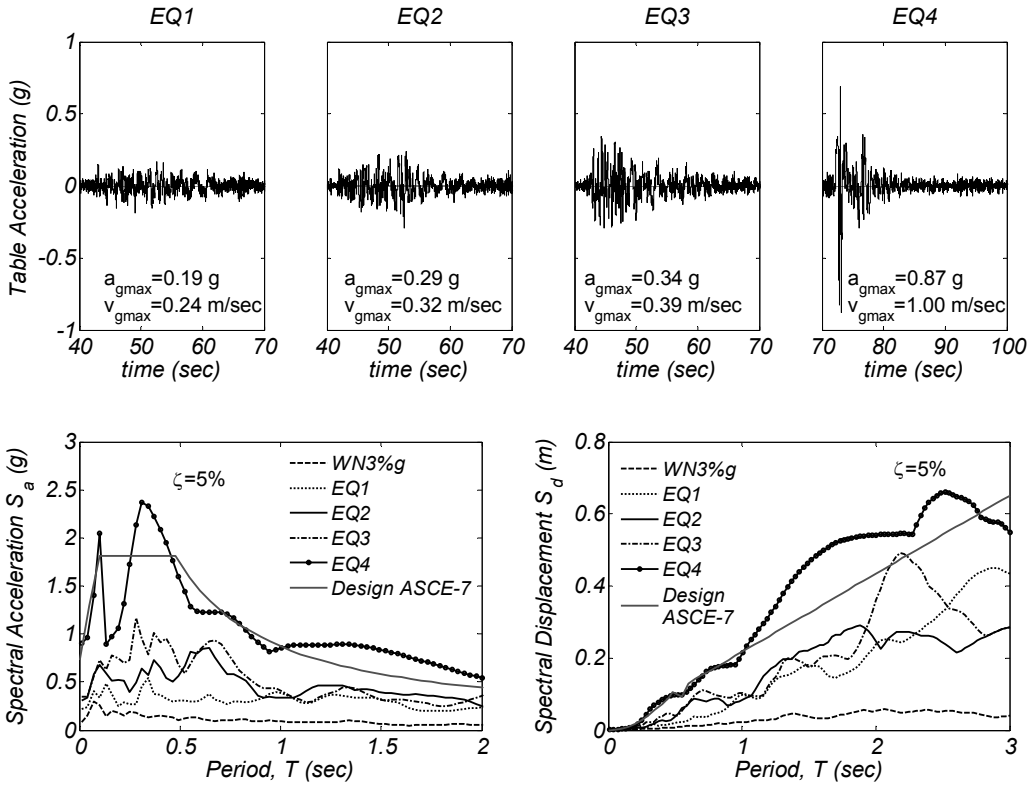

Figure 7.5. Phase I Time Histories and Response Spectra of Table Ground Motions.

7.4.3 Instrumentation

An extensive ensemble of sensors was deployed throughout the building to measure its response. The ensemble comprised 139 DC-coupled accelerometers, 88 displacement transducers, and 314 strain gages. These sensors were sampled at 240 Hz and subjected to an antializing filter at 50 Hz. Finally, 17 cameras recorded and broadcast online the response of different parts of the building.

Fig. 7.6(a) shows the horizontal and vertical accelerometers on the roof. Fig. 7.6(b) shows the external and internal concrete instrumentation on the first two levels of the T-wall. The displacement transducers attached externally to the concrete close

to the West end of the web wall and the East face of the flange wall recorded fixed-end rotations, and smeared surface strains and curvatures. Horizontal displacement transducers near the base of each level recorded sliding shear displacements. Diagonal string potentiometers recorded wall panel shear deformations. Fig. 7.6(b) shows also the strain gages placed on the reinforcing bars on levels 1 and 2 of the web wall.

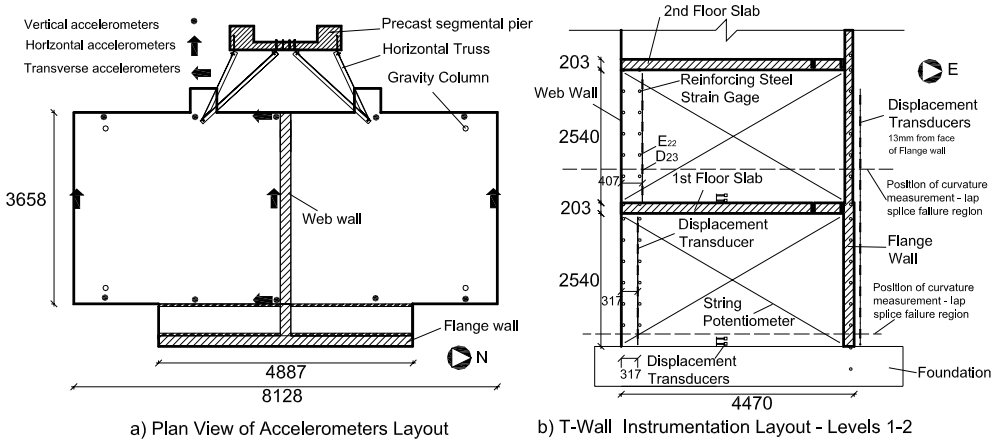

Figure 7.6. (a) Plan view of position of accelerometers, (b) Elevation of displacement transducers and strain gages on levels 1 and 2 of web wall.

7.5 Damage at Completion of Phase I – Structure Repair before Phase II

At the end of Phase I a flexural plastic hinge had developed at the first level of the web wall. The maximum reinforcing steel tensile strain measured during Phase I exceeded 2.5% at both ends of the web wall. Limited spalling of the unconfined concrete occurred on the West end of the web wall. Flexural cracks were also developed on the second level of the web wall with limited yielding (less than 0.5%) of the reinforcing steel. In addition a vertical split crack developed at the West end of the web wall close to bottom of level 2 due to bond slip and failure of the lap splice. Before initiation of Phase II the flexural cracks and the limited concrete spalling at the

base of the web wall were fully repaired with low viscosity epoxy injection. The flexural cracks of level 2 were not repaired. The damaged lap splice region of the west end was partially repaired by use of six 4 by 4 in. externally steel plates providing active pressure of this region. Fig. 7.7 shows a view of the bottom two levels of the building indicating the repaired regions. The lap splice failure at the West end and close to the bottom of the second level during Phase I and the type of repair of this region affected the Eastwards response of the test structure during Phase II.

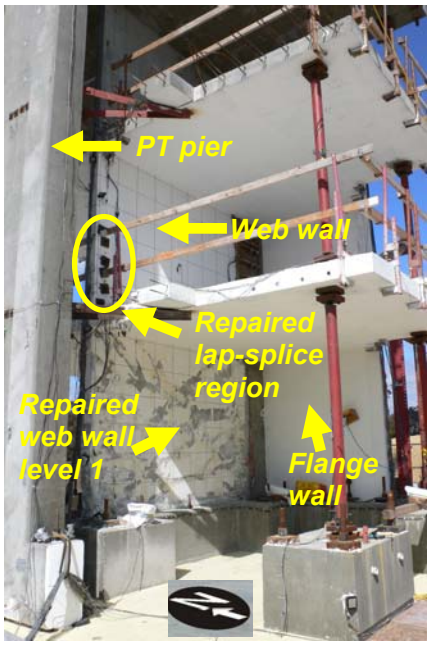

Figure 7.7. SW View of repaired regions Levels 1 and 2 of web wall.

7.6 Test Results

7.6.1 General Observations

The use of four earthquake input motions with distinct features and intensities allowed the monitoring of the development of different damage states in the test structure. The response of the system had distinct characteristics in the two

longitudinal directions. The Westwards response was characterized by the effect of flange in tension. The Easrwards response, with the flange in compression, was characterized by the localized lap splice failure at the West end of the web wall and close to the bottom of level 2. Failure of this region caused the development of a crack which propagated almost half the length of web wall causing rocking of the wall around the base of the second floor.

For Westwards response, with the flange in tension, the response was linear for motion EQ1. Very limited nonlinear response occurred for the "medium" intensity motions EQ2 and EQ3. For test EQ4 limited nonlinear response occurred with the development of a flexural plastic hinge on the bottom two floors of the flange wall. For Eastwards response, with the flange in compression, limited nonlinear response occurred in the reinforcing steel for all the tests. This was due to the rebar, concrete bond slip in the region of the lap splice failure. The lap splice failure caused rocking of the web wall around this point and development of large concrete tensile strains locally in this region. Table 7.2 lists the maximum values of relevant response variables measured in tests EQ1 to EQ4. All the strains and elongation results provided do not account for the residual strains at the end of Phase I of testing.

Fig. 7.8 shows the variation of the first two modal periods with testing. The experimental program clearly showed the dependency of the fundamental period on the intensity of the WN tests. Periods cited below were extracted from 3%g RMS WN tests. At the end of Phase I and before any repair the fundamental period was T=1.16

sec. At initiation of Phase II, after the partial repair of the specimen and the establishment of the T-wall, the fundamental period was T=0.47 sec. This was mainly due to the effect of the flange wall which stiffened the system. After test EQ1 the fundamental period shifted to T=0.56 sec. After test EQ2 changed to 0.64 sec. No data exist after test EQ3. Finally, after test EQ4 the fundamental period augmented to T=0.77 sec. The changes in period were the result of the gradual loss of tension stiffening across the cracked concrete as well as to the damage in the lap splice region. In contrast with the first mode, the second mode period is slightly affected from the induced damage and remains almost constant and equal to T_2=0.13 sec.

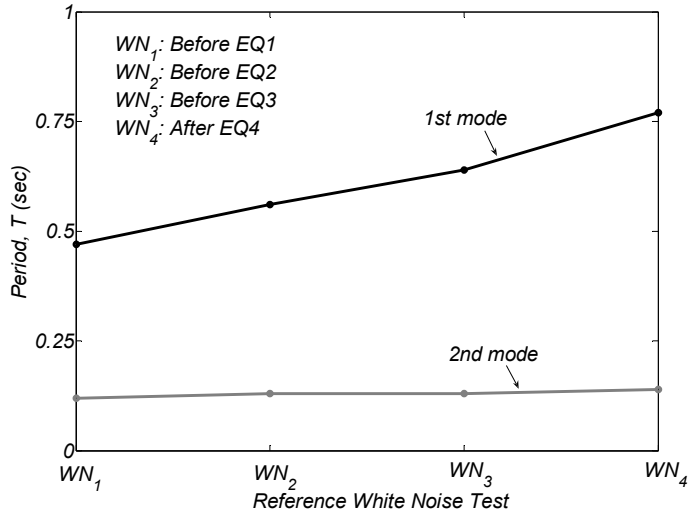

Figure 7.8. Variation of period of first two longitudinal modes.

The reference yield curvature calculated from a moment-curvature analysis of the critical section was φ_y=0.0039 / l_w where l_w is the length of the web wall. Due to the lap splice failure, the maximum curvature for all EQ tests was measured 254 mm from the top of the first floor slab, always for Eastwards response. This curvature can't be correlated with the reinforcing steel strain demand due to bar bond slip in the

region of lap splice failure. Because of this, in addition to the measured curvature in the region of the lap splice failure, Table 7.3 also gives the maximum measured curvature at the base of the wall. This curvature can be used for estimation of the curvature ductility demand in the wall as well for estimation of the theoretical moment at the base of the T-wall.. Figure 7.6(b) shows the position of the measured curvatures given in Table 7.2.

The curvature ductility based on the measurement at the base of the wall and defined as the ratio of the maximum measured base curvature to the reference yield curvature, was 0.8, 1.3, 1.5 and 3.0 in tests EQ1 to EQ4, respectively. Curvature ductilities observed confirms that under tests EQ1 to EQ4 the reinforcing steel exhibited limited nonlinear response.

Test EQ1 displaced the building to maximum roof drift ratio $\Theta_r = 0.27\%$. The maximum recorded intersory drift ratio was 0.34%. The tensile strain recorded in the web wall longitudinal reinforcement in level 1 during test EQ1 reached 0.65%. The compressive strain in the concrete cover at the base of the wall reached -0.09% in this test. Maximum shear deformations along the construction joints were 0.7 mm. Except the lap splice failure region, minor cracking developed at the base of the flange wall. This cracking was due to loss of concrete tension stiffening.

Table 7.2. Maximum Recorded Values of Relevant Parameters

		EQ1	EQ2	EQ3	EQ4
	Roof Relative Lateral Displacement (m)	0.05	0.12	0.18	0.23
	Roof Drift Ratio (%)	0.27	0.60	0.92	1.17
	Interstory Drift Ratio (%)	0.34	0.73	1.11	1.40
	System Base Moment (kN-m)	8626	10763	12069	15557
	System Base Shear Force (kN)	689	827	867	1641
	Roof Acceleration (g)	0.60	0.88	0.93	1.33
	Peak Ground Acceleration (g)	0.19	0.29	0.34	0.87
	Roof / Peak Ground Acceleration	3.14	3.03	2.74	1.53
	Longitudinal Bar Tensile Strain (%)	0.65	1.81	1.89	3.57
	Concrete Compressive Strain (%)	-0.09	-0.15	-0.14	-0.20
	Shear (Sliding) deformations along construction joints (mm)	0.7	1.7	2.6	3.6
Westwards Response	Web Wall Base Curvature x Wall Length (254 mm from top of foundation)	0.0032	0.0051	0.0057	0.0116
	Tensile Chord Growth at top of level 2 (mm) East face of flange wall (midlength)	1.8	5.6	8.5	23.6
	Compressive Chord Shortening (mm) East face of flange wall (midlength)	-0.39	-1.02	-0.36	-0.27
Eastwards Response	Web Wall Base Curvature x Wall Length (254 mm from top of first floor slab)	0.0043	0.0275	0.0705	0.1018
	Tensile Chord Growth at top of level 2 (mm) West end of web wall (400 mm from West end)	7.0	21.6	38.2	47.1
	Compressive Chord Shortening (mm) (400 mm from web wall end)	-2.0	-2.9	-3.2	-3.6

During tests EQ2 and EQ3 the roof drift ratios measured in these tests were Θ_r = 0.60 and 0.92% respectively. Recorded interstory drift ratios in these tests were 0.73 and 1.11%, respectively. Moderate yielding occurred in the longitudinal reinforcement, which reached a tensile strain of 1.81% and 1.89% in these tests. The concrete compressive strain measured in tests EQ2 and EQ3 was -0.15% and -0.14%, respectively. Maximum shear deformations along the construction joints were 1.7 and 2.6 mm for tests EQ2 and EQ3, respectively. During tests EQ2 and EQ3 minor flexural cracking developed at the base of the flange wall.

In test EQ4 the maximum roof drift and interstory drift ratios were 1.17% and 1.40%, respectively. In this test the tensile strain in the longitudinal reinforcement at the base of the flange wall reached 3.57% and the concrete compressive strain there reached -0.20%. Maximum shear deformations along the construction joints were 3.6 mm. Assuming that all the measured shear force V was resisted from the web wall with area A_w, the ratio V/A_w was equal to $0.32\sqrt{f_c'}$, where f_c'=32.4 MPa. This value of shear stress was significantly smaller than value $0.66\sqrt{f_c'}$ of eq. 11.5.7.9 of ACI-318 (ACI 2005) corresponding to the upper bound of the probable shear strength provided from the shear reinforcement (V_s).

Fig. 7.9 illustrates the developed crack pattern in the first two levels of the web and flange wall after EQ4. Fig. 7.9(a) shows the developed flexural cracking on the North face of the first level of the web wall. Fig 7.8(b) shows the crack pattern which becomes gradually horizontal in the midlength of the flange wall for level 1. Fig. 7.9(c) shows the developed cracking at the South face of the second level of the web wall. At the west end of the web wall a big vertical crack developed due to failure of the lap splice. Fig. 7.9(d) shows the damaged region at the West end of the web wall at Level 2 due to lap splice failure and shows the split vertical crack. Overall for the tests the single curtain of reinforcement had excellent behavior. In spite the thin aspect ratio of the web wall, and the lap splice failure no out of plane stability deformations were measured. In all the EQ tests the torsional response of the structure was limited.

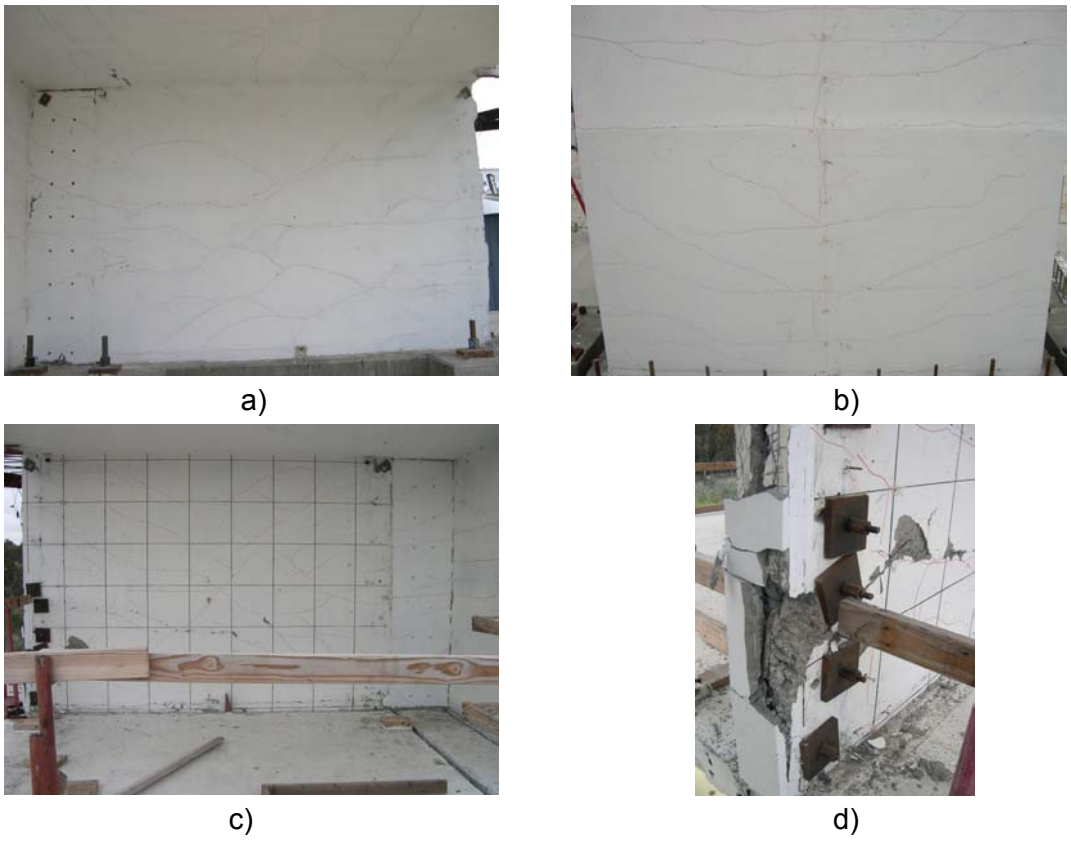

Figure 7.9. Observed damage of the web wall after test EQ4. a) North side view of web wall – level 1, b) West bottom end of web wall – level 1, c) West bottom end of web wall – level 2.

7.6.2 Hysteretic Response

Fig. 7.10 shows the system base moment versus roof lateral relative displacement response for tests EQ1 to EQ4. Positive displacement is towards West. The system base moment was estimated as the tributary seismic mass times total floor acceleration and times the distance of the mass to the base of the wall. The system base moment also accounted for the small P-Delta effects as well as for the small mass rotatory moment. Total floor accelerations were calculated as the average of the three horizontal accelerometers at each floor (see Fig. 7.6 (a)). All total floor accelerations

were low-pass filtered at 25 Hz. Lateral displacements were calculated from the acceleration measured in the three horizontal accelerometers at every floor by use of an appropriate algorithm.

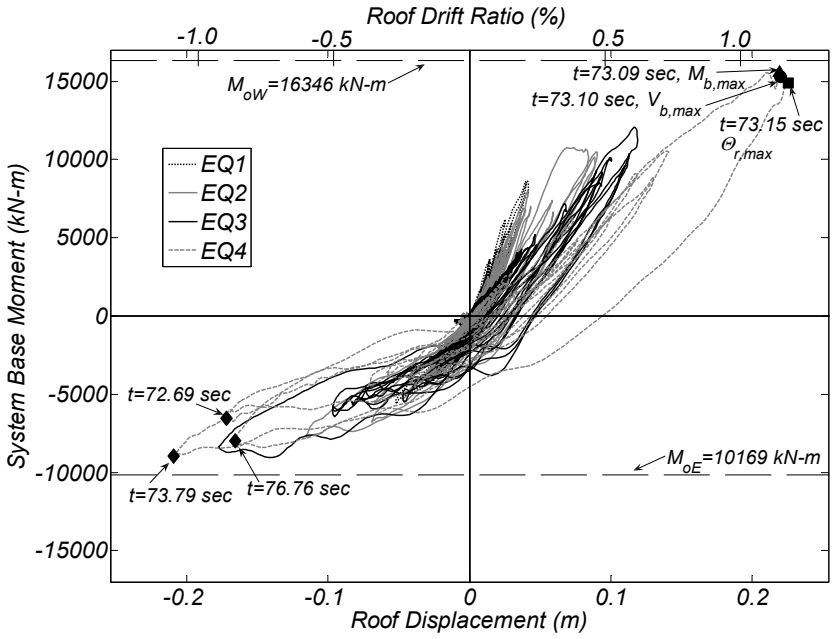

Figure 7.10. Roof Relative Lateral Displacement vs System Base Bending Moment.

Fig. 7.10 also shows the theoretical flexural strengths of the T-wall M_{oE}, M_{oW} calculated for the maximum East and Westwards measured curvature, respectively. The maximum measured base wall curvature for East and Westwards response was 0.84×10^{-3} and 2.60×10^{-3} rad/m, respectively. Flexural strengths M_{oE} and M_{oW} were calculated from a moment-curvature analysis for the "as-built" section, using measured material properties for an axial force of P=1166 kN. For the system moment capacity important was the: (i) effect of flange in tension, and (ii) kinematic overstrength. These two aspects will be examined in detail in the following sections. Fig. 7.10 shows that the theoretical strength for these curvatures exceeds the measured

moment for both directions of the response. This is due to the partial loss of tension stiffening in the flange and web wall during Phase I of the test. The theoretical moment curvature analysis considered full contribution of tension stiffening. The base shear force versus roof lateral displacement hysteretic response is plotted in Fig. 7.11. This figure also shows the base shear forces, V_{oE}, $V_{oW,}$ calculated using an adaptive pushover analysis (Satyarno et al. 1998) of the web wall only when it reached the flexural strengths M_{oE} and M_{oW}.

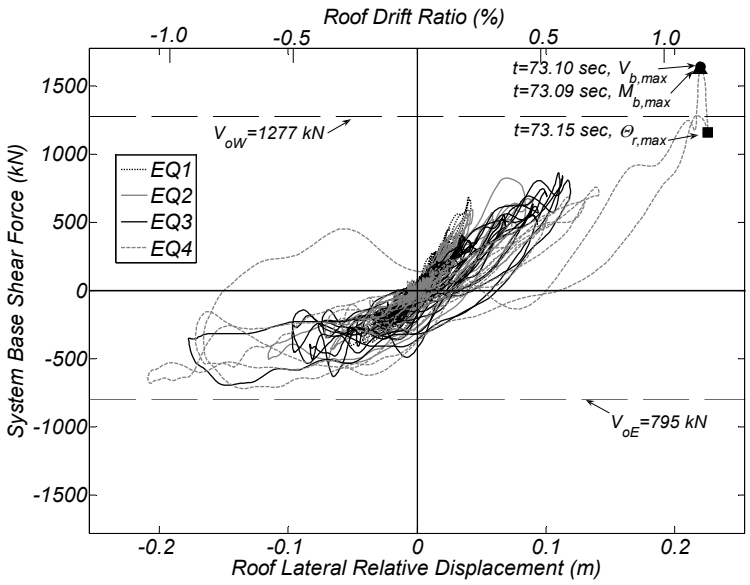

Figure 7.11. Roof Relative Lateral Displacement vs System Base Shear Force.

Examination of the system base moment and base shear force hysteretic responses shows erratic loop traces in the base shear force hysteretic response when compared to the hysteretic loops observed from the base moment traces. This is due to the effect of higher modes in the response of the test structure. The influence of the higher modes will also be discussed below.

7.6.3 Flange in tension

The ACI-318 (ACI 318-05) code recommends using an effective flange for T-walls derived for T-section beams. The intention of the design recommendations for T-beams is to provide a close and conservative approximation to this width. As in other provisions that are given for gravity load design, conservative estimates are reckoned to be adequate. In seismic design this philosophy no longer holds true. An apparent underestimation of the flange width in a T-wall that will develop a flexural plastic hinge, will result in shear forces that are greater than those used in design. Given the consequences of shear failures in reinforced concrete gravity load carrying members, such failures should be avoided as far as practicable.

Fig. 7.12 plots the reinforcing steel tensile strain profile at the base of the flange wall. Fig. 7.12 shows that the flange wall was fully effective in resisting flexure in all the EQ tests. The peak tensile strain in the reinforcing bars of the flange reached 3.57%, while the reinforcing steel yielded along all the length of the flange wall in earthquakes 2, 3 and 4. The effectiveness of the flange in tension to resist flexure caused the significant increase of the moment capacity of the T-wall in comparison to the rectangular web wall of Phase I.

Fig. 7.13 compares the hysteretic response in terms of roof lateral displacement versus system base moment between Phases I and II. As shown in the positive quadrant of Fig. 7.13 when the flange wall was engaged to resist flexure in Phase II, it significantly contributed to the flexural strength of the T-wall. The flange wall would

also had caused an increase of the moment capacity for response with the flange in compression, but this did not occur due to the failure of the lap splice region.

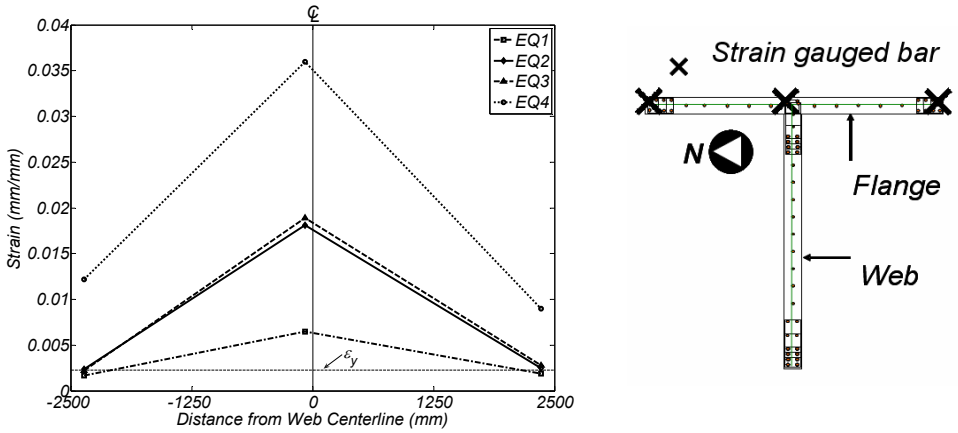

a) Recorded Strains b) Strain gage location

Figure 7.12. Level 1 - T-wall cross-section showing strain gauged flanged longitudinal bars and tensile strain profile envelope of Level 1 bars.

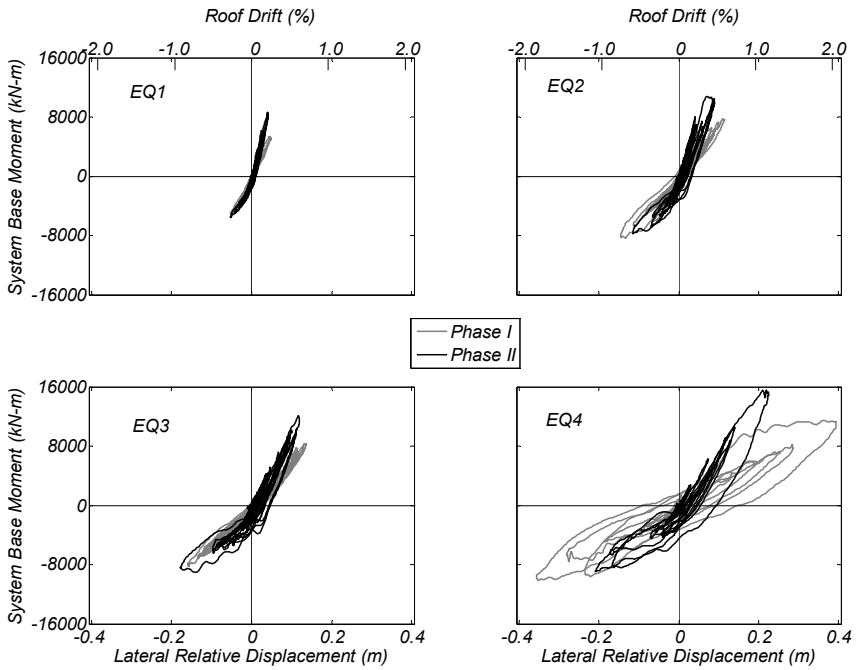

Figure 7.13. Roof Relative Lateral Displacement vs System Base Bending Moment. Comparison of Phase I and II.

7.6.4 Kinematic Overstrength

Similar to Phase I of the test, presented in Chapter 6, the effect of kinematic overstrength caused increase of the stiffness and strength of the system. The effect of kinematic overstrength was smaller during Phase II of the test due to the smaller magnitude of nonlinear response of the T-wall. The kinematic overstrength in this phase of the test was almost exclusively due to the interaction between the T-wall, the slab and the gravity columns, while the effect of the slotted connection was minimal.

Table 7.2 lists the elongation and shortening the tensile and compressive chord of the web wall during the tests. During test EQ4 the tensile chord lengthened 47.1 mm. Significant tension and compression axial forces developed in the gravity columns. Fig. 7.14 plots the base moment resisted by the two pairs of gravity columns versus the roof relative lateral displacement during tests EQ1 to EQ4. This moment was calculated by taking moments about the centerline of the web wall of the axial forces measured in the gravity columns. The axial force in the gravity columns was calculated from the measured strain in a column calibrated in a universal testing machine. In test EQ4 the maximum moment resisted by the first level gravity columns was 6.5% of the maximum measured system base moment.

The decomposition of the system base moment resistance for Westwards response shows: (i) 92% of the maximum moment recorded in test EQ4 was due to the moment capacity of the web wall, (iii) 6.5% was carried by the pairs of gravity columns, and (iv) 1.5% was carried by the PT wall. The increase of the system base

moment due to kinematic overstrength increased the shear force demand on the web wall. Besides, such force increase was greater than the base moment increase because the kinematic interaction lowered the height of the resultant lateral force (chapter 3).

The author notes that any direct extrapolation of the kinematic interaction observed to building systems is premature. The presence of the gravity columns in such close location to walls is not a common case in many buildings. However, there are cases where such columns are in the near proximity of walls. In such cases a first order analysis, as commonly used in office practice, is unable to indicate the large compression and tension axial forces these columns will carry.

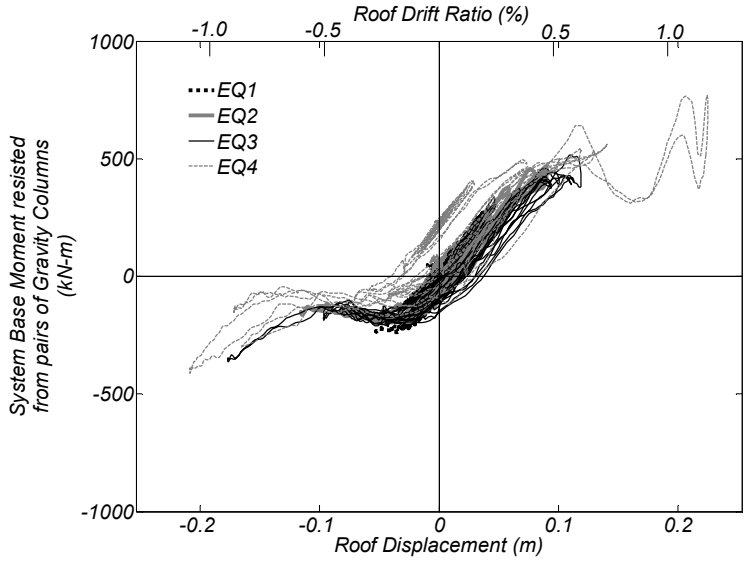

Figure 7.14. Roof Relative Lateral Displacement vs Overturning Moment resisted by the two pairs of gravity columns.

7.6.5 Higher Mode Effects

Previous sections dealt with sources of overstrength that a static analysis of a well-conceived analytical model can reproduce. However, some response quantities are affected by the building's dynamic response. In the literature this is commonly referred to as the higher modes (Park and Paulay, 1975).

Fig. 7.15 plots the table acceleration, the roof relative displacement, the system base shear force and the system base moment time-histories for test EQ4 between t=72.2 and 74.2 sec. Maximum test response quantities occurred during this time bracket. The maximum base system base moment, $M_{b,max}$ occurred at t = 73.09 and almost coincides with t= 73.10 sec, where the maximum shear force, $V_{b,max}$, was measured. The maximum roof drift ratio $\Theta_{r,max}$, was recorded at t =73.15 sec. All these events are also plotted in the system base moment and shear force hysteretic responses depicted in Figs. 7.10 and 7.11, respectively.

For these three characteristic instants of time the relative lateral displacement and system base moment is almost constant and equal to the maximum recorded value. The maximum system base shear force at t = 73.10 sec is significantly larger than the instant t=73.15 of the maximum roof relative lateral displacement. The maximum system base shear force, $V_{b,max}$ was measured slightly after the instant of time of peak ground acceleration $a_{g,max}$. The peak ground acceleration in this motion is the result of a local pulse override with amplitude of about 0.4g and 0.1 sec duration. The frequency content and amplitude of this local acceleration pulse affected the excitation

and contribution of the second mode that had a period of about 0.13 sec. The ground acceleration at t=73.10 sec, which is close to the peak ground acceleration, and the high contribution of the second mode at this instant of time resulted in the increase of the base shear force.

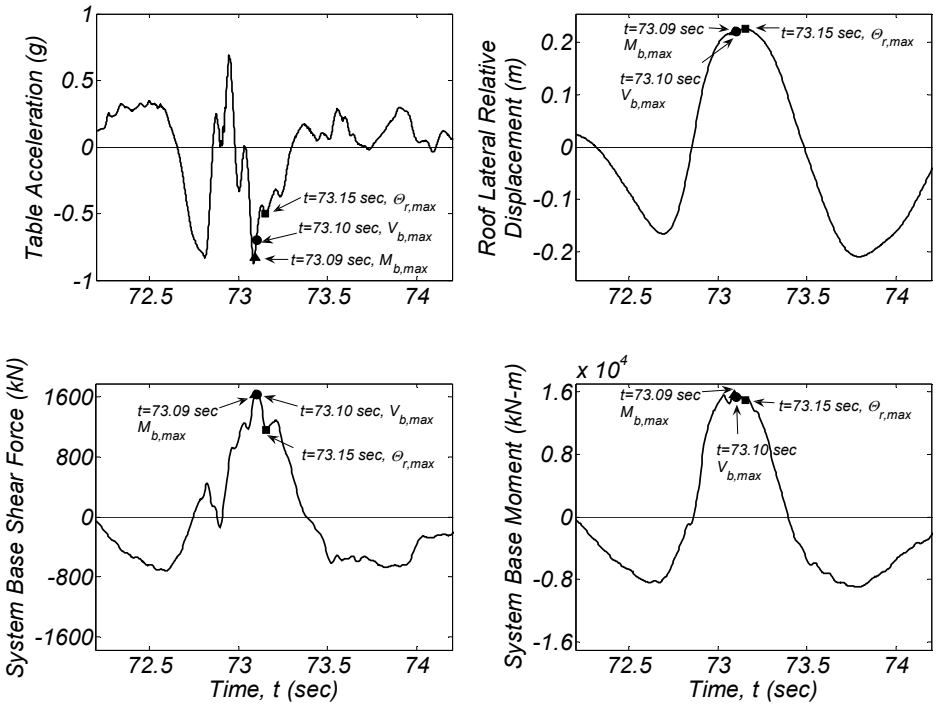

Figure 7.15. EQ4 – time histories between time t=72.2 sec and 74.2 sec of a) table acceleration, b)roof relative lateral displacement, c) system base shear force, d) system base moment.

The total acceleration profile in the building at t=73.10 sec. is plotted in Fig. 7.16. The acceleration profile at this instant of time is significantly affected by the ground acceleration. Note that the resultant lateral seismic force at this time is located at 49% of the height of the building. Fig. 7.16 also shows the measured horizontal acceleration profiles at the $M_{b,max}$ and $\Theta_{r,max}$. The acceleration profile at $\Theta_{r,max}$

significantly varies from the profile on the other two instants of time, with significantly smaller accelerations below the fifth floor. It is characteristic that the three acceleration profiles have a common point between floors 4 and 5. This location is the nodal point of the second mode-shape.

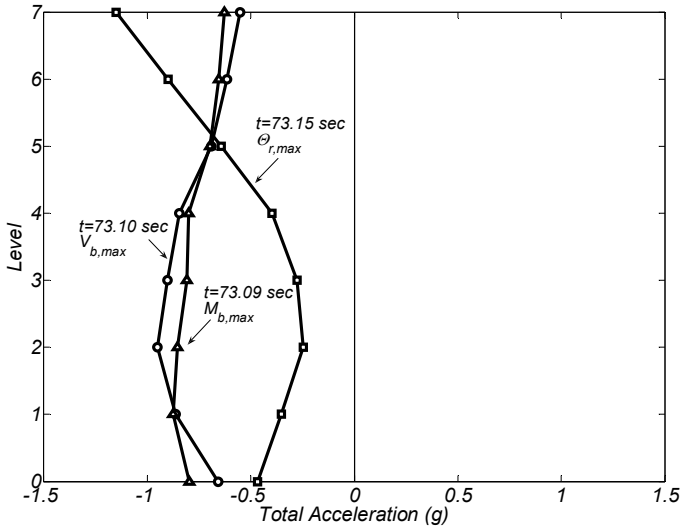

Figure 7.16. Total acceleration profile at characteristic instants of time during Test EQ4.

Fig. 7.17 plots the position of the resultant lateral force in tests EQ1 to EQ4 and in two WN tests versus the base shear coefficient. The position was determined as the ratio of the measured system base moment and the base shear force. WN1 and WN4 were 3% g RMS WN tests before EQ1 and before EQ4, respectively. The points plotted in Fig. 7.17 are for those cases where the system base moment exceeded 90% of the maximum overturning moment measured in each test. This figure also shows the seismic coefficient obtained from the adaptive pushover analysis when the web wall reached its flexural strength M_{oW}. Note that in all tests except test EQ4 the

resultant lateral force varied little with an average location about 70 and 80% of the height of the building.

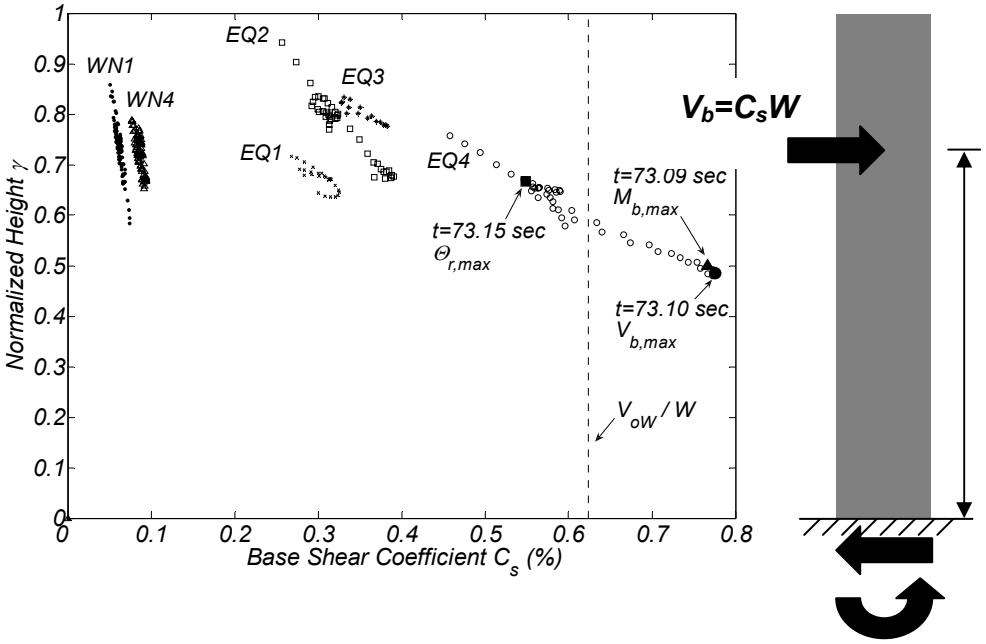

Figure 7.17. Normalized effective height of resultant system seismic force versus base shear coefficient.

For test EQ4 the lateral force resultant varies more significantly in this test. At t = 73.10 sec this force was only at 49% of the building height. This explains the increase of the base shear force while the system base moment remained almost constant. EQ4 excited more the second mode in comparison with the other EQ tests due to the motion characteristics of this record. The rich frequency content of this motion in the frequency range of the second mode can be seen from the acceleration response spectra (see Fig. 7.5). The reduction in the location of the lateral force resultant occurred because of (i) the second mode of response, (ii) the ground

acceleration during maximum base moment response, and (iii) the coupling of the web and flange walls through the slab.

7.6.6 Response Envelopes

Fig. 7.18 plots the envelopes of the main response quantities for tests EQ1 to EQ4. Fig. 7.18(a) shows the lateral relative displacement envelope. Characteristic is the almost linear profile above the second floor. Fig. 7.18(e) illustrates the interstory drift ratio envelopes. In all tests, interstory drift ratios increased in each level up to level 3 and then remained nearly constant. The linear displacement profile and the constant interstory drift profile above the second floor is because most of the rotation was developed on the bottom two floors of the wall. For Westwards response, the rotation on the bottom two floors was due to plastic hinge development in the flange wall. For Eastwards response most of the rotation occurred at 610 mm from the top of the first floor slab due to failure of the lap splice region and rocking of the wall.

Figs. 7.18(b) and (c) depict the system bending moment and shear force envelopes, respectively. Figure 7.18(c) also plots the probable shear strength of the web wall calculated from ACI-318 (2005) building code for a concrete compressive strength of 37.9 MPa and reinforcement yield strength of 455 MPa. The bending moment and shear force envelopes are dominated by the Westwards response of the structure. For this direction of response, with the flange in tension, the system was much stronger and developed larger bending moments and shear forces.

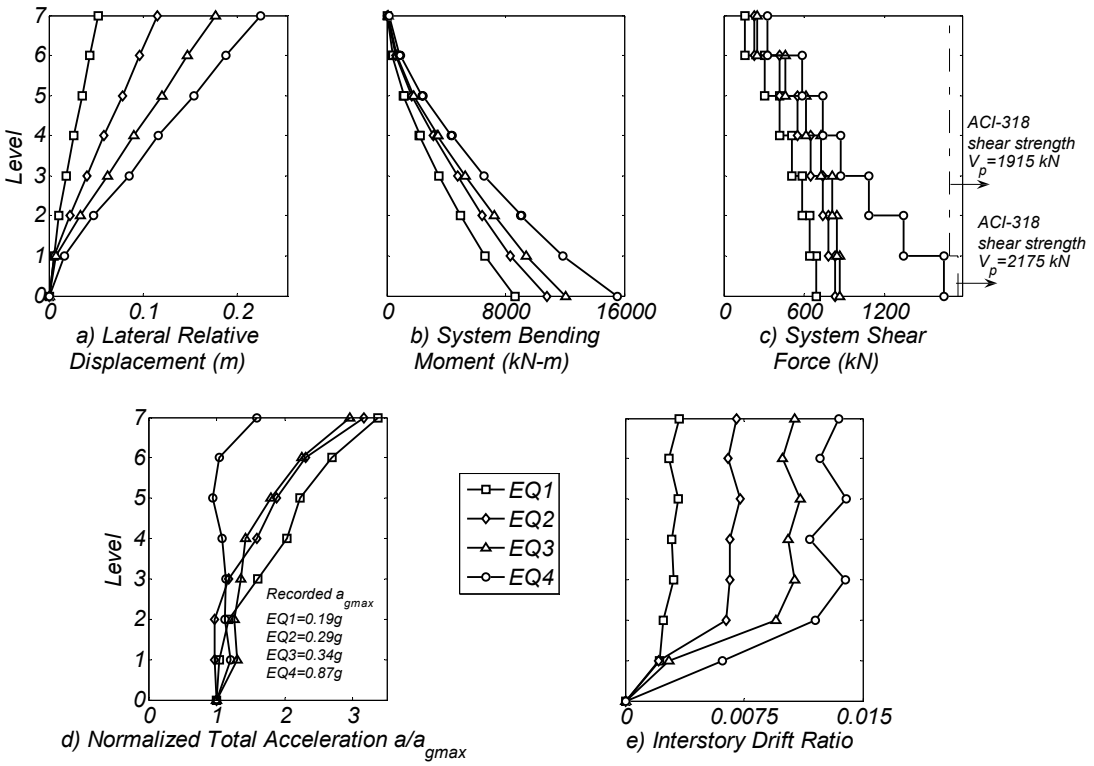

Figure 7.18. Response Envelopes.

The shape of the shear force envelope in test EQ4 differs from the envelopes observed for tests EQ1 to EQ3. The shear force envelope in test EQ4 has a nearly constant step per floor, while the shear force envelope in the other tests is closer to that expected from a first mode distribution of lateral forces. Panagiotou and Restrepo (2007) showed the second mode and coupling of the web and the flange walls through the slab were responsible for the shape of the shear force envelope observed in test EQ4.

Figure 7.18(d) plots the normalized total floor acceleration envelopes. Total floor accelerations were normalized by the peak ground acceleration. For as long as

the building responded nominally linear, floor accelerations were greater than the peak ground acceleration. This is consistent with the dynamic amplification expected for a linear system. The roof magnification reached 3.14, 3.03, 2.74 and 1.53 in tests EQ1 to EQ4, respectively. In test EQ4, where limited nonlinear response occurred, total floor accelerations were closer in magnitude to the peak ground acceleration, indicating saturation of the response. This observation is consistent with the theoretical work presented by Rodriguez et al. (2002). Another reason for the smaller amplification of the peak ground acceleration in test EQ4 is that the peak ground acceleration in this motion is the result of a local acceleration pulse of high frequency.

7.6.7 Strain Envelopes and Lap-splice Response

Fig. 7.19 shows the concrete and reinforcing steel tensile strain envelopes of levels 1 and 2 on the West end of the web wall and the East face of the flange wall. For the East face of the flange wall the maximum tensile strains were observed to the bottom of level 1 and close to the bottom of level 2. The local maximum local tensile strains are not observed on the bottom of level 2 due to the effect of the overlap of the reinforcement in this region. The reinforcing steel did not yield for EQ1 except at the interface with the foundation, while limited nonlinear response occurred during EQ2 and EQ3, except the interface with the foundation where a strain of 1.81 and 1.89% was locally measured, respectively. During EQ4 the tensile strain in the reinforcing steel exceeded 1% close to the base of the flange wall, while reached 3.57% at the interface with the foundation. Of the same order were the measured tensile strains

measured externally in the concrete. Small differences do exist due to bond slip as well as to local maximum strains recorded on the gauged bars.

The tensile strain profile of the West end of the web wall was dominated from the lap splice failure close to the bottom of level 2. Due to this large concrete tensile strains, reaching 10% for test EQ4, measured in this region. Only the concrete tensile strains were large due to concrete and rebar bond slip. Concentration of damage at the base of the second floor and the concrete, rebar bond slip at this region restricted the reinforcing steel strains at the West end of Levels 1 and 2 (see Fig. 7.19 (c)). The maximum tensile strain at the West end of level 1 exceeded the yield strain for all the four earthquakes without exceeding 0.6%.

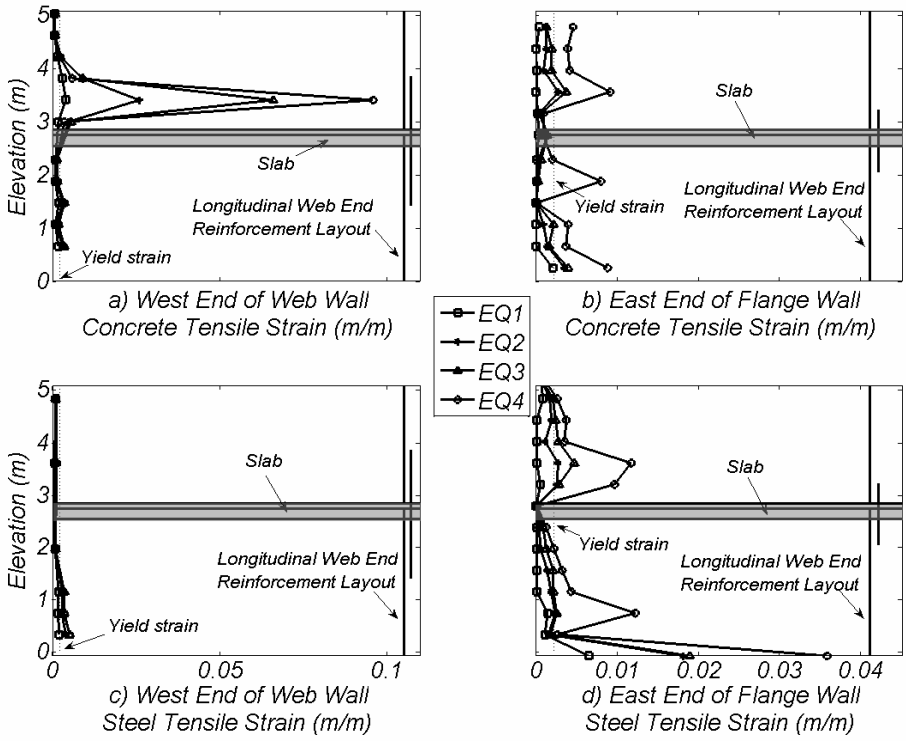

Figure 7.19. Concrete and Reinforcing Steel Tensile Dynamic Strain Envelopes.

Fig. 7.20 plots the concrete and steel strain time histories in the lap-splice from time t=72 to t=77.5 sec. The instant of times where $V_{b,max}$, $M_{b,max}$ and $\Theta_{r,max}$ occur are marked. The three instants of time where the peak Eastwards displacement response happened are at t=72.69, 73.79, 76.76 sec. The later three instants of time are also marked in the hysteretic response of Fig. 7.9. The exact position of the externally attached to concrete displacement transducer and the strain gage attached to the reinforcing steel rebar are indicated in Fig. 7.6(b). This plot shows the large concrete tensile strains developed locally and measured in this region of the lap splice failure while the tensile strain in the reinforcing steel is small.

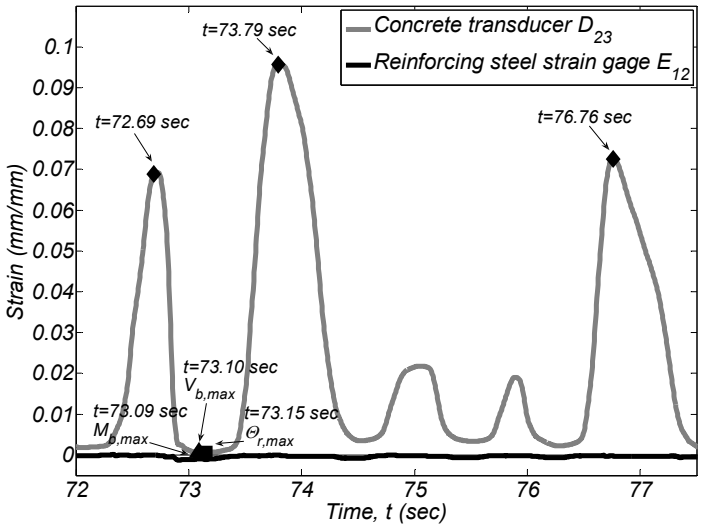

Figure 7.20. Comparison of concrete surface and bar dynamic strains in level 2 of West end of web wall during test EQ4.

7.7 Conclusions

This Chapter described Phase II of the shake table test of a 7-story load bearing T-wall building slice built at full-scale. The building was tested under four historical

earthquake records of Southern California, including the strong intensity near-field motion recorded at the Sylmar station during the 1994 Northridge Earthquake. The response spectrum from the Sylmar motion matched closely that of the design earthquake calculated for the site. The main purpose of Phase II was to test the effect of the flange wall in a load bearing T-wall. Despite the fact that the building was tested during Phase I up to the design earthquake and was partially repaired, its performance during Phase II of the test was very satisfactory. From the response observed we can draw the following conclusions:

1. The flange wall was fully effective in resisting flexure and caused significant increase of the system moment capacity.
2. The increase of the moment capacity due to the flange wall in tension caused increase of the maximum shear force in the web wall and consequently of its required shear strength.
3. 3-D interaction effects between the wall and the slabs referred here to as kinematic overstrength can cause significant increase of the shear force demand in the walls.
4. Dynamic effects observed in the response of the building system can augment the shear force demand in individual walls and significantly increase the total accelerations along the height of the structure.
5. Given the undesirable outcomes of shear failures in reinforced concrete buildings, such larger force demands due to the combined effect of flange in tension, kinematic overstrength and higher modes should be accounted for in design.

6. Lap-splices should be avoided at least twice the depth of a wall from the critical region at which a plastic hinge will develop. Other means of providing bar splicing should be considered instead.
7. A single curtain of transverse reinforcement was successfully used in the test building. The use of such detail can result in accelerated construction and should be allowed in design.

CHAPTER 8

8. PERFORMANCE OF SUSPENDED PIPES AND THEIR ANCHORAGES DURING THE 7-STORY BUILDING TEST

8.1 Summary

This Chapter presents results of the response of pipe systems anchored in the 7-story building during Phase II of the experimental program. The purpose of the tests was to investigate the forces that act on post-installed anchors in buildings during a diverse range of earthquake ground motions as well as to observe the floor acceleration amplification for nonstructural components in buildings during seismic events.

8.2 Introduction

Phase II of the UCSD 7-story full-scale building test described in chapter 7 provided a unique opportunity to take a closer look at floor accelerations and acceleration amplification of non-structural components for a building responding from the nearly elastic to the nonlinear range. The response of the anchors is discussed in Hoehler et al (2008). This chapter focuses on the response of the pipes.

8.3 Pipe System

L-shaped (side length = 10 ft (3 m)) groups of six, 6 in. (150 mm) diameter, cast-iron pipes attached to trapezes were mounted on the 1st, 4th and 7th floors of the building (Fig. 8.1).

(a) (b)

Figure 8.1. (a) 7-story building slice on the LHPOST and (b) Nonstructural system on 1st floor.

The trapezes were approximately 40 in. (1 m) long and constructed of 1–5/8 in. (41 mm) square steel channel strut placed back-to-back (Fig. 8.2). The trapezes were suspended 18 in. (460 mm) from the slab using threaded rods anchored with Hilti Kwik Bolt TZ (KB-TZ) and HSC-I anchors. The trapezes were braced at five locations to resist horizontal seismic forces. Special hinges located at both ends of the braces

allowed rotation perpendicular to the longitudinal axis of the brace. At every seismic brace, the hanger of the gravity support was surrounded by a piece of steel strut to prevent buckling of the threaded rod in compression. The pipes were strapped to the trapezes to prevent slipping and filled with water prior to the test to add mass to the system. The total mass of the pipe system (including water) was about 2900 lb (1300 kg).

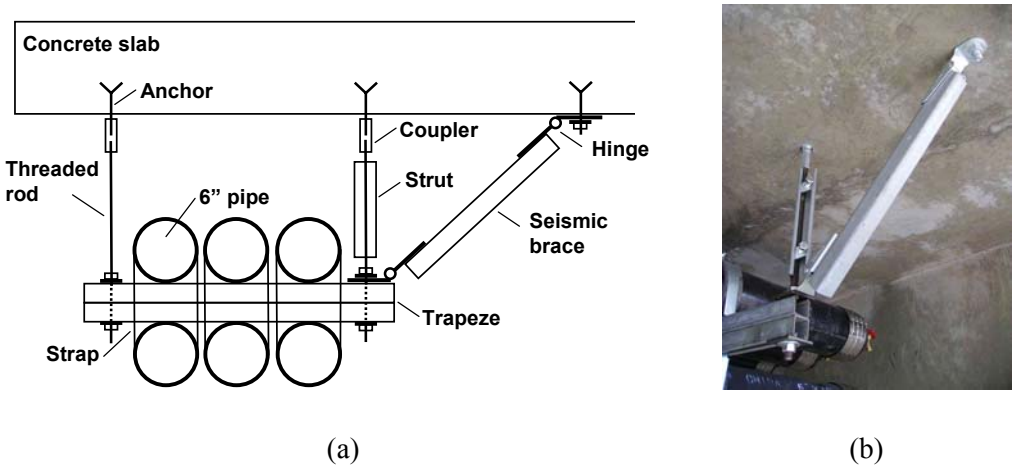

(a) (b)

Figure 8.2. (a) Schematic of pipe system (elevation) and (b) Typical trapeze connection detail.

At the connection between the threaded rod and the trapeze, the rod passed through oversized, slotted-holes in the backs of the channels and was fastened from above and below using nuts and plate washers. Additionally, the hinges at the ends of the seismic brace were designed to allow some axial movement for thermal expansion. The combination of these factors allowed for quite a bit of movement at this connection point.

8.3.1 Anchors and Instrumentation

16 axial strain gauges were installed centrically in the anchor bolt shaft or attached couplers. Of the 39 anchors used to secure the pipe systems (13 per floor) a total of 16 were instrumented. The locations of the instrumented anchors are given in Fig. 8.3. On the 1st and 4th floors, three of the 5/8" Kwik Bolt TZ anchors used to secure the seismic braces were instrumented with axial strain gauges (Fig. 8.4a). On the 7th floor, four of the seismic brace anchors were instrumented. Two of the eight gravity supports on each pipe system were attached using M12 HSC-I anchors with instrumented couplers (Figure 8.4b). The remaining 23 anchors were non-instrumented 5/8" Hilti Kwik Bolt TZ anchors.

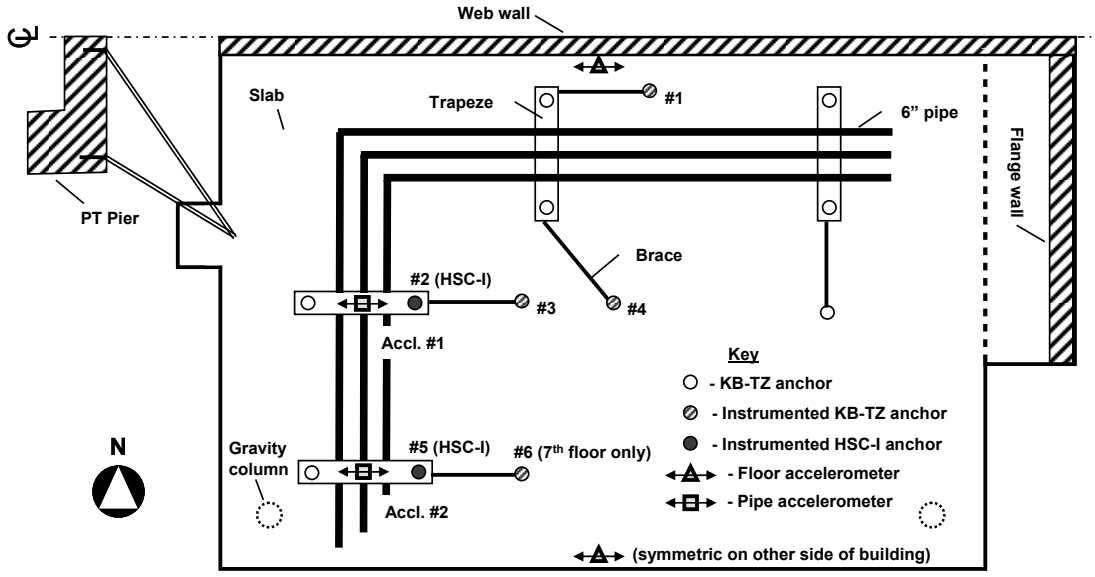

Figure 8.3. Anchor and accelerometer locations (plan view).

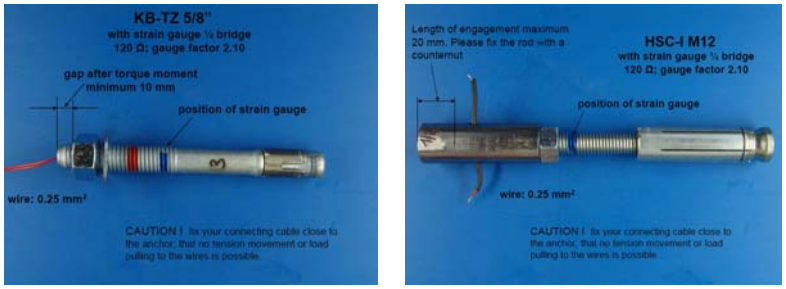

(a) (b)

Figure 8.4. (a) Instrumented KB-TZ and (b) Instrumented HSC-I.

8.4 Pipe Response

8.4.1 Modal Frequencies of Pipe System

The pipe frequencies were determined from the transfer functions between the floor absolute acceleration and the absolute acceleration recorded on the pipes. Identification of the first and second pipe modal frequencies was possible on 1st and 4th floors. For the 4th floor where two modes were identified and data from two accelerometers existed, both mode shapes exhibited coupled longitudinal-torsional motion.

Pipe modal frequencies are listed in Table 8.1 for white noise excitation of the building prior to EQ3. The frequencies identified by the two accelerometers on each pipe (see Fig. 8.3) did not differ significantly (less than 5%) and were averaged to obtain the reported value. The pipe mode shapes were strongly influenced by the initial slackness (slip) of the trapeze connections. This slip likely contributed to the relatively low observed frequencies. Table 8.2 lists the Mode 1 frequencies for the pipes on the 7th floor for all of the white noise input. Similar to the building, the

frequency decreased after each earthquake. This is attributed to accumulated damage in the pipe systems; mainly loosening of the trapeze.

Table 8.1. Pipe modal frequencies obtained from test WNEQ3.

	Pipe frequency (Hz)		
Mode	Floor 1	Floor 4	Floor 7
1	3.59	3.14	3.4
2		5.16	

Table 8.2. Pipe fundamental frequencies on the 7th floor for WN time-histories.

	Pipe fundamental frequency (Hz)			
	WNEQ1	WNEQ2	WNEQ3	WNEQ4
Floor 7 (Mode 1)	4.22	3.64	3.4	2.7

8.4.2 Force-Displacement Response

Fig. 8.5 plots measured pipe absolute acceleration as a function of the relative pipe displacement on the 4th floor during EQ3. The relative displacement of the pipe was calculated as the total displacement of the pipe minus the total floor displacement. Total displacements were calculated from the recorded absolute accelerations using a process of filtering and double integration. The hysteretic response in Fig. 8.5 (left) indicates slackness in the trapeze and brace connections. After a relative displacement of about 8 mm (0.3 in.) the system regains stiffness. The amount of slack, however, depended on the installation and was less prominent in some connections (Fig. 8.5 (right)). Similar trends were observed for the other pipes for all the EQ tests. The

specific nonlinear force-displacement behavior of the pipe systems, i.e., the increase in stiffness after some amount of relative displacement, affected the acceleration response of the pipes.

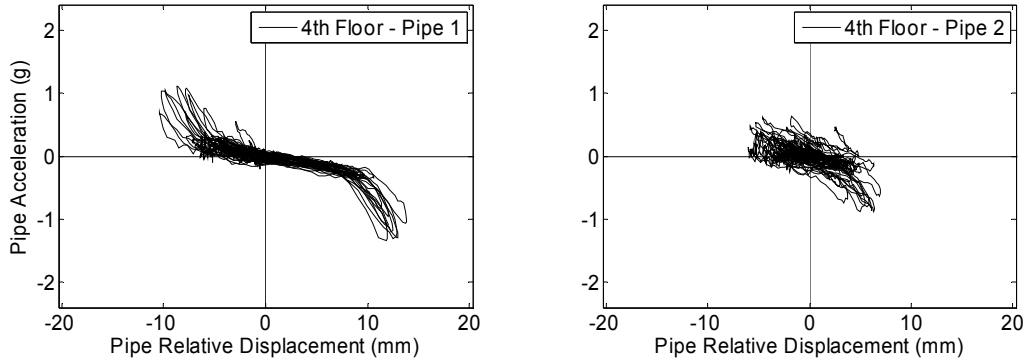

Figure 8.5. Pipe force-displacement response during EQ3.

8.4.3 Amplification

In the discussion below, the author distinguishes between two types of acceleration amplification: "correlated" and "uncorrelated." Uncorrelated amplification refers to the ratio of the maximum absolute acceleration of the nonstructural component to the maximum absolute acceleration of the forcing motion, i.e., coincidence in time is not considered. Correlated amplification refers to the amplification of the component acceleration related to a specific modulation of the pipe's response over the floor acceleration.

Fig. 8.6 plots the strong motion portions of the recorded floor (average) and pipe (Accl. #2 only; see Figure 8.3) acceleration time histories on the 1st, 4th and 7th floors for EQ2 and EQ4. Figure 8.6 illustrates that the maximum pipe acceleration

($a_{p,max}$) is not necessarily correlated with the maximum floor acceleration ($a_{f,max}$). Although ultimately it is the correlated amplification that is the "real" amplification of the component acceleration relative to the floor motion, definition of this quantity is beyond the scope of this Chapter. Moreover, for nonstructural design purposes the designer typically has the peak ground acceleration as a design quantity and is thus forced into the concept of uncorrelated amplification.

As can be seen in Fig. 8.6, floor accelerations for EQ2 are characterized by multiple cycles of significant, similar-amplitude, acceleration. The main frequency content of these cycles is close to the fundamental frequency of the structure as it will be shown in more detail below. The floor acceleration characteristics for EQ1 and EQ3 were similar to those for EQ2. The input ground motion in EQ4 is characterized by a distinct acceleration pulse, which also characterizes the floor acceleration response. Because of this, for EQ4 the maximum floor and pipe acceleration are well correlated in time since the maximum response of both systems occurs during the distinct acceleration pulse. In most of the successive cycles (see Figure 8.6), the pipes amplify the input floor acceleration. This amplification occurs close to the instant of time of maximum floor acceleration in a given cycle.

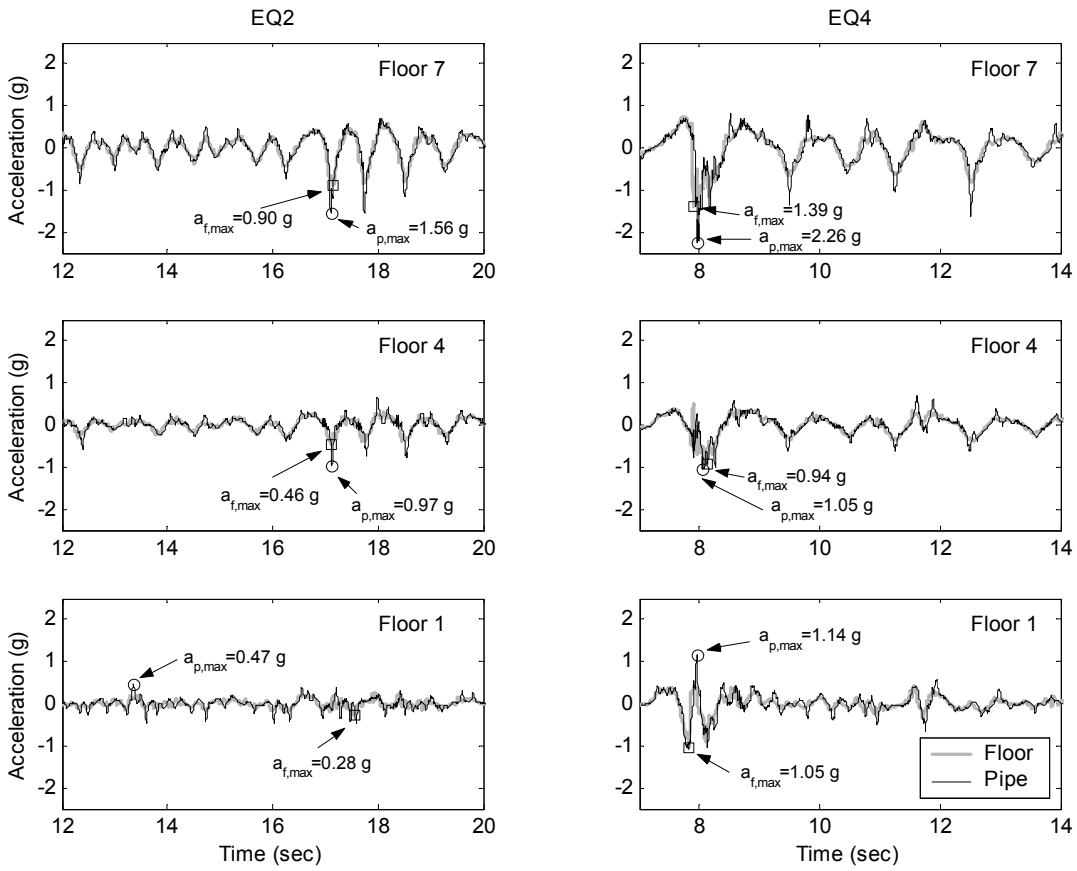

Figure 8.6. Recorded floor and pipe accelerations on the1st, 4th and 7th floors during EQ2 and EQ4.

Table 8.3 lists the average of the maximum absolute pipe accelerations measured by the two accelerometers on each floor. The absolute pipe accelerations generally increase with increasing earthquake intensity. The nonstructural component design acceleration according to Section 13.3 of ASCE 7 (2005) is provided for comparison. The ASCE 7 values were calculated using $S_{DS} = 1.81$ g, $a_p = 2.5$, $I_p = 1.0$, $W_p = 1.0$ and $R_p = 3.0$. Keeping in mind that the seismic design spectrum nearly matches the spectrum for EQ4, the design accelerations slightly underestimate the observed values. It is significant to note that nearly all the nonlinearity occurred in the pipe support system, i.e., the trapeze, rather than in the pipes themselves, therefore an

increase in R_p for a different type of pipe, e.g., highly deformable steel instead of cast-iron, would have been unwarranted in this case. The uncorrelated pipe-to-ground and pipe-to-floor acceleration amplifications are presented in Table 8.4. The pipe-to-ground amplification decreased with increasing earthquake magnitude due to the increasingly nonlinear behavior of the building, which limited the floor accelerations; particularly in EQ4 (Fig. 8.7a). The pipe-to-floor acceleration amplification is more uniform between the earthquakes (Fig. 8.7b) and depends mainly on the relation between the frequency content of the floor acceleration to the fundamental frequency of the piping system, the force-displacement characteristics of the pipe connections and the damping of the nonstructural component.

Table 8.3. Maximum pipe total accelerations (absolute values).

	Pipe acceleration (g)				
Pipe	ASCE 7	EQ1	EQ2	EQ3	EQ4
Floor 7	1.80	1.30	1.64	1.72	2.23
Floor 4	1.28	0.79	1.12	1.11	1.26
Floor 1	0.76	0.38	0.47	0.72	1.14

Table 8.4. Mean uncorrelated pipe amplifications.

	Amplification (pipe-to-ground)				Amplification (pipe-to-floor)			
Pipe	EQ1	EQ2	EQ3	EQ4	EQ1	EQ2	EQ3	EQ4
Floor 7	6.8	5.6	5.0	2.5	2.1	1.8	1.8	1.6
Floor 4	4.1	3.8	3.2	1.4	2.1	2.5	2.4	1.3
Floor 1	2.0	1.6	2.1	1.3	2.0	1.7	1.7	1.1

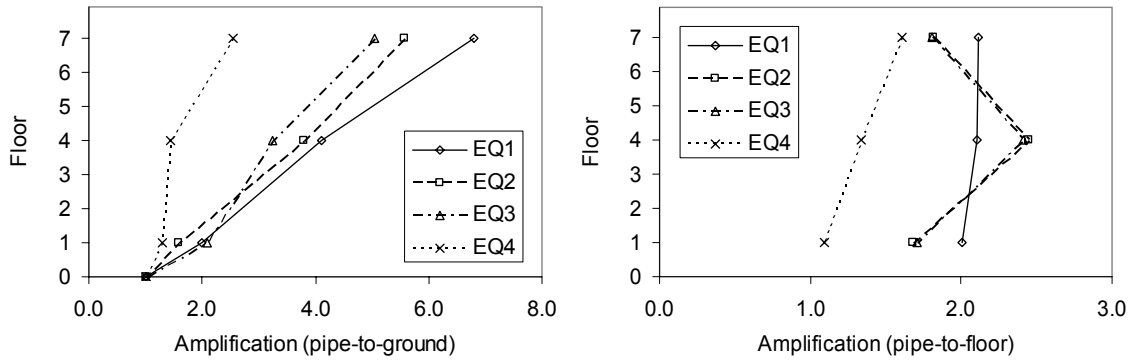

(a) (b)

Figure 8.7. Distribution of mean uncorrelated pipe amplifications along building height.

Fig. 8.8 plots the floor acceleration response spectra of floors 1, 4 and 7, as well as the ground motion spectra, for 5% damping ratio. Due to the measured nonlinearity in the force-displacement behavior of the pipe connections, estimation of damping of the piping system is not attempted. A damping ratio of 5% was used only for presenting the acceleration floor response spectra and is not recommended for general use for nonstructural systems. Figure 8.8 indicates that for all four earthquakes, the floor acceleration response spectra have a local peak at a frequency slightly smaller than the fundamental frequency of the structure determined from the characterization with low-amplitude white noise shaking (see Chapter 7), indicating that the main frequency content of the floor accelerations is close to the fundamental frequency of the structure. This frequency is smaller because, during the earthquakes, the nonlinear building response results in smaller effective stiffness and a corresponding decrease in the fundamental frequency. During the white noise tests, the building response was nearly linear elastic. While for floors four and seven the floor

acceleration response spectra are greatly influenced by the building's dynamic response, the floor acceleration response spectra of floor one is better correlated to the ground acceleration response spectra.

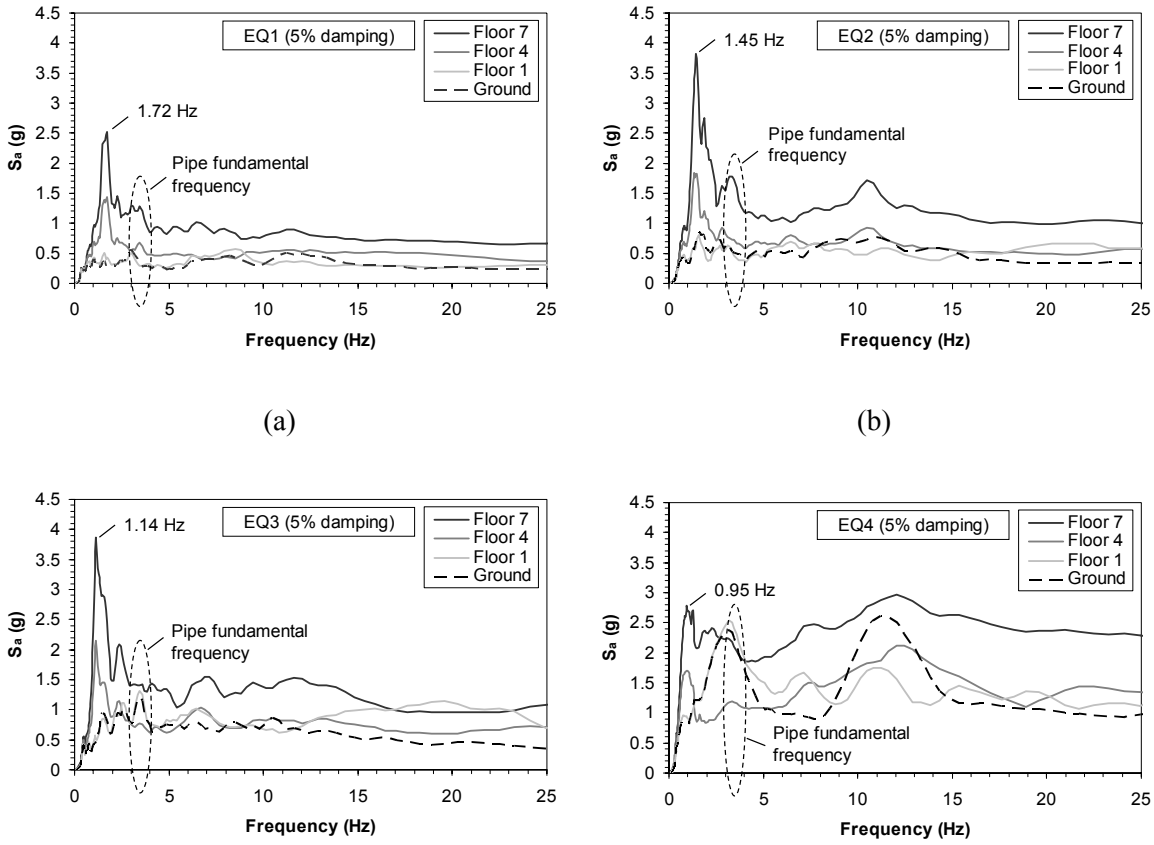

Figure 8.8. Floor 1, 4 and 7 acceleration response spectra (5% damping): (a) EQ1, (b) EQ2, (c) EQ3 and (d) EQ4.

Fig. 8.8 also indicates that amplifications greater than two times those observed could be expected if the pipes had had a fundamental frequency of 1 Hz to 2 Hz, i.e., if they were in resonance with the fundamental building mode. The reader

will note that for EQ4, due to nonlinear response of the structure, the dominance of the 1st mode in the floor acceleration response spectra diminishes and the second mode dominates. This agrees with theoretical work by Rodriguez et al. (2002).

8.5 Conclusions

The following conclusions are drawn from the test results:

1. The maximum recorded pipe accelerations increased with increasing ground motion magnitude.
2. Amplification of the ground acceleration experienced by the pipes at the roof level varied from 2.5 to 6.8. The amplification decreased with increasing ground motion magnitude due to the increasingly nonlinear behavior of the building.
3. The accelerations measured on the pipes were slightly larger than those predicted by the ASCE 7 (2005) Section 13.3.1 equations for nonstructural components. However, the modal frequencies of the pipes did not coincide with any building modal frequencies, therefore, larger pipe acceleration amplifications were possible.
4. Nonlinearity in the investigated nonstructural systems came almost exclusively from the supporting structures (trapezes) rather than from the pipes themselves.

CHAPTER 9

9. DYNAMIC NONLINEAR STRUT AND TIE MODEL CALIBRATION FOR THE UCSD 7-STORY FULL-SCALE BUILDING TEST

9.1 Summary

This chapter describes a computational model developed to verify the design and reproduce the experimental response of Phase I of testing of the 7-story full-scale building slice discussed in chapter 6. A variable angle nonlinear truss approach modeled the primary lateral force resisting wall in this building. The proposed model directly accounts for shear-flexure interaction in a reinforced concrete wall. Simple piecewise linear hysteretic rules were used to model the hysteretic behavior of different the members. The model predicted very well the lateral displacement, force, acceleration and strain demands in four input ground motions of increased intensity resulting from near-elastic to highly nonlinear structural response. Particular importance was given to model the 3-D effect of coupling between the walls, the slab, and the gravity columns. Important results regarding the small amount of viscous damping are also discussed.

9.2 Introduction

The assessment of the nonlinear dynamic response of structural building systems to earthquake excitation is an area that has gained significant attention among

practicing structural engineers. To this end practicing engineers make use of state-of-the-art documents such as FEMA-356 (2000) and ATC-40 (1996).

Strut-and-tie and lattice models have been used to successfully evaluate the nonlinear behavior of reinforced concrete (RC) members and components. To et al. (2001, 2003) and Park et al. (2007) used strut-and-tie models for the nonlinear analysis of beams, columns, and subassemblies subjected to monotonic or cyclic loading. Miki (2004) used a nonlinear lattice model to estimate the monotonic, cyclic and the dynamic response of columns and piers.

This chapter describes a computational 2-D model developed to verify the design and reproduce the experimental response of Phase I of testing of the 7-story building test discussed in chapter 6. A nonlinear strut-and-tie formulation was used to model the wall that provided the primary lateral force resistance to the building. The 3-D coupling between the walls, the slab and the gravity system, which had a significant influence on the building's dynamic response, was also implemented in the 2-D model.

9.3 Description and Objectives of the Computational model

As it was described in chapter 6 the building was imposed to four earthquake ground motions of increased intensity. The building responded to these input ground motions with increased level damage starting from nearly elastic response, response with limited nonlinearity and highly nonlinear response. The majority of damage was

developed in the web wall. For all the EQ tests the system's response was influenced by the coupling between the walls, the slab and the gravity system (kinematic system overstrength) as explained in chapter 6. Summarizing, the main objectives of the computational model were i) to compute the different damage states in the web wall under different levels of excitation ii) to model adequately the 3-D effects of kinematic interaction between the web wall, the slab and the gravity columns, iii) verify the experimental system response in terms of all the response quantities such as forces, displacements and strains.

9.4 Description of the Model

The computational model used a nonlinear strut and tie model for the web wall, described below. For the post tensioned precast segmental pier and the flange wall, simple two – component Giberson (Giberson 1969) beam elements were used. The effect of coupling between the slab, the walls and the gravity system was modeled with nonlinear springs. The mass was lumped at the mid-length of the web wall, at mid-height of the slab at every floor. The effect of the rotational inertia was ignored as Chapter 6 showed that it was negligible. Fig. 9.1 shows a schematic representation of the main elements in the computational model.

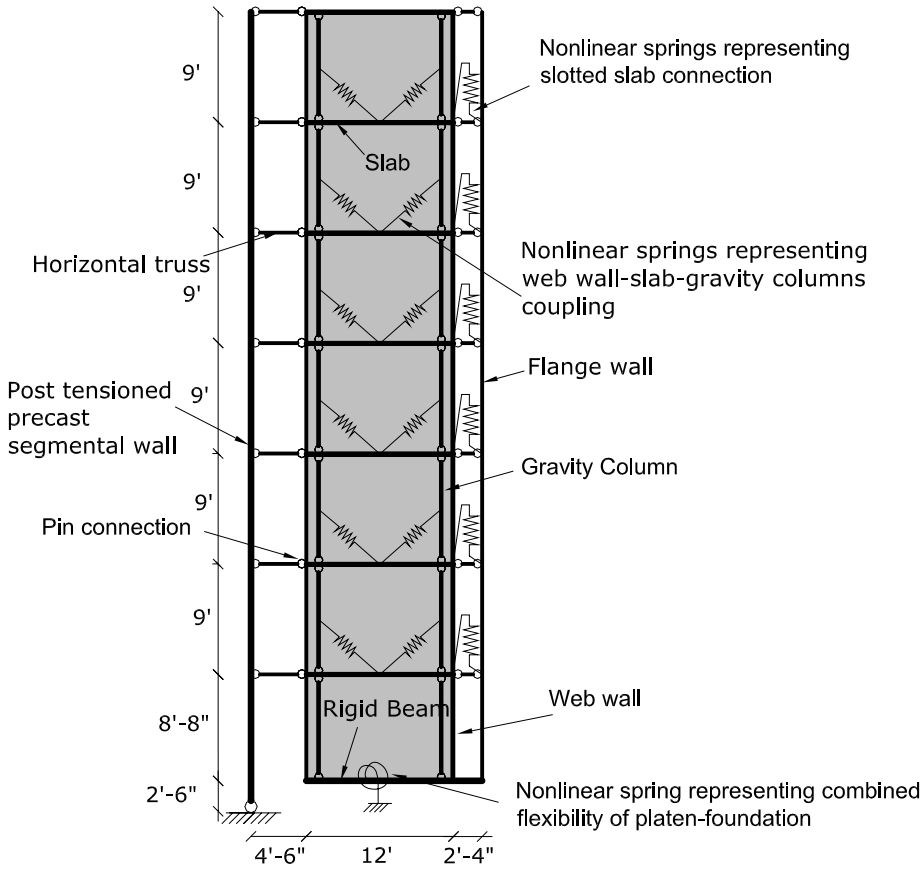

Figure 9.1. Elevation showing the elements in the 2-D analytical model.

9.4.1 Nonlinear Strut and Tie Model of Web Wall

To model the web wall, a nonlinear variable angle strut and tie approach was used. Fig. 9.2 shows the strut and tie model of a wall panel between two floor slabs. Vertical overlapping nonlinear truss elements were used for the concrete and the reinforcing steel. The area of the vertical truss elements representing steel corresponds to the area of the reinforcing steel. The area of the vertical truss elements representing concrete corresponds to the effective concrete area around the reinforcing steel. Additional truss elements, with the area of the corresponding reinforcing steel, are used for modeling the wall horizontal reinforcement. Truss elements also represent the

diagonal concrete carrying compressive and tensile forces. The area A_{cd} of the truss element representing the diagonal concrete struts is the product of the effective width of every strut (L_d / n), where L_d is the length of the panel diagonal and n the number of diagonals in each direction used, multiplied by the width of the wall b_w. Frame elements representing the properties of the slab of an effective slab width are used on the bottom and the top of each wall panel. The vertical, the horizontal as well as the diagonal truss elements are interconnected at nodes. Perfect bond between concrete and reinforcing steel is assumed.

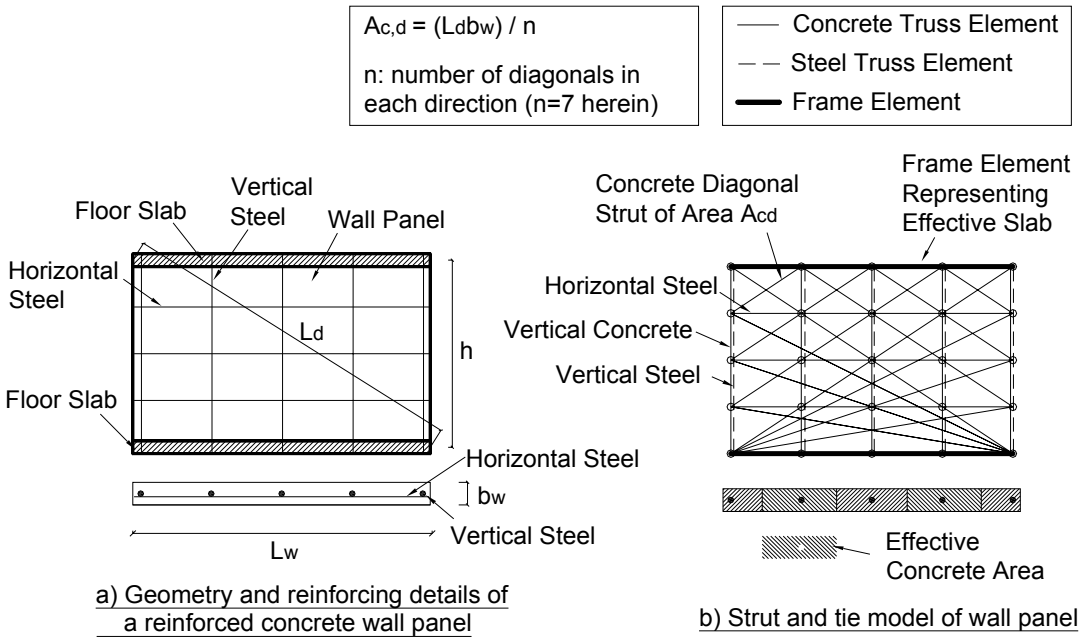

Figure 9.2. Load bearing wall panel and refined variable-angle truss model.

Two different levels of trusses were used. A refined truss was employed on the first two levels because the majority of the inelastic response was expected there. The first level wall panel was discretized in four parts along its height whereas the second

level wall panel was discretized in five parts. This was done to capture the gradual spread of plasticity and the plasticity-constraining effect of the lap splices. On the second level an additional layer was used to model the potential development of concentrated plasticity at the interface between levels 1 and 2 due to the specific reinforcement detailing characteristics there. Levels 3-7 were expected to respond elastically and thus were discretized with a less refined truss to capture the loss of tension stiffening.

Along its width, the web wall section was subdivided in 15 layers, each associated with the location of the longitudinal reinforcement. Each of these 15 layers consisted of two overlapping vertical truss elements, to represent the reinforcing steel and the effective concrete around the reinforcing steel. The horizontal reinforcement was lumped in three and four positions respectively in levels 1 and 2 and concentrated at the midheight in levels 3 to 7.

For the diagonal concrete struts the area was estimated as described above for each wall panel corresponding to each level. Seven, eight and three diagonal struts were used at each direction in levels 1, 2 and 3 to 7, respectively. For levels 3 to 7 less diagonals were used since the response was anticipated and finally verified to be elastic.

The response of each of the different elements was represented by simple piecewise linear hysteretic rules. At the expense of more computational time, but not

necessarily of significant gain in accuracy, other more complex formulations could have been used. Fig. 9.3 shows the different hysteretic rules used for modeling the different members. A study of the sensitivity of the response to the refinement of the hysteretic models is under progress.

The axial force-axial deformation of reinforcing steel was represented by a bi-linear inelastic hysteretic rule (see Fig. 9.3a). To determine the yielding stress and the post-yield stiffness ratio material test data were used (Panagiotou et al. 2007). The average yield strength of the reinforcing steel used was 66 ksi and the average post yield stiffness ratio was r = 2.2%.

The axial force-axial deformation of the confined reinforced concrete struts was represented by a bi-linear inelastic hysteretic rule of zero post yield stiffness (see Fig. 9.3b). For the unconfined concrete used in the vertical as well in the diagonal trusses strength degradation was used after yield in compression (see Fig. 9.6b). An origin oriented hysteretic rule was used to model the response of concrete in tension. The tensile strength of concrete was taken equal to $f_{ct}' = 4\sqrt{f_c'}$. Fig. 9.3b shows the stress strain relation assumed for the concrete in tension. For the stiffness of concrete an average value of modulus of elasticity E_c was used based on the material testing data of concrete cylinders in compression (Panagiotou et al. 2007).

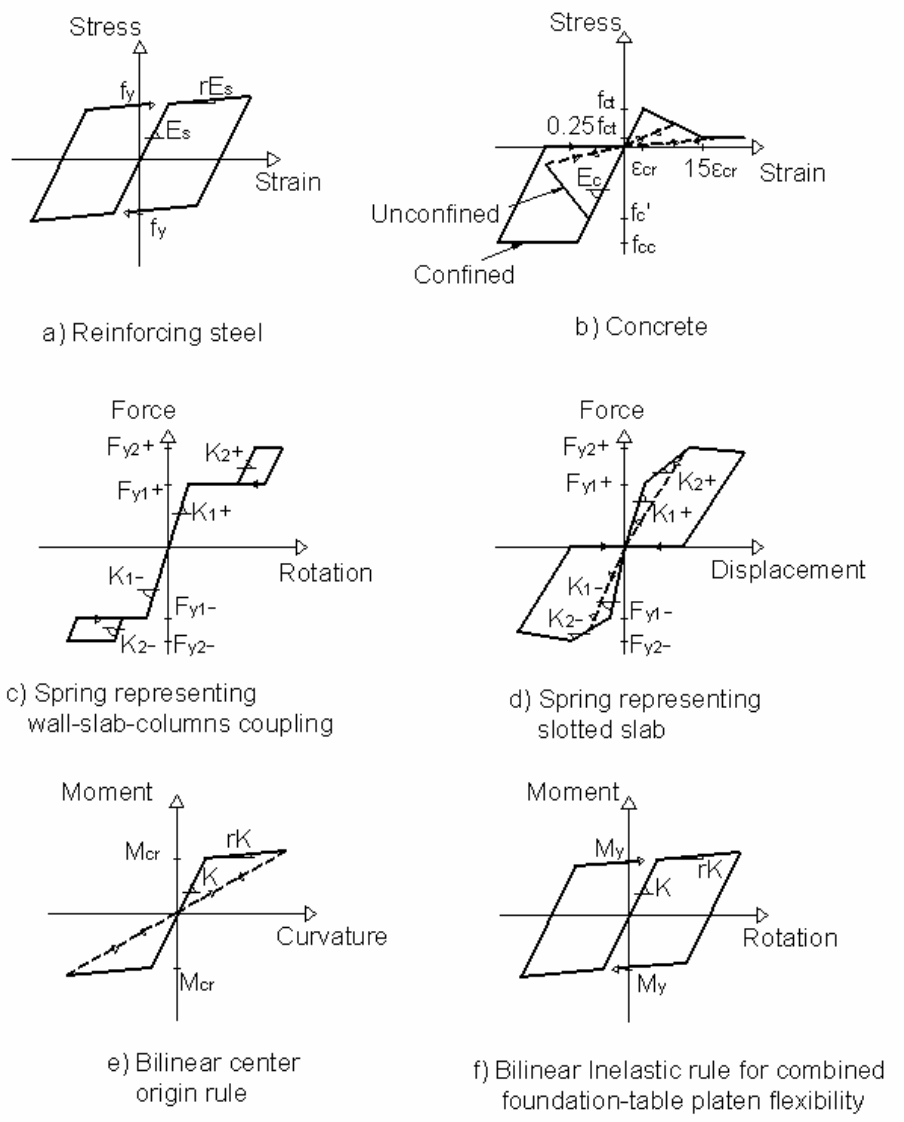

Figure 9.3. Hysteretic rules used for modeling of the different elements.

9.4.2 Modeling of Coupling between Walls, Slab and Gravity System

Special consideration was given for the implementation of the 3-D effects of the interaction between the web wall, the slab the flange wall and the gravity columns as described in chapters 3 and 6. To achieve this multiple nonlinear springs were used. For the interaction between the web wall, the slab and the gravity columns nonlinear

springs between the midlength of the web wall at each floor slab and the gravity columns were used (see Fig. 9.3c). These springs were calibrated to capture the axial force in the gravity columns caused by the expected deformation of the web wall (Panagiotou et al. 2007). For the coupling between the web wall, the slotted slab and the flange wall nonlinear springs with force displacement characteristics shown in Fig. 9.3d were used. These springs were also calibrated based on 3-D finite element (F.E.) results of the slab (Panagiotou et. al 2007).

9.4.3 Modeling of Flange Wall, PT Segmental Pier and Support Flexibility

Bi-linear origin oriented hysteretic responses were assigned to the beam elements used to model the precast segmental column and the flange wall. Both of them were anticipated to respond in the elastic range and bilinear loops were used for capturing the reduction of the concrete contribution towards tension stiffening (see Fig. 9.3e). The horizontal steel truss between the precast wall and the web wall was modeled with pin-pin nonlinear frame elements. Pin-pin linear frame elements were used also for modeling the gravity columns. The axial behavior of the slab connection between the web and the flange wall was modeled with pin-pin elements representing the axial response of the reinforcing steel and concrete. The effect of the table-foundation flexibility was considered by the addition of a rotational spring at the base with properly calibrated bilinear characteristics based on measured rotation on top of the foundation (see Fig. 9.6f).

9.4.4 Additional Model Parameters

Rayleigh damping based on the initial stiffness was used. The first two modes were used for the determination of the Rayleigh damping model. The results presented are for a damping ratio of 0.5% on the first mode and 2% on the second mode. The total number of nodes of the model was 434 and the total number of elements 1494. All analysis used large-displacement theory. The computer platform Ruaumoko (Carr 1998) was used. The Newmark constant average acceleration method was used to solve numerically the equations of motion. The time step of the input motions was equal to 0.02 sec and the integration time step was 0.005 sec.

9.5 Analysis Results

9.5.1 Monotonic Pushover Analyses

Fig. 9.4 shows the measured system base bending moment versus roof displacement. The measured response is compared with the computed monotonic responses. Pushover response “Wall + Slot + Columns” considers all the structural elements in the building. Pushover responses “Wall+Slot ”, “Wall + Columns” and “Wall Only” were performed to elucidate on the relative importance of the structural elements that contributed to kinematic overstrength.

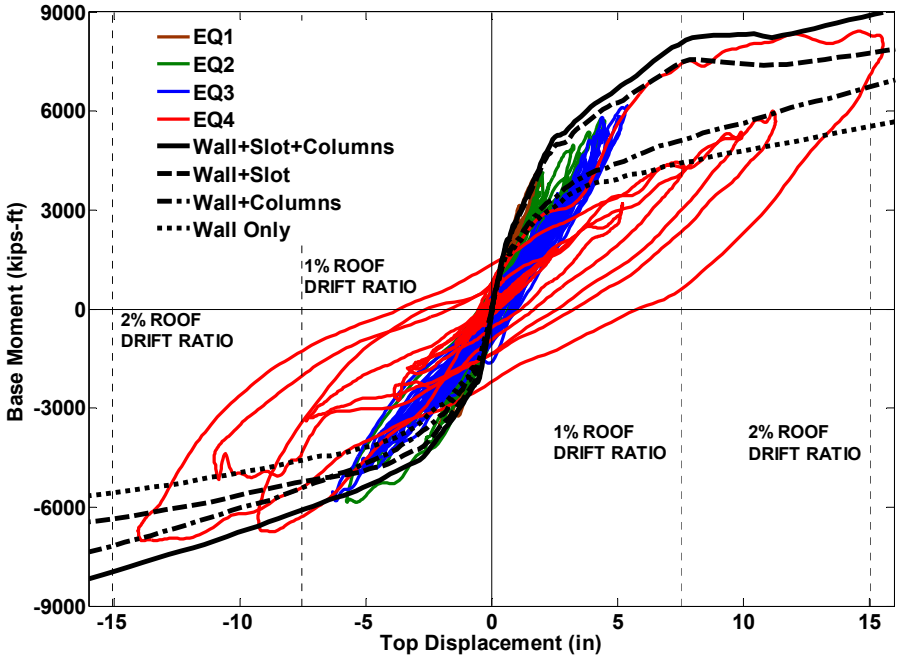

Figure 9.4. Measured hysteretic and computed monotonic response.

The computed monotonic response "Wall+Slot+Columns" is in good agreement with that observed in the experiment. The monotonic computed system capacity exceeds the measured capacity. This is because the monotonic response does not account for the stiffness degradation due to loss of concrete tension stiffening that occurs under cyclic response. Fig. 9.4 shows also the monotonic response of the web wall only and the response of the web wall with the slotted connection. This was done in order to decompose the contribution of the different system parts in the moment capacity of the system. Fig. 9.4 shows that the capacity of the web wall (for compression axial force N=180 kips) alone is 55% of the system capacity, while 11% of the maximum moment is due to the effect of the slab, 30% the effect of the slotted connection, and 4% due to the capacity of the two transverse walls.

9.5.2 Nonlinear Dynamic Response

Fig. 9.5 plots the measured and computed hysteretic response in terms of system base moment versus roof lateral relative displacement. The model overall gave a very satisfactory prediction of the measured hysteretic response. Difference is observed in the last cycles of EQ4 due to the lap splice failure occurred after the peak response which was not implemented in the model. In addition for Eastwards response during test EQ4 the moment is slightly underestimated. This is because the model did not account for the small increase of the web wall strength due to strain aging effects (Panagiotou et al. 2007). Fig. 9.6 plots the measured and computed hysteretic response in terms of axial force in the gravity columns versus roof lateral relative displacement.

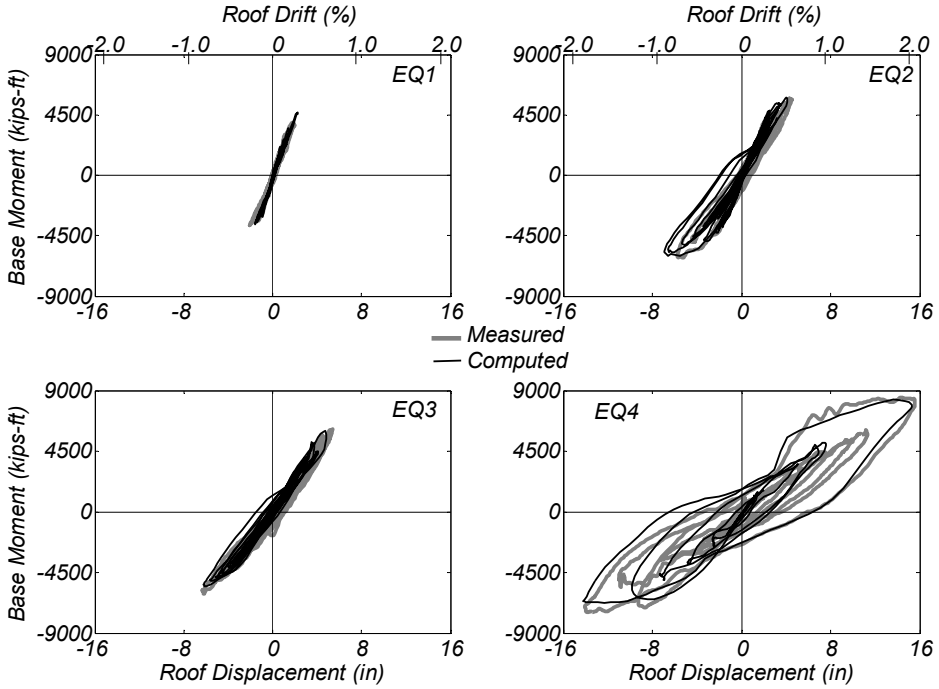

Figure 9.5. Measured and computed base system moment versus roof displacement.

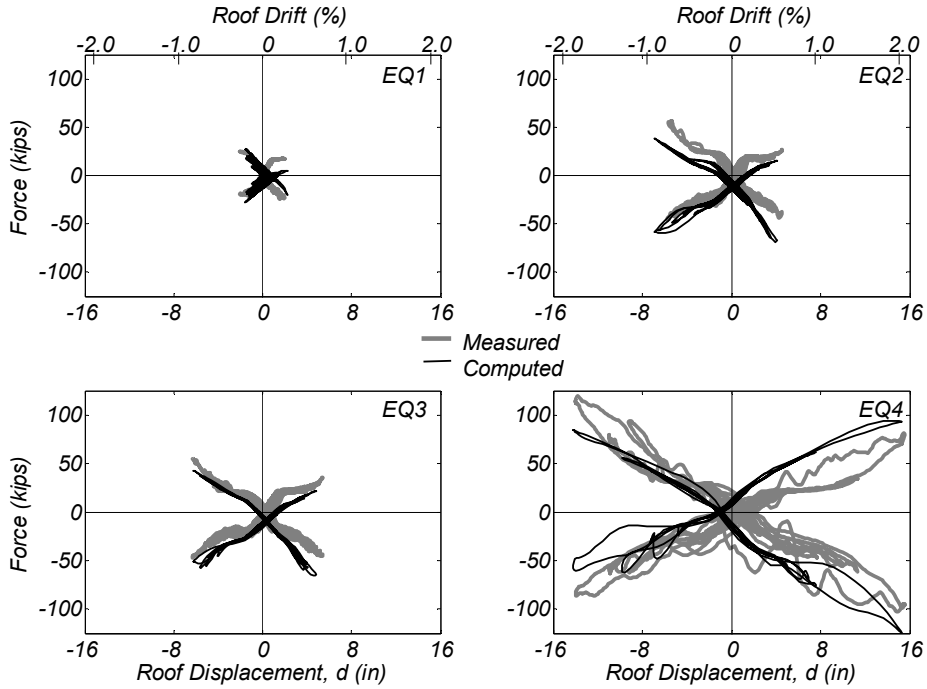

Figure 9.6. Measured and computed gravity columns axial forces versus roof displacement hysteretic response.

Fig. 9.7 plots the measured and computed hysteretic response in terms of system base shear force versus the shear deformations of the first level of the web wall. The model was able to reasonably estimate the shear deformations for all the EQ tests. We note that the current model does not include the effect of sliding shear which contributed to the shear deformations.

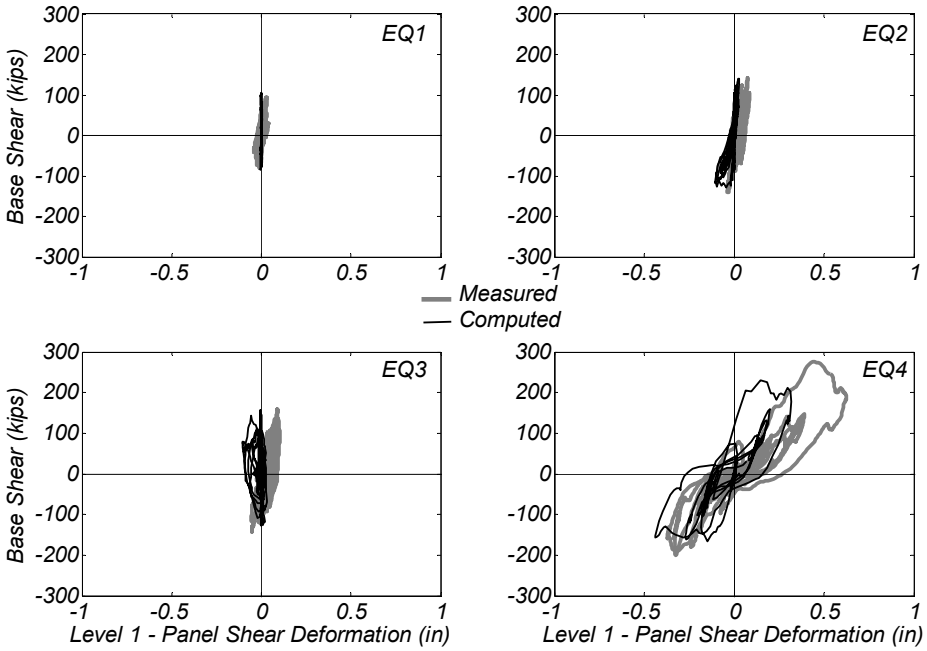

Figure 9.7. Measured and computed first level shear deformations versus base shear force hysteretic response.

Fig. 9.8 compares the measured and computed roof lateral relative displacement for all the EQ tests. Excellent agreement is achieved in terms of amplitude and stiffness (frequency content) under the multiple cycles of the response. Difference between the measured and the computed response is observed after the peak displacement response of test EQ4. This was due to the effect of the lap splice failure which was not implemented in the model as explained above.

Fig.9.9 plots the comparison of the measured and the computed system base shear force time histories. Fig.9.10 plots the comparison of the measured and the computed roof total acceleration time histories. Both the system base shear and roof total acceleration were very good estimated in terms of amplitude and frequency

content. Fig. 9.11 plots the measured and computed strain time histories at the base of the West end of the web wall. Very good agreement was also observed.

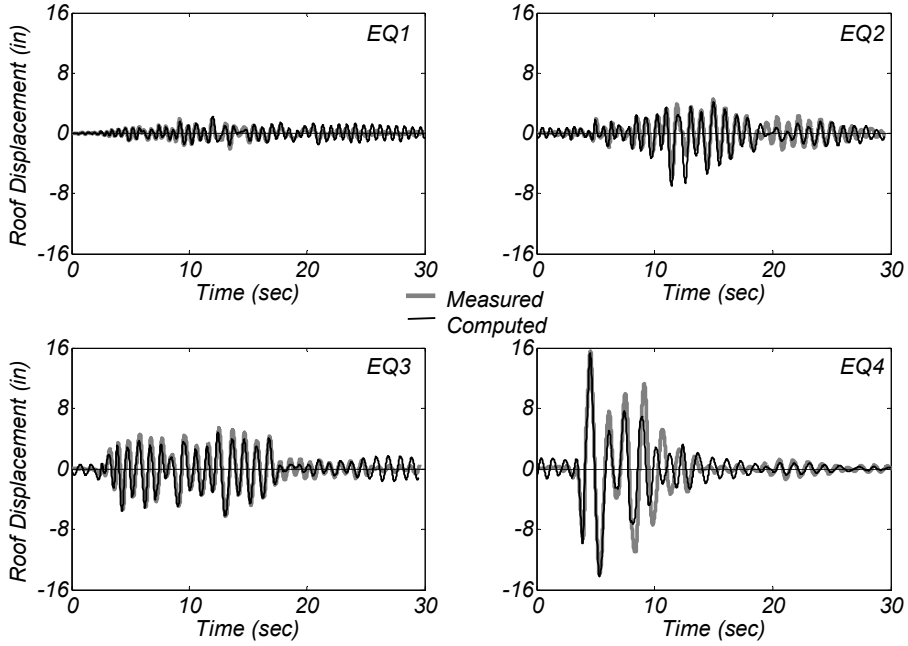

Figure 9.8. Measured and computed roof displacement time-histories.

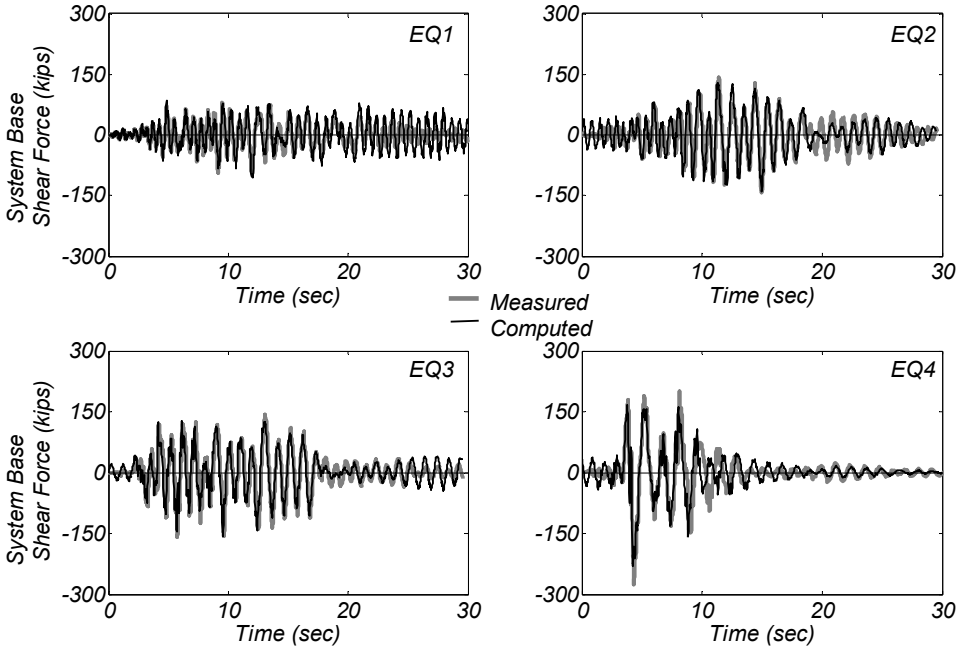

Figure 9.9. Measured and computed system base shear force time-histories.

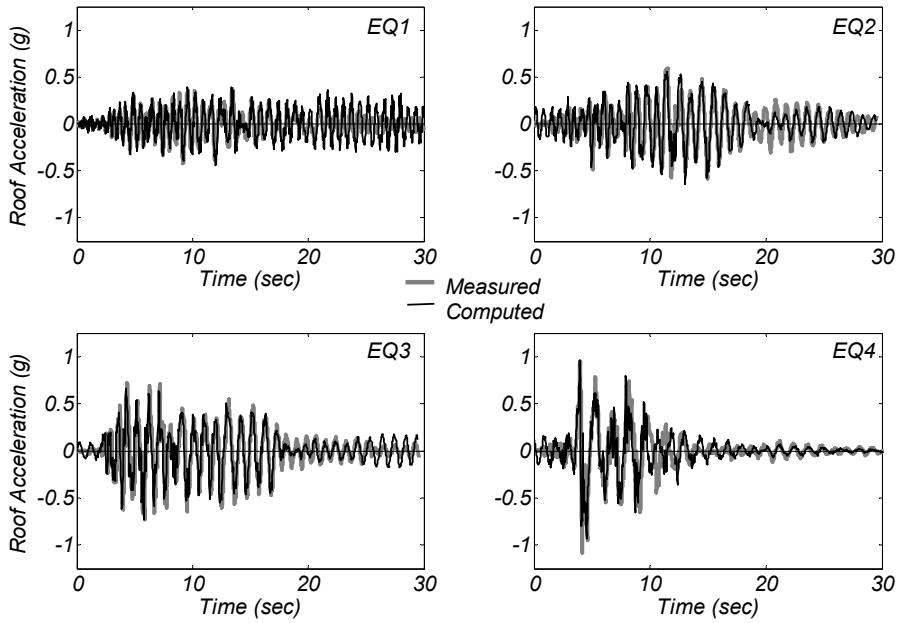

Figure 9.10. Measured and computed roof acceleration time-histories.

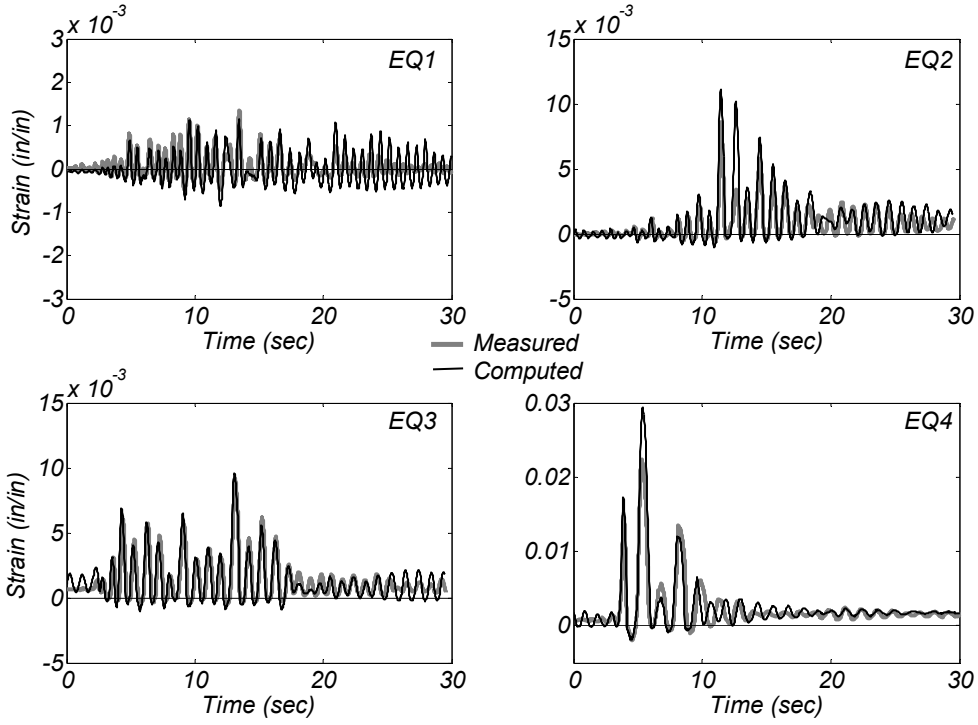

Figure 9.11. Measured and computed strain time-histories at bottom of the West end of web wall.

9.5.3 Envelopes of Key Response Quantities

This section compares the measured versus the computed response in terms of the main response quantities. Figs 9.12 to 9.15 give the comparison between the measured and computed response envelopes of the system moment, shear force, acceleration and displacement for the four EQ tests, respectively. From these figures we can see that the model predicted excellent the main response quantities along the height of the building with maximum difference of the order of 10%.

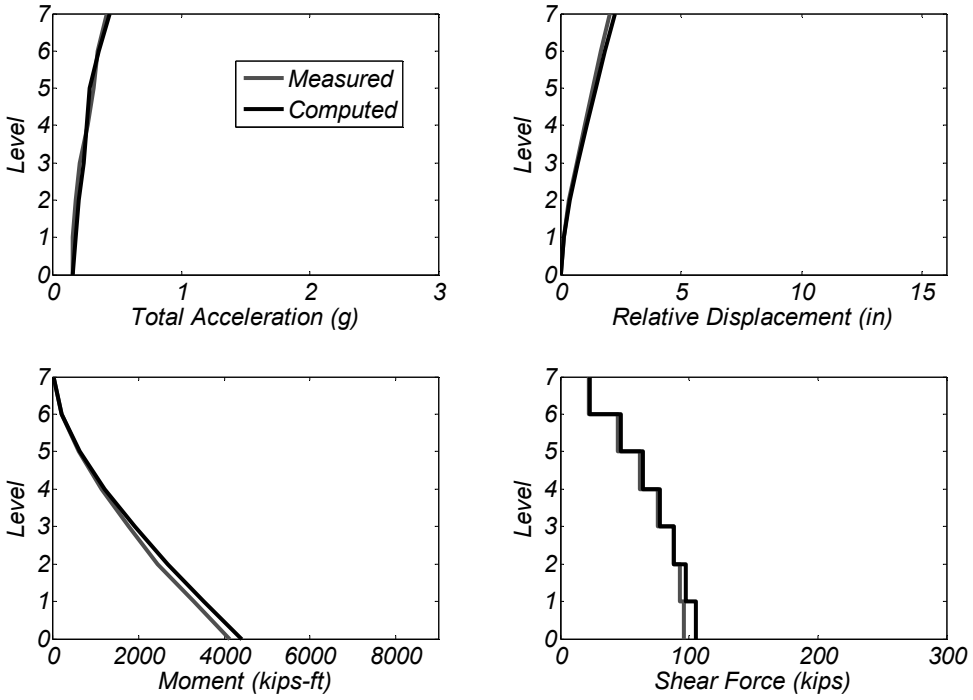

Figure 9.12. EQ1 - Measured versus computed envelopes of key response quantities.

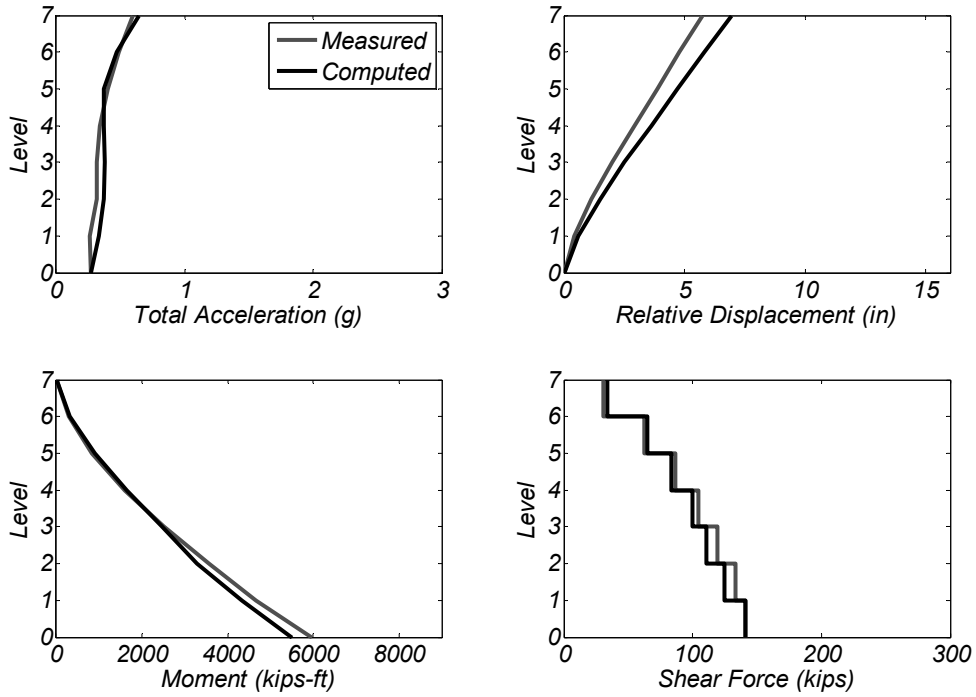

Figure 9.13. EQ2 - Measured versus computed envelopes of key response quantities.

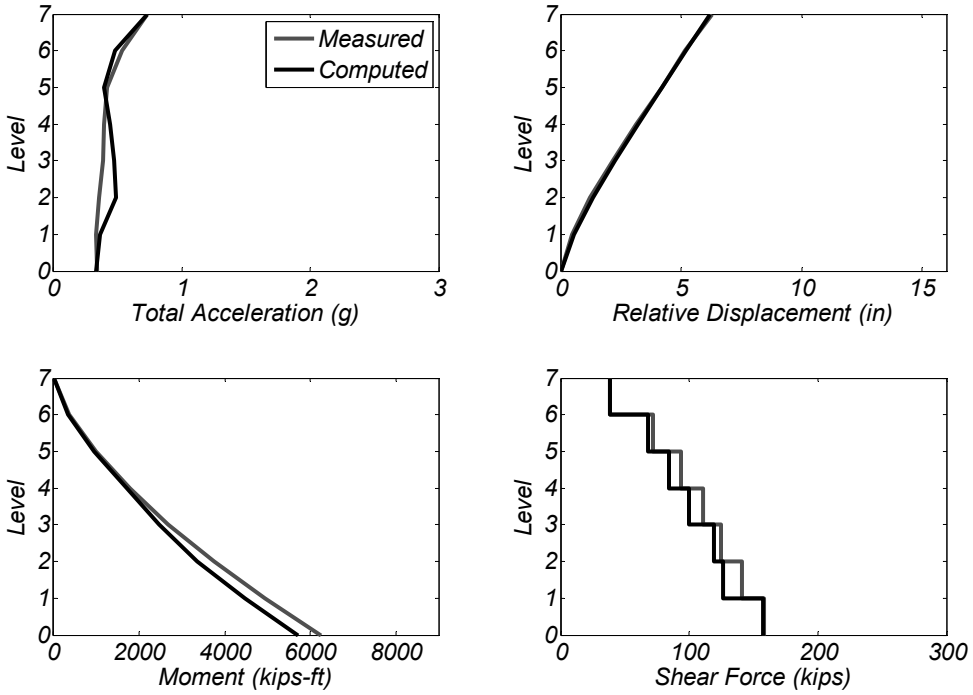

Figure 9.14. EQ3 - Measured versus computed envelopes of key response quantities.

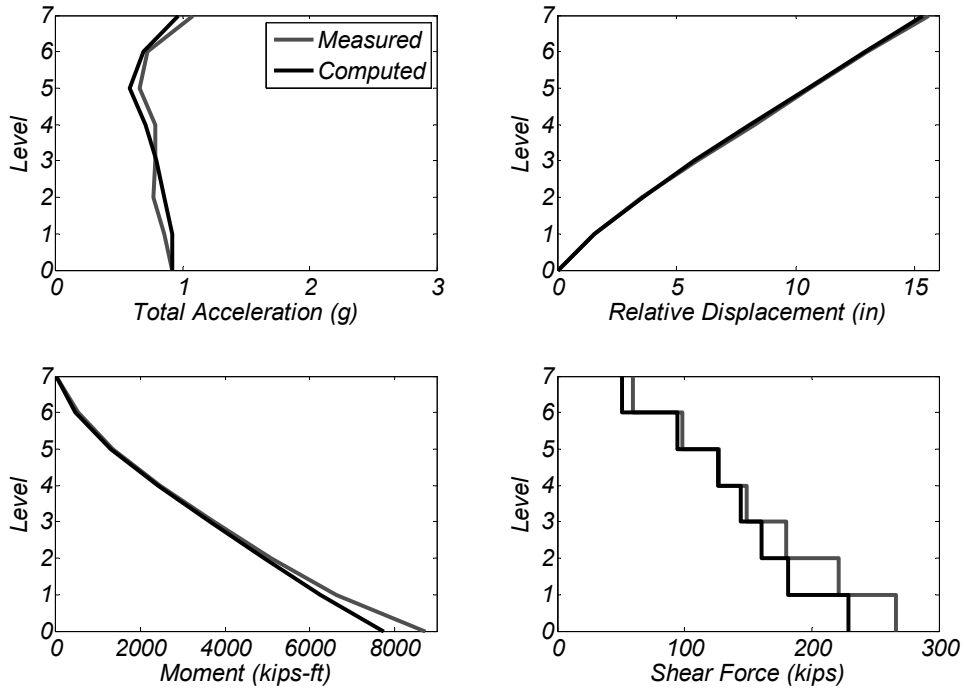

Figure 9.15. EQ4 - Measured versus computed envelopes of key response quantities.

Fig. 9.16 plots the concrete tensile strain profile envelopes of the first floor for all the four earthquakes. Very reasonable was the estimation of longitudinal concrete tensile strains on Level 1 of the web wall with capturing well the spread of plasticity constraint due to the lap splice starting at 62 in. from wall base. Difference is observed in the strain at 40% of the height of level 1 for motions EQ2 to EQ4. It is noted that the estimation of the strain at this elevation is sensitive to the lap-splice length considered in the model. Also for motion EQ4 overestimation of the base strain of the order of 30% is observed

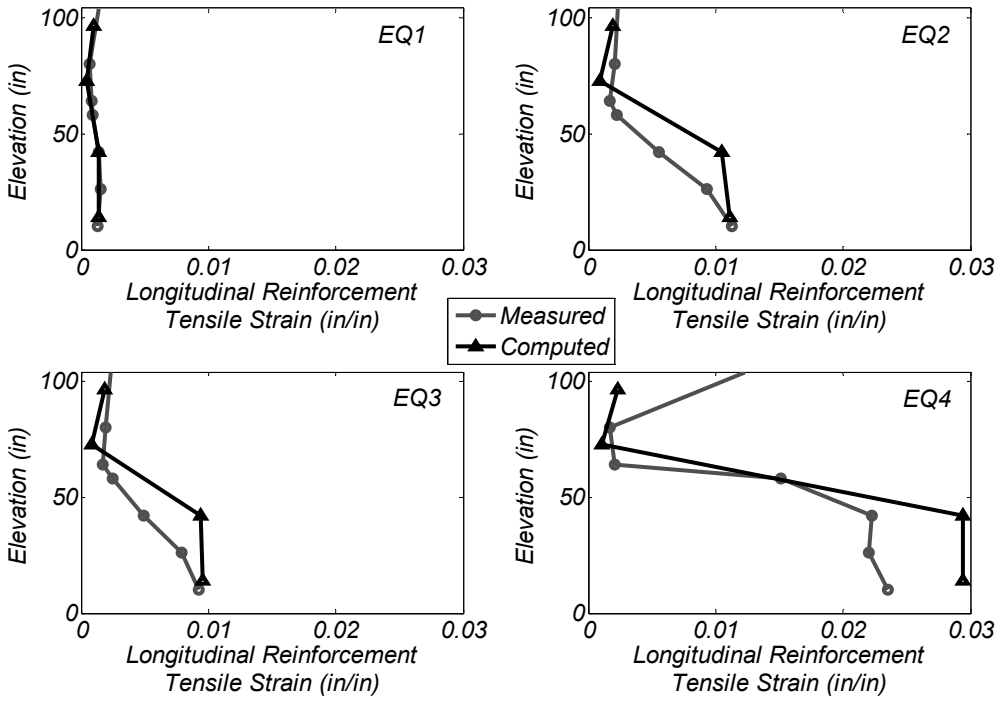

Figure 9.16. Measured versus computed concrete tensile strain envelopes of Level 1- (7 in. from West end of web wall).

9.6 Discussion

The model was able to compute the different levels of response of the building. For this study three distinguished levels of the response, all of them flexural dominated, were determined. The first had to do with nearly elastic response with very limited nonlinear response of the steel and nonlinear response of concrete in tension. The second level of response was characterized by limited nonlinear response with limited inelastic response of the reinforcing steel and extensive inelastic response of the concrete in tension. The third was the level of the response related with events that cause extensive inelastic response. At this range the response of the reinforcing steel is highly nonlinear and the concrete may also yield in compression. An additional stage

would be the stage close to the collapse of the structure which was not considered in this study.

The computed response was very satisfactory in terms of displacements, floor accelerations and internal strains of steel and concrete. The model was efficient both under many cycles of low or moderate amplitude displacement response where limited inelastic response is observed and under highly nonlinear events. Regarding EQ4 the computed response is considered valid only until t=6.0 sec because at this point initiation of failure of the lap splice region was observed during the experimental response. The current model doesn't include any type of modeling of this type of behavior.

Estimation of floor accelerations was more sensitivity in the modeling details of the nonlinear inelastic response. Some artificial high frequency spikes were observed during the computed acceleration response. These were due to the sudden regain of stiffness that takes place in the different concrete elements modeled with the bilinear origin centered hysteretic behavior.

For the computation of the response the effect of system overstrength, as defined before, played a decisive role. Coupling between the walls, the slab and the gravity system caused significant increase of the system strength, stiffness and determined the dynamic response. The effect of system overstrength was efficiently implemented in the 2-D model. Important for this was the accurate computation of the

deformed state at the ends of the web wall. The strut and tie model of the web wall resulted in accurate tension chord growing and compression chord shortening which are required to accurately model the interaction of the web wall with the surrounding elements (slab, flange wall). Fig. 9.17 plots the displacement snapshots of the computed response for the three instants of time of maximum relative lateral displacement response.

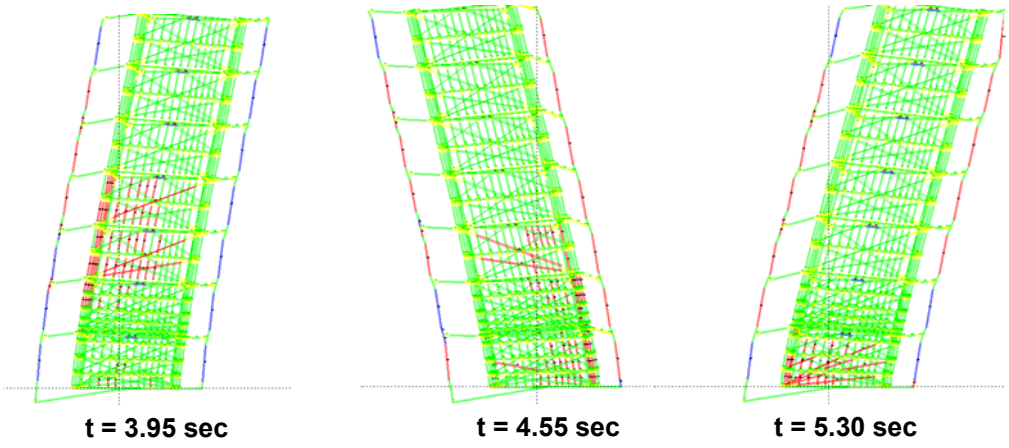

Figure 9.17. Snapshots of dynamic strut and tie model response, during the three peaks of maximum lateral relative displacement.

9.6.1 Modeling of Shear-Flexure Interaction

The proposed approach physically implements the effect of shear-flexure interaction. This is achieved by the yield of the horizontal reinforcement, the loss of concrete tension stiffening in the diagonals as well as the crushing of diagonal concrete in compression. For the specific study case the response of the building was flexural dominated with neither yielding of the shear reinforcement nor crushing of the concrete in the diagonal.

The maximum average tensile strain in the main diagonal of level 1 during tests EQ1 to EQ3 was smaller than 0.1%. For such level of transverse tensile strains the reduction in stiffness and compressive strength of concrete is small (Vecchio and Collins 1986). In test EQ4 where the majority of the nonlinear response occurred with significant tensile chord growing and compressive chord shortening the maximum tensile strain computed in the diagonal of the first floor was 0.45%. For such level of tensile strain (if we assume that a crack will be developed perpendicular to the main diagonal of the wall panel) the reduction of the concrete compressive strength is significant (Vecchio and Collins 1986). Although due to the moderate amount of longitudinal reinforcement of the web wall, the maximum developed concrete compressive force in the main diagonal was not large enough to cause crushing of the concrete with reduced compressive strength.

The effect of flexure-shear interaction is of paramount importance when the response is shear dominated. In these cases yielding of the shear reinforcement and crushing of the diagonal concrete dominate the response and should be modeled. A study is under progress (Panagiotou et al. 2008) where the experimental response of shear critical wall specimens has been reproduced with the previously described approach. During this study the softening of concrete in compression due to normal tensile strain is also implemented.

9.6.2 Modeling of damping

To be able to calibrate properly a damping model based on the experimental results an accurate computational model in terms of stiffness and strength is required. When uncertainties exist regarding the cyclic strength and stiffness of the computational model, small variations in these parameters may be compensated by small variations of damping. This is a critical point in the verification of the experimental response as well as the calibration of a computational model. While the amount of damping in the first mode determined the response in terms of displacements and forces, the amount of damping in the higher modes, and especially on the second mode determined the computation of the floor total accelerations.

This section presents the results of a parametric study to evaluate the effect of initial stiffness Rayleigh damping. Initially the appropriate first mode damping ratio ζ_1 is investigated. This is done since the displacement response is mainly dominated by the first mode of response. After investigating the effect of first mode damping, the higher mode damping will be also investigated. Values of ζ_1 equal to 0.5, 1, 2, and 5% are examined. The analysis with the computational model as described in section 9.4 was conducted for the above damping values. The damping ratios ζ_1 and ζ_2 in the first two modes are used to define the damping.

Figs. 9.18 to 9.21 compare the measured and computed roof displacement time history response for motions EQ1 to EQ4, respectively. Fig.9.18 shows that values of ζ_1 = 2% give the best estimation of the response for all its amplitude range. Smaller

values of ζ_1 overestimate more than 200% the small amplitude displacement response towards the end of the motion (after t = 20 sec). For ζ_1 = 5% underestimation of the higher amplitude response is observed. For motion EQ1, as it will be seen after the presentation of the response for all the four motions, the first mode damping value has the smallest influence in the displacement response.

For input motion EQ2, Fig. 9.19 shows that values of ζ_1 equal to 0.5 and 1% estimate the large amplitude displacement response with less than 10% difference, except a specific excursion in the response a t = 12 sec. Values of ζ_1 equal to 2% and 5% result in more than 30% underestimation of the part of the response with larger amplitude. These values cause also phase shifts of the response. For these values it is noted that after t = 20 sec the smaller amplitude of response result in a different frequency content (higher frequency) of the response in comparison with measured one. For the part of the response with smaller amplitude (after t =2 0 sec) values of ζ_1 equal to 1% give a better estimation of the response.

Fig. 9.20 shows that for motion EQ3, for values of ζ_1 = 0.5 and 1% the computed response better estimates the measured displacement response for the larger amplitude response. Values of ζ_1 equal to 2 and 5% result in more than 40% underestimation of the strongest phase of the response. For the part of the response with smaller amplitude (after t = 25 sec) values of ζ_1 = 0.5% overestimate the displacement response.

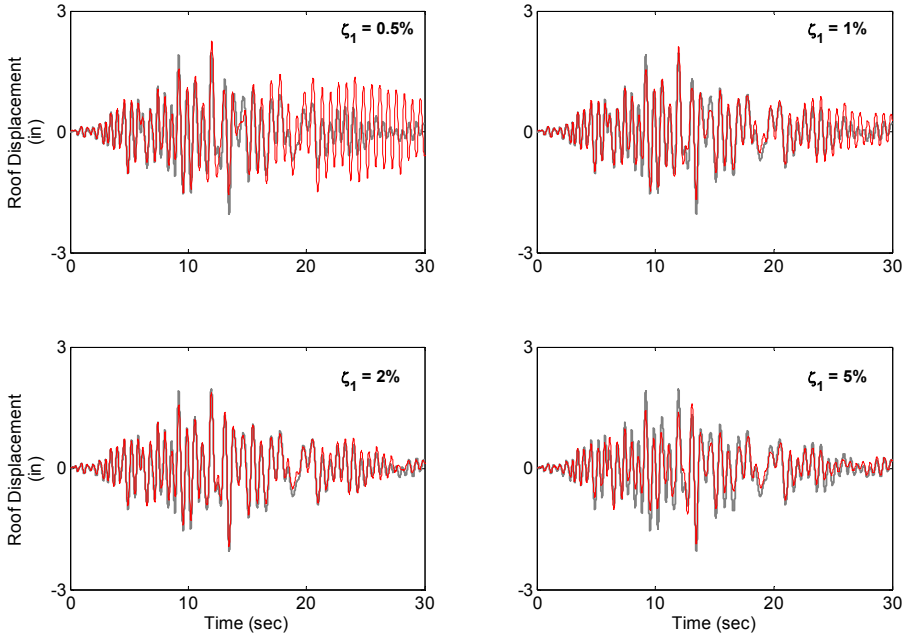

Figure 9.18. Measured and computed roof displacement time history response for motion EQ1 for four values of first mode damping ratio ζ_1 and for $\zeta_2 = 2\%$.

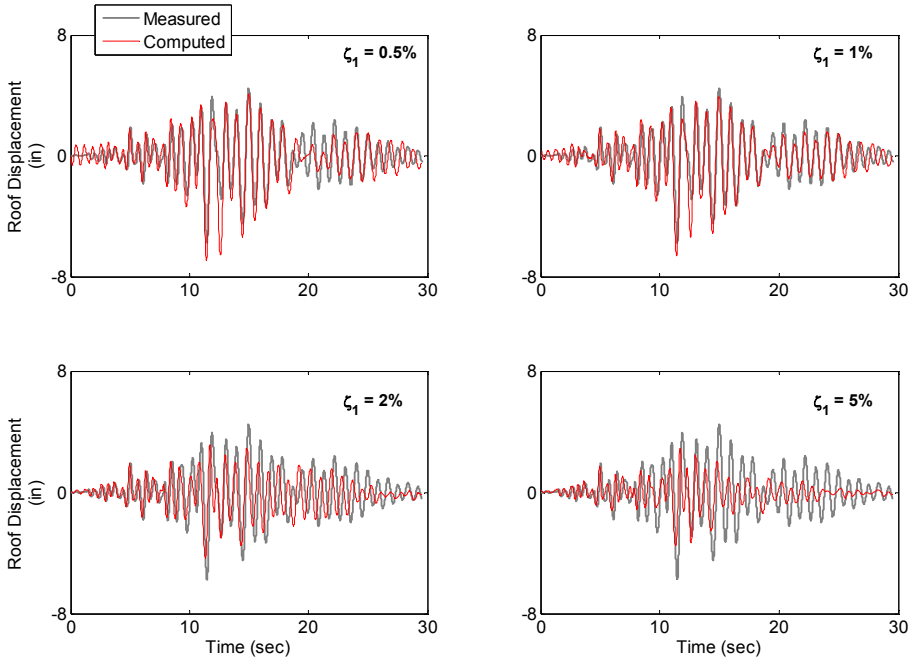

Figure 9.19. Measured and computed roof displacement time history response for motion EQ2 for four values of first mode damping ratio ζ_1 and for $\zeta_2 = 2\%$.

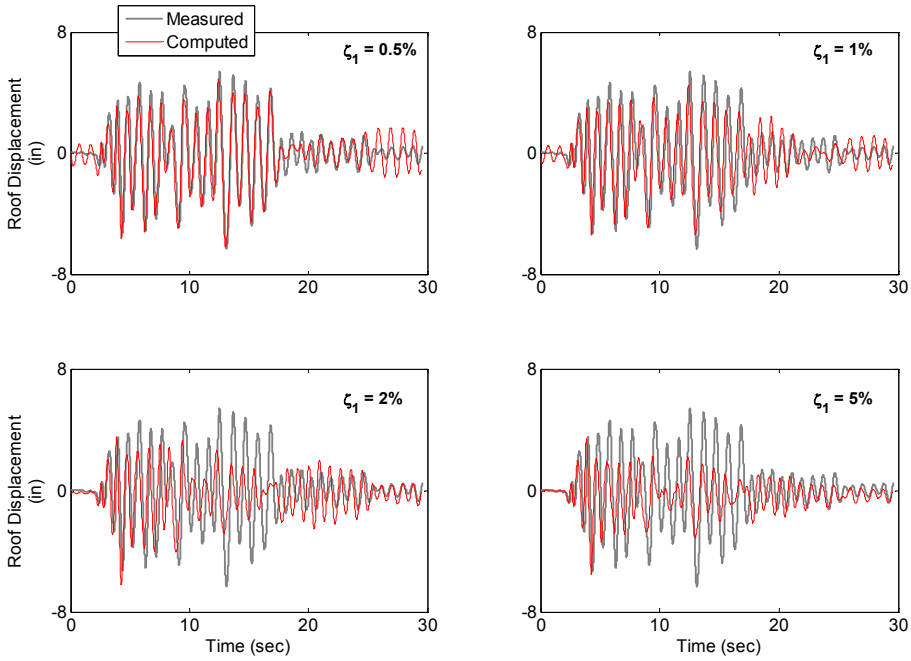

Figure 9.20. Measured and computed roof displacement time history response for motion EQ3 for four values of first mode damping ratio ζ_1 and for $\zeta_2 = 2\%$.

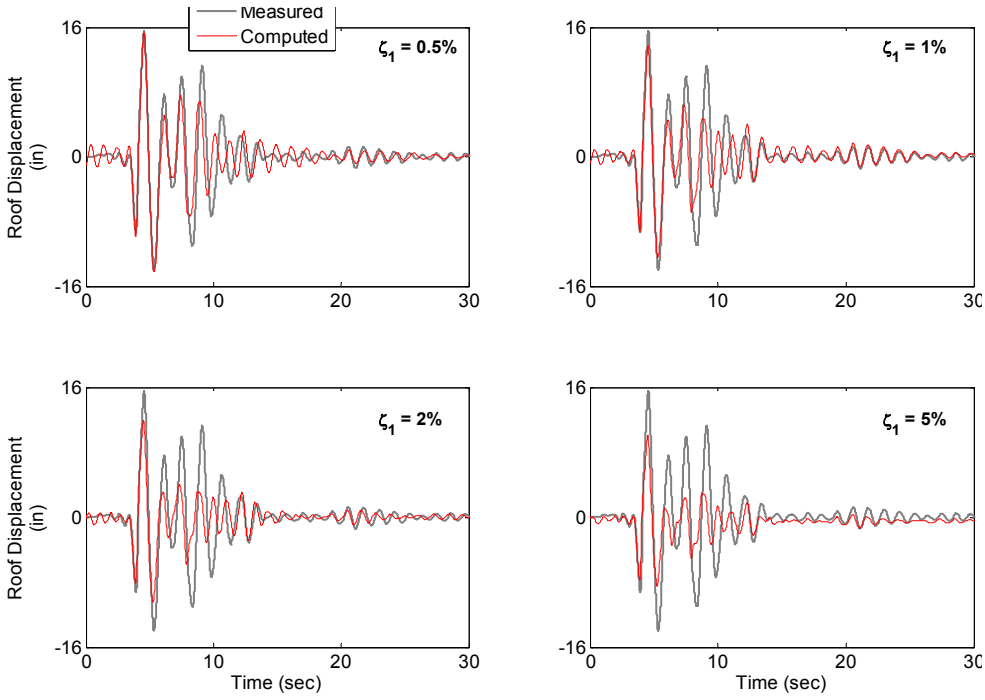

Figure 9.21. Measured and computed roof displacement time history response for motion EQ4 for four values of first mode damping ratio ζ_1 and for $\zeta_2 = 2\%$.

For input motion EQ4, see Fig. 9.21, the best fit of the strong phase of the response is obtained for values of ζ_1 = 0.5 and 1%. Values of ζ_1 equal to 2 and 5% result in over 35% underestimation of the strong phase of the response. It is repeated that the estimation of the response after t = 5.8 sec is not discussed since the model cannot capture the failure of the lap splice regions at the bottom of level two on both ends of the wall. Regarding the part of the response with smaller amplitude, after t = 15 sec, values of ζ_1 = 1% give the best estimation of the response.

The relative lateral displacement envelopes are plotted in Fig. 9.22. This figure compares the measured and computed envelopes for motions EQ1 to EQ4 for the four values of first mode damping. For EQ1 the computed response for ζ_1 equal to 1% and 2% gives the best estimation of the response. For motion EQ2 damping values of ζ_1 smaller than 1% gives the best estimation of the response. For input motion EQ3 we observe that both values of ζ_1=0.5 and 2% give similar envelopes. This is because the displacement envelope is controlled from the response at t = 5 sec, see Fig. 9.20. Although as it can be seen from Fig. 9.20 for ζ_1=2% the response is underestimated for all the other part of the response with larger amplitude. Especially for motions EQ2 and EQ3 where the response is characterized by multiple cycles, different values of damping can result in similar envelopes (controlled from the maximum response) while significant differences exist in the time history response.

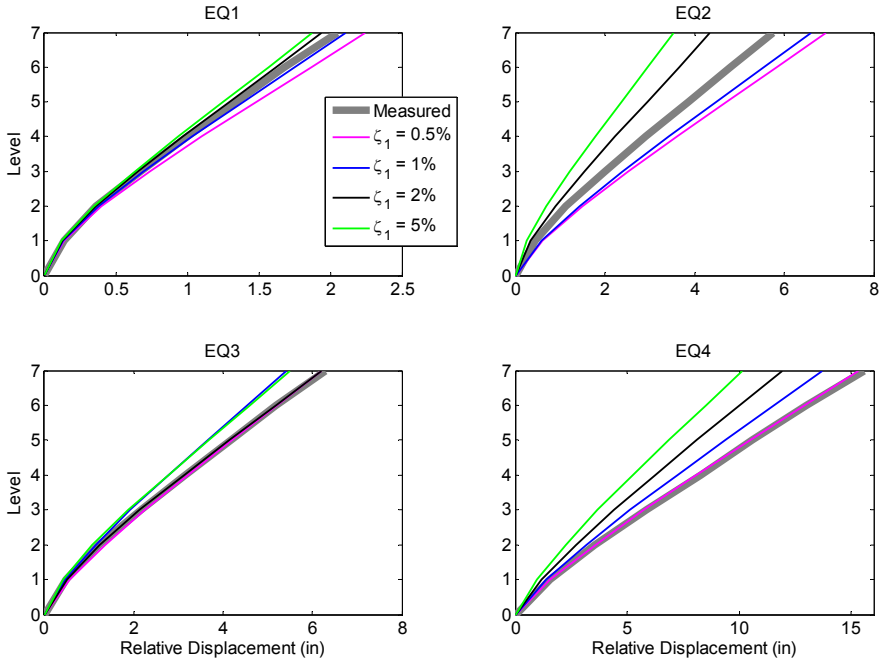

Figure 9.22. Measured and computed relative displacement envelopes for motions EQ1 to EQ4 for four values of first mode damping ratio ζ_1 and for ζ_2 = 2%.

For all motions EQ1 to EQ4 we observe that the small amplitude response with is predicted with larger values of damping. This observation to the opinion of the author should not directly result to the conclusion that for smaller amplitude response the damping is higher. The computation of the small amplitude response is very sensitive to the initial stiffness properties of the model and mainly to the modeling of the initial stiffness of concrete as well as to the history of the computed excitation. It is reminded that in this model the pre-yield stiffness of concrete was modeled linearly.

Having investigated the effect of first mode damping ratio ζ_1 the effect of the second mode damping ζ_2 is now considered. Four values of ζ_2 equal to 0.75, 1, 1.5 and 2% are considered. The smallest value of 0.75% was considered since a value of ζ_2

resulted in computational instability. It is mentioned that due to the type of hysteretic rules used in this model, large spikes in the acceleration response occur when the model regains stiffness. Because of this a minimum value of second mode damping equal to 0.75% was required for the stability of the analysis. In addition the largest value of ζ_2 considered was 2% since for larger values the factor a_0 required to determine the Rayleigh damping was computed negative.

Figs 9.23 to 9.26 compare the measured and computed response for ζ_1=0.5% for four values of ζ_2 for motions EQ1 to EQ4, respectively. Fig. 9.23 shows that when ζ_2 =0.75% small amplitude response is overestimated by more than 300% for motion EQ1. It is noted that value of ζ_2 equal to 2% result in larger small amplitude in response in comparison with the case of ζ_2 = 1%.

Fig. 9.24 and 9.25 shows that for motions EQ2 and EQ3, respectively, values of ζ_2 closer to 2% give a better estimation of the response for all the range of amplitude with no significant sensitivity of the response to values of ζ_2 between 1 and 2%. Fig. 9.26 shows that for motion EQ4 the second mode damping values ζ_2 from 0.75 to 2% result in minor differences in the computed response until t = 5.8 sec which is considered herein.

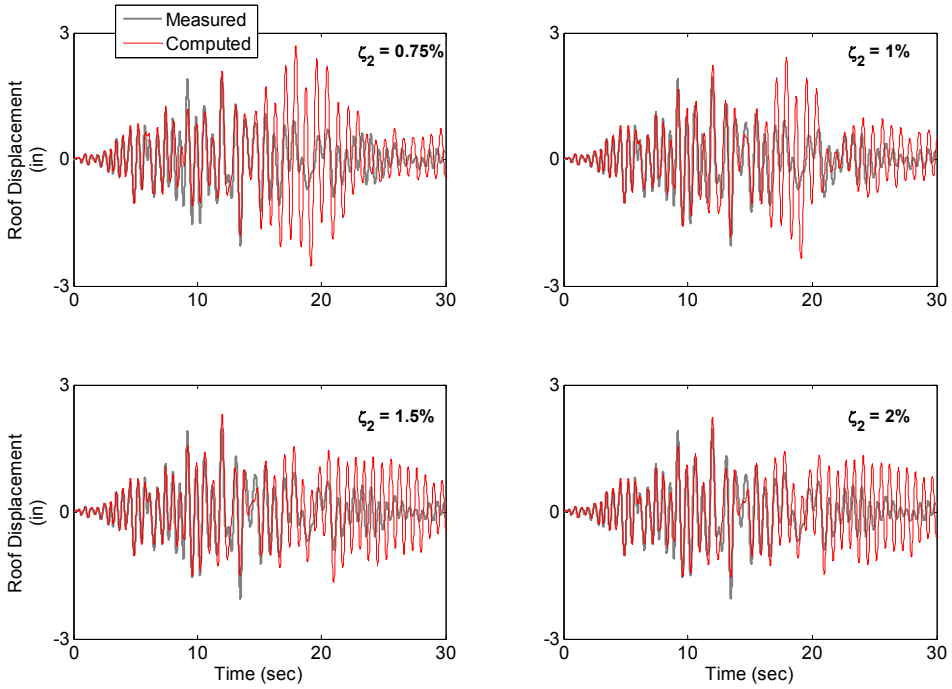

Figure 9.23. Measured and computed roof displacement time history response for motions EQ1 for four values of second mode damping ratio ζ_2 and for ζ_1 = 0.5%.

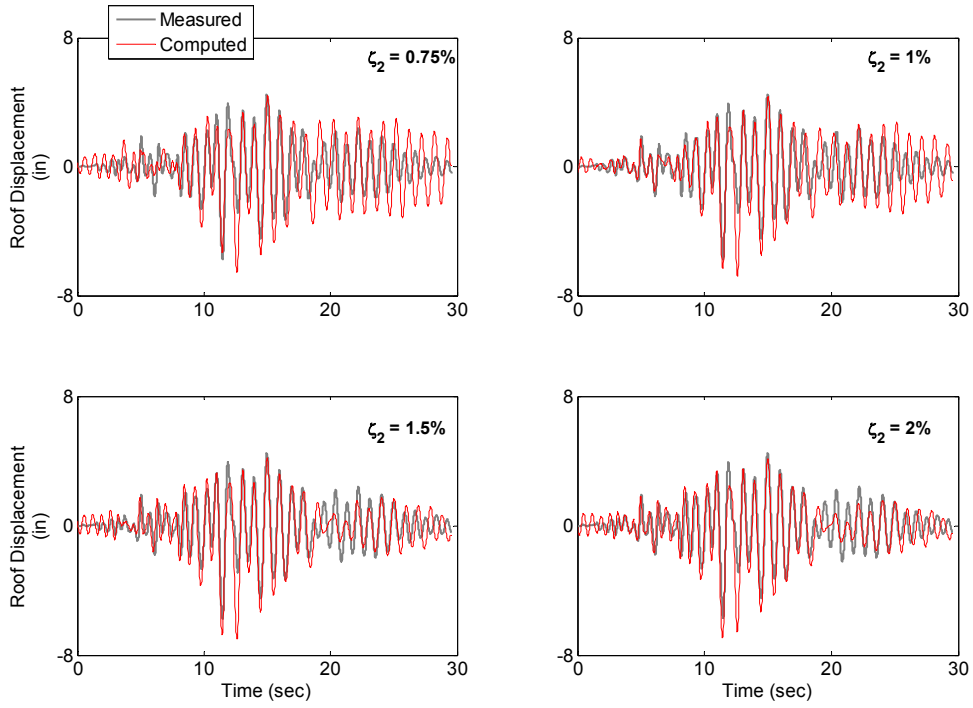

Figure 9.24. Measured and computed roof displacement time history response for motions EQ2 for four values of second mode damping ratio ζ_2 and for ζ_1 = 0.5%.

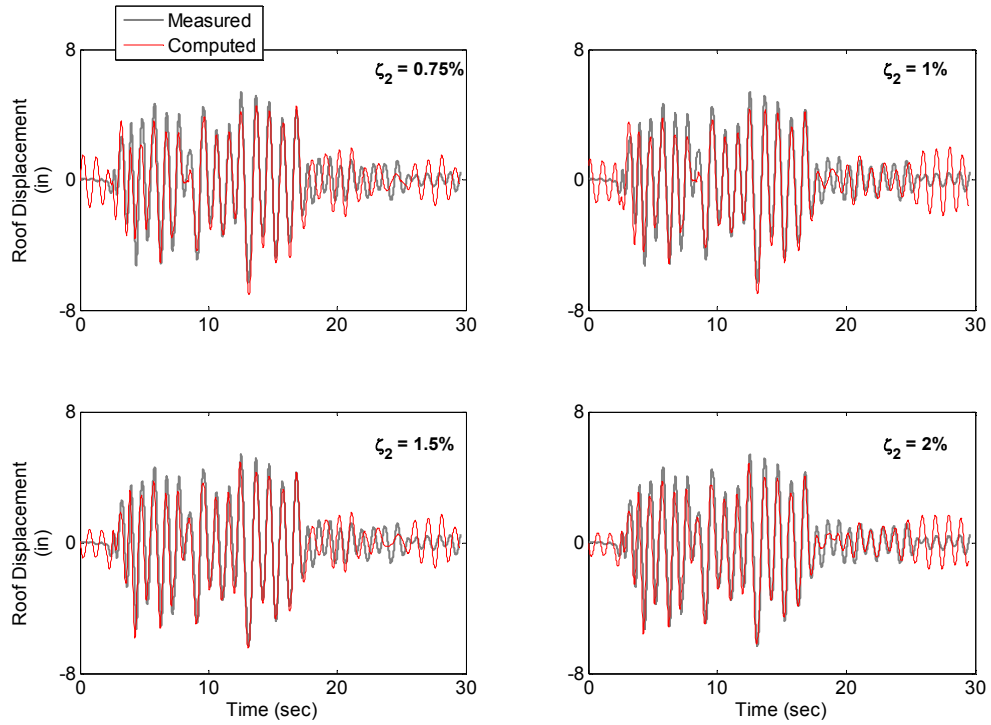

Figure 9.25. Measured and computed roof displacement time history response for motion EQ3 for four values of second mode damping ratio ζ_2 and for ζ_1 = 0.5%.

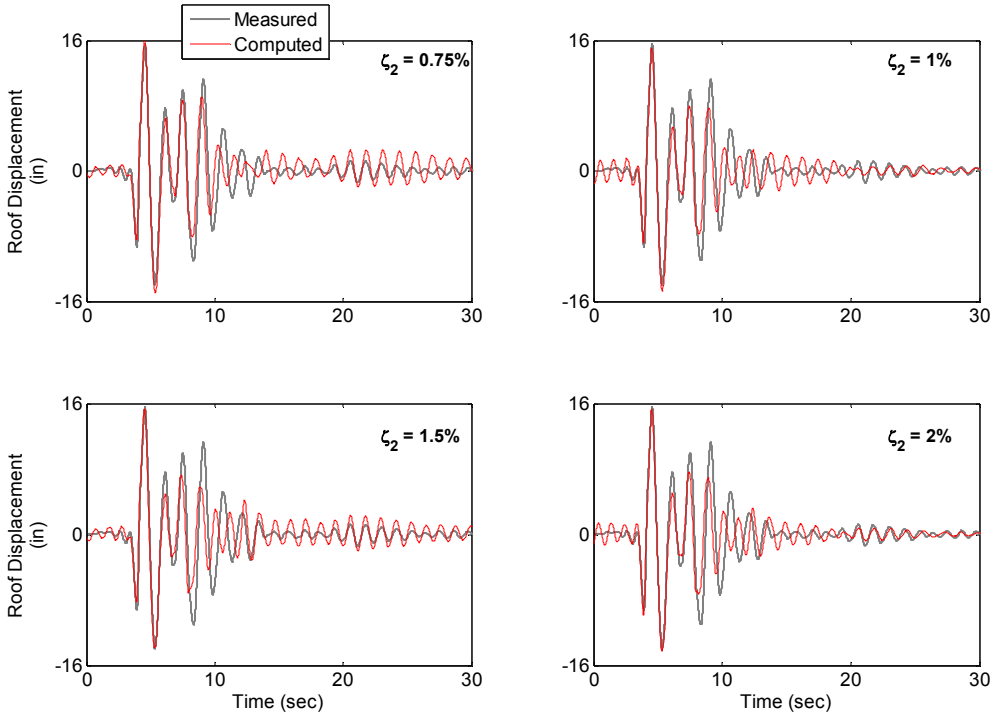

Figure 9.26. Measured and computed roof displacement time history response for motion EQ4 for four values of second mode damping ratio ζ_2 and for ζ_1 = 0.5%.

In terms of displacement envelope response Fig. 9.27 shows that for the small amplitude motion EQ1 the difference is the largest and of the order of 25%. For motions EQ2 and EQ3 the effect of the second mode damping on the response is smaller for the range of values ζ_2 considered. Some difference of the order of 15% is observed for motion EQ3.

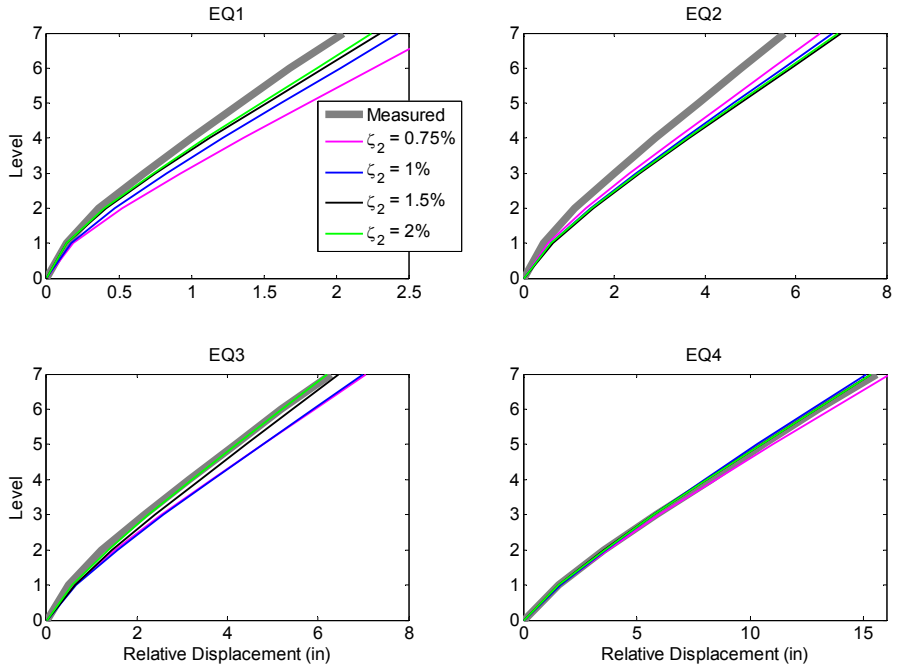

Figure 9.27. Measured and computed relative displacement envelopes for motions EQ1 to EQ4 for four values of second mode damping ratio ζ_2 and for ζ_1 = 0.5%.

Finally the additional cases of $\zeta_1 = \zeta_2$ equal to 1, 2, and 5% as well as the case ζ_1 = 1% and ζ_2 = 2% are considered. Figs. 9.28 to 9.31 present the comparison of the measured and computed roof displacement response for these cases for motions EQ1 to EQ4, respectively.

For motion EQ1, see Fig. 9.28, the cases of $\zeta_1 = 1\%$, $\zeta_2 = 2\%$ and $\zeta_1 = \zeta_2 = 2\%$ give the best estimation of the response. The cases with $\zeta_1 = 5\%$ underestimate the response even for this case of very small amplitude response. For motions EQ2 and EQ3, see Fig. 9.29 and 9.30, the cases with values of ζ_1 equal to 0.5 and 1% give the best estimation of the response. The cases with $\zeta_1 = 2$ and 5% underestimate the response and result in phase shift of the response. Similar conclusions are drawn for motion EQ4, see Fig. 9.31.

Fig. 9.32 compares the measured and computed response envelopes. For motion EQ1 the smallest sensitivity in the damping values exists. For this case, damping value in the second mode equal to 1% result in overestimation of the response of the order of 25%. For motion EQ2 values of damping equal or larger to 2% result in underestimation of the response of more than 30%. Small sensitivity to the damping values for the envelope response is observed for motion EQ3. Although is reminded that for this motion the envelope is the result of an instantaneous response while different values of damping result in large difference in the computation of the response, see Fig. 9.31. Finally for motion EQ4 values of damping equal or larger to 2% result in underestimation of the response of more than 30%. It is noted also that the cases of $\zeta_1 = \zeta_2 = 5\%$ and $\zeta_1 = \zeta_6 = 5\%$ result in about 15% difference for motions EQ2 and EQ4.

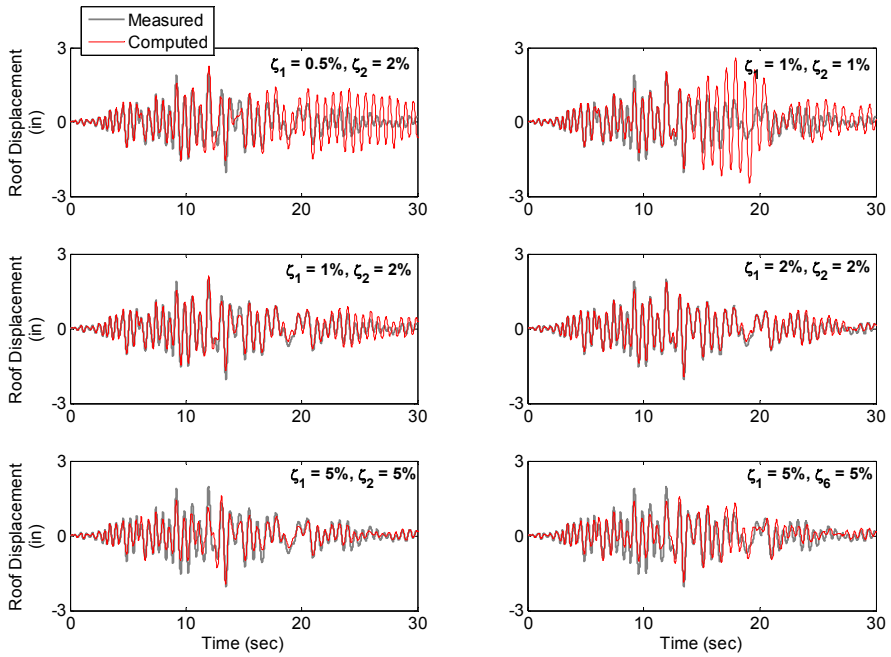

Figure 9.28. Measured and computed roof displacement time history response for motion EQ1 for six combinations of values of first and second mode damping ratio ζ_1 and for ζ_2.

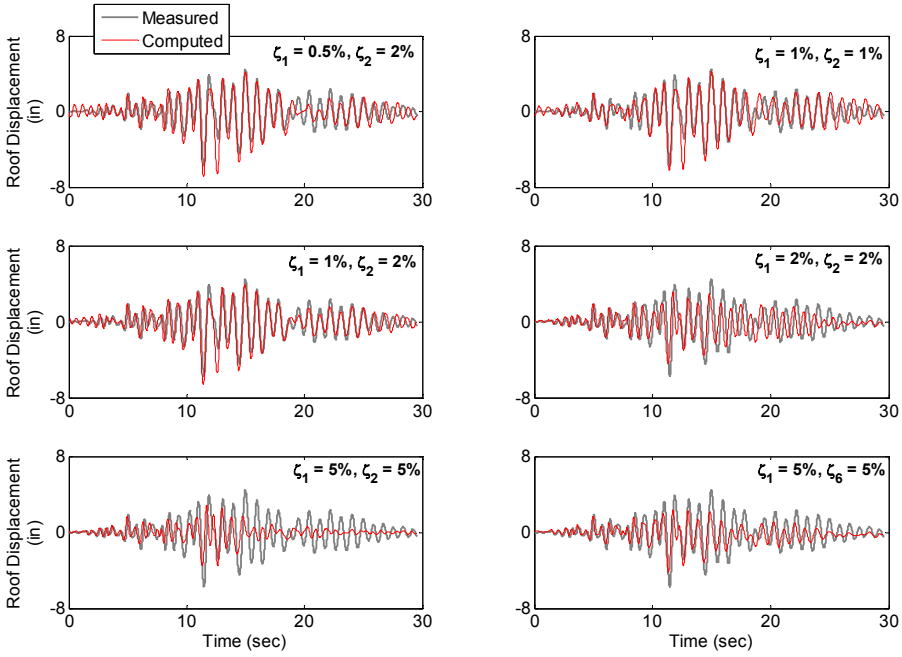

Figure 9.29. Measured and computed roof displacement time history response for motion EQ2 for six combinations of values of first and second mode damping ratio ζ_1 and for ζ_2.

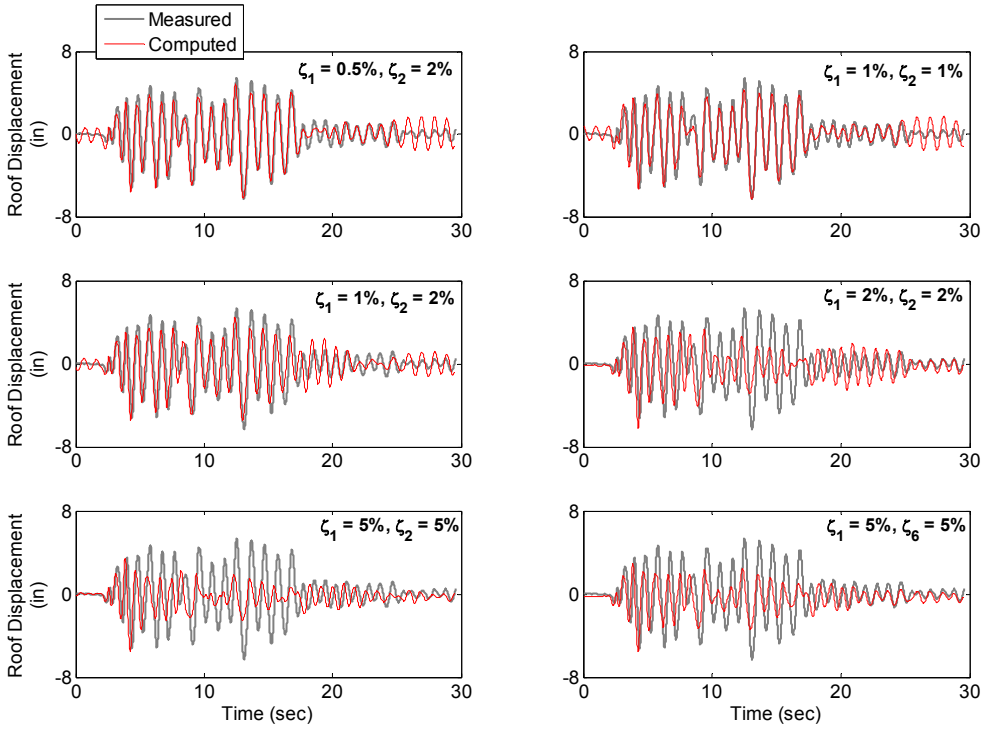

Figure 9.30. Measured and computed roof displacement time history response for motion EQ3 for six combinations of values of first and second mode damping ratio ζ_1 and for ζ_2.

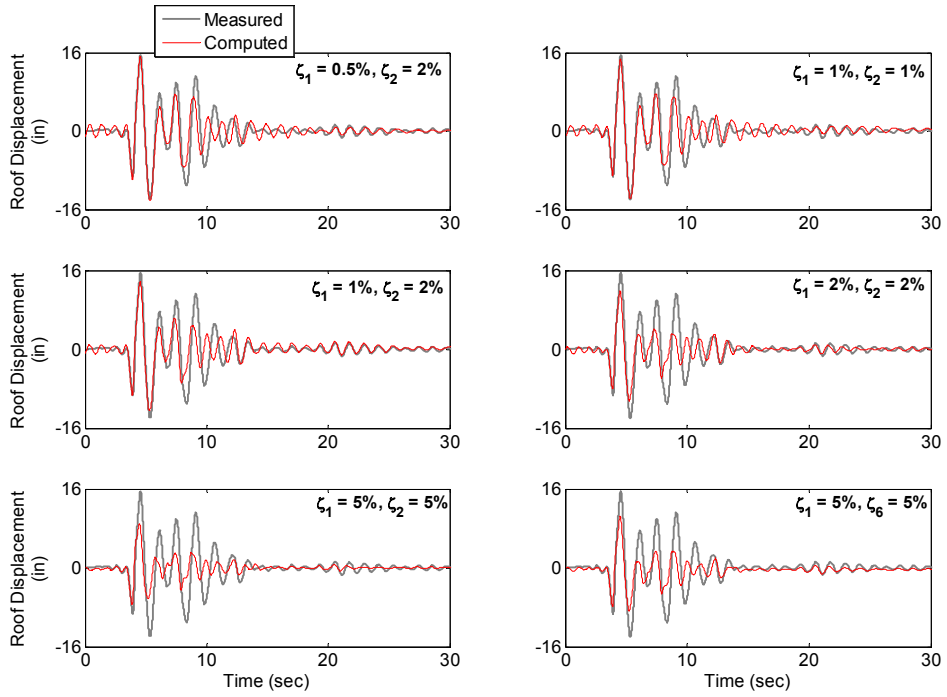

Figure 9.31. Measured and computed roof displacement time history response for motion EQ3 for six combinations of values of first and second mode damping ratio ζ_1 and for ζ_2.

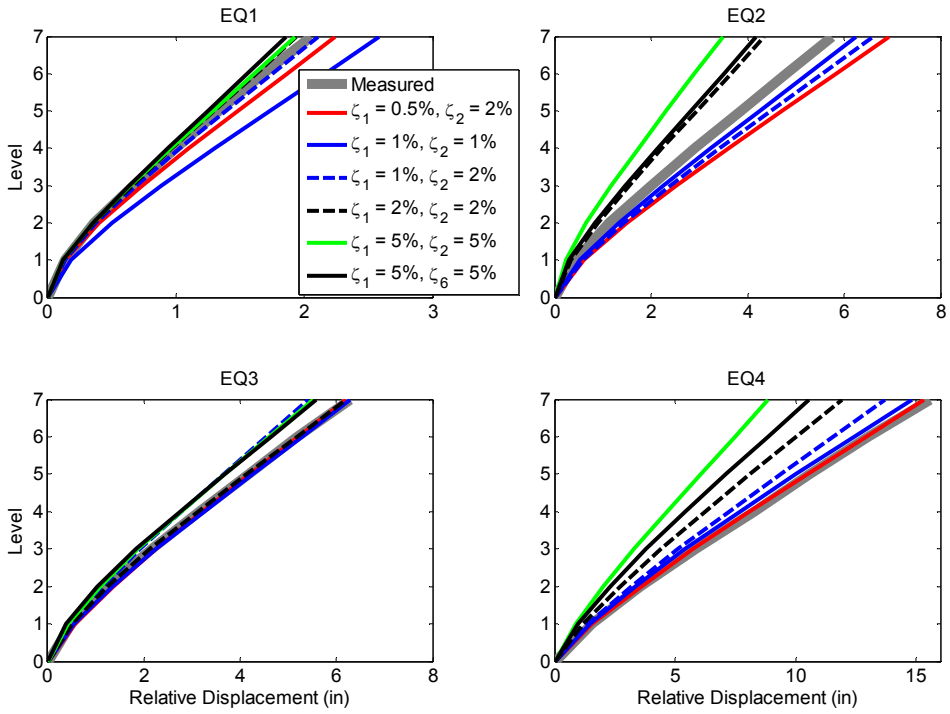

Figure 9.32. Measured and computed roof displacement time history response for motion EQ3 for six combinations of values of first and second mode damping ratio ζ_1 and for ζ_2.

The main conclusion from this parametric study is that for damping values in the first two modes equal or larger than 2%, significant underestimation of the response of more than 30% is observed for the levels of the response characterized from limited nonlinearity to highly nonlinear response.

9.6.3 Modeling of Concrete – Effect of History of Excitation

The computation during lower amplitude earthquakes (EQ1 to EQ3) was sensitive to the value of concrete modulus of elasticity E_c and to the behavior of concrete in tension. The effect of loss of tension stiffening in terms of tensile strength and rate of softening is predominant. For such level of response the initiation point and the path of any non-linearity like the loss of tension stiffening is important especially

under earthquake excitations of multiple cycles. The response during test EQ4 was characterized by highly nonlinear response. The maximum nonlinear response during EQ4 was affected from the history of the response during tests EQ1 to EQ3. The maximum displacement response during tests EQ1 to EQ3 determined the system's strength and stiffness at initiation of test EQ4. This happens due to the effect of loss of tension stiffening on the tensile strength and stiffness of concrete. For the study case considered adequate modeling of concrete in tension was very important because the structure was imposed to more than 30 cycles of small and moderate amplitude of excitation. The effect of excitation history is more extensively discussed in Panagiotou et al. 2007.

9.7 Conclusions

The computational model for verification of the experimental response of the UCSD 7-story full-scale building slice was presented. A nonlinear strut and tie truss approach was used to model the web wall, which was the lateral force resisting element of the building. Simple piecewise linear rules were used to model the hysteretic behavior of the different elements. The model gave excellent results in terms of displacements, forces, accelerations and material strains. The following conclusions are drawn:

1. Non linear strut and tie truss models can be a valuable tool to compute the nonlinear dynamic response of buildings with load bearing walls. The analytical force displacement results of the elements in such models can be directly used in design of RC walls.

2. The proposed approach directly implements the effect of shear-flexure interaction in structural walls.
3. 3-D effects of coupling between the walls, the slab and the gravity system were efficiently implemented in the 2-D model and were decisive for the accurate computation of the system's strength, stiffness and thus of its dynamic response.
4. Computation of the response in the limited nonlinear range showed sensitivity to the modeling of concrete hysteretic behavior in terms of stiffness, tensile strength and loss of tension stiffening.
5. The response history affects computation of the future response due to the effect of loss of concrete tension stiffening.
6. Small amount of viscous damping was required in the first mode for the analytical reproduction of the experimental response.

CHAPTER 10

10. SUMMARY AND RECOMMENDATIONS

10.1 Summary

A research work was conducted at University of California San Diego (UCSD) on the i) seismic design, ii) experimental response and iii) computational modeling of medium- and high-rise RC wall buildings.

In the first part a displacement-based seismic design method for RC wall buildings for use within performance-based design was developed. Capacity design was used to control the mechanism of inelastic deformation. Based on principles of plastic analysis and structural dynamics the new formulation computed the effects of kinematic system overstrength and of the higher modes of response. Equal emphasis was given to displacement, force and acceleration demand parameters. The ground motion destructiveness potential was also determined. The method was validated with the experimental response of the UCSD full-scale 7 story building. In addition a dual plastic hinge design concept for improving the performance and optimizing the construction of high-rise core-wall buildings was presented.

The second part presented the experimental research program, with extensive shake table tests, of a full-scale 7-story reinforced concrete wall building slice, that was conducted at UCSD. The base shear coefficient obtained by the proposed method, of the first part of the research work, described above was 50% of that required by the

equivalent static method prescribed by the ASCE-7 code. In spite of the reduced amount of longitudinal reinforcing steel, all performance objectives were met. The response of the building was significantly influenced, as expected, by the interaction of the main lateral force resisting wall with other structural elements (kinematic system overstrength) and by the higher modes of response.

Finally the third part presented a dynamic nonlinear strut-and-tie modeling approach developed for the analysis and evaluation of damage limit-states in reinforced concrete walls. The modeling approach was verified with the response of the UCSD 7-story building test. This approach was able to physically implement the effect of flexure-shear interaction in RC walls.

10.2 Contribution

10.2.1 Relation of Linear and Nonlinear Displacement Demand of SDOF Oscillators subjective to Impulsive Excitation.

The main contribution of this part was the determination of the relation of the maximum displacement demand of a linear and nonlinear SDOF oscillator, of same initial period, subjective to sinusoidal impulsive excitation. This type of excitation can represent many of the characteristics of strong near-fault ground motions. Nonlinear SDOF oscillators of different hysteretic behavior, corresponding to different structural systems were considered. For all cases the relation between the linear and nonlinear displacement demand depends mainly on the ratio T / T_P of the initial period of the SDOF oscillator to the period of the sinusoidal pulse. Knowing this the elastic

response spectrum can be modified accordingly to estimate nonlinear displacement demand.

10.2.2 Kinematic System Overstrength in RC Wall Buildings.

Based on principles of structural mechanics and plastic analysis the effect of interaction between the walls, the slabs and the gravity system in RC wall buildings was determined and quantified. Simple expressions of the additional lateral forces, bending moments, shear forces and floor accelerations due to the effect of framing were presented. In this way i) the maximum shear force required for the capacity design of the walls is determined and ii) the increase of the system moment capacity is estimated and can be employed to reduce the required flexural strength of the walls.

10.2.3 Effect of Higher Modes in RC Wall Buildings.

Based on principles of structural dynamics and the notion of instantaneous modal characteristics the effect of second and higher modes on the response of cantilever wall buildings was determined. Different systems in terms of location of nonlinear response were considered. Second mode response is not significantly affected by the development of plasticity at the base of the walls. With consideration of the second mode of response, in a very simple way, the force and acceleration demand along the height of RC wall buildings can be very well estimated in the nonlinear range.

10.2.4 A Dual Plastic Hinge Concept for the Seismic Design of High-Rise RC Wall Buildings.

The proposed dual plastic hinge design concept, in which plastic hinges are allowed to form at the wall base and near mid-height while ensuring elastic response elsewhere, was found to have significant advantages: reduction in the amount of longitudinal reinforcement when compared to the EC8, NZS-3101 and NBCC designs, and ease of detailing along most of the height. This concept can be easily implemented in design, bringing a reduction in the amount of longitudinal reinforcement and of transverse reinforcement in a significant portion of the walls.

10.2.5 Displacement Based Design Approach for RC Wall Buildings.

A displacement-based seismic design method for use within performance-based was developed. The method explicitly considered two performance levels. It considered the effects of ground motion destructiveness potential in terms of displacement and force demands. The effects of kinematic system overstrength and of the higher modes were explicitly considered to determine shear force and floor acceleration demand.

10.2.6 Experimental Testing of RC Wall Buildings.

The experimental research program verified the seismic design of medium-rise RC wall buildings designed with the developed displacement based design approach, resulting in 50% smaller base shear coefficient. The shake table tests of the full-scale specimen provided a unique set of data for the understanding of nonlinear dynamic

response of such building systems. The effects of kinematic system overstrength and of the higher modes were clearly observed-measured in the test response.

10.2.7 Dynamic Nonlinear Strut-and-Tie Approach Modeling of RC Wall Buildings.

A dynamic nonlinear strut-and-tie modeling approach was developed for the analysis and evaluation of damage limit-states in reinforced concrete walls. The modeling approach was verified with the response of the UCSD 7-story building test. Excellent results were obtained in terms of displacements, forces, accelerations and strains. This approach was able to physically implement the effect of flexure-shear interaction in RC walls and can be directly used for design.

10.3 Future Work

The work presented in this dissertation combined elements of structural design, testing and analysis. All these three substances are required to develop reliable models for simulation, prediction, control and design of structural and nonstructural response.

In the framework of performance-based design more specific determination of structural and nonstructural performance for different levels of excitation will be required in the future. In addition to the life safety and collapse prevention performance objectives under strong excitation, which are fundamental considerations of traditional seismic design, the limitation of structural and non structural damage under excitations of moderate intensity will be of increased interest.

The development of reliable models for the prediction of structural and non-structural response, for different levels of excitation, will require the consideration of the complete soil-foundation-superstructure system. This creates a challenging field for future research with the goal to incorporate the nonlinear soil-foundation-superstructure interaction (SFSI) in performance-based seismic design. The term nonlinear SFSI refers to the nonlinear soil behavior, the nonlinear foundation response, and foundation uplift.

In addition to the characterization of the soil-foundation-structure system the earthquake ground motion destructiveness potential for different intensities and different SFS systems should be determined. The destructiveness potential of the ground motion should be studied not only in terms of displacement demand but also in terms of developed forces and floor accelerations.

In addition to the structural wall systems studied in this dissertation, extended study of frame and especially of frame-wall dual systems may be required. In an attempt to limit structural and nonstructural damage and improve performance the theoretical and experimental response of innovative structures like rocking systems, systems incorporating un-bonded post-tensioning and systems with supplemental damping devices will be of increased interest.

Lastly in the field of analysis of RC structures, efficient modeling approaches for cases where the flexure-shear interaction is predominant will be required. As an

example analysis of high-rise core-wall structures with openings is a case where significant room for improvement exists.

REFERENCES

Abrahamson, N.A. (2000). "Effects of Rupture Directivity on Probabilistic Seismic Hazard Analysis". Proceedings of the 6th International Conference on Seismic Zonation, Palm Springs, Earthquake Engineering Research Institute.

ACI 318-05. (2005). "Building Code Requirements for Structural Concrete and Commentary", ACI Committee 318, Farmington Hills, 430 pp.

Alavi, B. and Krawinkler, H. (2000). "Design Considerations for Near-Fault Ground Motions". Proceedings of the U.S. – Japan Workshop on the Effects of Near-Fault Earthquake Shaking, San Francisco, March 20-21.

ASCE 7-2005. (2006). "Minimum Design Loads for Buildings and Other Structures", ASCE/SEI 7-05, American Society of Civil Engineers, Reston, VA.

ATC-40. (1996). "Seismic Evaluation and Retrofit of Concrete Buildings". Redwood City, California.

Bertero, V.V., Atkan, A.E., Charney, F. and Sause, R. (1984). "Earthquake Simulator Tests and Associated Experimental, Analytical and Correlation Studies of One-Fifth Scale Model". in Earthquake Effects on Reinforced Concrete Structures, U.S.-Japan Research, ACI Publication SP-84, American Concrete Institute, Detroit, , pp. 375-424.

Bertero, V.V., Mahin, S.A., and Herrera, R.A. (1978). "Aseismic Design Implications of Near Fault San Fernando Earthquake Records", Earthq. Engrg. and Struc. Dynamics, 6(1), 31-42.

Blakeley R.W.G., Cooney R.C and Megget L.M. (1975). "Seismic Shear Loading at Flexural Capacity in Cantilever Wall Structures". Bulletin New Zealand National Society Earthquake Engineering, 8, 278–290.

Bock, Y., Panagiotou, M., Yang, F., Restrepo, J.I. and Conte, J.P. (2006). "Shake Table Tests of a Full Scale Reinforced Concrete Wall Building: Real Time 50 Hz GPS Displacement Measurements". 8NCEE Conference, San Francisco, CA, USA.

Carr, A.J. (1998). "Ruaumoko – A program for Inelastic Time-History Analysis". Department of Civil Engineering, University of Canterbury, New Zealand.

Cervenka, V., and Gerstle, K.H. (1971). "Inelastic Analysis of Reinforced Concrete Panels: Theory." Publ. IABSE, 31 (11), 31–45.

Chaudhuri S.R. (2007). "Change in Instantaneous Eigenproperties due to Yielding of a Structure". Journal of Sound and Vibration. Vol. 312, 2008; 754–768.

Chopra, A.K. and Chintanapakdee C. (2001). "Comparing Response of SDOF Systems to Near-Fault and Far-Fault Earthquake Motions in the Context of Spectral Regions". Earthquake Engineering and Structural Dynamics, Vol. 30, Issue 3, 417-442.

Chopra A.K. (2001). "Dynamics of Structures: Theory and Applications to Earthquake Engineering". Prentice Hall, Upper Saddle River, NJ.

Coelho E., Fischinger M., Campos Costa A., Falcao Silva M.J. and Kante P. (2006). "Shaking Table Tests on Thin Lightly Reinforced H-Shaped Structural Wall", 1st ECEES, Geneva, Paper No. 642.

Comité Euro-International du Béton/Fédération Internationale de la Précontrainte. (1993). CEB-FIP model code 1990: Design code, Thomas Telford, London, 437.

Coull A.A. and Hag E.L. (1975). "Effective Coupling of Shearwalls by Floor Slabs". ACI Journal, Vol. 72, issue 8.

Derecho A.T., Ghosh S.K., Iqbal M., Fintel M. (1979). "Strength, Stiffness, and Ductility Required in Reinforced Concrete Structural Walls for Earthquake Resistance". ACI Journal. Vol. 76, No. 8, 875-896.

Eberhard M.O., Sozen. M.A. (1993). "Member Behavior-Based Method to Determine Design Shear in Earthquake-Resistant Walls". Journal of Structural Engineering, Vol. 119, No 2, 619-640.

EC8: Design of Structures for Earthquake Resistance. (2004). European Committee for Standardisation: Brussels, Belgium.

Elgamal A.-W.M., Abdel-Ghaffar A.M., Prevost J.H. (1985). "Elasto-plastic Earthquake Shear-Response OF One-dimensional Earth Dam Models". Earthquake Engineering and Structural Dynamics, Vol. 13, 5, 617-633.

Englekirk, R.E. (2003). "Seismic Design of Reinforced and Precast Concrete Buildings". John Wiley & Sons, Inc., Hoboken, New Jersey.

Federal Emergency Management Agency (FEMA). (1997). "NEHRP Guidelines for the Seismic Rehabilitation of Buildings (FEMA 273)". Prepared by the Applied Technology Council. Washington, D.C.

Feenstra, P.H., and de Borst, R. (1993). "Aspects of Robust Computational Modeling for Plain and Reinforced Concrete." Heron, 38 (4), 5–26.

FEMA 356. (2000). "Prestandard and Commentary for the Seismic Rehabilitation of Buildings", Washington, D.C.

Fib. (2003). “Displacement-based Seismic Design of Reinforced Concrete Buildings State-of-art Report”, Federation International de Beton, Lausanne Switzerland, 196 p.

Filiatrault A., D’Aronco D., Tinawi R. (1994). “Seismic Shear Demand of Ductile Cantilever Walls: a Canadian Code Perspective”. Can. J. Civ. Eng., Vol. 21.

Fiorato A.E., Oesterle R.G., and Corley W.G. (1983). “Behavior of Earthquake Resistant Structural Walls Before and After Repair”. ACI Journal, Vol 80, issue 5.

Giberson M.F. (1969). “Two Nonlinear Beams with Definitions of Ductility”. Journal of the Structural Division ASCE, 137-157.

He, X., Moaveni, B., Conte, J.P., Restrepo, J.I., and Elgamal, A. (2006). “Damage Identification of a Seven-Story Reinforced Concrete Shear Wall Building Tested on the UCSD-NEES Shake Table”. Proceedings of the 4th World Conference on Structural Control and Monitoring, San Diego.

Housner, G.W., and Trifunac M.D. (1967). “Analysis of Accelerograms – Parkfield earthquake”. Bulletin of Seismological Society of America; 57:1193-1220.

Hoehler, M.S., Panagiotou, M., Restrepo, J.I.,. Silva, J.F, Floriani, L., Bourgund, U., and Gassnerc, H., “Performance of Anchored Pipes in a 7 Story Building During Full-Scale Shake Table Tests”. (Under Review - Earthquake Spectra).

Ile, N., and Reynouard, J.M. (2005). “Behaviour of U-Shaped Walls Subjected to Uniaxial and Biaxial Cyclic Lateral Loading”. Journal of Earthquake Engineering, Vol. 9, No. 1, pp. 67–94.

Lang, A. and Restrepo, J.I. (2006). “Seismic Performance Evaluation of Gypsum Wallboard Partitions”. Proc. 8th National Conference in Earthquake Engineering, San Francisco, United States.

Lestuzzi P., Bachmann H., (2007). “Displacement Ductility and Energy Assessment from Shaking Table Tests on RC Structural Walls”. Engineering Structures, 29, 1708–1721.

Maekawa K., Pimanmas A., and Okamura H. (2003). “Nonlinear Mechanics of Reinforced Concrete”. Spon Press. London.

Makris, N. and Black, C.J. (2004). “Dimensional Analysis of Rigid-Plastic and Elastoplastic Oscillators under Pulse-Type Excitations”. J. of Engrg. Mech., 130, 1006, ASCE.

Makris, N., Black, C.J. (2004). “Dimensional Analysis of Bilinear Oscillators under Pulse-Type Excitations”. J. of Engrg. Mech. 130, 1019, ASCE.

Massone L.M. and Wallace J.W. (2004). “Load-Deformation Responses of Slender Reinforced Concrete Walls”. Structural Journal, 101, 1.

Massone L.M. (2006). “RC Wall Shear – Flexure Interaction: Analytical and Experimental Responses”. PhD Thesis. University of California Los Angeles.

Mavroeidis, G. and Papageourgiou, A. (2003). “A Mathematical Representation of Near Fault Ground Motions”. Bull. Seismol. Soc. Am. 93, 1099-1131.

Mavroeidis, G.P., Dong, G.A., Papageorgiou S. (2004). “Near-fault Ground Motions, and the Response of Elastic and Inelastic Single-Degree-of-Freedom (SDOF) Systems”. Earthquake Engineering & Structural Dynamics, Vol. 33, Issue 9, Pages: 1023-1049.

Mestyanek J.M. (1986). “The Earthquake Resistance of Reinforced Concrete Structural Walls of Limited Ductility”. MS Thesis, University of Canterbury, Christchurch, New Zealand.

Miki, T. (2004). “Nonlinear Analysis of Reinforced Concrete Structures Subjected to Seismic Loads by Using Three-dimensional Lattice Model”. Ph.D. thesis, Department of Civil Engineering, Tokyo Institute of Technology.

Miller K.R., Iwan W.D. (1978). “The Peak Harmonic Response of Locally Non-linear Sysyems”. Earthquake Engineering and Structural Dynamics, Vol. 6, 1, 79-87.

Moehle J, Bozorgnia Y, Yang TY. (2007). The Tall Buildings Initiative. Proceedings SEAOC Convention. 315-324.

National Research Council of Canada. (2005). “National Building Code of Canada, 12th Ed.”. Ottawa, Canada.

NEHRP. (2006). “NEHRP Recommended Provisions: Design Examples”. Washington DC.

Newmark, N.M. (1965). “Effects of Earthquakes on Dams and Embankments”. Fifth Rankine Lecture, Geotechnique 15, 139-160.

NZS 3101. (1995). “New Zealand Standard, Part 1- The Design of Concrete Structures”. Standards New Zealand, Wellington, New Zealand.

Orakcal, K., Wallace, J.W., and Conte, J.P. (2004). “Nonlinear Modeling and Analysis of Slender Reinforced Concrete Walls”. ACI Structural Journal, Vol. 101, No. 5, pp. 688 - 699.

Ozcelik, O., Luco, J.E., Conte, J.P., Trombetti, T.L., and Restrepo, J.I. (2008). “Experimental Characterization, Modeling and Identification of the NEES-UCSD

Shake Table Mechanical System". Earthquake Engineering & Structural Dynamics, Vol. 37, pp:243-264.

Panagiotou M., Restrepo J.I., Conte J.P. "Shake Table Test of a 7-Story Full Scale Reinforced Concrete Wall Building Slice - Phase I - Rectangular Wall". (To be submitted in ASCE Journal of Structural Engineering).

Panagiotou M, Restrepo J.I. (2007). "Lessons Learnt from the UCSD Full-scale Shake Table Testing on a 7-Story Residential Building Slice". Proceedings SEAOC Convention. 57-73.

Panagiotou, M., Restrepo., J.I. and Conte, J.P. (2007). "Shake Table Test of a 7-Story Full Scale Reinforced Concrete Structural Wall Building Slice Phase I: Rectangular Wall". SSRP 07-07 Report, Department of Structural Engineering, University of California at San Diego.

Panagiotou, M., Restrepo., J.I. and Conte, J.P. (2007). "Shake Table Test of a 7-Story Full Scale Reinforced Concrete Structural Wall Building Slice Phase II: T-Wall". SSRP 07-08 Report, Department of Structural Engineering, University of California at San Diego.

Panagiotou, M. and Restrepo., J.I. (2007). "Design and Computational Model for the UCSD 7-Story Structural Wall Building Slice". SSRP 07-09 Report, Department of Structural Engineering, University of California at San Diego.

Panneton M, Léger P, Tremblay R. (2006). "Inelastic Analysis of a Reinforced Concrete Shear Wall Building according to the National Building Code of Canada" Can. J. Civ. Eng., Vol. 33, 2006; 854-871.

Park R. and Paulay T. (1975). "Reinforced Concrete Structures". John Wiley & Sons, Inc., Hoboken, NJ.

Paulay, T., and Priestley M.J.N. (1992). "Seismic Design of Reinforced Concrete and Masonry Buildings". John Wiley & Sons, Inc., Hoboken, New Jersey.

Park, H., and Eom, T. (2007). "Truss Model for Nonlinear Analysis of RC members Subject to Cyclic Loading". J. Struct. Eng., 133, 1351.

Park, H., and Klingner, R. E. (1997). "Nonlinear analysis of RC members using plasticity with multiple failure criteria." J. Struct. Eng., 123 (5),643–651.

Petrangeli M. (1999). "Fiber Element for Cyclic Bending and Shear of RC Structures. II: Verification". Journal of Engineering Mechanics, Vol. 125, No. 9.

Pinho R. (2000). "Shaking Table Testing of RC Walls". ISET Journal of Earthquake Technology, Ppaer No. 405, Vol. 37, No. 4., pp.119-142.

Priestley M.J.N., Calvi G.M., Kowalsky M.J. (2007). "Displacement Based Seismic Design of Structures". IUSS Press, Pavia, Italy.

Restrepo, J.I. and Preti, M.A. (2006). "Two-level Displacement-based Design Methodology for Structural Wall Buildings". 2nd fib Congress, Naples, Italy.

Restrepo-Posada, J.I., Dodd, L.L., Park, R. and Cooke N. (1994). "Variables Affecting Cyclic Behavior of Reinforcing Steel". J. Struct. Engrg., Vol. 120, Issue 11, pp. 3178-3196.

Rodriguez, M.E., Restrepo, J.I. and Carr, A.J. (2002). "Earthquake-Induced Floor Horizontal Accelerations in Buildings". Earthquake Engineering and Structural Dynamics, Vol. 31, pages 693-718.

Ruiz-Garcia, J., and Miranda, E. (2003). "Inelastic Displacement Ratios for Evaluation of Existing Structures". Earthquake Engng. and Struct. Dyn., 32: 1237-1258.

Rutenberg A, Nsieri E. (2006). "The Seismic Shear Demand in Ductile Cantilever Wall Systems and the EC8 Provisions". Bulletin of Earthquake Engineering,, Vol. 4, 1–21.

Salonikios, T.N., Kappos, A.J., Tegos, I.A. and Penelis, G.G. (1999). "Cyclic Load Behavior of Low-Slenderness Reinforced Concrete Walls: Design Basis and Test Results". ACI Structural Journal, Vol. 96, 4.

Satyarno, I., Carr, A.J. and Restrepo, J.I. (1998). "Refined Pushover Analysis for the Assessment of Older Reinforced Concrete Buildings". Proceedings of the New Zealand Society for Earthquake Engineering Technical Conference, Wairakei, pp. 75-82.

SEAOC. (1995). "Vision 2000 - A Framework for Performance Based Earthquake Engineering". Vol. 1.

Sittipunt, C., and Wood, S.L. (1995). "Influence of Web Reinforcement on the Cyclic Response of Structural Walls". ACI Structural Journal, Vol 92, No. 6, pp. 745-756.

Sittipunt, C., Wood, S.L., Lukkunaprasit, P., and Pattararattanakul, P. (2001). "Cyclic Behavior of Reinforced Concrete Structural Walls with Diagonal Web Reinforcement," ACI Structural Journal, Vol. 98, No. 4, pp. 554-562.

Skinner, R.I., Robinson W.H., McVerry G.H. (1993). "An Introduction to Seismic Isolation", Wiley & Sons Ltd, Chichester, England.

Somerville, P.G., Krawinkler, H. and Alavi, B. (2000). "Development of Improved Ground Motion Representation and Design Procedures for Near-Fault Ground Motions". Final Report to CSMIP Data Utilization Program, Contract No. 1097-601.

Somerville, P.G. (2003). “Magnitude Scaling of the Near Fault Rupture Directivity Pulse”. Physics of the Earth and Planetary Interiors, 137, 201-212.

Sullivan T.J., Calvi G.M., Priestley M.J.N., Kowalsky M.J. (2003). “The Limitations and Performances of Different Displacement Based Design Methods”, Journal of Earthquake Engineering, Vol. 7, Special Issue, 201-241.

Taylor C.P., Cote P.A., and Wallace J.W. (1998). “Design of Slender Reinforced Concrete Walls with Openings”. ACI Structural Journal, 95, 4.

Thomsen J.H. and Wallace J.W. (2004). “Displacement-Based Design of Slender Reinforced Concrete Structural Walls-Experimental Verification”. J. Struct. Engrg. 130, 618.

To, N.H.T., Ingham, J.M., and Sritharan, S. (2001). “Monotonic Nonlinear Strut-and-Tie Computer Models”. New Zealand Nat. Soc. Earthquake Eng. Bull, 34 (3), 169–190.

To, N.H.T., Ingham, J.M., and Sritharan, S. (2003). “Cyclic Strut-and-Tie Modeling of Reinforced Concrete Structures”. Pacific Conf. on Earthquake Engineering, Paper No. 102, Christchurch, New Zealand.

Van Den Einde, L., Restrepo, J., Conte, J., Luco, E., Seible, F., Filiatrault, A., Clark, A., Johnson, A., Gram, M., Kusner, D. and Thoen, B. (2004). “Development of the George E. Brown Jr. Network For Earthquake Engineering Simulation (NEES) Large High Performance Outdoor Shake Table at the University of California, San Diego”. 13th World Conference in Earthquake Engineering, Paper # 3281, Vancouver, Canada.

Vecchio, F.J., Collins, M.P. (1986). “The Modified Compression Field Theory for Reinforced Concrete Elements Subjected to Shear”. Journal of the American Concrete Institute, vol. 83, No. 2, pp. 219-231.

Veletsos, A.S., Newmark, N.M. (1960). “Effects of Inelastic Behavior on the Response of Simple Systems to Earthquake Motions. Proceed. 2nd World Conf. on Earthq. Engrg., Tokyo, Japan. Vol II, 895-912.

Veletsos, A.S., Newmark, N.M., Chelepati, C.V. (1965). “Deformation Spectra for Elastic and Elastoplastic Systems Subjected to Ground Shock and Earthquake Motions”. Proceed. 3rd World Conf. on Earthq. Engrg., Wellington, New Zealand, Vol. II, 663-682.

Uniform Building Code UBC-1997. (1997). International Conference of Building Officials, Whittier, California, USA.

Wallace J.W., Orakcal K. ACI 318-99 Provisions for Seismic Design of Structural Walls. ACI Structural Journal, No. 4, 2002; 499-508.